Measurement of the inclusive numu Charged Current cross section in the Near Detector of the T2K experiment

Ravonel Salzgeber, Melody

UNIVERSITÉ DE GENÈVE
Département de Physique Nucléaire et Corpusculaire

FACULTÉ DES SCIENCES
Prof. A. Blondel

Measurement of the Inclusive ν_μ Charged Current Cross Section in the Near Detector of the T2K Experiment

THÈSE

présentée à la Faculté des Sciences de l'Université de Genève
pour obtenir le grade de Docteur ès sciences, mention physique

par

Melody Ravonel Salzgeber

de Genève, Suisse

Thèse N° 4465

GENÈVE
Atelier d'impression ReproMail
2012

Cette thèse donne lieu à une publication à paraître en 2013 sous le même titre:
Measurement of the Inclusive ν_μ Charged Current Cross Section in the Near Detector of the T2K Experiment

UNIVERSITÉ DE GENÈVE

FACULTÉ DES SCIENCES

Doctorat ès sciences
Mention physique

Thèse de *Madame Melody RAVONEL SALZGEBER*

intitulée :

" Measurement of the Inclusive ν_μ Charged Current Cross Section in the Near Detector of the T2K Experiment "

La Faculté des sciences, sur le préavis de Messieurs A. BLONDEL, professeur ordinaire et directeur de thèse (Département de physique nucléaire et corpusculaire), M. POHL, professeur ordinaire (Département de physique nucléaire et corpusculaire), F. SANCHEZ NIETO, professeur (Institut de Fisica d'Altes Energies, Universitat Autonoma de Barcelona, España), A. WEBER, docteur (University College Oxford & Science & Technology Facilities Council, Department of physics, Oxford, United Kingdom) et B. POPOV (Laboratoire de Physique Nucléaire et de Hautes Energies, Université de Paris VI, France), autorise l'impression de la présente thèse, sans exprimer d'opinion sur les propositions qui y sont énoncées.

Genève, le 17 septembre 2012

Thèse - 4465 -

Le Doyen, Jean-Marc TRISCONE

N.B. - La thèse doit porter la déclaration précédente et remplir les conditions énumérées dans les "Informations relatives aux thèses de doctorat à l'Université de Genève".

Acknowledgments

Durant les cinq années de ma thèse, j'ai eu la chance de rencontrer beaucoup de personnes, dont certaines sont devenues des amis. En tout premier lieu, je voudrais remercier le Professeur Alain Blondel pour m'avoir donné l'opportunité de travailler avec lui dans l'expérience T2K. Son soutien et sa compréhension dans les différentes étapes de ma vie ont été essentiels. J'ai également apprécié sa confiance et la très grande liberté d'action. Cette liberté et cette confiance conjuguées ont su me donner une certaine indépendance et responsabilité dans mes choix tout au long de ma thèse. Je remercie également la fondation Boninchi et le fond national pour la recherche en Suisse pour avoir sponsorisé ces cinq années de recherche.

Quisiera también agradecer al Profesor Federico Sanchez por haberme integrado en los distintos grupos de trabajo, por ayudarme durante todo el tiempo de mi tesis con distintos consejos. Gracias Federico por el tiempo que me has dado y por las distintas conversaciones que hemos podido tener. También quisiera agradecer a Anselmo y al grupo de Valencia por haber podido trabajar con ellos al volver de mi baja por maternidad de forma mas cercana. Gracias, en general, por el ambiente acogedor que he podido vivir con ustedes en distintas ocasiones.

I also would like to specially thanks Alfons Weber for his time, for helping me in this last year of my thesis. I appreciate a lot your support, disponibility and advises that have been very helpful. I am also grateful to Boris Popov that gave me many advises for the redaction of my thesis, and for the discussions that helped me in enlarging my physical views. In addition to them, many other people inside the collaboration have been helping me with advises and support (Emilio Radiconi, Gabriela Cartanesi, Kendall Mahn, Mark Hartz, Martin Tzanov, Roman Tacic, Steve Manly, Christophe Bronner, Morgan Wasco, Scott Oser, ...).

Je remercie également les différents techniciens qui m'ont beaucoup aidé au début de ma thèse. Merci à Florian Mascciocchi, Pierre Béné, et Eric Périn, ainsi que les secrétaires Catherine, Peggy et Liliane pour votre aide tout au long de ma thèse. Travailler au sein du groupe de Genève a été un immense plaisir pour moi. J'ai beaucoup apprécié l'ambiance amicale qui régnait entre nous. Merci à Marie, Andrea, Gustav, Raphaël, Nicolas, Sébastien, Alexis, Alexander, Mark, Enrico, et Fanny pour les différents moments que nous avons passé ensemble au bureau ou ailleurs. Merci, en particulier, à Fanny pour ton amitié, ton soutien et ta compréhension. Merci également pour le temps que tu as passé a relire cette thèse, pour tes commentaires et encouragements. Thank you too, Mark, for the great corrections and suggestions you provided me in the first attempt of reading my thesis, and thanks also to all of you who read this thesis and shared your opinions with me.

Je voudrais également remercier ma famille, ma belle-famille, mes parents et beau-parents ainsi que mes amis pour leur soutien inconditionnel et aide durant mes différents voyages. Merci à mes parents, pour m'avoir soutenu durant toutes mes études et au water-polo pour m'avoir changé les idées, et permis de me défouler le moment venu. Pour terminer, merci à toi Daniel, mon mari. Ton amour, ton soutien, ta compréhension dans les moments où je n'étais pas présente pour notre famille m'ont aidés et motivés. Le temps que tu m'as donné et ton écoute m'ont portés et m'ont permis d'achever ce qui avait été commencé sans souci additionnel.

Résumé

T2K (Tokai-vers-Kamiokande) est une expérience visant à étudier les propriétés des neutrinos. Elle se situe au Japon et inclut un détecteur proche et un détecteur lointain. Elle a été construite pour mesurer précisément le dernier angle de mélange, θ_{13}, à travers l'observation de l'apparition de neutrinos électroniques dans un faisceau constitué principalement de neutrinos muoniques. De plus, elle peut également mesurer les paramètres liés à la disparition des ν_μ (θ_{23} and Δm^2_{23}). T2K est la première expérience à avoir observé l'apparition de neutrinos électroniques dans son détecteur lointain. Cette observation a permis la mesure de l'angle θ_{13} avec une valeur non nulle en 2011. En 2012, d'autres expériences, en particulier les expériences utilisant des réacteurs nucléaires, ont confirmé cette mesure avec une bonne précision.

Dans l'expérience T2K, le faisceau de neutrino est créé à Tokai (J-PARC) via l'accélération de protons jusqu'à une énergie de 30 GeV. Ceux-ci interagissent avec une cible en graphite de 90 cm de long produisant des mésons principalement des pions et des kaons. Les mésons chargés positivement sont focalisés de manière à produire essentiellement un faisceau de neutrinos muoniques avec une énergie d'environ 600 MeV (pic d'énergie). Le faisceau est dirigé vers le détecteur proche constitué de deux détecteurs. Le premier ce trouve sur l'axe du faisceau et mesure son profile, tandis que le deuxième se trouve hors axe, à un angle de 2.5^o. Il en va de même pour le détecteur lointain, Super-Kamiokande (SK). Cet angle a été choisi de manière à avoir une distribution en énergie du faisceau avec un pic à 600 MeV. Ceci, de manière à observer un maximum d'oscillations des ν_μ pour la distance donnée entre Tokai et SK de 295 km.

Le détecteur proche, hors axe, est appelé ND280. Il est utilisé pour mesurer le taux d'interactions de neutrinos avant qu'ils n'aient le temps d'osciller ainsi que les différents bruits de fond liés à la mesure d'apparition des neutrinos électroniques dans le détecteur lointain. Il permet ainsi de contraindre les sections efficaces et le flux à SK pour l'analyse d'oscillation. La mesure du taux d'interaction permet également la mesure de sections efficaces. Celles-ci sont, pour l'instant, très peu connues à basse énergie. Pour pouvoir fournir des résultats précis sur les différentes inconnues restantes dans la physique des neutrinos, il est nécessaire d'augmenter nos connaissances dans ce domaine; ceci constituant l'objectif de cette thèse.

Cette thèse a pour but de fournir une mesure de la section efficace des neutrinos muoniques interagissant par courants chargés en utilisant une méthode dépendant très peu des modèles inclus dans les simulations. Les courants chargés ont été choisis car ils correspondent à la majeure partie de la statistique. Leur sélection est basée sur l'observation d'une trace compatible avec un muon de charge négative. Le résultat de la mesure est présenté comme une section efficace différentielle moyennée en flux en fonction de l'angle et de l'impulsion du muon. Bien que ce format ne soit pas le plus pratique pour le comparer à d'autres expériences, il fournit aux théoriciens un bon terrain pour tester leurs derniers modèles.

Le flux est donné par le Monte Carlo du faisceau et est optimisé à travers des données extérieures à T2K, comme par exemple les mesures prises par NA61. L'analyse présentée dans cette thèse utilise les données prises en 2010 et 2011 comprenant 10.796×10^{19} interactions de protons avec la cible. 4485 événements ont été sélectionnés comme des interactions via courants chargés dans le premier scintillateur du ND280. La section efficace totale moyennée en flux au détecteur proche obtenue est de,

$$\langle\sigma_{\mathrm{CC}}\rangle_\phi = (6.91 \pm 0.13(stat) \pm 0.84(syst)) \times 10^{-39} \frac{\mathrm{cm}^2}{\mathrm{nucleon}} \quad (1)$$

Durant ces cinq années de thèse, j'ai en premier été impliquée dans le banc de test des Micromegas utilisés pour amplifier les signaux produit par des particules chargés traversant des chambres à projection temporelles (TPCs). Ensuite, j'ai passé beaucoup de temps à analyser différentes sélections de courants chargés. Ceci a permis de vérifier systématiquement les aptitudes du détecteur proche à reconstruire les traces. Durant la dernière année, j'ai eu le plaisir de commencer l'analyse des sections efficaces des courants chargés, dont les premiers résultats sont présentés dans cette thèse et constitue la première analyse officielle.

Le premier chapitre décrit de façon générale la physique d'oscillation des neutrinos, tandis que le deuxième chapitre résume la physique de leurs interactions. En particulier les différents modèles utilisés dans les Monte-Carlo pour calculer les sections efficaces seront décrits. L'expérience T2K et le banc de test au CERN sont décrits dans le chapitre 3 et 4. Les mesures du banc de test sont maintenant utilisées lors de la calibration des données. Calibration, reconstruction et sélection des événements sont décrites dans le chapitre 5. Les erreurs systématiques sont ensuite résumées dans le chapitre 6, tandis que la description de la méthode et les résultats finaux sont donnés dans les chapitres 7 et 8.

Abstract

The T2K (Tokai-to-Kamiokande) experiment is a long baseline neutrino experiment. It has been built in order to precisely measure the last unknown neutrino mixing angle, θ_{13}, by the observation of the $\nu_\mu \rightarrow \nu_e$ appearance. In addition, it can also refine the parameters related to the ν_μ disappearance (θ_{23} and Δm^2_{23}). T2K has been the first experiment to observe the appearance of the electron neutrinos providing the first hint for a non-zero value of θ_{13} in 2011. The statistical significance of this measurement was, however, not high enough to call it a discovery. In 2012, other experiments, in particular, reactor experiments have now measured this angle with good precision.

T2K is located in Japan. The neutrino beam is created at Tokai (J-PARC) via the acceleration of protons up to 30 GeV that impinges on a long graphite target (90 cm). The result of the proton interactions with the graphite target is the production of mainly pions and kaons. The positively charged mesons are focused and decay into neutrinos with a peak energy around 600 MeV. The neutrino beam is aimed towards the near detector complex, at 280 meters from the target. There, there are two main detectors, the on-axis detector that measures the beam profile and the magnetized off-axis detector at 2.5^o with respect to the beam direction. The far detector, Super-Kamiokande (SK), is located at the same off-axis angle. This angle has been chosen so that the neutrino beam energy is peaked at 600 MeV. For this energy, the effect of muon neutrino oscillation is maximal for the given distance between SK and the target at Tokai, which is 295 km.

The off-axis near detector (ND280) is used to measure the muon neutrino interactions and the several backgrounds for the ν_e appearance searches at the far detector. While the rate of muon neutrino interactions can be used to constrain cross section and flux at the far detector for the oscillation analysis, it can also be used to measure the cross section itself at the near detector. Cross sections at low energies are actually not well known, and any information about them in this energy range is essential to decrease systematic errors on cross sections.

The goal of this thesis is to provide a model independent measurement of the muon neutrino charged current cross section. Charged current interactions have been chosen, as they correspond to the largest sample of available data. It uses mainly the tracker region of ND280 to reconstruct trajectories of charged particles. The selection is based on the observation of a track compatible with a negatively charged muon. The measurement is given as a flux-averaged double differential cross section in muon momentum and angle. Although this format is less practical to compare with other experiments, it provides a useful input for theorists to test their latest models.

The flux is given by the beam Monte-Carlo and tuned to in-situ and external data, including the NA61/SHINE experiment. The analysis presented in this thesis uses the data taken in 2010 and 2011, comprising a total of 10.796×10^{19} protons on target. A total of 4485 inclusive charged current interaction candidates were selected in the first fine-grained scitillator detector of ND280 (FGD1). The flux-averaged total cross section measured at the near detector is,

$$\langle \sigma_{\mathrm{CC}} \rangle_\phi = (6.91 \pm 0.13(stat) \pm 0.84(syst)) \times 10^{-39} \frac{\mathrm{cm}^2}{\mathrm{nucleon}} \quad (2)$$

During the five years of my thesis, I have first been involved in the testing of the readout of the ND280 Time Projection Chambers (TPCs). After that, I have spent time in analyzing different muon neutrino charged current selections. This has proven to be very useful in understanding the detector performance and in finding bugs at the lower reconstruction level. Finally, in the

last year, I have started the charge current inclusive cross section analysis, whose results are presented in this thesis and constitute the first official T2K cross section analysis.

The first chapter is an overview of the neutrino oscillation physics, while the second chapter describes the neutrino interactions and the various models used currently in the Monte-Carlo generators to calculate the different cross sections. These models are sometimes very simplified and source of discussions between theorists and experimentalists. Chapter 3 describes the T2K experiment in details. The tests and the validation of the readout used for the Time Projection Chambers (TPCs) of ND280 is presented in Chapter 4. These measurements have been made at CERN before and during the construction of the near detector. They are now used in the calibration of the data which is explained briefly together with the event reconstruction and selection in Chapter 5. The several systematic uncertainties taken into account in the final results are summarized in Chapter 6. The method used to obtained them and the final results themselves are given in Chapters 7 and 8.

Contents

1 Introduction **1**

1.1 The neutrino in the Standard Model (SM) . . . 1
1.2 The neutrino oscillation history . . . 2
1.2.1 The solar neutrino problem . . . 2
1.2.2 The solution . . . 3
1.3 The neutrino sources . . . 6
1.4 Neutrino oscillation theory . . . 8
1.4.1 Three-flavor oscillations in vacuum . . . 8
1.4.2 Two flavor oscillations approximation . . . 11
1.4.3 Neutrino oscillations in matter . . . 12
1.5 Principles of neutrino oscillation experiments . . . 13
1.5.1 The mass hierarchy and CP phase . . . 14
1.6 Current status and future of the neutrino physics . . . 15
1.6.1 Neutrino cross sections and oscillations . . . 18

2 Neutrino interactions **19**

2.1 The Weak Interaction . . . 19
2.2 Neutrino interactions with matter . . . 20
2.3 Neutrino cross sections . . . 21
2.4 Inclusive cross section . . . 23
2.5 Charged Current Quasi-Elastic (CCQE) interactions . . . 28
2.6 Single pion, photon, η and kaon production . . . 29
2.7 Neutrino-nuclei scattering . . . 30
2.7.1 The relativistic Fermi gas (RFG) . . . 32
2.7.2 Spectral Function . . . 34
2.8 Coherent pion production . . . 36
2.9 Deep Inelastic Scattering (DIS) . . . 38
2.10 Final State Interactions (FSI) . . . 39
2.11 Summary . . . 39

3 The T2K experiment **41**

3.1 The T2K beam . . . 42

3.1.1 The J-PARC Accelerator . . . 43

3.1.2 The Beamline . . . 43

3.1.3 The flux . . . 49

3.2 The T2K detectors . . . 52

3.3 The Far Detector: Super-Kamiokande (SK) . . . 52

3.3.1 Overview . . . 52

3.4 The Near Detector Complex . . . 55

3.5 On-axis detector (INGRID) . . . 57

3.5.1 Purpose . . . 57

3.5.2 The 16 modules . . . 58

3.5.3 The proton module . . . 58

3.5.4 Calibration . . . 58

3.6 The off-axis detector . . . 59

3.6.1 Purpose . . . 59

3.6.2 The Magnet . . . 60

3.6.3 Side Muon Range Detector (SMRD) . . . 61

3.6.4 Electromagnetic CALorimeter (ECal) . . . 62

3.6.5 π^0 Detector (P0D) . . . 63

3.6.6 Fine Grained Detectors (FGDs) . . . 65

3.6.7 Time Projection Chambers (TPCs) . . . 66

3.7 Summary . . . 69

4 Tests and validation of the TPC readout **71**

4.1 Micromegas . . . 71

4.2 The Test Bench . . . 73

4.2.1 The Test Box . . . 74

4.2.2 The sources . . . 74

4.2.3 The Gas system . . . 77

4.2.4 The electronic readout . . . 78

4.3 Characteristic measurements of the micromegas and results . . . 78

4.4 Summary . . . 85

5 Event reconstruction and selection in the ND280 **87**
5.1 The near detector software overview . . . 88
5.2 Samples . . . 89
5.3 Calibration . . . 90
5.3.1 Calibration of the electronics . . . 90
5.3.2 Physics calibration . . . 91
5.4 Reconstruction . . . 91
5.4.1 TPC reconstruction . . . 92
5.4.2 FGD reconstruction . . . 94
5.4.3 Global reconstruction . . . 95
5.4.4 Additional modifications to the reconstruction . . . 95
5.5 The charged current inclusive selection . . . 96
5.6 Stability and low-level cross-checks . . . 102
5.7 Event pile-up . . . 104
5.8 Performance . . . 105
5.9 Summary . . . 111

6 Systematic uncertainties **113**
6.1 Binning . . . 113
6.2 Detector response uncertainties . . . 115
6.2.1 Track Quality Cut . . . 116
6.2.2 TPC track efficiency . . . 117
6.2.3 TPC Particle IDentification (PID) . . . 119
6.2.4 TPC momentum scale systematics . . . 120
6.2.5 TPC momentum resolution . . . 122
6.2.6 TPC-FGD matching inefficiency . . . 122
6.2.7 Fiducial mass . . . 124
6.2.8 Charge miss-identification . . . 124
6.2.9 Backgrounds . . . 125
6.2.10 Total uncertainty . . . 130
6.3 Cross section model uncertainties . . . 130
6.3.1 Charged-current quasi-elastic scattering (CCQE) . . . 130
6.3.2 Charged-current inelastic scattering (CC-nQE) . . . 132
6.3.3 Charged current scattering uncertainties . . . 135
6.3.4 Final State Interaction (FSI) model . . . 136
6.4 Flux systematic uncertainties . . . 140
6.5 Summary . . . 143

7 Cross section measurement method **145**

7.1 The cross section definition . . . 145

7.2 The unfolding algorithm . . . 147

7.3 Reweighting the MC . . . 150

7.4 Uncertainty on the inferred number of events ($\widehat{N}_{t_k}$) . . . 156

7.4.1 Statistical uncertainty . . . 156

7.4.2 Systematic uncertainty . . . 159

7.5 The number of iterations . . . 161

7.6 Summary . . . 165

8 Cross section measurements **167**

8.1 Additional systematic error on the cross section measurement . . . 167

8.1.1 Integrated Flux . . . 167

8.1.2 Number of Target Nucleons . . . 169

8.1.3 Systematic uncertainty due to the algorithm . . . 172

8.1.4 Total systematic and statistical error . . . 174

8.2 Differential cross section results . . . 176

8.3 Total cross section results . . . 189

9 Conclusion **193**

A Calculation of the matter potential **197**

Chapter 1

Introduction

In December 1930, Wolfgang Pauli [1] proposed, for the first time, the existence of a new neutral particle with spin $\frac{1}{2}$ in order to save energy and angular momentum conservation in nuclear β decay. This new particle is now called *neutrino*. He gave an upper limit to the neutrino mass: $m_\nu < 1$ MeV which is now improved by six orders of magnitude.

Fermi included this particle in a point-like four-fermions interaction with a relatively weak coupling strength G_F [2]. The weak force is now best described as a field in the Standard Model (SM) of electro-weak interactions and is mediated by a neutral vector boson Z or a charged boson $W^\pm$, with a strength unified with the electromagnetic one: $G_F\ O(\alpha/M^2_{W,Z})$ (see Sec. 2.1 for more details).

1.1 The neutrino in the Standard Model (SM)

The SM is a theory describing the electromagnetic, weak, and strong nuclear interactions, which mediate the dynamics of the known subatomic particles. There are two kinds of particles in the SM, fermions and gauge bosons. While fermions are particles of spin 1/2, bosons are fields with integer spin mediating the strong, weak and electromagnetic interactions. According to the spin-statistics theorem, fermions respect the Pauli exclusion principle. Each fermion has a corresponding antiparticle. The fermions can be divided into two families: quarks and leptons. Leptons do not interact via strong interactions contrary to quarks. The current knowledge of the elementary particles is given in Fig. 1.1. As neutrinos only feel the weak force, they are leptons with no charge. The three generations of neutrinos have been discovered as flavor eigenstates of the interactions by measuring the energy of the final state particles containing a definite charged lepton. The neutrinos were then called after the charged lepton name as electron muon and tau neutrinos. The observations were all consistent with a single helicity state: all neutrinos are left-handed (LH) and all anti-neutrinos are right-handed. The simplest case in order to describe this situation is that the neutrinos are massless: $m_\nu = 0$, as assumed in the SM.

This simplest possibility has now been refuted by experimental data. The next-to-simplest possibility does not require new neutrino states or interactions but only that neutrinos are massive and mix.

The fact that the mass eigenstates are different from the flavor eigenstates can lead to neutrino flavor changes $\nu_\alpha \leftrightarrow \nu_\beta$. In the case of a coherent superposition of the mass eigenstates, the

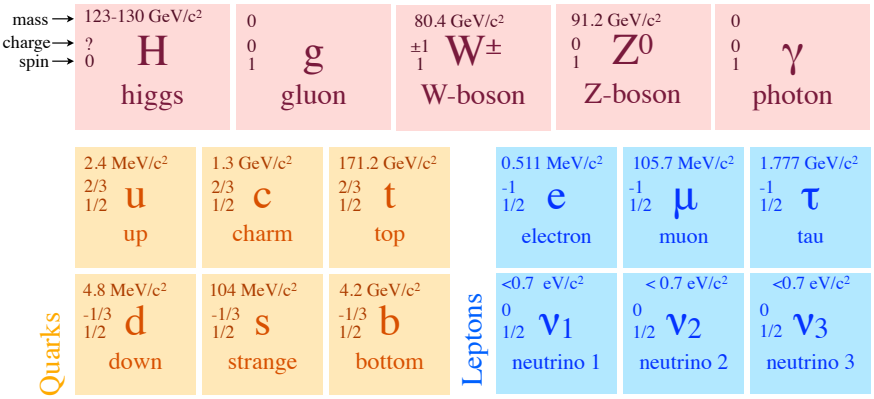

Figure 1.1: SM of elementary particles given in term of mass eigenstates.

flavor of the neutrino can change as a function of the distance. This is generally called neutrino oscillation. Oscillation is then possible, if the neutrinos, in a certain flavor state, are a linear superposition of mass eigenstate (ν_1, ν_2, ν_3) with definite masses (m_1, m_2, m_3) different from the mixed one, with mass differences smaller than the typical quantum uncertainty in the process, as realized by Pontecorvo, Maki, Nakagawa, and Sakata [3].

1.2 The neutrino oscillation history

1.2.1 The solar neutrino problem

During the first half of the twentieth century, physicists became convinced that the source of the sun's energy was fusion reactions in its core. According to this theory, four protons (or hydrogen nuclei) are converted into a helium nucleus(^{4}He), two positrons(e^+) and two electron neutrinos (ν_e). Because of their very small cross section, the neutrinos escape easily from the sun. While this theory was widely accepted there was no way of observing the sun's core and directly testing the hypothesis.

Ray Davis's Homestake Experiment [4] was the first to detect solar neutrinos and its first results were announced in 1968. Over a period of decades the Homestake experiment consistently observed only about 1/3 the number of neutrinos predicted by the Standard Solar Models (SSM), calculated by John Bahcall. Three classes of explanation were suggested to solve the mystery: the calculations were wrong, Ray Davis's experiment was wrong, the SM was wrong by setting the neutrinos as massless particles. This last possibility was the less believed, as the SM has been validated very precisely by other kind of experiments like the measurement of the Z, W masses, etc.

The Homestake experiment was very technical relying on radio-chemical techniques rather than real time direct detection. Because of its difficulties, many physicists did not trust its results.

In 1989, the Kamiokande-II experiment confirmed that the number of neutrino events that were observed was less than predicted by the theoretical model of the Sun. The directional information

was the smoking gun signature of solar neutrinos, demonstrating directly for the first time that the sun is a source of neutrinos [5]. However their result was showing a smaller discrepancy. This experiment, using a water Cerenkov detector, was very sensitive but only to high-energy neutrinos that are produced by a rare nuclear reaction in the sun [6]. The original Homestake experiment with chlorine was not exclusively sensitive to the same high-energy neutrinos.

In the 1990s, three new solar neutrino experiments made additional confirmations favoring new physics: SAGE (Soviet-American Gallium Experiment) [7], GALLEX (GALLium EXperiment) [8], and Super-Kamiokande[9]. To prevent interferences from different backgrounds the experiments are underground. Therefore Homestake took place in the South Dakota Gold Mine 1460 m (4800 feet) underground, GALLEX inside the 2912 m high Gran Sasso mountain, and SAGE in the Baksan mountain, and Super-Kamiokande 1000 m underground in the Mozumi Mine.

Since the energy threshold of the chlorine is 0.814 MeV, Homestake could only see neutrinos coming with an energy $E_\nu > 0.814$ MeV. Therefore neutrinos coming from *pp* and *pep* reactions of the sun cannot be seen by this experiment.Therefore, GALLEX and SAGE were massive detectors containing ^{71}Ga as target and not ^{36}Cl. Their energy threshold was then 0.233 MeV which allows to see all the sun reactions as we can see in Fig. 1.2. The use of Gallium allows them to detect lower energy neutrinos. For this range of energy, the neutrino flux could be calculated more accurately. Super-Kamiokande was a much larger detector than the previous Kamiokande setup and was able to give a more precise measurement. The gallium experiments as well as the water experiment observed less neutrinos than expected, although not in the same proportions.

In 1997, precise measurements were published on the sound speed throughout the Sun [11]. It agrees to a precision of 0.1% with the theoretical calculation. These measurements suggested that the theoretical model of the Sun was correct.

To reconcile the results between the different experiments new neutrino physics was needed.

1.2.2 The solution

Neutrinos are created not only in the sun but also in the atmosphere. It is the Super-Kamiokande collaboration that presented first in August 1998 [12], in the atmospheric sector, anomalous flavor ratio involving a deficit of ν_μ coming from below (i.e., through the Earth). The data showed a clear up down angular asymmetry of the atmospheric ν_μ flux, with less ν_μ coming from the longest distances. This deficit together with the solar neutrino problem shows that the problem might be more at the level of the neutrino than at the level of the neutrino sources, since similar results are observed with neutrinos created by different sources. Although the final proof for neutrino oscillation was still missing, massive neutrinos started to be accepted by the scientific community.

It is the Sudbury Neutrino Observatory (SNO)[13] that reported first the direct solar neutrino oscillation evidence by using heavy water (D_2O) in June 2001. The heavy water target provided three different reactions for ^8B solar neutrinos: electron neutrino charged current scattering on deuteron (CC), neutrino neutral current scattering on deuteron (NC) and elastic scattering of neutrinos on electrons (ES). While CC is only sensitive to electron neutrinos, NC measurements are equally sensitive to all neutrino flavors while elastic scattering is sensitive to all flavors but not in the same proportions. Each channel provided a measure of the different neutrino flux: $\phi_{CC} = \phi_e$, $\phi_{NC} = \phi_e + \phi_\mu + \phi_\tau \equiv \phi_e + \phi_{\mu\tau}$, $\phi_{ES} = \phi_e + \alpha\phi_{\mu\tau}$ ($\alpha \approx 0.154$).

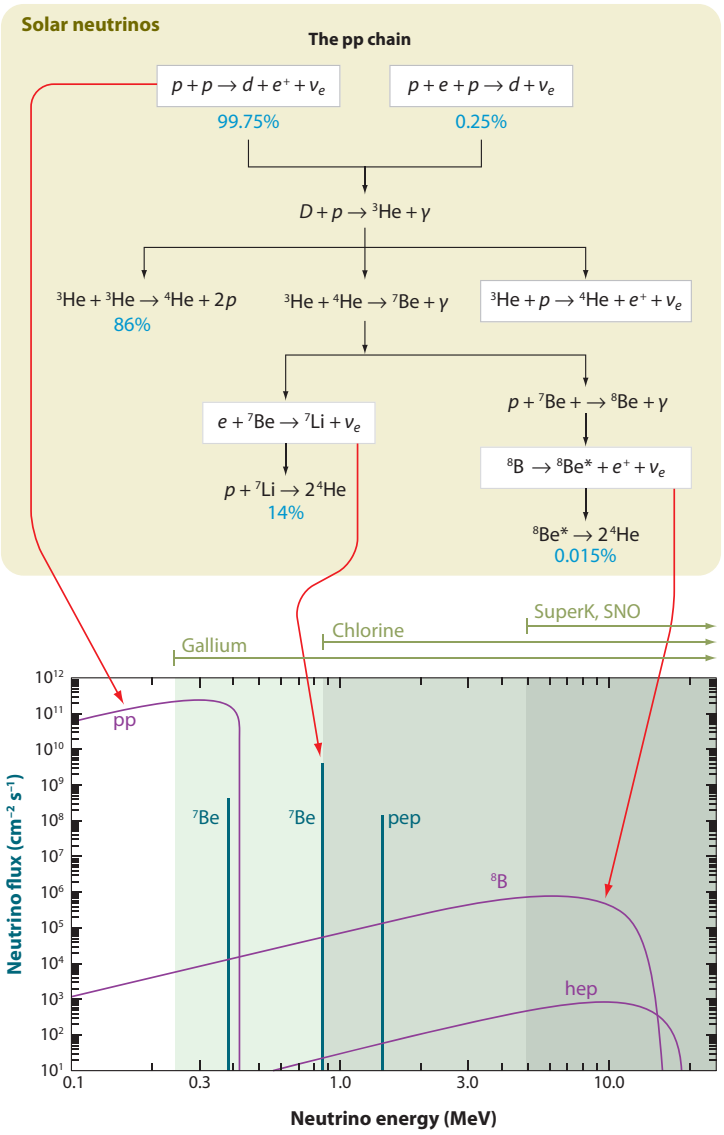

Figure 1.2: The solar cycle and the resulting solar neutrino energy spectrum. Abbreviations: SNO (see Sec.1.2.2), Sudbury Neutrino Observatory; SuperK, Super-Kamiokande. [10].

For their first measurement the SNO collaboration used their detector in a mode that is sensitive only to electron neutrinos. They found that one third of the arriving solar neutrinos are electron neutrinos. Which corresponds to the chlorine and gallium experiment. Super-Kamiokande observed about half of the predicted number. If the SM were right the two measurements should be the same and all neutrinos observed should be electron neutrinos. They concluded that Super-Kamiokande not only measured electron neutrinos but also the muon neutrinos.

They determined the total number of solar neutrinos of all types combining the SNO and the Super-Kamiokande measurements. The total number agreed with the number predicted by the theoretical model of the Sun [14] as shown in Fig. 1.3. This measurement constitutes the final proof needed for neutrino oscillation.

After extensive statistical analysis, it was found that about 35% of the arriving solar neutrinos

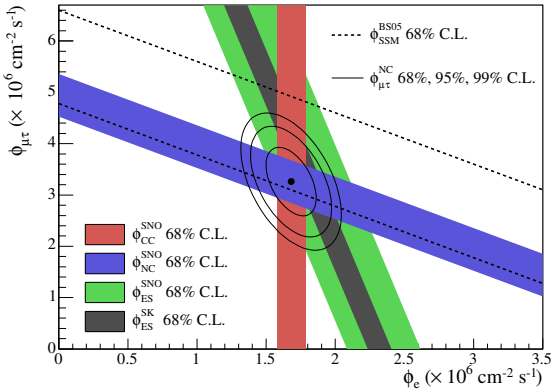

Figure 1.3: Combined flux of ν_μ and ν_τ ($\phi_{\mu\tau}$) versus the flux of ν_e. The charged current (CC), neutral currents (NC), and elastic scattering (ES) flux measurements are indicated by the filled bands. The total ^8B solar neutrino flux predicted by the Standard Solar Model (SSM) is shown in dashed black lines, and the flux measured with the NC channel is represented by the solid blue band parallel to the model prediction. The narrow gray band parallel to the Sudbury Neutrino Observatory (SNO) ES result corresponds to the Super-Kamiokande (SK) result. The intercepts of these bands with the axes represent the $\pm 1\sigma$ uncertainties. The non-zero value of $\phi_{\mu\tau}$ provides strong evidence for neutrino flavor transformation [15].

are electron-neutrinos, with the others being muon- or tau-neutrinos. In addition, they provide also the total number of high energy neutrinos of all types in the heavy water detector. This result alone shows that most of the neutrinos produced in the Sun are changed into muon and tau neutrinos by time they reach the Earth. This neutrino flavor transformation is called oscillation and is only possible if the neutrinos have masses, which was in contradiction with the SM.

The theoretical description of neutrino oscillation was first suggested by Bruno Pontecorvo, in 1957, which proposed that neutrino-antineutrino transitions may occur in analogy with neutral kaon mixing [16]. Although such matter-antimatter oscillation has not been observed, this idea formed the conceptual foundation for the quantitative theory of neutrino flavor oscillation, which was first developed by Maki, Nakagawa, and Sakata in 1962[3] and further elaborated by Pontecorvo in 1967 [17]. The theoretical interpretation has now converged, and is called, the neutrino standard model, in which three different neutrino masses m_i in the sub-electronvolt range are involved together with three different mixing angles θ_{ij}, where θ_{12} is generally referred to as the solar angle and θ_{23} the atmospheric angle.The data from atmospheric ν_μ oscillation is now interpreted as arising from dominant $\nu_\mu \to \nu_\tau$, with a subdominant contribution of $\nu_\mu \to \nu_e$.

In 2011, the Borexino experiment [18] published a precision measurement of the Beryllium-7 neutrino flux as well as the first evidence for the pep solar neutrinos.

In the same year, the T2K collaboration has been the first experiment to show with confidence a non-zero value for the last missing angle θ_{13}. This measurement is now being improved by the Daya Bay, Reno and Double Chooz collaborations, in March 2012, which reported the θ_{13} angle with a good precision.

In this section, the key experiments that have shown the existence of neutrino oscillation have been introduced. While the first experiments have used *natural* neutrinos created in the sun or in the atmosphere, the latest results have used *man-made* neutrinos (see Sec. 1.3 for more details).

1.3 The neutrino sources

As already seen in the previous section, the neutrino sources can be divided into *natural* and *man-made* neutrinos.

- The natural sources:
  - *The primordial neutrinos:* The primordial neutrinos are the neutrinos that have been created during the primordial nucleosynthesis (see Fig. 1.4) and later during the growth of matter fluctuations. It constitutes the cosmic neutrino background (CνB) with a predicted neutrino temperature $T_\nu^0 = 1.945$ K [19]. Cosmological data

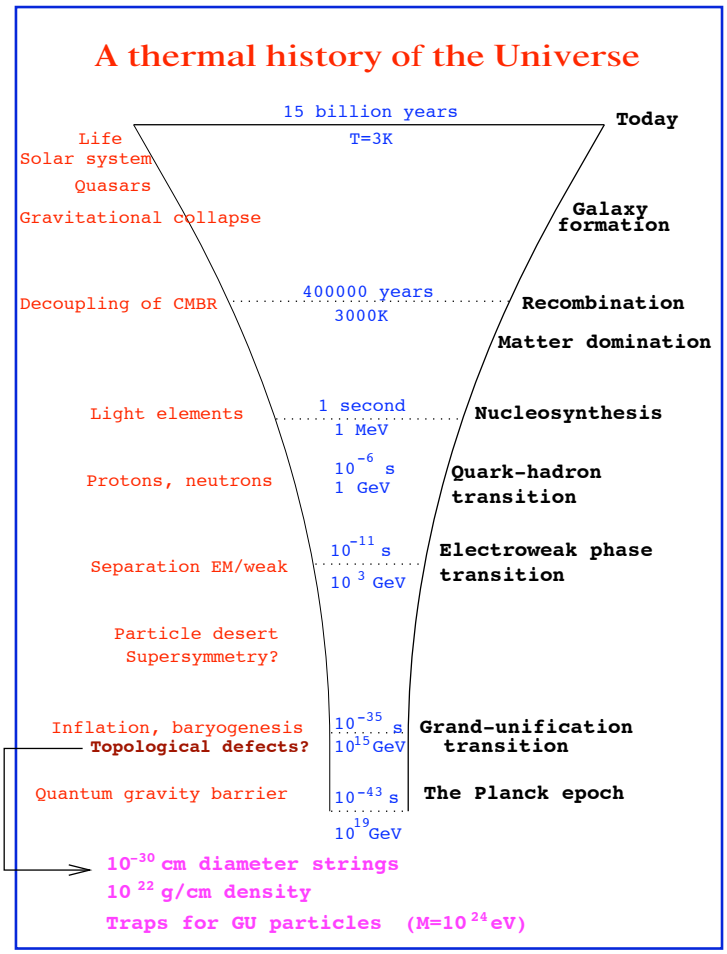

Figure 1.4: A thermal history of the universe [20].

is able to give an upper limit on neutrino masses in the sub-electronvolt range and is consistent with the three families of neutrinos [19, 21].

- *Cosmogenic neutrinos:* Cosmogenic neutrinos are produced when very high energy cosmic rays, mainly protons, interacts with the cosmic microwave background (CMB) via photo-pion production at energies $E > 10^{20}$ eV. The neutrinos are then produced during the decay of the pions following the reaction: $p + \gamma \rightarrow n + \pi^+$ or $p + \gamma \rightarrow p + \pi^+ + \pi^-$. This leads to an important decrease of the proton energy that is generally called the GZK (after Greisen[22], Zatseptin and Kuzmin [23]) cutoff[1]. The flux of such high energetic neutrinos is expected to be in the range of 0.001 - 0.1 $km^{-2}\ year^{-1}$ [24, 25].
- *The neutrinos from fusion processes in the stars:* As already seen in the previous section (see Fig. 1.2), they are produced mainly in 3 reactions that are part of the proton-proton chain in the core of the stars.
  - $p + p \rightarrow d + e^+ + \nu_e$ (pp neutrinos)
  - $e^- + {}^7Be \rightarrow {}^7Li + \nu_e$ (beryllium neutrinos)
  - ${}^8B \rightarrow {}^8Be^* + e^+ + \nu_e$ (boron neutrinos)

  The Sun, for example, produces electron neutrinos with a flux of $6.4 \times 10^{10} cm^{-2} s^{-1}$ on Earth [10].

  Neutrinos are also produced in explosive stellar processes [26]. When the core of a large star ($M \geq 8M_\odot$) runs out of nuclear fuel, it collapses to proton-neutron star. About 99% of the gravitational binding energy change, about 3×10^{53} ergs, is carried away, from the inner part of the collapse, by neutrinos of all flavors and energies of order ∼20 MeV [27].
- *The neutrinos coming from the Earth:* The neutrinos coming from the different nuclear reactions inside the Earth (geo-neutrinos) or in several physical processes that make life on Earth possible. They come from the decays of radiogenic elements as uranium, thorium or potassium that keep our planet heated and produce flux of $\bar{\nu}_e$. They constitute a background to the solar neutrino searches.
- *The atmospheric neutrinos:* The atmospheric neutrinos, that come from the interactions of cosmic rays in the atmosphere, producing charged pions and kaons that decay into muons and ν_μ. The muons decay afterwards into e, ν_e and ν_μ [28]:

$$\begin{aligned} K, \pi \rightarrow &\quad \mu &+ &\quad \nu_\mu \\ \mu \rightarrow &\quad \nu_\mu + \nu_e + e \end{aligned} \tag{1.1}$$

- The man-made neutrinos:
  - *Nuclear reactors*: The fission of the ^{235}U, for example, produces two new elements with atomic massed centered near 95 and 135 and free neutrons. These new elements are extremely unstable, since they are too rich of neutrons, and decay toward stable nuclei with an average of 6 beta decays: $n \rightarrow p + e^- + \bar{\nu}_e$. This corresponds to a very intense and isotropic flux of $\bar{\nu}_e$: $9.3 \times 10^{20}\ \bar{\nu}_e s^{-1}$ for a 5-GW(thermal) reactor [10, 29].
  - *Accelerators*: Accelerators, as in T2K, can also produce Neutrinos, using a beam of protons that interact in a target producing mesons, mainly pions and kaons. They are focused by a set of magnetic horns and directed onto a long decay tunnel in

[1]Note that generally the neutron convert itself to a proton via beta decay producing besides the neutrinos from the pion decay additional anti-neutrinos

which they will decay and produce mainly muon neutrinos. Depending on the horn current, one can focus positively or negatively charged particles that will give a flux of neutrinos or anti-neutrinos. This will be explained in more details in Sec. 3.1.

Depending on the sources, different kinds of neutrinos are produced. While the sun and the reactors produce electron neutrinos and anti-neutrinos respectively, atmospheric processes and accelerators produce mainly muon neutrinos or anti-neutrinos. This allows different studies of the neutrino oscillation probabilities that are explained in more details in the next section.

1.4 Neutrino oscillation theory

The physics of neutrino oscillations is based on the understanding that neutrino flavor states, the states that participate in the weak interaction, are superpositions of the neutrino mass states.

In this section, we will simply describe the neutrino in terms of wave functions, since the additional terms coming from a complete treatment of the neutrino as a spinor field [30] are suppressed at $O(m_\nu/E)$. Therefore the spinor properties of neutrinos will be ignored during their propagation.

A neutrino in a certain flavor state is denoted as $|\nu_\alpha\rangle$ ($\alpha = e,\ \mu,\ \tau$). Assuming now that the state $|\nu_\alpha\rangle$ is a plane wave solution of the Schroedinger equation, we have:

$$i\frac{\mathrm{d}}{\mathrm{dt}}|\nu_\alpha(\mathrm{t})\rangle = \hat{\mathrm{H}}^{\mathrm{f}}|\nu_\alpha(\mathrm{t})\rangle \quad \Rightarrow\ |\nu_\alpha(\mathrm{t})\rangle = \mathrm{e}^{-\mathrm{i}\hat{\mathrm{H}}^{\mathrm{f}}\mathrm{t}}|\nu_\alpha(0)\rangle$$

where $\hat{H}^f$ is the Hamiltonian in the flavor basis.

If neutrinos have non-zero masses, their flavor eigenstates do not necessarily coincide with their mass eigenstates. The flavor eigenstates $|\nu_\alpha\rangle$ are then described by a linear superposition of the mass eigenstates through a nontrivial unitary matrix U ($U \neq 1$ and $UU^\dagger = 1$). A state after traveling a certain distance produced originally with a flavor α evolves then as follows:

$$|\nu_\alpha(t)\rangle = \sum_j\ U^*_{\alpha j}\ |\nu_j(t)\rangle \quad ,\ \text{with j} = 1,\ 2,\ 3.$$

The amplitude of probability that this state $|\nu_\alpha\rangle$ at time t is detected as a state $|\nu_\beta\rangle$ at time $t = 0$ after a charge current interaction, $\nu_\alpha(t)N' \to l_\beta N$, is given by:

$$\begin{aligned} A_{\alpha\beta} &= \langle\nu_\beta|\nu_\alpha(t)\rangle \\ &= \sum_i\sum_j U_{\beta i}\ U^*_{\alpha j}\langle\nu_i(0)|\nu_j(t)\rangle \end{aligned} \tag{1.2}$$

1.4.1 Three-flavor oscillations in vacuum

We now only consider, the case where neutrinos propagate in vacuum. We denote by, $\hat{H}^n_{free} \equiv U^\dagger\hat{H}^f U$ the Hamiltonian operator that is diagonal for the mass eigenstates and E_j ($j = 1, 2, 3$), the eigenvalues. The amplitude of probability can be rewritten as

$$A_{\alpha\beta} \ = \ \sum_i\sum_j\ U^*_{\alpha j}U_{\beta i}\langle\nu_i(0)|e^{-i\hat{H}^n_{free}t}|\nu_j(0)\rangle$$

$$= \sum_i \sum_j U^*_{\alpha j} U_{\beta i} e^{-E_j t} \langle \nu_i(0) | \nu_j(0) \rangle$$
$$= \sum_j U^*_{\alpha j} U_{\beta j}\ e^{-iE_j t} \tag{1.3}$$

where we used the propriety that the eigenstates are orthogonal.

In general, a unitary matrix is parameterized by $n(n-1)/2$ angles and $n(n+1)/2$ complex phases where n is the dimensionality. Some of the phases can be absorbed into the definitions of the particle wave functions. As the unitary matrix is unchanged, if all the particles are changed by the same phase, $2n-1$ phases can be absorbed by the particle wave functions. For the three flavor case, this leaves only one phase δ [17, 3] and 3 angles. In consequence, the coupling of leptons versus anti-leptons can be different from each other in CC weak interactions. In other terms, a non-zero δ means the violation of the CP symmetry in the leptonic sector. However, this is subject to a few conditions: the masses must not be degenerate, and the mixing matrix must have three non-zero angles (i.e. there is no parameterization that describes the mixing with only two angles). If these conditions are met, then it is possible to have a non-trivial complex phase and CP violation. This possibility is tantalizing because the amount of known CP violation in the quark sector is not enough to explain the matter and anti-matter asymmetry in the universe.

The neutrino mixing matrix can be expressed as the multiplication of two matrices:

$$V = UA, \tag{1.4}$$

where,

$$A = \begin{pmatrix} e^{i\alpha} & 0 & 0 \\ 0 & e^{i\beta} & 0 \\ 0 & 0 & 1 \end{pmatrix},$$

is the Majorana phase matrix, which does not enter into oscillation phenomena and U is often called the Pontecorvo-Maki-Nakagawa-Sakata (PMNS or MNS) matrix [31],

$$U = \begin{pmatrix} U_{e1} & U_{e2} & U_{e3} \\ U_{\mu 1} & U_{\mu 2} & U_{\mu 3} \\ U_{\tau 1} & U_{\tau 2} & U_{\tau 3} \end{pmatrix} \tag{1.5}$$
$$= \begin{pmatrix} 1 & 0 & 0 \\ 0 & c_{23} & s_{23} \\ 0 & -s_{23} & c_{23} \end{pmatrix} \begin{pmatrix} c_{13} & 0 & s_{13}e^{-i\delta} \\ 0 & 1 & 0 \\ -s_{13}e^{i\delta} & 0 & c_{13} \end{pmatrix} \begin{pmatrix} c_{12} & s_{12} & 0 \\ -s_{12} & c_{12} & 0 \\ 0 & 0 & 1 \end{pmatrix} \tag{1.6}$$
$$= \begin{pmatrix} c_{12}c_{13} & s_{12}c_{13} & s_{13}e^{i\delta} \\ -s_{12}c_{23} - c_{12}s_{13}s_{23}e^{i\delta} & c_{12}c_{23} - s_{12}s_{13}s_{23}e^{i\delta} & c_{13}s_{23} \\ s_{12}s_{23} - c_{12}s_{13}c_{23}e^{i\delta} & c_{12}s_{23} - s_{12}s_{13}c_{23}e^{i\delta} & c_{13}c_{23} \end{pmatrix}, \tag{1.7}$$

where $s_{ij} = \sin\theta_{ij}$ and $c_{ij} = \cos\theta_{ij}$. The 3×3 unitary mixing matrix, U, can be then understood for leptons as the analog of the CKM matrix used in the quark sector.

We have seen that the Hamiltonian in the mass eigenstate basis is diagonal. Assuming that the mass eigenstates with masses (m_1, m_2, m_3) are relativistic and move with same momentum[2]

[2]This assumption is in fact not correct but leads to the right result as pointed out in [32]. It can be justified in the wave-packet formalism. In this formalism, the same momentum assumption means that the wave-packet description becomes unnecessary in stationary situations, when the temporal structure of the neutrino emission and detection processes is irrelevant and the complete information on neutrinos is contained in their spectrum which is correct.

$p \gg m_i$, then $E_i = \sqrt{p^2 + m_i^2} \simeq p + \frac{m_i^2}{2p}$ and :

$$\hat{H}^n_{free} = diag(E_1, E_2, E_3) \simeq p1 + diag(m_1^2, m_2^2, m_3^2)/2p \tag{1.8}$$

The probability of a neutrino emitted with a flavor α interacting at time t and detected with a flavor β is then given by:

$$\begin{aligned} P(\nu_\alpha \to \nu\beta; t) &= |A_{\alpha\beta}|^2 \\ &= |U^*_{\alpha j} U_{\beta j} e^{-iE_j t}|^2 \\ &= |U^*_{\alpha j} U_{\beta j} e^{-i(p+m_i/2p)t}|^2 \end{aligned}$$

The multiplication by a phase will not change the result of the probability:

$$\begin{aligned} P(\nu_\alpha \to \nu\beta; t) &= |U^*_{\alpha j} U_{\beta j} e^{-i(p+m_j^2/2p)t} \times e^{i(m_1^2+m_2^2)/4p} \times e^{ip}|^2 \\ &= |U^*_{\alpha j} U_{\beta j} e^{-i((m_j^2-(m_1^2+m_2^2)/2)/2p)t}|^2 \end{aligned} \tag{1.9}$$

This means that the Hamiltonian, $\hat{H}^n_{free}$, can be re-written as:

$$\hat{H}^n_{free} = \frac{1}{2E} \begin{pmatrix} -\delta m^2/2 & 0 & 0 \\ 0 & \delta m^2/2 & 0 \\ 0 & 0 & \pm\Delta m^2/2 \end{pmatrix} \tag{1.10}$$

where we have set $p \simeq E$, and defined two independent squared mass differences:

$$\delta m^2 = m_2^2 - m_1^2 (> 0 \text{ by convention}) , \tag{1.11}$$

$$\Delta m^2 = |m_3^2 - (m_1^2 + m_2^2)/2| \tag{1.12}$$

The same equations hold for anti-neutrinos with $U \to U^*$. In the literature, we often see $\delta m^2 \equiv \Delta m^2_{12}$ and $\Delta m^2 \approx \Delta m^2_{31} \approx \Delta m^2_{32}$. We here choose to describe it with the lower- and uppercase deltas to refer to the experimental fact that $\delta m^2 \ll \Delta m^2 \simeq |m_3^2 - m_{1,2}^2|$, which means that the mass spectrum is composed of two close mass states $\nu_{1,2}$ and another state, ν_3, which is more separated in mass. However the mass hierarchy of those states is not yet known. If ν_3 is heavier than $\nu_{1,2}$, we will refer to as normal hierarchy ($+\Delta m^2$). On the contrary if ν_3 is lighter, we will refer to as an inverted mass hierarchy ($-\Delta m^2$) as depicted in Fig. 1.5.

With the constant Hamiltonian, and assuming that for relativistic point-like particle the distance L they propagate during the time interval t satisfies: $L \simeq t$. In this case, we have:

$$P(\nu_\alpha \to \nu\beta; L) = |U^*_{\alpha j} U_{\beta j} e^{-i((m_j^2-(m_1^2+m_2^2)/2)/2E)L}|^2 \tag{1.13}$$

With appropriate mass mixing parameters, a 2ν approximation works well in a variety of situations essentially because experiments thus far have been sensitive primarily to only one of the two well separated squared mass differences, and also because θ_{13} is small. The two flavor oscillation approximation is explained in more detail in Sec. 1.4.2. To test CP symmetry violation ($U \neq U^*$), sensitivity to all 3ν mass-mixing parameters is crucial. In vacuum, the violation of

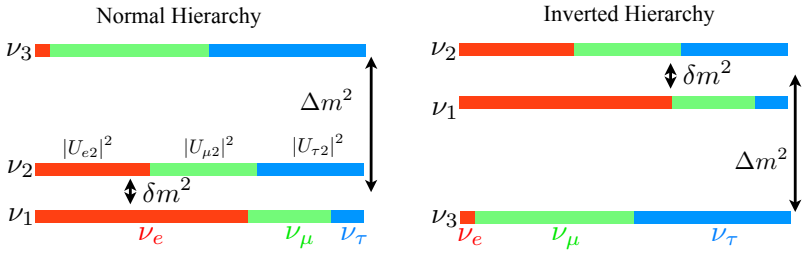

Figure 1.5: Flavor neutrino amount in the neutrino mass eigenstates, with their mass differences.

the CP symmetry can be observed by comparing the oscillation probability of neutrinos and anti-neutrinos

$$P_{\alpha\beta}(\nu) - P_{\alpha\beta}(\bar{\nu}) = 2\sin 2\theta_{12}\sin 2\theta_{23}\sin 2\theta_{13}\cos\theta_{13}\sin\delta \times \sin\left(\frac{\Delta m^2 - \frac{\delta m^2}{2}}{4E}L\right)\sin\left(\frac{\Delta m^2 \frac{\delta m^2}{2}}{4E}L\right)\sin\left(\frac{\delta m^2}{4E}L\right) \tag{1.14}$$

where we denoted $P_{\alpha\beta}(\nu) = P(\nu_\alpha \to \nu\beta; L)$ and $P_{\alpha\beta}(\bar{\nu}) = P(\bar{\nu}_\alpha \to \bar{\nu}_\beta; L)$ and $\alpha\beta = e\mu,\ \mu\tau$, or τe. In the case of oscillation in the vacuum, CP violation means different probabilities of oscillation for neutrinos and anti-neutrinos. Note, however, that if neutrinos are travelling in matter instead, their probability of oscillation are different than anti-neutrinos due to matter effects even if there is no CP violation (see Sec. 1.4.3).

1.4.2 Two flavor oscillations approximation

Although we now know that all observations have to be understood in the scope of three flavor oscillations, the measurements were first compared to the case of two flavor oscillations, where the probability is much simpler. Fig. 1.6 shows the ratio of muon-like data events in SK to no-oscillation Monte Carlo prediction in the case of two flavor oscillations of $\nu_\mu \to \nu_\tau$.

This special case offers, a simpler comprehension of the oscillation, where the transformation matrix is a simple rotation, $U(\theta_0) = \begin{pmatrix} \cos\theta_0 & \sin\theta_0 \\ -\sin\theta_0 & \cos\theta_0 \end{pmatrix}$, where θ_0 is the unique mixing angle.

Using 1.13, and replacing $m_j^2 - (m_1^2 + m_2^2)/2$ by the only mass squared difference in the two flavors case, Δm, we get:

$$P(\nu_\alpha \to \nu_\beta; L) = |A_{\alpha\beta}|^2 = |U^*_{\alpha j} U_{\beta j} e^{-i(\Delta m^2/2E)L}|^2 \tag{1.15}$$

$$= \sin^2(2\theta_0)\ \sin^2\left(\frac{\Delta m^2 L}{4E}\right) \tag{1.16}$$

For L given in [m] or [km], E in [MeV] or [GeV] and δm^2 in [eV^2], the probability is given by:

$$P(\nu_\alpha \to \nu_\beta; L) = \sin^2(2\theta_0)\ \sin^2\left(1.27\frac{\Delta m^2 L}{E}\right). \tag{1.17}$$

If $\theta_0 = 0$ or neutrinos have the same masses, there are no oscillations.

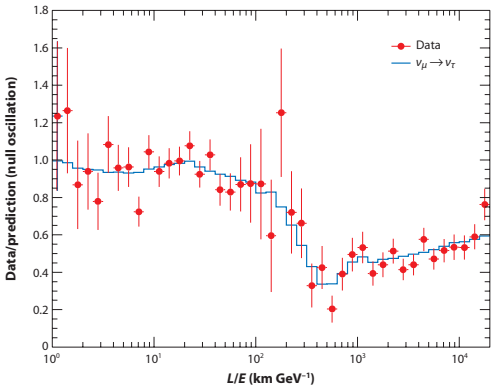

Figure 1.6: The ratio of the muon-like data events in Super-Kamiokande to no-oscillation Monte Carlo predictions (red data points) versus the reconstructed neutrino path length-to-energy ratio (L/E). The first half-cycle of oscillation is visible as a dip, whereas subsequent oscillations at large L/E are completely averaged out ($P_{\mu\mu} \sim 1/2$). The L/E position of the dip fixes $\Delta m^2 \sim 2.5 \times 10^{-3} eV^2$, while its depth fixes $\sin^2 2\theta_{23} \sim 1$ (nearly maximal mixing). The ratio is consistent with $\nu_\mu \to \nu_\tau$ oscillations (solid blue line) [10].

We see that the same value of $\sin^2 2\theta_0$ can be obtained either for $\theta_0 < \pi/4$ or for the complementary angle $\pi/2 - \theta_0 > \pi/4$. This is generally referred to as the octant ambiguity of vacuum 2ν oscillations in literature.

1.4.3 Neutrino oscillations in matter

In the next chapter, we will study in more detail the neutrino interactions. In this section, we study the effect of neutrino interactions with the background fermions when they propagate in matter. Scattering via Neutral Currents (NC) proceeds with the same amplitude for all neutrino flavors and cannot be observable on flavor oscillation since it will change an immeasurable phase to all neutrino states. The scattering via Charged Current (CC) interaction, however, involves only ν_e, as matter ordinary contain electrons and not muons nor taus. ν_e acquires then an extra CC interaction energy, generally called potential, and denoted V_{CC}. The explicit calculation of this potential is done in the Appendix A and we find: $V_{CC} = \pm\sqrt{2} G_F n_e$, where n_e is the electron number density [33, 34] and $\pm$ is for neutrinos and anti-neutrinos respectively.

The effective Hamiltonian in the flavor basis is now given by:

$$\hat{H}^f_{mat} = U \hat{H}^n_{free} U^\dagger + \hat{H}^f_{int} \tag{1.18}$$

$$= \frac{1}{2E} U \begin{pmatrix} -\delta m^2/2 & 0 & 0 \\ 0 & \delta m^2/2 & 0 \\ 0 & 0 & \pm\Delta m^2/2 \end{pmatrix} U^\dagger + \begin{pmatrix} V_{CC} & 0 & 0 \\ 0 & 0 & 0 \\ 0 & 0 & 0 \end{pmatrix} \tag{1.19}$$

The total Hamiltonian is thus the sum between the Hamiltonian for a free particle and the Hamiltonian for a particle interacting with matter.

Because the potential is not identical for neutrino and anti-neutrino, matter effects can lead to different probabilities of interaction for neutrino and anti-neutrino. The observation of this

difference only reflects the fact that our universe is principally composed of matter and is not the manifestation of the CP violation.

In the case of a constant density, $\hat{H}^f_{tot}$ can be diagonalized in a new basis $|\nu^m_i\rangle$. In this basis the evolution of the mass eigenstates will follow the Schroedinger equation as:

$$i\ \frac{\mathrm{d}}{\mathrm{dt}}\nu_{\mathrm{m}} = \hat{\mathrm{H}}^{\mathrm{m}}_{\mathrm{tot}}\nu_{\mathrm{m}} = \epsilon_{\mathrm{m}}\nu_{\mathrm{m}},$$

where ϵ_i $(i = 1, 2, 3)$ are the eigenvalues of the Hamiltonian.

For non-constant density, the evolution of the flavor eigenstates of a neutrino is then given by,

$$i\frac{\mathrm{d}}{\mathrm{dt}}\nu_\alpha = \hat{\mathrm{H}}^{\mathrm{f}}_{\mathrm{mat}}\nu_\alpha \tag{1.20}$$

Eq. 1.20 can be rewritten as,

$$i\ \frac{\mathrm{d}}{\mathrm{dt}}\nu_{\mathrm{m}} \quad = \quad \left(\hat{H}^m_{mat} - iU^\dagger_t\frac{\mathrm{d}}{\mathrm{dt}}\mathrm{U_t}\right)\nu_m \tag{1.21}$$

where we defined, $U(\theta_m(t)) \equiv U_t$ and expressed the flavor eigenstates in terms of mass eigenstates $\nu_\alpha = U_t\ \nu_m$. One can show that if the density variation is very slow (adiabatic case - $\frac{\mathrm{dV}}{\mathrm{dt}} \ll 1$), a neutrino eigenstate of $\hat{H}^m_{tot}$ at time t remains an eigenstate over time. When $n_e = 0$ (e.g. $V_{CC} = 0$), as in vacuum, the propagation eigenstate is always $|\nu_2\rangle$ in our convention and there is no oscillation. This situation can be applied to the case of a ν_e production in the sun. At the beginning, $|\nu_e\rangle$ is close of being an eigenstate of propagation and remains in this state, if we consider that the density of the sun varies slowly, as in the adiabatic approximation. When the neutrino reaches the vacuum where $n_e = 0$, its eigenstate becomes $|\nu_2\rangle$ and stays as such until it interacts in the detector. The probability to observe an electron neutrino from the sun on earth is then $|\langle\nu_e|\nu_2\rangle|^2 = \sin^2\theta_{12}$ which is about $\sin^2\theta_{12} \approx 1/3$ which is effectively equal to the fraction of ν_e's observed on earth with respect to the prediction of the solar model.

1.5 Principles of neutrino oscillation experiments

There are two ways of measuring the oscillation parameters. Firstly, we can directly measure the probability that a neutrino of flavor α at the origin is measured of flavor β in the far detector (ν_β appearance) or one minus the probability that the neutrino remains of the same flavor α (ν_α disappearance). Depending on the type of the oscillation experiments both or only the disappearance method can be employed. In the case of the T2K experiment, we can measure the muon neutrino disappearance as well as the appearance of electron neutrinos.

Neutrino oscillation experiments can be divided into two categories depending on the sources of neutrinos: *natural* experiments, and *man-made* experiments. In the natural experiments, there are two main kinds of oscillation experiments depending on the source of the neutrinos: solar neutrino and atmospheric neutrinos. As already pointed out in Section 1.2, the first observation of oscillation effects was the oscillation of the neutrinos coming from the sun. Atmospheric neutrino oscillations were observed afterwards by Super-Kamiokande, where they could see a clear deficit of neutrinos coming from long distances through the Earth. Depending where the neutrinos are created in the atmosphere, matter effects can change the probabilities of neutrino

oscillations, therefore atmospheric neutrinos are good complementary studies for mass hierarchy determination.

There are two kinds of man made neutrino oscillation experiments: reactors and accelerators. The product of the nuclear fission decays into electron anti-neutrinos with low energies $E_{\bar{\nu}_e} < 10$ MeV. Therefore, the reactor oscillation experiments are only measuring $\bar{\nu}_e$ disappearance, since the energies are too low to produce leptons in a charged current reaction of $\bar{\nu_\mu}$ and ν_μ. The current detectors are, in general, filled with liquid scintillator loaded with Gadolinium. The $\bar{\nu}_e$ are detected by inverse beta decay: $\bar{\nu}_e + p \rightarrow n + e^+$, where they detect a prompt signal from the annihilation of the positron and a delayed signal of the photons coming from the neutron capture on Gadolinium.

Accelerator sources can produce muon neutrinos in a wide range of energies. These experiments with detectors at different baselines and energies provide a wide range of mixing angles. Neutrinos created with the accelerators come from the decay of pions and kaons produced in the bombardment of a fixed target with high-energy protons. They can use on-axis beams as K2K [35], MINOS [36], NOMAD [37] and CHORUS [38], which provide a wide spectrum suitable to measure probabilities for different energies or off-axis beam, as T2K or NOVA [39], in order to maximize the flux in the oscillation region at the far detector. Accelerator experiments can provide very precise measurement of ν_μ disappearance channel, and can therefore give good complementary results to the atmospheric oscillation studies. They can provide also good precision of the ν_e appearance channel and are good complementary results to the $\bar{\nu}_e$ disappearance channel of the reactor experiments. As the tau production threshold is 3 GeV in reactor experiments, ν_τ appearance can only be studied with high energy accelerator facilities.

As already pointed out, the knowledge of the mass hierarchy and CP phase are one of the main unknowns still remaining. Reactor and accelerator experiments as well as atmospheric neutrinos can address these questions.

1.5.1 The mass hierarchy and CP phase

The way reactor and accelerator experiments have sensitivity to the mass hierarchy is different. While accelerator experiments use the matter effect to distinguish between the two, reactor experiments use Fourier transform to put in evidence Δm_{31} in the $\bar{\nu}_e$ disappearance probability as given in Eq. 1.23,

$$\begin{aligned} P(\bar{\nu}_e \rightarrow \bar{\nu}_e) &= P(\nu_e \rightarrow \nu_e) && (1.22) \\ &= 1 - c_{13}^4 \left[\sin^2 2\theta_{12} - \sin^2 2\theta_{13} \sin^2 \Delta_{31}\right] \\ &\quad + \sin^2 2\theta_{13} s_{12}^2 \left[\sin^2 \Delta_{31} - \sin^2(\Delta_{31} - \Delta_{21})\right] && (1.23) \end{aligned}$$

where we defined $c_{ij} = \cos\theta_{ij}$ and $s_{ij} = \sin\theta_{ij}$, $\Delta_{ij} \equiv \frac{|\Delta m^2_{ij}|L}{4E_\nu}$ [3] . The difference Δm_{31} for the normal mass hierarchy and the inverted mass hierarchy is not the same. This implies a very small differences in the probabilities that can be better observed via Fourier transform [40].

In the case of the accelerators, the observation of the mass hierarchy effects can be achieved in the case of long baseline where matter start affecting the oscillation probabilities. In this case

[3] Note that Eq. 1.22 is only true if neutrino are in vacuum. As these kind of experiments use relatively short baseline this assumption can be done.

the ν_e appearance probability is given in Eq. 1.24 [41]:

$$P(\nu_\mu \to \nu_e) = x^2 f^2 + 2xyfg(\cos\delta\cos\Delta_{31} - \sin\delta\sin\Delta_{31}) + y^2 g^2 \quad (1.24)$$
$$P(\bar{\nu}_\mu \to \bar{\nu}_e) = x^2 \bar{f}^2 + 2xy\bar{f}g(\cos\delta\cos\Delta_{31} + \sin\delta\sin\Delta_{31}) + y^2 g^2 \quad (1.25)$$

where,

- $x \equiv \sin\theta_{23}\sin 2\theta_{13}$,
- $y \equiv \alpha\cos\theta_{23}\sin 2\theta_{12}$,
- $\alpha \equiv |\Delta m^2_{21}/\Delta m^2_{31}|$
- $f, \bar{f} \equiv \frac{\sin((1\mp\hat{A})\Delta_{31})}{1\mp\hat{A}}$,
- $g \equiv \frac{\sin(\hat{A}\Delta_{31})}{\hat{A}}$,
- $\hat{A} \equiv |A/\Delta_{31}m^2_{31}|$,
- $A = V_{CC}E_\nu$,

To get the probabilities for $\Delta m^2_{31} < 0$, the transformations:

- $\hat{A} \to -\hat{A}$,
- $\Delta \to -\Delta$ (implying $f \leftrightarrow \bar{f}$ and $g \leftrightarrow -g$)

can be applied to Eqs. 1.24 and 1.25.

From Eq. 1.24, we see that appearance probabilities depend on the CP phase, which is not the case of the disappearance probability in Eq. 1.23. In the appearance probability the effects of the CP phase can appear either as, a difference between neutrino and anti-neutrino probabilities. In this case, the method is sensitive to the term depending on $\sin\delta$ that vanishes when $\delta = 0$ or 180^o.

The other possibility is to have the complete L/E behavior of the ν_e appearance probability. For a fixed distance between detector and source, as can be achieved by accelerator experiments, L/E behavior can be easily translated to the neutrino energy spectrum. If good resolution can be achieved in the far detector in order to distinguish the first and second oscillation maximum, invaluable spectral information is available to unambiguously extract the oscillation parameter. For this occasion, on-axis beam should be adopted as it gives a wider spectrum.

1.6 Current status and future of the neutrino physics

In 2011, T2K was the first experiment to directly measure a non-zero value of θ_{13}. The precision on this value has then strengthened by subsequent results from MINOS [36] and Double-CHOOZ [42], culminating in the recent announcement of a 5.2σ and 4.9σ by Daya Bay [43] and RENO [44] respectively. Thanks to these experiment the value of θ_{13} is now known at the same level of precision as the other mixing angles.

In the following, the current knowledge of angle and mass differences is given [45]. We have in the solar sector,

$$\Delta m^2_{21} = (7.62 \pm 0.19) \times 10^{-5} eV^2 \quad (1.26)$$
$$\sin^2 \theta_{12} = 0.320^{+0.015}_{-0.017} \quad (1.27)$$

In the atmospheric sector and 1-3 sector, we have in the case of normal hierarchy $\Delta m^2_{31} > 0$,

$$\Delta m^2_{31} = 2.53^{+0.08}_{-0.10} \times 10^{-3} eV^2 \quad (1.28)$$
$$\sin^2 \theta_{23} = 0.49^{+0.08}_{-0.05} \quad (1.29)$$
$$\sin^2 \theta_{13} = 0.026^{+0.003}_{-0.004} \quad (1.30)$$
$$(1.31)$$

and for the inverted hierarchy case $\Delta m^2_{31} < 0$

$$\Delta m^2_{31} = -2.40^{+0.10}_{-0.08} \times 10^{-3} eV^2 \quad (1.32)$$
$$\sin^2 \theta_{23} = 0.53^{+0.05}_{-0.07} \quad (1.33)$$
$$\sin^2 \theta_{13} = 0.027^{+0.003}_{-0.004} \quad (1.34)$$

The latest result given from the different experiments are shown in Figs. 1.7 and 1.8.

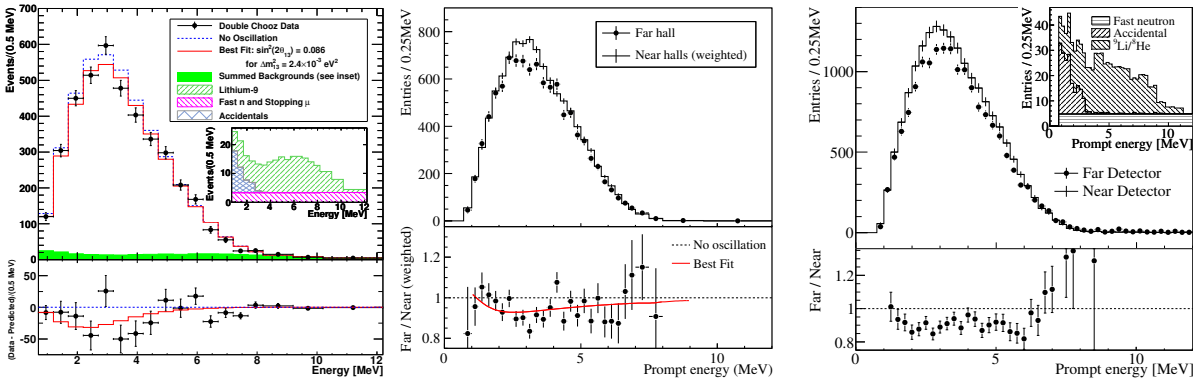

Figure 1.7: Results from the Double-CHOOZ, Daya Bay and RENO experiment (left, middle and right respectively). Each result is shown in the same unified manner: Top: Measured prompt energy spectrum of the far detector compared with the no-oscillation prediction from the measurements of the two near detectors. Spectra were background subtracted (for Daya Bay and RENO), includes background for Double-CHOOZ. Inset (Double-CHOOZ and RENO): stacked histogram of backgrounds. Uncertainties are statistical only. Bottom: The ratio of measured and predicted no-oscillation spectra. The red curve is the best-fit solution and the dashed line is the no-oscillation prediction [42, 43, 44].

They found:

$$\sin^2 2\theta_{13}|_{\text{Double-CHOOZ}} = 0.109 \pm 0.030(stat) \pm 0.025(syst) \quad (1.35)$$
$$\sin^2 2\theta_{13}|_{\text{Daya Bay}} = 0.089 \pm 0.010(stat) \pm 0.005(syst) \quad (1.36)$$
$$\sin^2 2\theta_{13}|_{\text{RENO}} = 0.113 \pm 0.013(stat) \pm 0.019(syst) \quad (1.37)$$
$$\sin^2 2\theta_{13}|_{\text{MINOS}} = 0.094^{+0.04}_{-0.05} \quad (1.38)$$
$$\sin^2 2\theta_{13}|_{\text{T2K}} = 0.104^{+0.060}_{-0.045} \quad (1.39)$$

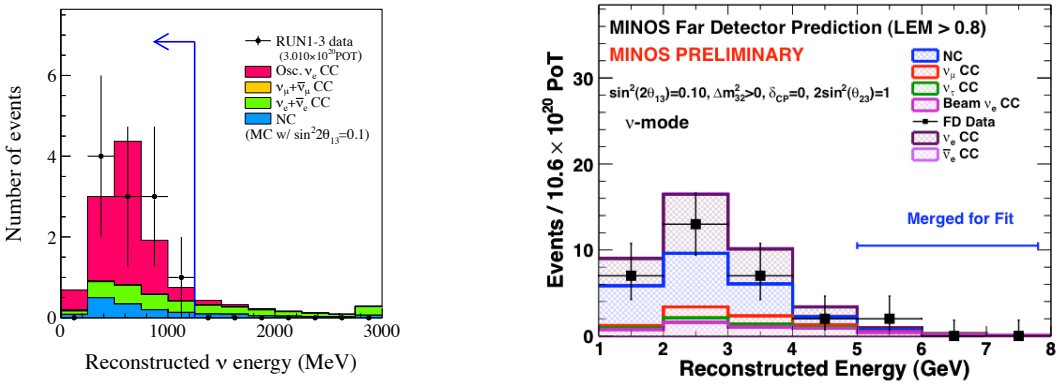

Figure 1.8: Left: T2K distributions of ν_e event selection variables (for all data taken up to March 2012) vs reconstructed neutrino energy. Blue arrows indicate the selection criteria. MC distributions are for $\sin^2 2\theta_{13} = 0.1$ and normalized to data using POT. Right: Minos reconstructed neutrino distribution. MC is for $\sin^2 2\theta_{13} = 0.1$ and normalized to data POT. The NC background is shown in blue.

These latest results open the possibility that neutrinos violate CP and therefore have played an important role in the early age of the Universe contributing to the creation of the baryon asymmetry, which is responsible for the dominance of the matter in our universe. The observation of the CP violation in the leptonic sector is therefore very important to improve considerably the knowledge beyond the standard model. To reach this goal, several unknowns need to be solved first, like the mass hierarchy of the neutrino eigenstates or the maximality of the θ_{23} angle. While existing, or near future experiments as NOVA [39] (2014) or INO [46] (2017), might be able to have sensitivity to the mass hierarchy, there is a clear need to improve considerably current experiments or build new experiments to reach the sensitivity needed to measure the CP phase. This second phase of experiments are meant to deliver precise measurement 20 years from now. To reach this goal, there are mainly two pathes consisting in building huge detectors, as Hyper-Kamiokande [47] (1 Mton detector). The second path is also challenging and consists in using relatively big detectors of the same order of SK for example, but with higher granularity and energy resolution. This might be achieved with liquid argon TPCs, that needs however to prove different technological goals, as being able to multiply the signal or work with a relatively big drift distance.

At the same time, the nature of the neutrino is also a fundamental unknown to be determined. Because neutrinos are massive they can be of different nature. Charged fermions are Dirac particle because of the electric charge conservation. Lepton number conservation is less fundamental than charge conservation and does not govern the dynamics [48]. Therefore total lepton number can be broken, as predicted by many extensions of the Standard Model. Since neutrinos do not have any other quantum numbers but the lepton number, they can be identical to their own antiparticles. In this case, they are called Majorana particles [49]. Dirac and Majorana mass effects are indistinguishable in typical experiment with the exception of the neutrino-less double-β decay.

There are many models implementing Dirac or Majorana mass terms or both in an extension of the standard model. One of them is called the seesaw mechanism, which add one heavy right handed neutrino per family. The right handed neutrino having a Majorana mass and the left handed neutrino being Dirac particles, with the possibility for the heavy neutrino to be sterile

(e.g. do not feel any other force than the gravitation). The existence of sterile neutrinos can explain partially different anomalies observed in reactor and short base line experiments [50], and are therefore an important question.

Many experimental setups exist and try to understand the nature of neutrinos. The methods applied involve nuclear beta decay (KATRIN [51] and MARE [52]) or neutrino-less double beta decay (e.g. GERDA [53], CUORE [54], EXO [55] and Kamland-zen [56]). Now, they are dominated by background and are working hard to reduce it. The knowledge of the mass hierarchy is here also important in terms of neutrino-less double beta decay rates. In the case of inverted hierarchy, the effective neutrino mass, $m_{\beta\beta}$ is expected to be in the range $10^{-2}\ eV < |m_{\beta\beta}| < 5 \times 10^{-2} eV$ [57], that can be reachable by various proposed experiments designed to test the Majorana nature of neutrinos.

1.6.1 Neutrino cross sections and oscillations

As more precise measurements are needed to answer these questions, systematic errors need to be decreased. The two major systematic uncertainties are the neutrino flux uncertainties in the different experiments and cross section uncertainties. In this thesis, we will concentrate on the ν_μ cross section measurement on Carbon at the near detector of the T2K experiment. From the general point of view of future experiments, not only cross section on Carbon are needed but also on water (that can also be achieved by the T2K near detector), iron, Argon, etc. Cross sections are currently modeled in the simulations with different approximations that will be explained in the next chapter. Depending on the assumptions, cross sections can vary by about 20 %. In order to decrease significantly systematic errors in the cross sections, theorists and experimentalists have to work together. One of the major request of the theorists to the experimentalists, has been to give them the results in a format where the minimum of assumptions has been done. This is the aim of the analysis presented here.

Chapter 2

Neutrino interactions

2.1 The Weak Interaction

The weak interaction, is one of the four fundamental forces of nature alongside gravity, electromagnetism and the strong force. Above the unification energy, of the order of 100 GeV, electromagnetism and the weak interaction merge in a single interaction called the electroweak interaction, which is mediated by four massless bosons: $W^{0,\pm}$, B^0. In the Standard Model, the Z^0 and $W^{\pm}$, and the photon are produced by the spontaneous symmetry breaking of the electroweak symmetry $SU(2) \times U(1)$, where the W^0 and B^0 coalesce into two different bosons. The left-handed fermion fields of the i^{th} fermion family transform as doublets $\psi = \begin{pmatrix} \nu_i \\ l_i^- \end{pmatrix}$ and $\begin{pmatrix} u_i \\ d'_i \end{pmatrix}$ under SU(2), where $d'_i \equiv \sum_j V_{ij} d_j$, and V is the Cabbibo-Kobayashi-Maskawa (CKM) mixing matrix. As already introduced in the preceding chapter, the minimal extension of the Standard Model is that neutrinos mix in the same way, $\nu'_i \equiv \sum_j U_{ij} \nu_j$, where ν_j are mass eigenstates.

In spontaneous symmetry breaking, the bosons acquire a non-vanishing mass through the absorption of Nambu-Goldstone bosons [58, 59]. This process is known as the Higgs mechanism. At low energy, the weak interaction is then mediated by the three bosons with significant masses: $W^{\pm}$, Z^0. The neutral vector bosons Z^0 mediate the neutral current interaction (NC) and the two charged bosons $W^{\pm}$ mediate the charged current interaction (CC). While charged leptons are converted into neutrinos (or vice versa) via the CC interaction, leptons do not change charge in the NC channel. Figures 2.1 and 2.2 show the possible interaction vertices.

Weak interaction is also the only force that violates parity, as Chen Ning Yang and Tsung-Dao Lee suggested it in the mid-1950. This parity violation is represented, in the following, by the term: $\gamma_\mu(1 - \gamma_5)$ or $\gamma_\mu(g_V^i - g_A^i \gamma_5)$, where γ_μ and γ_5 are the Dirac matrices, g_V^f and g_A^i are the vector and axial vector coupling constant for the i^{th} fermion family:

$$g_V^i \equiv t_{3L}(i) - 2q_i \sin^2 \theta_W \tag{2.1}$$

$$g_A^i \equiv t_{3L}(i) \tag{2.2}$$

where t_{3L} is the weak isospin of the fermion i ($+1/2$ for u_i and ν_i; $-1/2$ for d_i and l_i) and q_i the charge in units of the positron electric charge $e \equiv g \sin\theta_W$. For a given fermion f_i, neutral

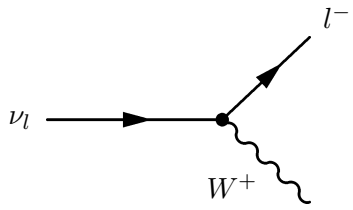

Figure 2.1: Feynman diagram of neutrino interaction vertex in the case of charged current interactions. The letter l denotes any lepton. The same diagram is valid for anti-particles and opposite charge for the W boson.

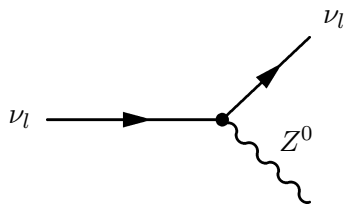

Figure 2.2: Feynman diagrams of neutrino interaction vertex in the case of neutral current interactions. The letter l denotes any lepton. The same diagram is valid for anti-neutrinos.

and charged currents can be expressed as:

$$J^{NC}_{f_i \to f_i,\mu}(x) = \bar{f}_i(x)\gamma_\mu \frac{(g^i_V - g^i_A\gamma_5)}{2} f_i(x) \tag{2.3}$$

$$J^{CC}_{f_i \to f'_i,\mu}(x) = \bar{f}'_i(x)\gamma_\mu \frac{(1-\gamma_5)}{2} f_i(x) \tag{2.4}$$

where we have used the notation $f_i(x)$ for the fermion field.

2.2 Neutrino interactions with matter

There are two possible targets for neutrino interactions. Firstly, neutrinos can interact with the atomic electrons, and secondly, with the nucleons within the nucleus, in charged or neutral current interactions.

Fig. 2.3 illustrates the possible neutrino interactions with matter. To understand when these two interactions are possible in the case of ν_μ interactions with matter, we can make a simple calculation of the threshold energy in the laboratory frame. Consider the electrons to be at rest, and the neutrino to be massless: $p_e = (m_e, 0, 0, 0)$ and $p_\nu = (E_\nu, 0, 0, E_\nu)$. We have:

$$\begin{aligned} s &> m_l^2 \\ s = (p_\nu + p_e)^2 &= (E_\nu + m_e)^2 - E_\nu^2 \\ \Rightarrow E_\nu &> \frac{m_e}{2}\left(\left(\frac{m_l}{m_e}\right)^2 - 1\right) \end{aligned} \tag{2.5}$$

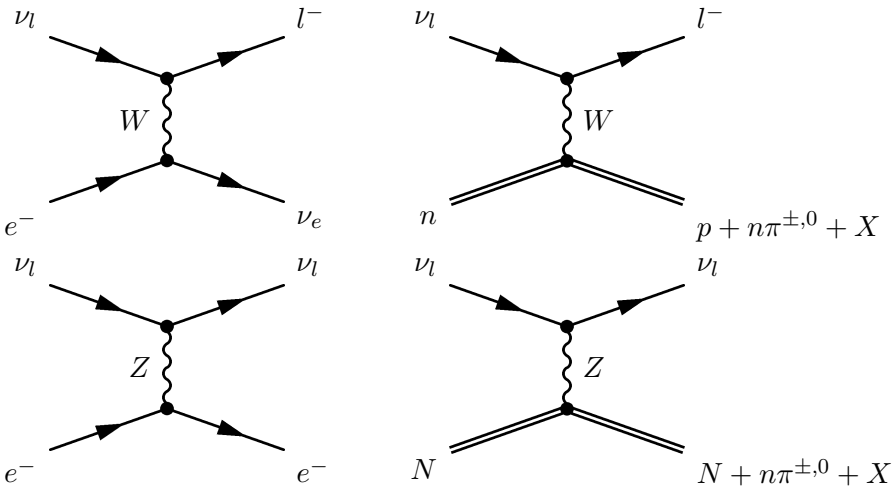

Figure 2.3: Feynman diagrams of neutrino interactions in matter in the case of charged and neutral current interactions. The letter l denotes any leptons. The same interactions hold for anti-neutrinos

where the Mandelstam variable s is the center-of-mass energy squared. In the case of muon neutrinos, we have $E_{\nu_\mu} > 11$ GeV.

By contrast, for an interaction with a nucleon at rest and considering only the lowest energy possibility of a neutron changing into a proton, we have:

$$\begin{aligned} s &> (m_l + m_p)^2 \\ s = (p_\nu + p_n)^2 &= (E_\nu + m_n)^2 - E_\nu^2 \\ \Rightarrow E_\nu &> \frac{(m_l + m_p)^2 - m_n^2}{2m_n} \end{aligned} \tag{2.6}$$

In this case, we see that for the case of muon neutrinos, the threshold energy is $E_{\nu_\mu} > 110$ MeV. Since T2K muon neutrino energy peak is around 600 MeV, we will from now on only consider neutrino interactions with nucleons for charged current interactions. For the neutral current interaction, we see that $E_\nu > 0$ for any flavor.

2.3 Neutrino cross sections

In nuclear and particle physics, the concept of a cross section is used to express the probability of interaction between particles. When particles in a beam impinge upon a target, the cross section is a hypothetical area that should have the target particles to reproduce the interaction probability. The interaction is described in Fig. 2.4.

In this section, we will derive the general cross section formula used in particle physics to calculate the cross section of any interaction theoretically. To do so, we will start from the cross section definition. From it, the probability of interaction can be factored out. Replacing then the probability of interaction by its theoretical expression, we obtain the general formula for the cross section in terms of initial and final states.

The number of scattering events, $\mathrm{d}N^{int}$, that take place per unit volume $\mathrm{d}V$ will be proportional to the incoming flux $\mathrm{d}\phi_A = n_A^{\mathrm{LF}} v_A \mathrm{d}t$ and to the density targets n_B^{LF}

$$\mathrm{d}N^{int} = \sigma n_B^{\mathrm{LF}} \mathrm{d}\phi_A \mathrm{d}V \tag{2.7}$$

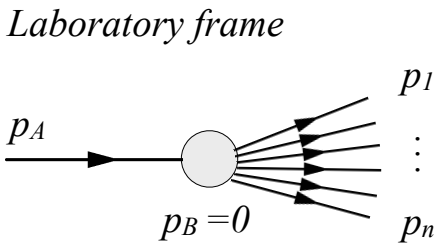

Figure 2.4: Definition of the variables for a n-body final state interaction in the laboratory frame, where $p_A,\ p_B,\ p_1,\ p_n$ are the four-momentum.

$$= \quad \sigma n_A^{\mathrm{LF}} v_A n_B^{\mathrm{LF}} \mathrm{d}V \mathrm{d}t \tag{2.8}$$

where σ is the cross section, and LF denotes the laboratory frame.

Eq. 2.8 can be generalized to any frame, using the Lorentz-invariant quantity[60],

$$n_A^{\mathrm{LF}} v_A n_B^{\mathrm{LF}} = n_A n_B \sqrt{(\vec{v_A} - \vec{v}_B)^2 - (\vec{v_A} \times \vec{v}_B)^2} \tag{2.9}$$

where n_A, n_B are the number densities of the two types of particles in the frame where their respective velocities are $\vec{v}_A$ and $\vec{v}_B$ (note that number density is not invariant, but transforms as the inverse of a spatial volume).

In the following, the cross section defined in Eq. 2.8 will be expressed in terms of final and initial states quantities, by using the definition of the interaction probability, in addition to the definition of the cross section given in Eq. 2.8.

Firstly, we express the information contained in Eq. 2.8 as the following,

$$\mathrm{d}N^{int} = \sigma \frac{I}{V E_A E_B} (n_A V)(n_B \mathrm{d}V)\mathrm{d}t \tag{2.10}$$

$$\Rightarrow \frac{N^{int}}{N_A N_B} = \sigma \frac{I}{V E_A E_B} \tag{2.11}$$

where the integration over $\mathrm{d}V$ gives the total number of target particle N_B and $n_A V$ the total number of incoming particles N_A and the quantity

$$I \equiv \sqrt{(p_A \cdot p_B)^2 - m_A^2 m_B^2} = E_A E_B \sqrt{(\vec{v_A} - \vec{v}_B)^2 - (\vec{v_A} \times \vec{v}_B)^2} \tag{2.12}$$

has been defined for convenience, with E_A, E_B and p_A, p_B the energy and four-momentum of the initial particles.

Secondly, the total number of events per particles of type A and type B in a total time T ($N^{int}/(N_A N_B)$) is, by definition, the probability of interaction:

$$\frac{N^{int}}{N_A N_B} = V \int \frac{|\langle f, \mathrm{out} | \mathrm{i}, \mathrm{in} \rangle|^2}{(2E_A V)(2E_B V)} \prod_i \frac{V \mathrm{d}^3 p_i}{(2E_i V)(2\pi)^3} \tag{2.13}$$

where we defined E_i as the energy of the final particles, and $|\langle f, out | i, in \rangle|^2$ is the probability of transition between the final states and initial states. This probability of transition contains the

Dirac distribution of the momentum conservation that can be expressed out as,

$$|\langle f, out|i, in\rangle|^2 = (2\pi)^4\delta^4\left(\sum_i p_i - p_A - p_B\right)|\mathcal{M}_{fi}|^2 \tag{2.14}$$

where $\mathcal{M}_{fi}$ is the transition amplitude between the initial states and final states.

Using now the fact that Eq. 2.11 and Eq. 2.13 are equal, and inserting Eq. 2.14 in Eq. 2.13, we can express the cross section in terms of initial and final states

$$\sigma = \frac{1}{4\sqrt{(p_A \cdot p_B)^2 - m_A^2 m_B^2}} \int |\mathcal{M}_{fi}|^2 (2\pi)^4 \delta^4 (\sum_i p_i - p_A - p_B) \prod_i \frac{\mathrm{d}^3 p_i}{(2E_i)(2\pi)^3} \tag{2.15}$$

where the energy of the initial particles cancel each other in the final expression of the cross section as well as the volume V and I has been expressed following the definition of Eq. 2.12.

Writing Eq. 2.15 in its differential form, we get

$$\mathrm{d}\sigma = \frac{|\mathcal{M}_{fi}|^2}{4\sqrt{(p_A \cdot p_B)^2 - m_A^2 m_B^2}} \mathrm{d}\phi^{(n)}(p_A, p_B; p_1, ..p_n) \tag{2.16}$$

where we defined the differential *n-body phase space* $\mathrm{d}\phi^{(n)} \equiv (2\pi)^4\delta^4(\sum_i p_i - p_A - p_B)\prod_i \frac{\mathrm{d}^3 p_i}{(2E_i)(2\pi)^3}$

In most experiments, the incoming particle as well as the outgoing particles are unpolarized. In order to compare predictions with these measurements, we need to calculate the cross section for an interaction where the initial and final states have a definite momentum but with any spin polarization. Therefore, we average over the polarization of the initial state particles and sum over all the possible spin polarizations of the final state particles. In this case, $|\mathcal{M}_{fi}|^2$ is replaced in Eq. 2.15 and Eq. 2.16 by the spin-averaged square of invariant amplitude $\overline{|\mathcal{M}_{fi}|^2}$ which is defined as,

$$\overline{|\mathcal{M}_{fi}|^2} = \frac{1}{2s_A + 1}\frac{1}{2s_B + 1}\sum_{s_A, s_B}\sum_{s_f}|\mathcal{M}_{fi}|^2 \tag{2.17}$$

where s_A, s_B, s_f are the initial and final states spins. This will be done, for example, in the next section while deriving the general formula of the neutrino cross section for charged and neutral current inclusive interactions.

2.4 Inclusive cross section

In this section, the general formula of inclusive neutrino cross section will be derived. This will be done in the scope of the charged current interactions. The same steps can be followed for the neutral currents with minimal changes that will be explicitly described at the end of the section.

Let neutrino interactions be described by the following charged and neutral current reactions:

$$\nu + N \to l^- + X \tag{2.18}$$

$$\nu + N \to \nu + X \tag{2.19}$$

where N is the target nucleon and X is the hadron final state, as described by Fig. 2.5.

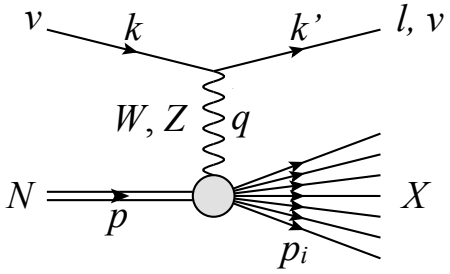

Figure 2.5: Definition of the variables for a (n+1)-body final state, k, k' being the four-momentum of the neutrino and out-going lepton or neutrino (for NC) and $p, p_1 ... p_n$ being the four-momentum of the initial and final hadrons.

The differential cross section for neutrino scattering, in the center of mass frame of the nucleon, is given by

$$\begin{aligned} \mathrm{d}\sigma &= \frac{|\mathcal{M}|^2}{4(M_N|\vec{k}|)} d\phi^{(n+1)}\left(k, p; k', p_1, .., p_n\right) && (2.20)\\ &= \frac{|\mathcal{M}|^2}{8(2\pi)^3 M_N|\vec{k}|}\frac{\mathrm{d}^3k'}{\epsilon'} d\phi^{(n)} && (2.21)\\ &= \frac{|\mathcal{M}|^2}{8(2\pi)^3 M_N|\vec{k}|\epsilon'}|\vec{k}'|\epsilon'\mathrm{d}\epsilon'\mathrm{d}\Omega d\phi^{(n)} && (2.22)\\ \frac{\mathrm{d}^2\sigma}{\mathrm{d}\epsilon'\mathrm{d}\Omega} &= \frac{1}{2\pi^2}\frac{|\vec{k}'|}{|\vec{k}|}\frac{|\mathcal{M}|^2 d\phi^{(n)}}{8\cdot 2M_N\cdot 2\pi}, && (2.23) \end{aligned}$$

where

- we assumed that the neutrino is massless and the neutrino and charged lepton four-momentum given by $k = (E_\nu, 0, 0, E_\nu),\ k' = (\epsilon', \vec{k}')$.
- we defined the four-momentum transfer $q = k' - k$, as the difference with the charged lepton and neutrino four-momentum.
- we used the fact that $d^3k' = |\vec{k}'|^2\mathrm{d}|\vec{k}'|\mathrm{d}\Omega$, where Ω describes the solid angle ($\mathrm{d}\Omega = \mathrm{d}(\cos\theta)\mathrm{d}\phi$).
- we used that $|\vec{k}'|\mathrm{d}|\vec{k}'| = \epsilon'\mathrm{d}\epsilon'$
- we used the definition of the n-body phase space Eq. 2.16: $d\phi^{(n)} \equiv (2\pi)^4\delta^4(\sum_i p_i - p - q)\prod_{i=1}^n \frac{\mathrm{d}^3p_i}{(2E_i)(2\pi)^3}$

We first calculate the invariant amplitude, $\mathcal{M}_{CC}$, for a charged current interaction is

$$\mathcal{M}_{CC} = \left(\frac{g}{2\sqrt{2}}\right)^2 \bar{l}(k')\gamma_\alpha(1-\gamma_5)\nu(k)\frac{-i(g^{\alpha\beta} - q^\alpha q^\beta/M_W^2)}{q^2 - M_W^2}\langle X(p_1,..,p_n)|J_\beta^{CC}|N(p)\rangle, \quad (2.24)$$

where $\nu(k)$ and $l(k')$ are the neutrino and lepton spinors.

Assuming low momentum transfer ($|q^2| \ll M_W^2$) the propagator can be approximated as,

$$-ig^2\frac{(g^{\alpha\beta} - q^\alpha q^\beta/M_W^2)}{8(q^2 - M_W^2)} \approx -ig^{\alpha\beta}\frac{G_F}{\sqrt{2}} \quad (2.25)$$

where the Fermi constant is defined as $G_F = \frac{\sqrt{2}g^2}{8M_W^2}$.

Applying this transformation to Eq. 2.24, we obtain,

$$\mathcal{M}_{CC} = \frac{G_F}{\sqrt{2}}\bar{l}(k')\gamma_\alpha(1-\gamma_5)\nu(k)\langle X|J_{CC}^\alpha|N\rangle. \quad (2.26)$$

and therefore the spin-average squared amplitude is,

$$\overline{|\mathcal{M}_{CC}|^2} = \frac{G_F^2}{2}\left(\sum_{s_\nu}\sum_{s_\mu}\left([\bar{l}\gamma_\alpha(1-\gamma_5)\nu][\bar{l}\gamma_\beta(1-\gamma_5)\nu]^\dagger\right)\frac{1}{4}\sum_{s_N}\sum_{s_X}\langle X|J^\alpha|N\rangle\langle X|J^\beta|N\rangle^\dagger\right) \quad (2.27)$$

where the factor 1/4 corresponds to $\frac{1}{(2s_\nu+1)(2s_N+1)}$ with $s_\nu, s_N = 1/2$ the neutrino and nucleon spin value.

We see that in the calculation of $\overline{|\mathcal{M}_{CC}|^2}$, the following leptonic term appears:

$$\begin{aligned}
\sum_{s_\nu}\sum_{s_\mu}[\bar{l}\gamma_\alpha(1-\gamma_5)\nu][\bar{l}\gamma_\beta(1-\gamma_5)\nu]^\dagger &= Tr\left([\bar{l}\gamma_\alpha(1-\gamma_5)\nu][\bar{\nu}\gamma_\beta(1-\gamma_5)l]\right) && (2.28)\\
&= 8[k'_\alpha k_\beta + k'_\alpha k'_\beta - g_{\alpha\beta}k\cdot k' + \epsilon_{\alpha\beta\rho\sigma}k^\rho k'^\sigma] && (2.29)\\
&\equiv 8L_{\alpha\beta} && (2.30)
\end{aligned}$$

where we defined the leptonic tensor $L_{\alpha\beta}$ as in [61], and the factor of eight will be cancelled in Eq. 2.23.

Defining, in addition a hadronic tensor, $W^{\alpha\beta}$, we can express Eq. 2.23 as the multiplication of the leptonic tensor with the hadronic tensor defined as in [61],

$$\begin{aligned}
W^{\alpha\beta} &= \frac{1}{2M_N}\sum_X\frac{(2\pi)^4\delta^4(P_X - p_N - q)}{2\pi}\langle X|J^\alpha|N\rangle^\dagger\langle X|J^\beta|N\rangle && (2.31)\\
&= \frac{1}{2M_N}\sum_X(2\pi)^3\delta^4(P_X - p_N - q)\langle X|J^\alpha|N\rangle^\dagger\langle X|J^\beta|N\rangle && (2.32)
\end{aligned}$$

where the sum includes the sum on the final states as well as the average over the initial spins and the integration over $\frac{dp_i^3}{2E_i(2\pi)^3}$, and $P_X = \sum_i p_i$ is the total four momentum of the hadronic final state. With the definitions given in Eqs. 2.30 and 2.32 used together in Eq. 2.23, we obtain the general expression of the differential cross section

$$\frac{d^2\sigma}{d\epsilon' d\Omega} = \frac{G_F^2}{4\pi^2}\frac{|\vec{k}'|}{|\vec{k}|}L_{\alpha\beta}W^{\alpha\beta} \quad (2.33)$$

where $L_{\alpha\beta}$ and $W^{\alpha\beta}$ are the leptonic and hadronic tensor defined in Eqs. 2.30 and 2.32.

For neutral currents, the derivation is very similar. The general expression for $\mathcal{M}_{NC}$ can be obtained by changing $g \to \bar{g} = \frac{g}{\cos\theta_W}$, $M_W \to M_Z$, $\bar{l} \to \bar{\nu}$ and $J_{CC} \to J_{NC}$ in Eqs. 2.24, 2.25 and 2.27.

From Eqs. 2.30 and 2.32, we see that while the leptonic tensor is exactly calculable, the hadronic tensor is not and depends on the energy transferred.

At very high energies, the cross section for neutrinos to interact with other leptons or asymptotically free quarks is exactly calculable. However, at lower energies where the neutrinos interact only with bound nucleons or the entire nucleus, strong interactions prevent the hadronic current from being exactly calculable.

At low neutrino energies, the most common neutrino interaction energies are those that minimally affect the interaction target. In the case of the charged current interaction, this implies the change of electric charge in the baryon target: this interaction is called quasi-elastic interaction (see Sec. 2.5). If the $W^{\pm}$ transfers enough momentum, so that the target gets a resonance state, the decay of the resonance will typically produce a nucleon and a pion (see Sec. 2.6).

At low energies, the neutrino interacts with bound nucleons. Hence any interactions with a bound nucleon will affect the other nucleons in the nucleus. Therefore nuclear effect has to be taken into account. In the following, we will first study the simple neutrino interaction with a free nucleon in Sec. 2.5 and Sec. 2.6, while the interaction with bound nucleons is introduced in Sec. 2.7.

In Sec. 2.8, we will study the particular case of neutrinos interacting with the entire nucleus producing coherently a pion without changing the nucleus. At higher energies, many mesons and baryons can be produced. This case is called deep inelastic scattering (see Sec. 2.9). Finally, in Sec. 2.10, we will consider the interactions of that happen to the final state particles when crossing the nuclear medium.

Fig. 2.6 shows the actual knowledge of the total cross section interactions for different neutrino energies.

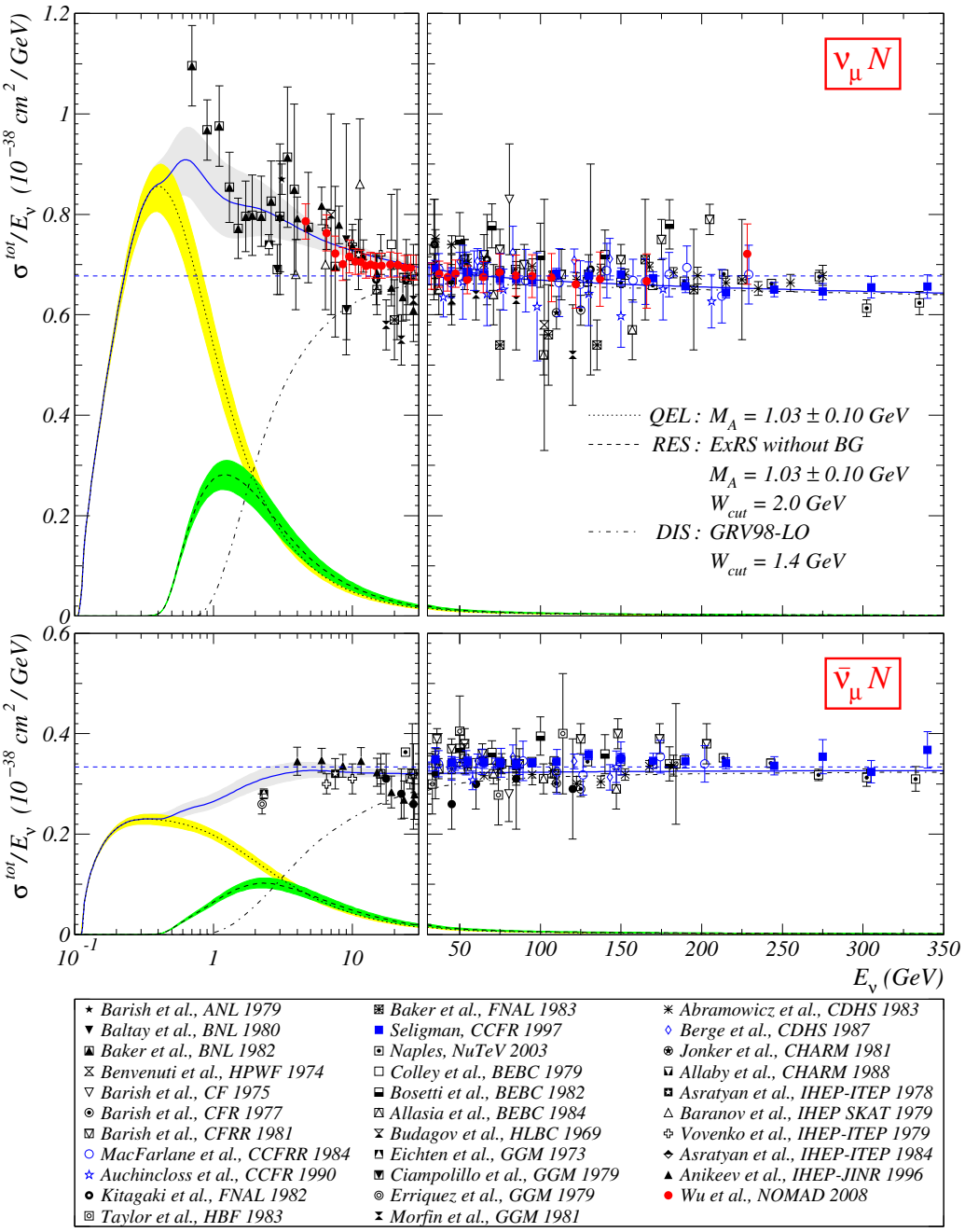

Figure 2.6: Total charged current ν_μ (top) and $\bar{\nu}_\mu$-nucleon (bottom) inclusive cross section as a function of neutrino energy. The low energy region is dominated by the quasi-elastic (QE) contribution (dotted), the high energy region by the deep inelastic (DIS) contribution (dashed-dotted). The intermediate regime is dominated by the resonance (RES) contribution (dashed). Points with errors bars show sparse measurements of various experiments listed in the caption. As can be seen, measurements mainly concentrate in the DIS region and measurements in the RES region suffer from larger uncertainties, while very few measurements cover the QE region [62].

2.5 Charged Current Quasi-Elastic (CCQE) interactions

In this section, we study the neutrino charged current quasi-elastic (CCQE) interaction where the initial free neutron is changed to a proton. In particular, we give the cross section result following the model of Llewellyn-Smith [63].

The interaction is depicted in Fig. 2.7.

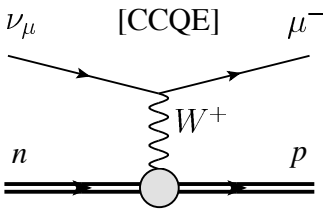

Figure 2.7: Feynman diagram of a CCQE interaction

In this model, the neutrino is assumed massless and the neutron is at rest.

The cross section for the neutrino nucleon charged current quasi-elastic scattering is evaluated based on the model of Llewellyn-Smith. The differential cross section formula for neutrino interactions is given by

$$\frac{d\sigma}{dQ^2} = \frac{G_F^2 M_N^2 \cos^2\theta_c}{8\pi E_\nu^2}\left[A + B\frac{(s-u)}{M_N^2} + C\frac{(s-u)^2}{M_N^4}\right], \tag{2.34}$$

where G_F is the Fermi coupling constant, $Q^2 = -q^2 > 0$ is the squared four-momentum transfer, M_N the mass of the nucleon, E_ν the incident neutrino energy, and $(s-u) = 4M_N E_\nu - Q^2 - m^2$, with m the muon mass. The complete calculation can be found in [64]. The factors $A,\ B$, and C are functions of the vector form factors[1] F_1 and F_2, the axial vector form factor F_A, and the pseudo-scalar form factor F_p:

$$\begin{aligned} A &= \frac{m^2+Q^2}{M_N^2}[(1+\tau)F_A^2 - (1-\tau)F_1^2 + \tau(1-\tau)F_2^2 + 4\tau F_1 F_2 \\ &\quad -\frac{m^2}{4M_N^2}\left((F_1+F_2)^2 + (F_A+2F_P)^2 - (\frac{Q^2}{M_N^2}+4)F_P^2\right)] \end{aligned} \tag{2.35}$$

$$B = \frac{Q^2}{M_N^2}F_A(F_1+F_2) \tag{2.36}$$

$$C = \frac{1}{4}(F_A^2 + F_1^2 + \tau F_2^2) \tag{2.37}$$

where $\tau = Q^2/4M_N^2$.

In general, the form factors $F_1,\ F_2,\ F_A$ and F_P are assumed to be dipole. However recent precise electron scattering experiments of the vector form factor show deviation from the simple dipole

[1] The nucleon form factors describe the spatial distributions of electric charge and current inside the nucleon and thus are intimately related to its internal structure.

form [65].

$$F_1(Q^2) = \frac{1+\tau(1+\xi)}{(1+\tau)\left(1+\frac{Q^2}{m_V^2}\right))} \tag{2.38}$$

$$F_2(Q^2) = \frac{\xi}{(1+\tau)\left(1+\frac{Q^2}{m_V^2}\right))} \tag{2.39}$$

$$F_A(Q^2) = \frac{g_A}{\left(1+\frac{Q^2}{m_A^2}\right)^2};\ g_A = -1.267 \tag{2.40}$$

$$F_P(Q^2) = \frac{2M_N^2}{m_\pi^2+Q^2}F_A(Q^2) \tag{2.41}$$

where m_π is the pion mass, $\xi = \mu_p - \mu_n = 3.71$ with μ_p and μ_n the proton and neutron anomalous magnetic moments, respectively, and the parameters m_V, m_A, and g_A are empirical inputs[2][67].

In our applications (electron and muon production), we can eliminate the lepton mass term ($\frac{m^2}{M_N^2} \ll 1$). In this case, the part in equation 2.35 where the pseudo-scalar form factor appears is erased.

2.6 Single pion, photon, η and kaon production

The Rein-Sehgal model describes single pion production in the charged (CC) and the neutral (NC) current neutrino scattering. The pions are produced by excitations of 18 resonances [68]. In resonant production the neutrino scatters from a free nucleon. A resonance of the nucleon is excited, and in the process of decaying back into the ground state the resonance emits one or more mesons. In this section, we consider a single nucleon resonance (see Fig. 2.8) that can be summarized by the following processes,

$$\nu + N \to l + N^* \tag{2.42}$$

$$\nu + N \to \nu + N^* \tag{2.43}$$

$$N^* \to N' + \pi \tag{2.44}$$

where N^* denotes one of the 18 nucleon resonances.

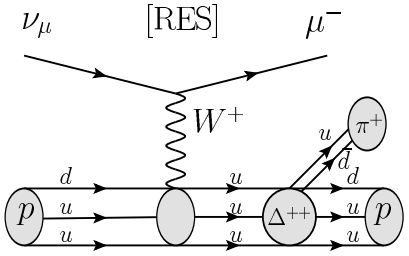

Figure 2.8: Feynman diagram of a single nucleon resonance [69]

[2] $m_V(m_A)$ is determined from $e^-(\nu)$ scattering data fits, and g_A is precisely determined from neutron beta decay. The best current value for g_A is -1.267 [66].

Because we are looking at only single pion production, the kinematical region of this reaction is restricted to the regime of low $Q^2 < 2$ GeV. At higher momentum transfer multi-meson resonances and deep inelastic scattering start to be important and are relatively well known (see Sec. 2.9). For resonant interaction, the amplitude of transition is given by,

$$\mathcal{M}_{CC} = \frac{G_F \cos\theta_C}{\sqrt{2}}[\bar{l}\gamma^\alpha(1-\gamma^5)\nu]\langle N^*|J_\alpha|N\rangle \tag{2.45}$$

$$\mathcal{M}_{NC} = \frac{G_F}{\sqrt{2}}[n\bar{u}\gamma^\alpha(1-\gamma^5)\nu]\langle N^*|J_\alpha|N\rangle \tag{2.46}$$

where J_α is the hadronic current operator containing a vector and an axial vector part.

To simplify, we consider only charged current interactions. The expression for neutral current can be obtained with the transformation $\bar{l} \to \bar{\nu}$ and $G_F \cos\theta_C \to G_F$.

The cross section for a single resonance with mass M_{N^*} and negligible width is given by,

$$\frac{\mathrm{d}^2\sigma}{\mathrm{d}Q^2\mathrm{d}E_q} = \frac{1}{32M_N E^2}\frac{1}{2}\sum_{\text{spins}}|\mathcal{M}|^2\delta(W^2 - M_{N^*}^2) \tag{2.47}$$

where M_N is the nucleon mass and W the observed resonance mass. In the case of non-negligible width, the delta function is replaced by a Breit-Wigner factor,

$$\delta(W - M_N) \to \frac{1}{2\pi}\frac{\Gamma}{(W - M_{N^*})^2 + \Gamma^2/4} \tag{2.48}$$

where Γ is the decay width of N^*, and E_q is the energy of the virtual $W_\pm$ or Z_0. In practice always several nearby resonances will overlap and even non-resonant background amplitude of various quantum numbers may interfere to produce the measurable final state. This is what Rein-Sehgal model tries to include. In this model, 14 reactions are considered in which the final hadronic state is selected to consist of a nucleon accompanied by a single pion. Six are mediated by charged current, and eight by neutral current (see [70]).

The model is based on the Feynman, Kislinger and Ravndal (FKR) approach [71], which was developed to describe photoelectric meson production. The FKR model is an example of a relativistic quark oscillator mode.

Since Rein and Sehgal's model provide the amplitudes of neutrino resonance production, it is possible to calculate the cross sections of single photon, K and η productions. In this case, we only need to change the decay probabilities of the resonances.

2.7 Neutrino-nuclei scattering

In order to obtain the cross section off nucleons in the nucleus, it is necessary to take into account the nuclear medium effects when dealing with relatively low q^2 as it is the case for quasi-elastic and single pion production through resonant processes [72]. In this section we consider the following processes:

$$\nu_l + A \to l^- + A' \tag{2.49}$$

where A and A' are the initial and final nuclei. Because the nucleons are bounded together inside the nucleus, any interaction with one nucleon will affect the rest of the nucleus.

The double differential cross section is given by Eq. 2.33. The hadronic tensor is given by Eq. 2.32

$$W^{\mu\nu} = \frac{(2\pi)^3}{2M_A}\sum_X \langle A|J_A^{\mu,\dagger}|X\rangle\langle X|J_A^{\nu}|A\rangle\delta^{(4)}(p_X - p_A - q) \tag{2.50}$$

where $p_A,\ p_X,\ q$ are the target initial and final four momentum and four momentum transfer respectively. The sum includes all final hadronic states.

At low q^2, the hadronic tensor can be calculated using non-relativistic wave functions to describe the initial and final states and expanding the current operator in powers of $|\vec{q}|/M_N$, M_N being the nucleon mass. At higher q^2, the description of the final states $\langle X|$ in terms of non-relativistic nucleons is no longer possible. In this case, some approximations are needed to take into account the relativistic motion of final state particle carrying momentum $\vec{q}$ as well as the occurrence of inelastic processes, leading to the appearance of hadrons other than protons and neutrons [73].

The impulse approximation (IA) is often the main scheme adopted. It is based on the assumptions that at large enough $q^2 \gtrsim 1$ GeV the target nucleus is seen by the probe as a collection of individual nucleons and that the particles produced at the interaction vertex and the recoiling (A − 1)-nucleon system evolves independently. Within this picture, the nuclear current can be written as a sum of one-body currents,

$$J_A^{\mu} = \sum_i j_i^{\mu} \tag{2.51}$$

while the final state reduces to the direct product of the hadronic state at the weak vertex (with momentum $\vec{p_x} = \vec{p} + \vec{q}$) and that describing the $(A-1)$-nucleons residual system, with momentum $\vec{p}_R$, mass M_{A-1} and recoil energy E_R:

$$\sum_X |X\rangle\langle X| = \sum_x \int \mathrm{d}^3p_x|x,\vec{p}_x\rangle\langle\vec{p}_x,x| \times \sum_R \int \mathrm{d}^3p_R|R,\vec{p}_R\rangle\langle\vec{p}_R,R| \tag{2.52}$$

The hadronic tensor inside this approximation can be cast in the following form [74]:

$$W^{\mu\nu} = \sum_i \int \mathrm{d}^3p\mathrm{d}E\ P(\vec{p},E)w_i^{\mu\nu}(\tilde{p},\tilde{q}), \tag{2.53}$$

where,

- the function $P(\vec{p},E)$ is the target *Spectral Function*, i.e. the probability distribution of having a nucleon with momentum $\vec{p}$ and removal energy E in the target nucleus. It describes then how nucleons distribute in momentum space:

$$P(\vec{p},E) = \sum_R |\langle A|R,-\vec{p};N,\vec{p}\rangle|^2\delta(M_N - E - (E_A - E_R)) \tag{2.54}$$

  where $|N,\vec{p}\rangle$ designs a free nucleon state, with energy $E_{|\vec{p}|}$.

- the description of the electromagnetic interactions of the i-th nucleon in *free space* is

$$w_i^{\mu\nu}(\tilde{p},\tilde{q}) = \sum_x \langle\vec{p},N|j_i^{\mu,\dagger}|x,\vec{p}_x\rangle\langle\vec{p}_x,x|j_i^{\nu}|N,\vec{p}\rangle\delta(\tilde{\nu} + E_{|\vec{p}|} - E_x) \tag{2.55}$$

- the four-momentum transfer is defined as $\tilde{q} = (\tilde{\nu}, \vec{q})$, and the effect of nuclear binding of the struck nucleon is accounted for by the replacement of $q \to \tilde{q}$

This procedure essentially amounts to assuming that [75]:

- the elementary scattering process can be described as if it took place in free space with energy transfer $\tilde{\nu} = E_{\vec{p}} - E_x$.
- a fraction $\delta\nu \equiv \tilde{\nu} - \nu = E_{\vec{p}} - E_x - (E_A - E_R - E_x) = E_{\vec{p}} - (M_N - E) = -E_B$ of the energy transfer goes into excitation energy of the spectator system, that is generally called binding energy.

Depending on the approximation chosen the spectral function $P(\vec{p}, E)$ can take different forms. In the following sections, we explain two approximations for the spectral function in detail. The first one corresponds to the simplest case adopted by Smith and Moniz [76] which corresponds to the Relativistic Fermi Gas (RFG) description of the nucleus.The second case is the Gaussian Spectral Function (GSF) [72]. In the literature, there are many other spectral functions, such as the LDA (Local Density Approximation) spectral function explained in detail in [75]. While the RFG model is used in general by the NEUT and GENIE neutrino Monte Carlo event generators, the NuWro neutrin event generator is also able to use the GSF and LDA spectral functions[3]. The difference between the result of the simplest case with the more sophisticated spectral functions will be one of the major cross section modeling uncertainty in our final result (see Chapter 6).

2.7.1 The relativistic Fermi gas (RFG)

In this model, the nucleus is considered as an ideal gas composed of weakly interacting fermions. In the nucleus, neutrons and protons are considered as distinguishable fermions, creating two potentials. The system obey Fermi-Dirac statistics, leading to the Pauli exclusion principle. The number of nucleons that can be contained in a certain volume of space is obtained by dividing that volume by the volume of one state in phase space: $(2\pi)^3$

$$\mathrm{d}n = \frac{V 4\pi p^2 \mathrm{d}p}{(2\pi)^3} \tag{2.56}$$

where V is the nuclear volume and n is the number of protons or neutrons. The total number of protons or neutrons will be then given by,

$$n = \frac{V 4\pi \int_0^{p_F} p^2 \mathrm{d}p}{(2\pi)^3} \tag{2.57}$$

$$n = \frac{p_F^3}{6\pi^2} V \tag{2.58}$$

$$\tag{2.59}$$

Taking $V = \frac{4}{3}\pi R_0^3 A$, with A the number of nucleons and $R_0 = 1.3$ fm, the nucleon radius, assuming an iso-scalar nucleus ($Z = A - Z$) to simplify, we get for both

$$p_F \approx 231 \text{ MeV/c} \tag{2.60}$$

$$E_F = E_{|\vec{p}|} - M_N = \sqrt{p_F^2 + M_N^2} - M_N \approx 28 \text{ MeV} \tag{2.61}$$

[3] In T2K the LDA spectral function is used for interaction in Carbon, while for oxygen, calcium and argon the Gaussian spectral function is used. LDA and Gaussian spectral function are similar. For simplicity, I decided to explain in more detail the gaussian spectral function.

where the Fermi energy E_F represents the energy of the highest occupied level (see Fig. 2.9).

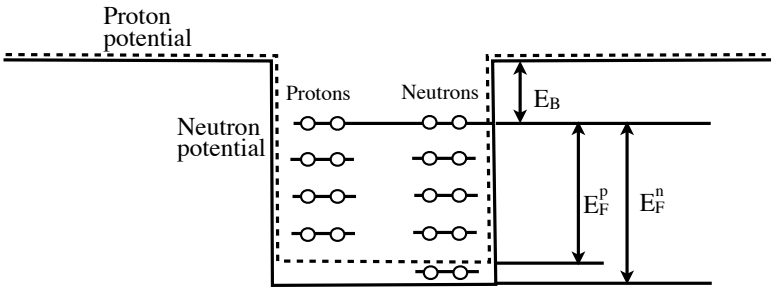

Figure 2.9: Sketch of the proton and neutron potential wells and states in the Fermi gas model. The difference between the edge of the potential well and the Fermi level is rather constant for different nuclei and equals the average binding energy per nucleon, $E_B \approx 7$ - 8 MeV (note that, since the potential well is created by the nucleons, removing a few of them changes the well depth in a way that E_B stays approximately constant) [77]. The neutron potential well is deeper than the proton one, since the former have no Coulomb interaction. On the other hand, for a stable nucleus, the Fermi levels of the protons and the neutrons have to be the same, otherwise it would decay to an energetically more favorable state through a β decay. As a result, there are more neutron states than proton states occupied, which explains the fact that $N > Z$ for heavier stable nuclei. Note, in addition, that normally coulomb repulsion should be included for the protons, taking that into account the well is no longer a rectangle.

The radius depends on the nucleus, the binding energy and Fermi momentum should be adjusted with experimental data. The lowest energy of a nucleon state being $E = -(E_B + E_F)$.

The spectral function for the relativistic Fermi gas model is then given by,

$$P_{RFG}(\vec{p}, E) = \theta(\bar{p}_F - |\vec{p}|)\delta(E_{|\vec{p}|} - M_N + E + E_B) \tag{2.62}$$

where $\theta(x) = 0$ for $x < 0$ and $\theta(x) = 1$ for $x \geq 0$ is the step function, E_B is the average binding energy, p_F the Fermi momentum. The function $\theta(\bar{p}_F - |\vec{p}|)$ in Eq. 2.62 describes the Fermi momentum distribution for the target nucleon in the nuclei.

The spectral function in Eq. 2.62 is non-vanishing only at $|\vec{p}| < p_F$. However, electron-nucleus scattering experiments have provided unambiguous evidence for strong nucleon-nucleon correlations that give rise to virtual scattering processes leading to the excitation of nucleons to states of large momentum [78]. Hence, the quantitative analysis of neutrino-nucleus interactions requires a more realistic spectral function, taking into account correlation effects. This can be done via the additional implementation of Pauli blocking function that describes the final nucleon states. In particular it takes into account the fact that if the states are already occupied, interactions do not happen (Pauli blocking). The additional function can be described by $\theta(\bar{p}_F - |\vec{p} + \vec{q}|)$ and spectral function for the relativistic gas model becomes [79],

$$P_{RFG}(\vec{p}, E) = \theta(\bar{p}_F - |\vec{p} + \vec{q}|)\theta(\bar{p}_F - |\vec{p}|)\delta(E_{|\vec{p}|} - M_N + E + E_B) \tag{2.63}$$

The next-to-simplest improvement to the Fermi gas model, in order to take these nucleon-nucleon correlations, is to replace the binding energy, E_B, by a nuclear potential, $V(|\vec{p}|)$, which depends on the momentum.

2.7.2 Spectral Function

Approximately 80% to 90% of the nucleons in a nucleus can be described as occupying shell-model[4] states and moving freely in a mean-field (MF) potential. The rest of them takes part in interactions. It is natural to decompose the spectral function into the sum of the MF and correlated parts:

$$P(\vec{p}, E) = P_{\mathrm{MF}}(\vec{p}, E) + P_{\mathrm{corr}}(\vec{p}, E). \tag{2.64}$$

The *Mean Field (MF)* spectral function is given by,

$$P_{\mathrm{MF}}(\vec{p}, E) = \sum_{\alpha=1}^{N_t} \frac{c_\alpha}{N_t} |\phi_\alpha(\vec{p})|^2 F_\alpha(E - E_\alpha), \tag{2.65}$$

where,

- the contributions from each shell-model state α belonging to the Fermi sea are summed
- $N_t = \int P(\vec{p}, E) \mathrm{d}^3 p \mathrm{d}E$ is the number of proton or neutrons
- $\phi_\alpha(\vec{p})$ is the squared momentum-space wave function of the α-shell model state,
- $F_\alpha(E - E_\alpha)$ is the Lorentzian describing the width of $\phi_\alpha(\vec{p})$. If interactions between nucleons disappeared, all the $c_\alpha \to 1$ and $F_\alpha(E - E_\alpha) \to \delta(E - E_\alpha)$.
- E_α is the level energy and c_α is the corresponding spectroscopic factor.

As the sum is extended to all occupied states of the Fermi sea, $P_{MF}(\vec{p}, E)$ vanishes at $|\vec{p}| > p_F$. Note that in absence of correlation $F_\alpha(E - E_\alpha)$ shrinks to a δ-function, and $c_\alpha / n_t \equiv 1$.

The Gaussian spectral function assumes in addition that, $\int F_\alpha(E) \mathrm{d}E = 1$ and the fact that each level contributes equally to the MF momentum distribution. In this case, the spectral function can be rewritten as [72],

$$P_{\mathrm{MF}}(\vec{p}, E) = \frac{n_t^{\mathrm{MF}}(\vec{p})}{N_t} \sum_{\alpha=1}^{N_t} F_\alpha(E - E_\alpha) \tag{2.66}$$

where $n_t^{\mathrm{MF}}(\vec{p}) = \int P_{\mathrm{MF}}(\vec{p}, E) \mathrm{d}E$ and F_α takes the form of a Gaussian distribution [72],

$$F_\alpha(\delta E_\alpha) = \sqrt{\frac{8}{\pi D_\alpha^2}} exp(-8\ \delta E_\alpha^2 / D_\alpha^2) \tag{2.67}$$

where D_α describes the width of the momentum distributions that has to be known as well as the values of the energy levels E_α and $\delta E_\alpha = E - E_\alpha$,

Interacting nucleons are described by the correlated part of the spectral function where the two-nucleon interactions dominate.

[4] In nuclear physics, the nuclear shell model is a model of the atomic nucleus which uses the Pauli exclusion principle to describe the structure of the nucleus in terms of energy levels. The shell model is partly analogous to the atomic shell model, which describes the arrangement of electrons in an atom, in that a filled shell results in greater stability.

The correlation contribution to the gaussian spectral function is given by,

$$P_{\rm corr}(\vec{p},E) = n_{corr}(\vec{p})\frac{2M_N}{|\vec{p}|}\sqrt{\alpha\pi}[e^{-\alpha p^2_{min}} - e^{-\alpha p^2_{max}}] \tag{2.68}$$

where $n_t^{corr}(\vec{p}) = \int P_{corr}(\vec{p},E)\mathrm{d}E$ and $\beta \equiv \frac{A-2}{A-1}$ and $\alpha \equiv \frac{3}{4\langle|\vec{p}_{MF}|^2\rangle}$, with

$$\langle|\vec{p}_{MF}|^2\rangle = \frac{\int |\vec{p}|^2 n_t^{MF}(\vec{p},E)\mathrm{d}^3p}{\int n_t^{MF}(\vec{p},E)\mathrm{d}^3p} \tag{2.69}$$

We have [72],

$$p^2_{min} = \left(\beta|\vec{p}| - \sqrt{2M\beta[E - E^{(2)} - T_{A-1}]}\right)^2 \tag{2.70}$$

$$p^2_{max} = \left(\beta|\vec{p}| + \sqrt{2M\beta[E - E^{(2)} - T_{A-1}]}\right)^2 \tag{2.71}$$

$$\tag{2.72}$$

where $E^{(2)} = M_{A-2} + 2M_N - M_A$ is the average excitation of the $A-2$ nucleon system, and T_{A-1} the recoil energy of the $A-1$ system.

To summarize, Fig. 2.10 shows the basic difference between the relativistic Fermi gas model and the Gaussian spectral function. We see in particular that the well is no longer a rectangle depicted by the function $\theta(|x|)$ but take a Gaussian form.

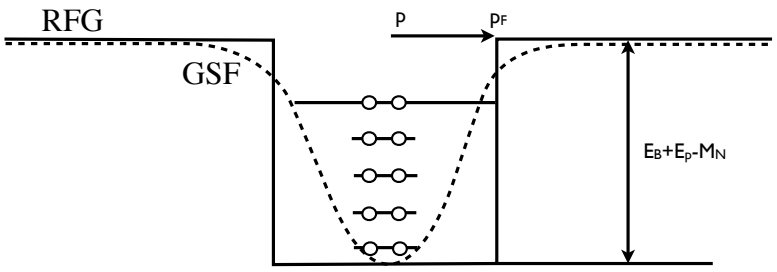

Figure 2.10: Sketch of the relativistic Fermi gas model (RFG) and Gaussian spectral function (GSF) potential.

2.8 Coherent pion production

In coherent production the neutrino scatters from the entire nucleus. These interactions characterized by a very low energy of the recoiling nucleus and a very low Q^2. Therefore the nucleus does not break up. Coherent production of pions by neutrinos can occur in both neutral current interactions and charged current interactions,

$$\nu + A \rightarrow \nu + \pi^0 + A \tag{2.73}$$
$$\nu + A \rightarrow l + \pi^+ + A \tag{2.74}$$

where A the target nucleus is unchanged.

Fig. 2.11 shows the Feynman diagram for a coherent pion production.

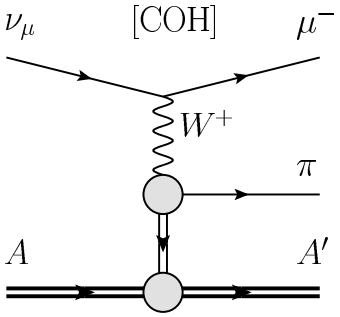

Figure 2.11: Feynman diagram of a coherent pion production [69]

The coherent π^0 cross section used in the model of Rein-Sehgal is based on the Adler's PCAC formula (Partially Conserved Axial-vector Current)[80]. In particular PCAC states that the hadronic axial current $J^a_{\mu 5}$ must satisfy the following continuity equation [81]

$$\partial^\mu J^a_{\mu 5} = -f_\pi m_\pi^2 \Pi^a \tag{2.75}$$

where Π^a is the pion field operator, $f_\pi (= 0.93 m_\pi)$ is the pion decay constant and m_π is the pion mass. It establishes a connection between perturbative and non-perturbative processes and shows the effect of non-perturbative dynamics on would-be-perturbative observables [82].

In the forward-scattering configuration, for any inelastic neutral current reaction $\nu + N \rightarrow \nu + X$, where X denotes an inelastic channel, the cross section is

$$\left(\frac{\mathrm{d}\sigma}{\mathrm{d}x\mathrm{d}y}\right)_{\mathrm{PCAC}} = \frac{G^2 M_N E_\nu}{2\pi^2}(1-y) f_\pi^2 \times \sigma(\pi^0 N \rightarrow X)\Big|_{E_\pi = Ey} \tag{2.76}$$

where the muon mass is neglected and the cross section is given in terms of the Bjorken kinematical variables,

$$\nu = \frac{p \cdot q}{M_N}, Q^2 = -(k-k')^2 \quad \Rightarrow \quad x = \frac{Q^2}{2M_N \nu}, y = \frac{\nu}{E_\nu} \tag{2.77}$$

Rein-Sehgal model have continued the PCAC formula to non-forward direction ($Q^2 \neq 0$) by attaching a slowly varying form-factor $(1 + Q^2/m_A^2)^{-2}$ [83]

$$\left(\frac{\mathrm{d}\sigma^{\pi^0}}{\mathrm{d}x\,\mathrm{d}y\mathrm{d}t}\right) = \frac{G^2 M_N E_\nu}{2\pi^2}(1-y) f_\pi^2 \times \frac{\mathrm{d}\sigma(\pi^0 A \to \pi^0 A)}{\mathrm{d}t}\left(\frac{m_A^2}{m_A^2 + Q^2}\right)^2 \tag{2.78}$$

where,

- $t = (p_\pi - q)^2$ and $m_A \sim 1\ GeV$ serves to define the mass scale in the light-flavor axial channel
- $\frac{\mathrm{d}\sigma(\pi^0 A \to \pi^0 A)}{\mathrm{d}t} = A^2 |F_A(t)|^2 \frac{\mathrm{d}\sigma(\pi^0 N \to \pi^0 N)}{\mathrm{d}t}$ is the pion-nucleus differential cross-section, with A the number of nucleons and $F_A(t)$ is the nuclear form factor (including the effect of absorption).
- $\frac{\mathrm{d}\sigma(\pi^0 N \to \pi^0 N)}{\mathrm{d}t} = \frac{1}{16\pi}\left[\sigma_{tot}^{\pi^0 N}(Ey)\right]^2 (1 + r^2)$ is the pion-nucleon differential cross-section, with $r = \frac{Re(f_{\pi,N}(0))}{Im(f_{\pi,N}(0))}$

In order to calculate the charged current cross section, $\nu + A \to l^- + X$, it is necessary to take into account the effect of lepton mass that is neglected in Eq. 2.76. The correction factor of the lepton mass ($\mathcal{C}$) is defined as follows [84]

$$\mathcal{C} = \left(1 - \frac{1}{2}\frac{Q^2_{\min}}{Q^2 + m_\pi^2}\right)^2 + \frac{1}{4} y \frac{Q^2_{\min}(Q^2 - Q^2_{\min})}{(Q^2 + m_\pi^2)^2} \tag{2.79}$$

where

$$Q^2_{\min} = m_l^2 \frac{y}{1-y}. \tag{2.80}$$

The range of the variable Q^2 is

$$Q^2_{\min} \leq Q^2 \leq 2\, M_N\, E\, y_{\max}, \tag{2.81}$$

where y lies between $y_{\min} = m_\pi/E$ and $y_{\max} = 1 - m_l/E$. Thus, the corrected PCAC formula, valid for small angle scattering, for $\nu + A \to l^- + X$ is [84]

$$\begin{aligned}\left(\frac{\mathrm{d}\sigma}{\mathrm{d}x\,\mathrm{d}y}\right)_{\mathrm{PCAC},\, m_l \neq 0} &= \frac{G^2 M_N E}{\pi^2} f_\pi^2 (1-y)\sigma(\pi^+ + A \to X)\Big|_{E_\pi = Ey} \\ &\quad \times \mathcal{C}\,\theta(Q^2 - Q^2_{\min})\,\theta(y - y_{\min})\,\theta(y_{\max} - y)\end{aligned} \tag{2.82}$$

The cross section for $\nu + A \to l^- + A + \pi^+$ is given by,

$$\left(\frac{\mathrm{d}\sigma^{\pi^+}}{\mathrm{d}x\,\mathrm{d}y\mathrm{d}t}\right) = \left(\frac{\mathrm{d}\sigma^{\pi^0}}{\mathrm{d}x\,\mathrm{d}y\mathrm{d}t}\right) \mathcal{C}\,\theta(Q^2 - Q^2_{\min})\,\theta(y - y_{\min})\,\theta(y_{\max} - y) \tag{2.83}$$

where $\left(\frac{\mathrm{d}\sigma^{\pi^0}}{\mathrm{d}x\,\mathrm{d}y\mathrm{d}t}\right)$ is given by Eq. 2.78.

The physical interpretation of the correction factor is as follows: when the muon mass is not neglected, the reaction $\nu + A \to l^- + X$, receives a contribution from the exchange of a charged pion between the lepton vertex and the hadron vertex. The coupling at the lepton vertex is $f_\pi m_l \bar{l}\gamma_5 \nu$, and the amplitude contains the characteristic pion propagator $(Q^2 + m_{m_\pi^2})^{-1}$. This so-called pseudo-scalar amplitude interferes with the remaining amplitude, which is free of the pion singularity. The two amplitudes interfere destructively and the destructive nature of the interference is visible in the first term of the correction factor.

2.9 Deep Inelastic Scattering (DIS)

Deep inelastic scattering are processes that start appearing at high neutrino energy and are well known at high $Q^2 > 2$ GeV^2. This scattering can be described by

$$\nu_l + A \to l^- + X \tag{2.84}$$
$$\nu_l + A \to \nu_l + X \tag{2.85}$$

where A is the nucleus and X a number of particle bigger than a single pion, where the Feynman diagram is shown in Fig. 2.12.

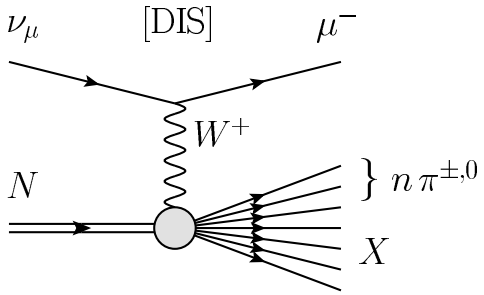

Figure 2.12: Feynman diagram of a deep inelastic scattering [69]

The differential cross section of the process $\nu + A \to l^- + X$ is given in its general form by Eq. 2.23,

$$\frac{\mathrm{d}^2\sigma}{\mathrm{d}\Omega \mathrm{d}\epsilon'} = \frac{G_F^2}{4\pi^2}\frac{|\vec{k'}|}{|\vec{k}|} L_{\mu\nu} W^{\mu\nu} \tag{2.86}$$

where ϵ' is the energy of the outgoing lepton, $W^{\mu\nu}$ can be expressed in its most general way as

$$W^{\mu\nu} = W_1(-g^{\mu\nu} + \frac{q^{\mu\nu}}{q^2}) + \frac{W_2}{M_N^2}(p^\mu - \frac{p\cdot q}{q^2}q^\mu)(p^\nu - \frac{p\cdot q}{q^2}q^\nu) - W_3\frac{i\epsilon^{\mu\nu\alpha\beta}}{2M_N^2}p_\alpha p_\beta \tag{2.87}$$

where M_N is the mass of the nucleon and the W_i are the hadronic structure functions. In the limit of high Q^2, they represent the parton distribution functions. This can be shown by changing to the Bjorken kinematical variables in the laboratory frame,

$$\nu = \frac{p\cdot q}{M_N}, Q^2 = -(k-k')^2 \quad \Rightarrow \quad x = \frac{Q^2}{2M_N(E_\nu - \epsilon')}, y = \frac{(E_\nu - \epsilon')}{E_\nu} \tag{2.88}$$

For high Q^2, we then have,

$$M_N W_1(Q^2, \nu) \to F_1(x) \tag{2.89}$$
$$\nu W_2(Q^2, \nu) \to F_2(x) \tag{2.90}$$
$$\nu W_3(Q^2, \nu) \to F_3(x) \tag{2.91}$$

where F_1, F_2 and xF_3, are the parton distribution function.

Using the relation of Callan-Gross, $2xF_1 = F_2$, we obtain

$$\frac{\mathrm{d}^2\sigma}{\mathrm{d}x\mathrm{d}y} = \frac{G_F^2 M_N E_\nu}{\pi}\left[(1-y+\frac{1}{2}y^2+C_1)F_2(x,q^2) \pm y(1-y+\frac{1}{2}y^2+C_2)xF_3(x,q^2)\right] \quad (2.92)$$

$$C_1 = \frac{1}{2E_\nu}\left(\frac{yM_l^2}{2M_N x} - xyM_N - \frac{M_l^2}{2E_\nu} - \frac{M_l^2}{2M_N x}\right) \quad (2.93)$$

$$C_2 = -\frac{M_l^2}{4M_N E_\nu x}, \quad (2.94)$$

where M_l is the mass of the lepton and E_ν is the energy of the incoming neutrino.

2.10 Final State Interactions (FSI)

Neutrino interaction models predict cross sections and kinematics of neutrinos scattering off bound or unbound nucleons. For bound nucleons within a nucleus, we call the neutrino-nucleon vertex the primary neutrino interaction vertex. The final state hadrons resulting from this interaction, for example the proton from a CCQE interaction or the pion from a CC1π interaction, must propagate through the nuclear medium before observation. Since these particles interact via the strong force, there is a significant probability of re-interaction within the nucleus prior to escape. We refer to this re-interaction as a *final state interaction* (FSI). FSI affect the observable final state via particle absorption, scattering and particle production making the interpretation difficult for direct cross section measurements at low energy ranges.

In the following, we only consider FSI of pions or nucleons that can be modeled by a microscopic cascade. For leptons, FSI is assumed to be negligible since they do not interact strongly. Also, FSI are not considered for hadrons produced off free protons, for example hydrogen in water, since the vertex is far from the nuclear medium.

The microscopic cascade model is a pion FSI model where the pion is propagated classically through the nuclear medium in finite steps. The probabilities per step of different interactions are calculated by the Δ-*hole* (Δh) model [85] or from free pion-proton or pion-deuterium (πp or πd) scattering cross sections [5]. In the Δh model, the pion generates a nucleon resonance Δ which may move in a different potential well, leaving a *hole* in the nucleon well [86].

A random number is generated to determine which, if any, interaction occurs at a given step. This allows the pion to undergo multiple interactions during its journey through the nucleus.

The microscopic cascade also provides the theoretical connection between pion scattering measurements, where the pion originates from outside the nucleus, to neutrino and photo-production measurements where the pion is produced within the nucleus.

2.11 Summary

In this chapter, we introduced the weak interaction that is the only force felt by the neutrino. By a simple calculation, we see that for a beam of muon neutrinos, the only possible reaction at low

[5] In NEUT, at momentum greater than 500 MeV/c, the probabilities are calculated from πp and πd scattering cross sections, where the nucleons begin to appear as free particle in the nucleus. At lower momentum ($p_\pi < 500$ MeV/c), the Δh model is used.

neutrino energies, is for the neutrino interacting with bound or unbound nucleons. Interactions with the electrons present in matter have a threshold of 11 GeV.

We defined the cross section as being the number of interaction per flux of the incident particle and per the number of target nucleons. The cross section can be expressed as the multiplication of leptonic and hadronic tensors. While the leptonic tensor can be exactly calculated, the hadronic tensor can not, at low energies, because of the strong interactions inside the nucleus. The hadronic tensor can be then expressed via different form factors or by the use of different approximations such as the impulse approximation where the nucleons inside the nucleus are seen as a collection of individual nucleons. The simplest model describing the distribution of the nucleons inside the nucleus is the relativistic Fermi gas model that is also employed in the Monte-Carlo neutrino interactions generators.

We studied, in particular, the quasi-elastic, resonant, coherent and deep inelastic scattering processes, where different approximations are used and the prediction given. The approximations employed are, generally, the same approximations employed in the Monte-Carlo generators. Nowadays, there are more sophisticated studies that have not been approached in this chapter [61].

While quasi-elastic interactions are dominant at energies below 1 GeV, deep inelastic scattering characterized by a high momentum transfer ($Q^2 > 2$ GeV) is dominant at high energies ($E_\nu > 10$ GeV). In this case, the nucleon tends to break up and produce new hadrons. At low $Q^2 < 2$ GeV, resonant processes are characterized by the production of a resonant state due to the excitation of the nucleon during the interaction process. They take generally place at energies of few GeV. The excitation, called resonance, decay then to its fundamental states producing other particles, like kaons and pions. When a pion is produced from the neutrino interaction on the whole nucleus that remain the same, the reaction is called coherent.

For bound nucleons within a nucleus, we call the neutrino-nucleon vertex the primary neutrino interaction vertex. The final state hadrons resulting from this interaction, for example the proton from a CCQE interaction or the pion from a CC1π interaction, must propagate through the nuclear medium before observation. Since these particles interact via the strong force, there is a significant probability of re-interaction within the nucleus prior to escape. We refer to this re-interaction as a *final state interaction* (FSI).

When a neutrino scattering occurs on bound nucleons inside a nucleus, the final state hadrons can re-scatter with the other nucleons. These interactions are called final state interactions and have to be taken into consideration when comparing with a measurement as they can mask the primary interaction cross section.

In the next chapter, the T2K experimental setup will be described. In particular, we will present how the flux of muon neutrino is created and describe the composition of the near detector that contain the target on which we measure the cross section. In addition to the near detector, we will also describe the far detector used for the T2K oscillation analysis.

Chapter 3

The T2K experiment

The T2K (Tokai-to-Kamioka) experiment is a long baseline experiment. It uses a neutrino beamline, a near detector at 280 m (ND280)[87] and the far detector, Super-Kamiokande (SK) [88] at 295 km from the neutrino source. Neutrinos are generated from the 30 GeV J-PARC (Japan Proton Accelerator Research Complex) proton beam located at Tokai-mura on the East coast of Japan as shown by Fig. 3.1.

Figure 3.1: Overview of the T2K experiment, where a high intensity beam of ν_μ is created at Tokai and sent 295 km under ground to Super-Kamiokande.

The first goal of the T2K experiment was to measure θ_{13}. Although Daya Bay and RENO have now already given precise measurement of this angle, T2K can still give complementary informations as it measures electron neutrino appearance as opposed to the reactor anti-neutrino disappearance measurements. In addition to the electron neutrino appearance measurement, the T2K experiment can give precise measurement on the atmospheric parameters θ_{23} and Δm_{23} by looking at the disappearance probability of the muon neutrino. Moreover, T2K can also help in understanding the mass hierarchy and CP violation.

T2K uses an off-axis method [89] to generate a narrow band neutrino beam, in order to maximize the neutrino event rate at the oscillation peak in the far detector. The off-axis angle has been chosen so that the peak of the neutrino energy spectrum corresponds to the energy needed to be

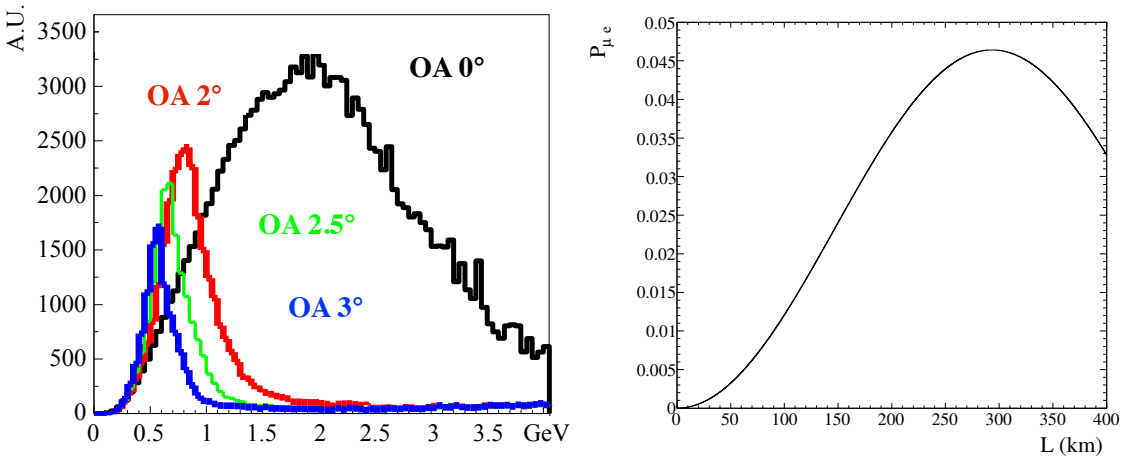

Figure 3.2: Left: neutrino energy spectrum for different off-axis angles given. Right: Probability to observe $\nu_\mu \to \nu_e \approx \sin^2(2\theta_{23})\sin^2(\theta_{13})\ \sin^2(1.27\Delta m_{23}L/E)$ as a function of the distance L in [km] for $\sin\theta_{13} = 0.026$ and $\sin\theta_{23} = 0.053$ and a peak energy of 0.6 GeV.

at the first maximum of the oscillation at Super-Kamiokande (see Fig. 3.2). The off-axis angle is set at 2.5° so that the muon neutrino beam has a peak energy around 600 MeV. The angle can be reduced to 2.0°, allowing variation of the peak neutrino energy.

At 280 m, the near detector is composed of an on-axis (INGRID) and a magnetized off-axis (ND280) detector. While the role of INGRID is to measure the beam profile and stability, the off-axis detector measures the muon neutrino event rate, the energy spectrum, and intrinsic electron-neutrino contamination in the beam in the direction of the far detector. These measurements are essential in order to characterize signals and backgrounds that are observed in the far detector. In addition, the near detector is able to measure different cross sections on carbon and water, to decrease systematic error from cross sections in the far detector.

While the T2K beam is explained in details in Sec. 3.1, the different detectors of the T2K experiment are described in Sec. 3.2. The complete description of the T2K experiment is explained in great detail in [90].

3.1 The T2K beam

In this section, the different stages of the neutrino beam creation are explained. The neutrino beam is obtained from the acceleration of protons (see Sec. 3.1.1). The protons are extracted and bent towards Kamioka, and then hit the graphite target. At this point, the mesons, produced and focused by the horns, decay principally into muons and muon neutrinos. The beam dump stops most of the remaining particles that are not neutrinos. The remaining high energy muons that managed to pass the beam dump are monitored by the muon monitor, which verifies the beam direction and its stability (see Sec. 3.1.2). The schematic description of the neutrino beam line and the near detectors is shown in Fig. 3.3.

The hadrons production obtained after the collision of the protons with the target is not well known. In order to decrease systematic uncertainties, the NA61/SHINE experiment has taken

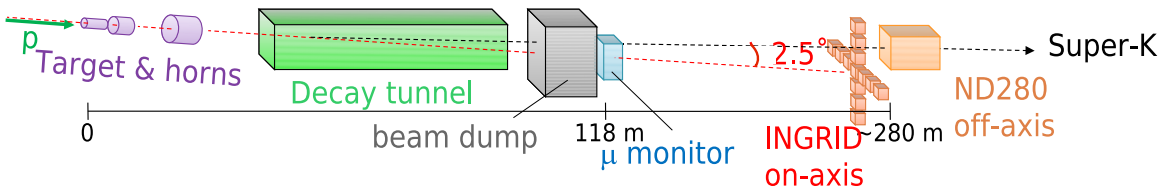

Figure 3.3: Schematic view of the T2K neutrino beamline and near detectors.

data with the same proton beam energy and similar graphite targets [1] to provide more information on hadrons production (see 3.1.3). The neutrino flux, in the T2K experiment, is then simulated based on NA61/SHINE data.

3.1.1 The J-PARC Accelerator

J-PARC is located in the Tokai prefecture, Ibaraki, and consists of three accelerators [91]: a linear accelerator (LINAC), a rapid-cycling synchrotron (RCS) and the main ring (MR) synchrotron.

- A cesium-free negatively charged hydrogen ion source driven with a lanthanum hexaboride (LaB_6) filament [92] is used to produce H^- that are accelerated by the LINAC up to a kinetic energy of 400 MeV (181 MeV at present). At the RCS injection, the beam is converted to a proton beam by charge-stripping foils.
- The RCS accelerates the protons up to a kinetic energy of 3 GeV with 25 Hz cycle. The harmonic number[2] of the RCS is 2, and there are two bunches in a cycle. About 5% of these bunches are supplied to the MR.
- The MR accelerates the protons up to a kinetic energy of 30 GeV in a circumference of 1567 m. The harmonic number of the MR is 9 and the RF frequency is between 1.67 and 1.72 MHz. The beam intensity is $3.3 \cdot 10^{14}$ proton per spill. The spill cycle is about 0.5 Hz and therefore the maximum beam power is 750 kW (the current beam power is 190 kW). The spill width is 5.6 μs and contains 8 bunches (6 before June 2010) each of a length of 58 ns. The eight bunches are extracted within a single turn by a set of five kicker magnets. The knowledge of the time structure of the proton beam is very important to be able to discriminate the different backgrounds, including cosmics.

3.1.2 The Beamline

The T2K neutrino beamline can be divided into two phases called primary and secondary beamlines. In the primary beamline, the extracted protons from the MR are bent toward Kamioka. In the secondary beamline, they collide with a graphite target, producing secondary pions, which are focused by magnetic horns and decay into neutrinos. An overview of the neutrino beamline is shown in Fig. 3.4.

[1] In fact, data have been taken with two different targets. The first target used was a thin graphite target in comparison to the T2K target. In 2009 and 2010, a T2K replica target has been used to decrease even more systematic uncertainties.

[2] The harmonic number, h, is the integer that relates the angular revolution frequency, ω_0, to the RF frequency, $\omega_{RF} = h\omega_0$

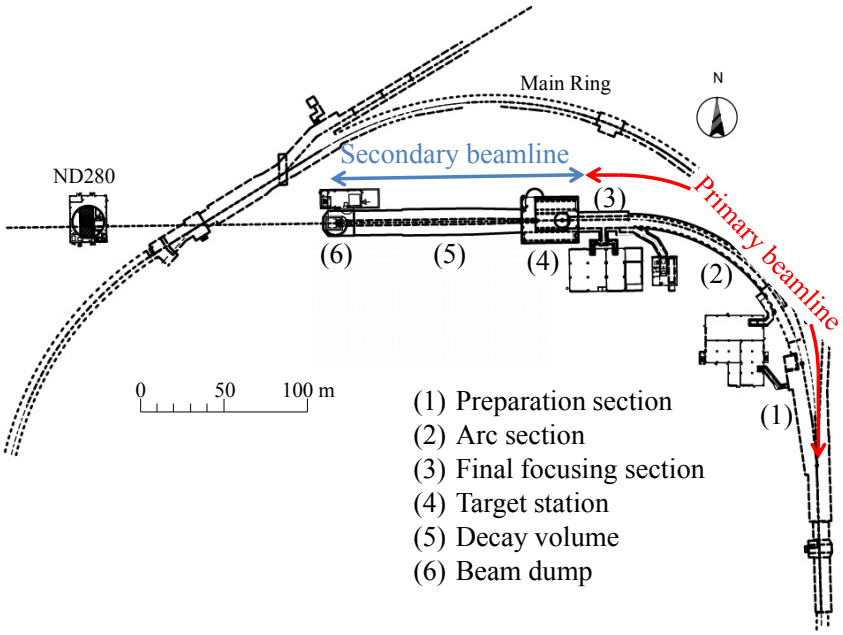

Figure 3.4: Overview of the T2K neutrino beamline

In the following we will describe the two beamline sections and then the beam monitoring detectors.

The Primary Beamline

The primary beamline consists of the preparation section (54 m long), arc section (147 m) and final focusing section (37 m).

- In the preparation section, the extracted proton beam is focused and deflected with a series of 11 normal conducting magnets so that the beam can be accepted by the arc section.
- In the arc section, the beam is bent toward the direction of Kamioka by 80.7^o, with a 104 m radius of curvature, using 14 doublets of superconducting combined function magnets (SCFMs) [93, 94]. These magnets incorporate a new concept in which a dipole field of 2.6 T is generated simultaneously with a quadrupole field of 19 T/m in a coil aperture of 173.4 mm. Thus, a single SCFM can provide beam bending and focusing.
- In the final focusing section, ten normal conducting magnets guide and focus the beam onto the target.

A well-tuned proton beam is essential for stable neutrino beam production, and to minimize beam loss in order to achieve high-power beam operation. Therefore, the intensity, position, profile and loss of the proton beam in the primary sections are precisely monitored. This is achieved by five current transformers (CTs), 21 electrostatic monitors (ESMs), 19 segmented secondary emission monitors (SSEMs) and 50 beam loss monitors (BLMs) [90]. Their location is shown in Fig. 3.5.

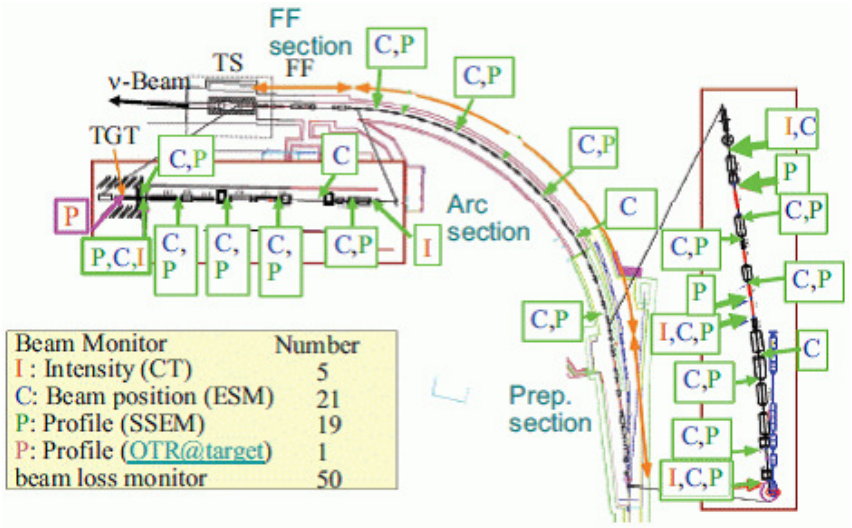

Figure 3.5: Location of the primary beam line monitors.

The Secondary Beamline

Protons from the primary beamline are directed to the target via the titanium-alloy beam window, which separates the vacuum in the primary beamline and the helium gas volume in the secondary beamline. The secondary beamline consists of three sections: the target station, decay volume and beam dump (Fig. 3.6). The produced mesons in the target station decay in flight inside a single volume of ∼1500 m^3 (target station, decay volume and beam dump together), filled with helium gas (1 atm) to reduce pion absorption and to suppress tritium and NO_x production by the beam.

- **The target station** is located 12 meters underground and it has been designed to contain the radiation and to assure the cooling of the T2K target and of the three magnetic horns with water. It contains also a baffle, which is a graphite collimator to protect the magnetic horns; an optical transition radiation monitor (OTR) to monitor the proton beam profile just upstream of the target. The target and the horns are contained in an aluminum volume filled with helium to avoid the air activation. Iron blocks are placed around the target station to assure the shielding of the region. The produced mesons are collected and focused by the three horns.

  - *The T2K target* is a graphite (1.8 g/cm^3) cylinder, 91.4 cm long, with a diameter of 2.6 cm. It is installed in the inner conductor of the first horn. About 80 % of the protons are interacting in the target generating pions and kaons that will decay into neutrino in the decay volume. The target is one of the limiting factor in the construction of intense neutrino beam. When the very intense beam hits the target, the temperature immediately rises due to the energy deposited by the protons and the material due to higher Z would be strongly damaged. The graphite has then been chosen for its low-Z propriety, its high melting point and good thermal stress resistance. It is also stable and easy to handle.

    The target is cooled by helium gas flowing through the various gaps keeping the temperature at the center around 700 ^{o}C where the radiation damage for the graphite

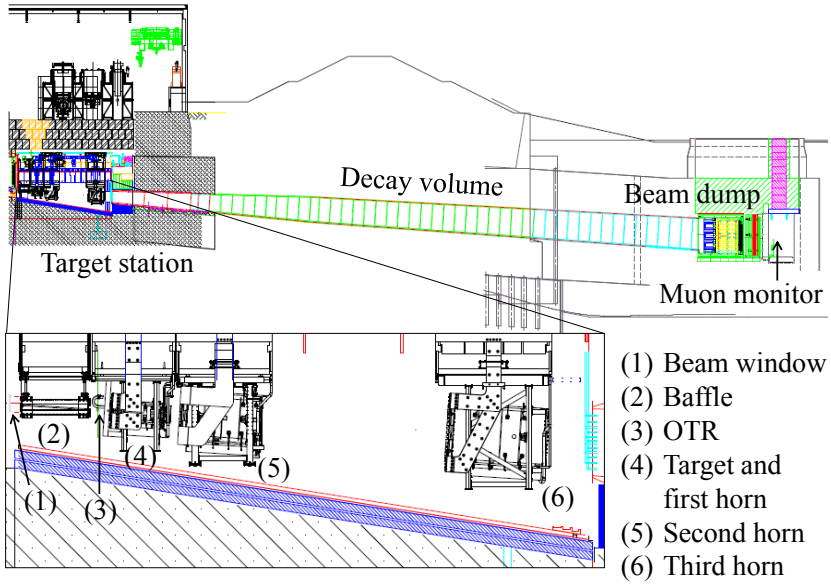

Figure 3.6: Side view of the secondary beamline. The length of the decay volume is ∼96 m.

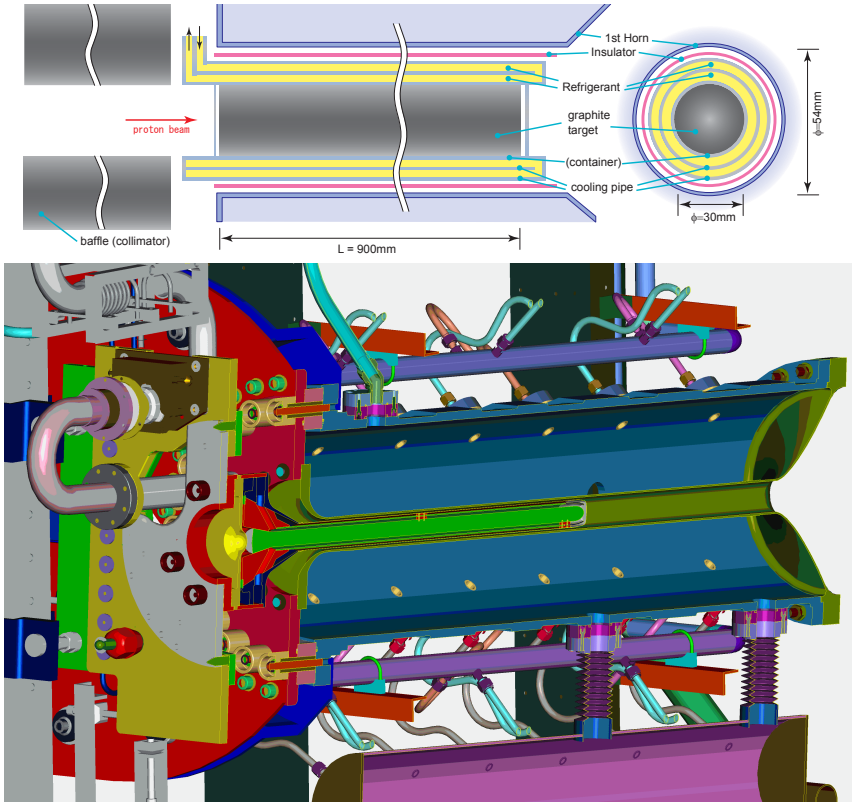

Figure 3.7: Top: Conceptual drawing of the target system of J-PARC neutrino beamline. Bottom: Cross section of the first horn and target.

is minimum. The radiation dose due to the activation of the target is estimated at a few Sv/h six months after a one year's irradiation by the 750 kW beam [95].

- *The Magnetic Horns:* In all neutrino beams, magnetic horns are used to focus charged hadrons that will decay into neutrinos so that the resulting neutrino beam is as narrow as possible. By changing the polarity of the magnetic field, positively or negatively charged mesons are selected and focused toward the decay tunnel where, depending on their charge, neutrino or anti-neutrino beams are produced. The T2K beamline uses

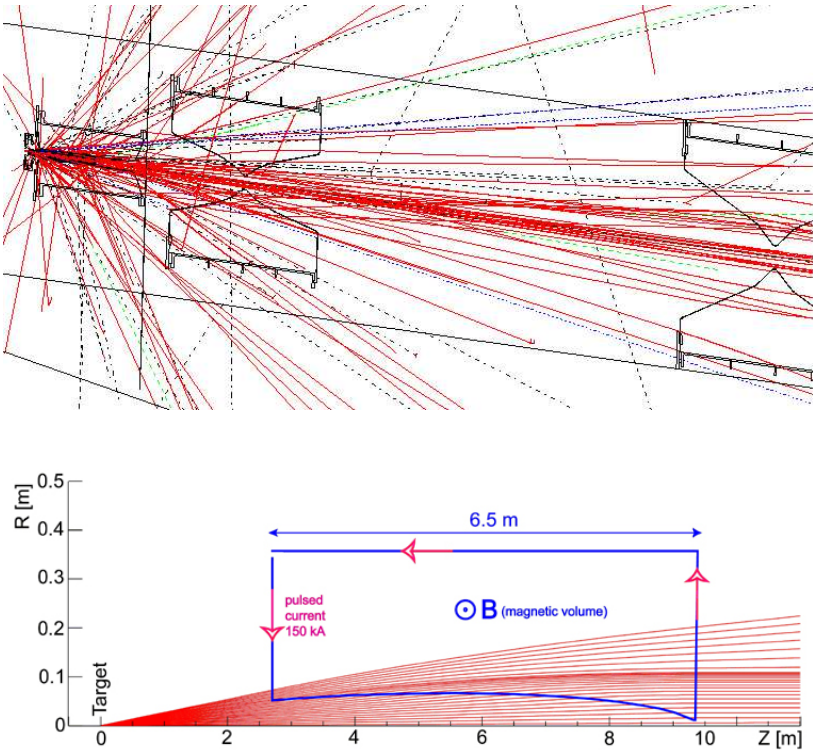

Figure 3.8: Top:Focusing system of the T2K beam line in the YZ projection. Charged hadrons (red) from the production target are focused by a system of three magnetic horns before entering the decay tunnel. Bottom: Principle of a magnetic horn.

3 horns. Each magnetic horn consists of two coaxial (inner and outer) conductors, which encompass a closed volume [96, 97] (see Fig. 3.8). A toroidal magnetic field is generated by a very intense current.

When the horn is run with an operation current of 320 kA, the maximum field is 2.1 T and the neutrino flux at Super-Kamiokande is increased by a factor of ∼16 (compared to horns at 0 kA) at the spectrum peak energy (∼0.6 GeV). The data analyzed in this thesis is obtained with horns running at 250 kA[3].

The horns are optimized to maximize the neutrino flux; the inside diameter is as small as possible to achieve the maximum magnetic field, and the conductor is as

[3]The data taken in 2012 has been split into two runs. The first part of data that has been used for the oscillation analysis at the far detector shown in June 2012 has been obtained with horn currents of 200 kA because of power supply failure. For the second run, the problem has been fixed and the data has been taken with horns with the same current as in 2011 and 2010.

thin as possible to minimize pion absorption while still being tolerant of the Lorentz force, created from the horn current, the magnetic field, and the thermal shock from the beam.

The first horn collects the pions, which are generated at the target installed in its inner conductor. The second and third horns focus the pions. The diameters, length and width dimensions of the horns are listed in Table 3.1.

Table 3.1: The horns dimensions.

	horn 1	horn 2	horn 3
Inner diameter	5.4 cm	8 cm	14 cm
Inner conductor thickness	3 mm	3 mm	3 mm
Outside diameter	0.4 m	1 m	1.4 m
Length	1.5 m	2 m	2.5 m

- **The decay volume** is a ∼96 m long steel tunnel. It is filled with Helium in which the secondary hadrons, mainly pions, decay into muons and muon neutrinos. The walls are made of iron plates equipped with a water cooling circuit to remove the heat load by secondary particles. The entire tunnel is surrounded by 6 meters of concrete to shield the radiation (see Fig. 3.6). Its vertical dimension is made so that the neutrino beam direction can be off-axis by an angle between 2^o and 3^o. The length of the tunnel has been chosen long enough to have as many muon neutrino as possible but short enough to avoid as possible the decay of the muon into ν_e and $\bar{\nu}_\mu$. All the hadrons, as well as muons below ∼5 GeV/c, are stopped by the beam dump at the end of the tunnel.

- **The beam dump** sits at the end of the decay volume. The beam dump's core is made of 75 tons of graphite (1.7 g/cm^3), and is 3.174 m long, 1.94 m wide and 4.69 m high. It is contained in the helium vessel. Fifteen iron plates are placed outside the vessel and two inside, at the downstream end of the graphite core, to give a total iron thickness of 2.40 m. The neutrinos pass through the beam dump and are used for physics experiments. Any muons above ∼5 GeV/c that also pass through the beam dump are monitored to characterize the neutrino beam.

The Muon Monitor Detectors and Emulsion Trackers

The neutrino beam intensity and direction can be monitored on a bunch-by-bunch basis by measuring the profile distribution of muons. Since the muons are produced from the same parent particles as the neutrinos, the measurement of their properties also provides information about the neutrino beam. To reduce systematic uncertainties and assure the measurement at Super-Kamiokande, it is necessary to control the beam direction.

This is achieved by the muon monitor [98, 99] that is designed to measure the neutrino beam direction with a precision better than 0.25 mrad[4] and to monitor the stability of the neutrino beam intensity with a precision better than 3%.

[4] Actually, in order to have $\delta(\Delta m) \equiv 10^{-4}\ eV^2$ [100], the precision on the neutrino beam direction has to be much better than 1 mrad.

The muon monitor is located just behind the beam dump. It consists of two types of detector arrays:

- **Ionization chambers at 117.5 m from the target**
  It is a simple device to monitor the beam for a long run period and it is also suitable to cover the large area of the beam profile. It has a slow response and a weak signal over the unknown background coming from the beam dump.
- **Silicon PIN photodiodes at 118.7 m from the target**
  They are used to overcome slow response and weak signals of the ionization chambers. They have a fast response and are less sensitive to the background because of the large and fast signal. Problems for the semiconductor may arise from the long term stability due to radiation damages.

A detector made of nuclear emulsion films is installed downstream the muon monitor. It is composed of two types of modules made to measure the flux and the momentum of the muons respectively. The flux is measured with a systematic uncertainty of 2%. The other module can measure the momentum of each particle by multiple Coulomb scattering with a precision of 28% at a muon energy of 2 GeV/c [101, 102].

3.1.3 The flux

The T2K beamline is simulated by the JNUBEAM code developed by the T2K collaborators. It has been developed and used to optimize the conception of the T2K target, horns and decay tunnel. JNUBEAM is also used to simulate the characteristics of the proton beam and the hadrons production cross sections.

The primary interaction of the 30 GeV proton with the graphite target is simulated based on NA61/SHINE [103, 104, 105] data, which fully covers the kinematic region of interest for T2K (see Fig.3.9).

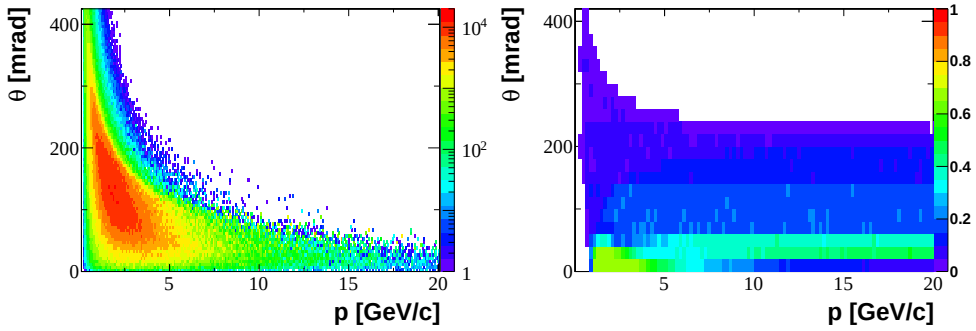

Figure 3.9: Left: The prediction from the T2K beam simulation: the $\{p, \theta\}$ distribution for π^+ weighted by the probability that their decay produces a muon neutrino passing through the SK detector. Right: Fraction of accepted particles as a function of momentum and polar angle, after the track acceptance cuts and ToF-F acceptance cut. The first polar angle bin, [0,20] mrad, is fully covered by accepted particles up to 7.6 GeV/c. [105].

The hadronic interactions inside the target are simulated by FLUKA [106]. The particle transport is based on GEANT 3.21 [107]. The interactions outside the target are simulated using

GEANT3/GCALOR [108] with the interaction cross sections tuned to experimental data. The secondaries and any un-interacted protons are tracked until they decay into neutrinos or are stopped at the beam dump. The particles considered in JNUBEAM as neutrino source and their decay are listed in Table 3.2.

Table 3.2: Neutrino-producing decay modes considered in JNUBEAM and their branching ratio in percentage. Decay modes for $\bar{\nu}_\mu$ and $\bar{\nu}_e$ are omitted in this table. The π^- and K^- modes are charge conjugates of the π^+ and K^+ modes, respectively [109].

	π^+	K^+	K^0_L	μ^+	μ^-
ν_μ	$\mu^+\nu_\mu$	$\mu^+\nu_\mu$, $\pi^0\mu^+\nu_\mu$	$\pi^-\mu^+\nu_\mu$		$e^-\nu_\mu\bar{\nu}_e$
%	99.9877	63.55, 3.353	27.04		100
ν_e	$e^+\nu_e$	$\pi^0 e^+\nu_e$	$\pi^- e^+\nu_e$	$e^+\bar{\nu}_\mu\nu_e$	
%	1.23×10^{-4}	5.07	40.55	100	

The beam ν_e background at SK mainly comes from the secondary π^+ via the following decay chains: $\pi^+ \to \mu^+\nu_\mu$, $\mu^+ \to e^+\bar{\nu}_\mu\nu_e$. Secondary K^+ and K^0_L are also important for the estimation of the beam ν_e background.

The trajectories of neutrinos are extrapolated to the near and far detectors, providing the predicted fluxes and energy spectra at both detector sites (see Fig. 3.10).

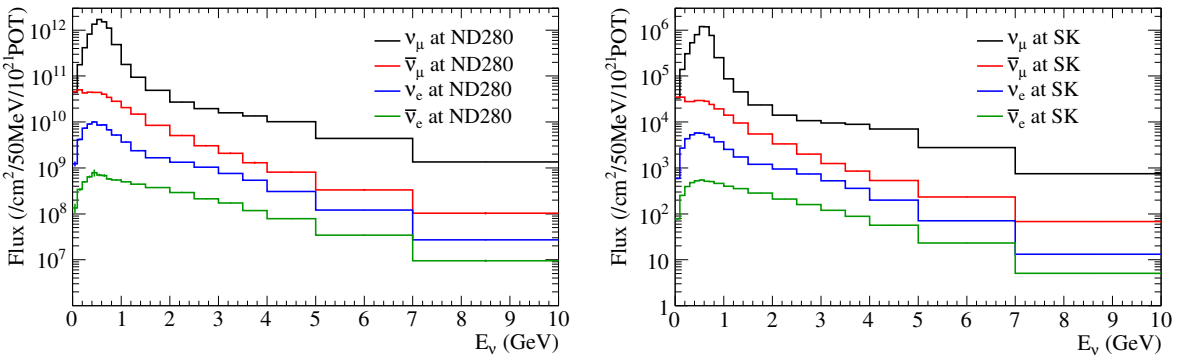

Figure 3.10: The ND280 and SK flux prediction for all flavors integrated over Runs 1 and 2 with POT weighting. Normalized to 10^{21} POT.

The NA61/SHINE measurements have allowed the decrease of the systematic errors due to the flux for the current analysis presented in this thesis. For the 2010a analysis, the uncertainty on the neutrino flux was as large as 20% [110]. Because of the latest kaon cross section production released in 2011 by the NA61 collaboration based on the data they have taken in 2007, the uncertainty is now reduced down to 10 %.

NA61/SHINE (SPS Heavy Ion and Neutrino Experiment)

The NA61/SHINE experiment at the CERN SPS pursues a rich physics program in various fields [103]. The purpose of the NA61/SHINE measurements for T2K is to provide precise

hadron production measurements at exactly the proton extraction energy of the MR, namely 30 GeV kinetic energy.

The setup of the detector is shown in Fig. 3.11. The main components of the current detector were constructed and used by the NA49 collaboration [111]. It is a large acceptance hadrons spectrometer. A set of scintillation and Cherenkov counters as well as beam position detectors (BPDs) upstream of the spectrometer provide timing reference, identification and position measurements of the incoming beam particles. The main tracking devices are large volume Time Projection Chambers (TPCs). Two of them, the vertex TPCs (VTPC-1 and VTPC-2 in Fig. 3.11), are located in a free gap of 100 cm between the upper and lower coils of the two superconducting dipole magnets. Two large TPCs (MTPC-L and MTPC-R) are placed downstream of the magnets symmetrically to the beamline. The particle identification capability of the TPCs based on measurements of the specific energy loss, dE/dx, is augmented by time-of-flight measurements using Time-of-Flight (ToF) detectors.

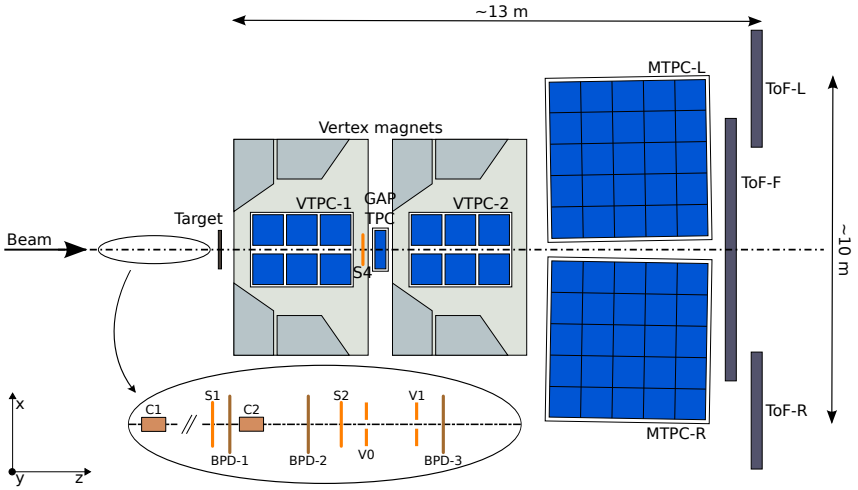

Figure 3.11: The layout of the NA61/SHINE experiment at the CERN SPS (top view, not to scale). The chosen right-handed coordinate system is shown on the plot. The incoming beam direction is along the z axis. The magnetic field bends charged particle trajectories in the $x - z$ (horizontal) plane. The drift direction in the TPCs is along the y (vertical) axis[105].

Presently, the T2K neutrino beamline is set up to focus positively charged hadrons, in such a way that it produces a ν_μ beam. Therefore, spectra of positively charged pions constitute directly an essential ingredient in the T2K neutrino flux calculation. The kinematic region of interest for positively charged pions whose daughter muon neutrinos pass through the SK detector is shown in Fig. 3.9.

Data were taken with a 2 cm thin carbon target (4% of nuclear interaction length) over two run periods in 2007 and 2009. Another set of data was taken with the 90 cm long T2K replica target.

The thin target data analysis has been finalized and results presented as double-differential ($\frac{d^2n}{dpd\theta}$) cross-sections [105]. These cross sections will partly constrain the neutrino flux prediction, while the simulation of secondary interactions will still require some tuning.

The systematic errors on the pion and kaon multiplicity is about 5% for the 2012 analysis compared to 10% for the 2010a. The complete list of systematic error and their uncertainties are given in Chapter 6.

These uncertainties should be reduced with the future NA61 analysis of 2009 thin target and long target data. Fits to other data using parameterized models may also decrease the uncertainties [110].

3.2 The T2K detectors

The T2K detectors are divided into the far detector, Super-Kamiokande, and the near detectors 280m away from the target. While the far detector goal is to measure the effect of neutrino oscillations, the near detectors measure the intrinsic properties of the neutrino beam such as its composition and the neutrino cross sections.

3.3 The Far Detector: Super-Kamiokande (SK)

3.3.1 Overview

SK is the largest land-based water Cherenkov detector in the world and is located 295 km west of the beam source where it is used to sample the beam's flavor composition and look for $\nu_\mu \rightarrow \nu_e$ appearance and ν_μ disappearance. Built 1 km deep within the center of Mt. Ikenoyama, SK is a cylindrical cavern filled with 50 kton of pure water within which the detector's roughly 13,000 photomultiplier tubes (PMTs) image neutrino interactions.

SK has been running since 1996 and has produced data for a number of well-known results that include world-leading limits on the proton lifetime [112, 113, 114] and the measurement of flavor oscillations in atmospheric, solar and accelerator-produced neutrinos [12, 115, 116, 117, 118]. Over this time there have been four running periods: SK-I, SK-II, SK-III, and SK-IV. The latest period, SK-IV, is still in progress and features upgraded PMT readout electronics. SK-IV is also the period in which the T2K experiment takes place.

Because of the detector's long-running operation, the SK behavior is well understood. The calibration of the energy scale is known to the percent level, and the software for modeling events in the detector matches calibration samples to the percent level as well.

Description

The geometry of the SK detector consists of two major volumes, an inner and an outer detector which are separated by a cylindrical stainless steel structure. Fig. 3.12 gives a schematic view of the SK detector geometry.

- *The inner detector (ID)*: is a cylindrical shell 33.8 m in diameter and 36.2 m in height which currently houses along its inner walls 11,129 inward-facing 50 cm diameter PMTs, representing 40% of surface coverage.
- *The outer detector (OD)*: is a cylindrical space about 2 m thick radially and on the axis at both ends. It contains along its inner walls 1,885 outward-facing 20 cm diameter PMTs. It is only sparsely instrumented but with PMTs capable of 100% rejection efficiency of cosmic ray muon backgrounds.

The ID and OD boundaries are defined by a cylindrical structure about 50 cm wide. This structure consists of a stainless steel scaffold covered by plastic sheets which serve to optically separate the ID and OD. The wall facing into the ID is lined with a black sheet of plastic meant to absorb light and minimize the number of photons which either scatter off of the ID wall back into the ID volume, or pass through from the ID to the OD (see Fig. 3.12).

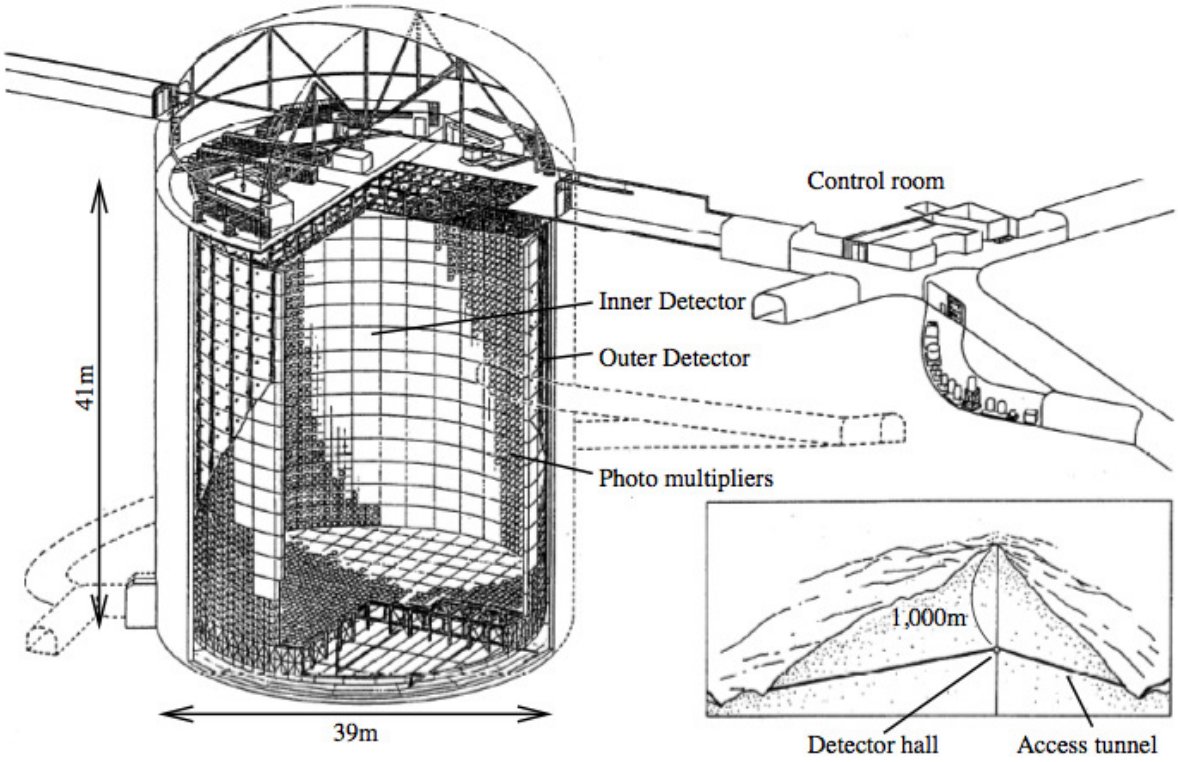

Figure 3.12: Diagram of the Super-Kamiokande Detector. The detector is mainly comprised of two segments, the inner and outer detectors. The boundary between the two segments is defined by a cylindrical scaffold used to mount photomultiplier tubes and optically separate the segments. The figure comes from [119].

Principle

Neutrino interactions often produce charged particles which, if above an energy threshold, produce a cone of Cherenkov photons as they go through the water. When the photons reach the PMTs on the detector walls they produce a ring-shaped hit pattern which is used to extract information about the interaction such as the event vertex position and momentum of product particles. Fig. 3.13 shows an example of muon ring at the far detector.

Strategy

The goal of the far detector is to measure the flavor composition of the T2K neutrino beam at SK, and thereby observe the oscillation of ν_μ to either ν_e or ν_τ as a function of the reconstructed energy of the neutrinos. To do so, the primary strategy consists in counting charged current

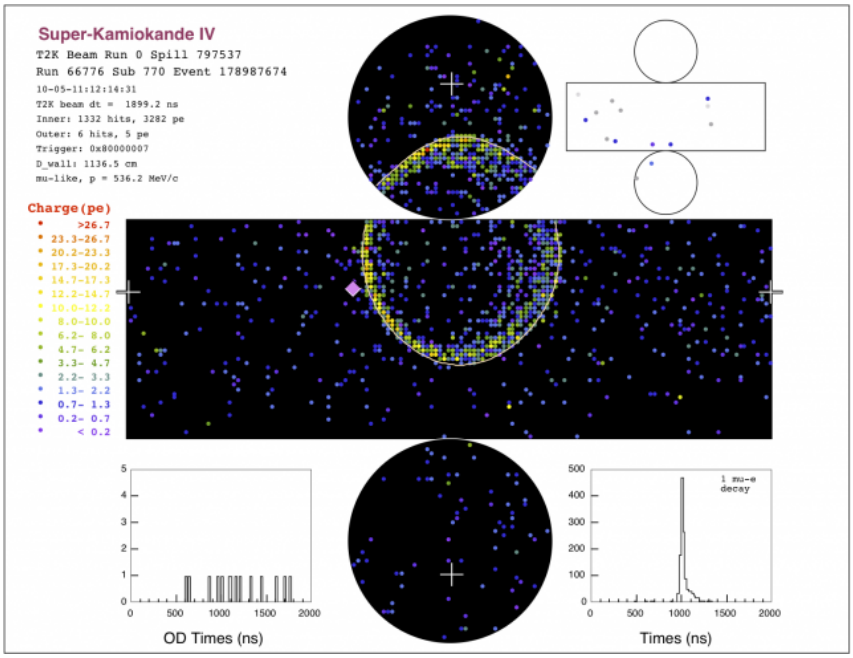

Figure 3.13: Example of muon ring at the SK detector.

quasi-elastic (CCQE) interactions for muon and electron neutrinos via the observation of the produced leptons of their respective flavor. Muons, counted to measure ν_μ disappearance, are resilient to changes in their momentum due to their relatively large mass. As a result, muons that travel through the detector produce a well-defined cone of Cherenkov radiation which leads to a clear, sharp ring of PMT hits seen on the detector wall. In contrast, electrons, used to search for ν_e appearance, scatter more easily because of their smaller mass and almost always induce electromagnetic showers at the energies relevant to SK. The result of an electron-induced shower is a "fuzzy" ring pattern seen by the PMTs, which can be thought of as the sum of many overlapping Cherenkov light cones. The routines in the SK event reconstruction software [90], use this difference between sharp and fuzzy to designate whether the rings imaged in the detector derived from muon-like or electron-like particles.

Readout system

In 2008, the SK collaboration completed an upgrade to the detector's readout electronics [120, 121] between the data-taking periods SK-III and SK-IV. This upgrade introduced, among others, a higher data processing rate and is capable of implementing a coincidence trigger with a beam arrival time as in the case of the T2K experiment. A more detailed description of the electronics can be found in [90].

For the T2K experiment, the data acquisition system was extended to trigger in time with the beam spills produced by the J-PARC accelerator. Each beam spill is given a GPS timestamp that is passed to the online Super-Kamiokande PCs. Each timestamp is used to define an additional software trigger that records all the hit information in a 1 ms window around the T2K beam arrival time. These spill events are then collected and written to disk. Later the events are fed into offline processing which applies the usual software triggers used to search for

neutrino events, and any candidate events found are extracted for further T2K data analysis.

3.4 The Near Detector Complex

The near detector complex is built at a distance of 280 m from the hadron production target.

The complex has two detectors:

- **The on-axis detector (INGRID) (see Sec. 3.5)** measures the on-axis neutrino beam profile at the 280 m site. It consists of 7+7 identical iron/scintillator detectors, arranged to form a "cross" configuration, and two diagonal modules positioned off the cross axes. The center of the cross, with two overlapping modules, corresponds to the neutrino beam center, defined as 0^o with respect to the direction of the primary proton beamline.
- **The off-axis detector (see Sec. 3.6)** is a magnetized tracking detector. Its elements are mainly contained inside the magnet recycled from the UA1 experiment at CERN. Inside the upstream end of this magnet sits a π^0 detector (POD) consisting of tracking planes of scintillating bars alternating with either water target/brass foil or lead foil. Downstream of the POD, the tracker, comprising three time projection chambers (TPCs) and two fine grained detectors (FGDs) consisting of layers of finely segmented scintillating bars, is designed to measure charged current interactions in the FGDs. The POD, TPCs, and FGDs are all surrounded by an electromagnetic calorimeter (ECal) for detecting γ-rays that do not convert in the inner detectors, while the return yoke of the magnet is instrumented with scintillator (SMRD) to measure the ranges of muons that exit the sides of the off-axis detector.

All detectors use the same coordinate convention: z is parallel to the nominal neutrino beam axis, and x and y are horizontal and vertical respectively. These detectors are housed in a pit inside the ND280 hall (see Fig. 3.14). The pit has a diameter of 17.5 m and a depth of 37 m, and has three floors.

- **B1 floor:** 24 m deep and houses the off-axis detector.
- **Service Stage:** 33 m deep and houses the horizontal modules of INGRID and the electronics of the off-axis detector.
- **B2 floor:** 37 m deep and houses the bottom modules of the vertical INGRID.

The off-axis detector is located along the line between the average pion decay point and the SK detector, at 2.5° relative to the proton beam direction, meaning an extrapolated on-axis beam passing at about 1 m above the Service Stage. The facility design can accommodate off-axis angles in the range of between 2.0 and 2.5°.

Off-axis and on-axis detectors make extensive use of scintillator detectors, wavelength-shifting (WLS) fiber readout, with light from the fibers being detected by photo-sensors. The signal coming from the scintillated light is generally multiplied by multi-anodes Photo-Multipliers Tubes (PMTs). Although PMTs have been successfully used in other scintillator and WLS based neutrino experiments, Multi-Pixel Photon Counter (MPPCs) have been chosen as photo-sensor because of their ability

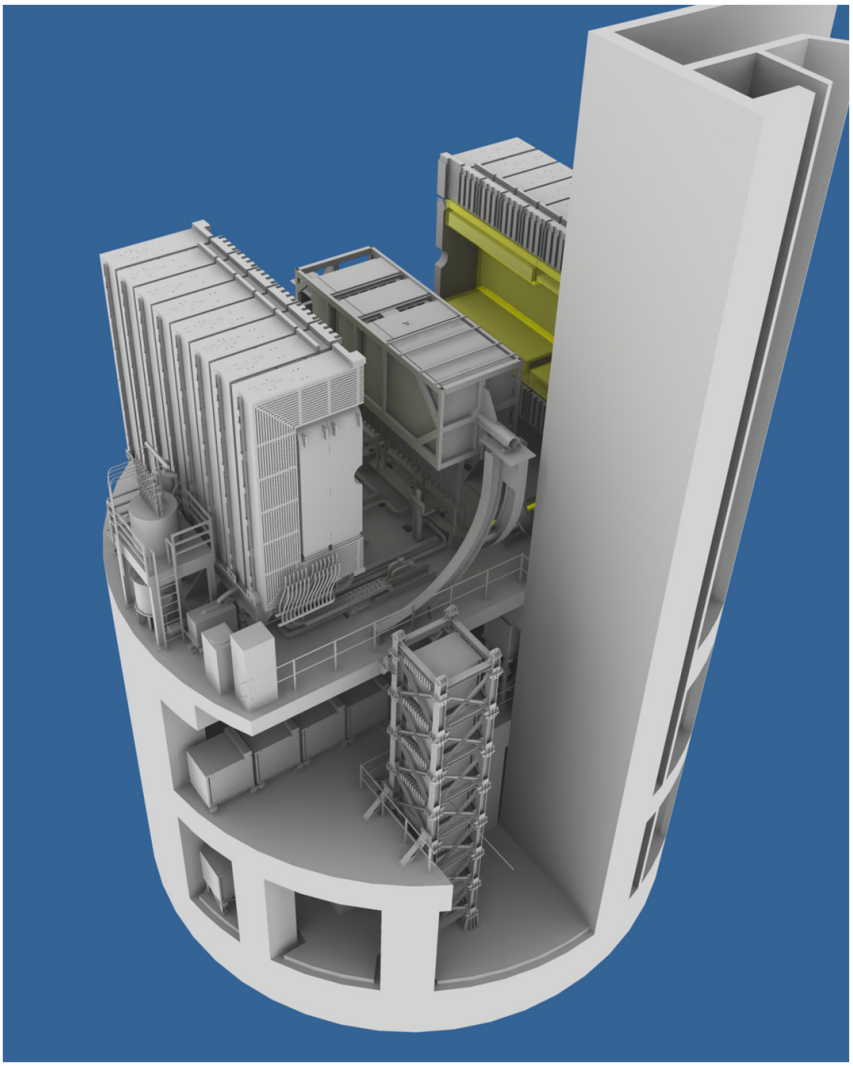

Figure 3.14: ND280 detector complex. The off-axis detector and the magnet are located on the upper level; horizontal INGRID modules are located on the level below; and the vertical INGRID modules span the bottom two levels. Note that the magnet in this figure is open.

- to operate in the magnetic field environment of 0.2 T.
- to fit into a limited space inside the magnet.

Detailed information and the basic principles of operation of multi-pixel photodiodes can be found in a recent review paper [122] and the references therein.

The main parameters of MPPCs are summarized in Table 3.3. The characterization of the MPPCs' response to scintillation light is presented in Ref. [122].

In the following, a more detail description of each detectors and sub-detectors is given.

Table 3.3: Main parameters of the T2K MPPCs

Number of pixels	667
Active area	1.3×1.3 mm^2
Pixel size	50×50 μm^2
Operational voltage	$68 - 71$ V
Gain	$\sim 10^6$
Photon detection efficiency at 525 nm	$26 - 30\%$
Dark rate, threshold = 0.5 p.e., T = 25 °C	≤ 1.35 MHz

3.5 On-axis detector (INGRID)

3.5.1 Purpose

INGRID (Interactive Neutrino GRID) is a neutrino detector centered on the neutrino beam axis. As shown in Fig. 3.15, this on-axis detector consists of:

- 16 identical modules of scintillator and iron plate where,
  - 14 modules are arranged as a cross of two identical groups along the horizontal and vertical axis.
  - 2 additional modules are located at the off-axis directions outside the main cross
- Proton Module only composed of scintillator bars.

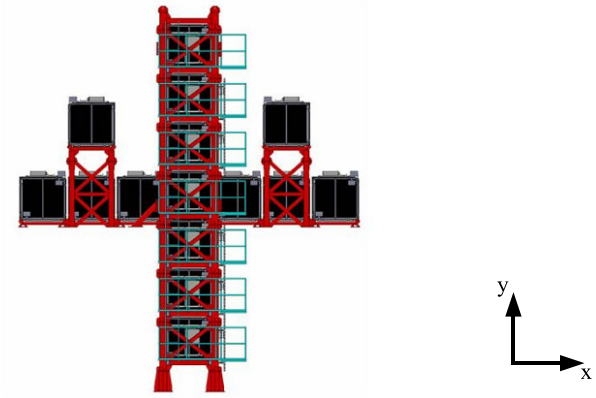

Figure 3.15: INGRID on-axis detector.

It was designed to monitor directly the neutrino beam direction and intensity by means of neutrino interactions in iron, with sufficient statistics to provide daily measurements at nominal beam intensity.

The purpose of the two off-axis modules is to check the axial symmetry of the neutrino beam.

The goal of the proton module is to identify the quasi-elastic channel for comparison with Monte Carlo simulations of beamline and neutrino interactions.

3.5.2 The 16 modules

The INGRID modules consist of a sandwich structure of 9 iron plates[5] and 11 tracking scintillator planes as shown in Fig. 3.16. Each of the 11 tracking planes consists of 24 scintillator bars, in the horizontal direction glued to 24 perpendicular bars. Veto scintillator planes surround them, to reject interactions outside the module. The total iron mass serving as a neutrino target is 7.1 tons per module. The dimensions of the scintillator bars used for the tracking planes are 1.0 cm $\times$ 5.0 cm $\times$ 120.3 cm.

More details on the scintillators, fibers and photo-sensors can be found in [90].

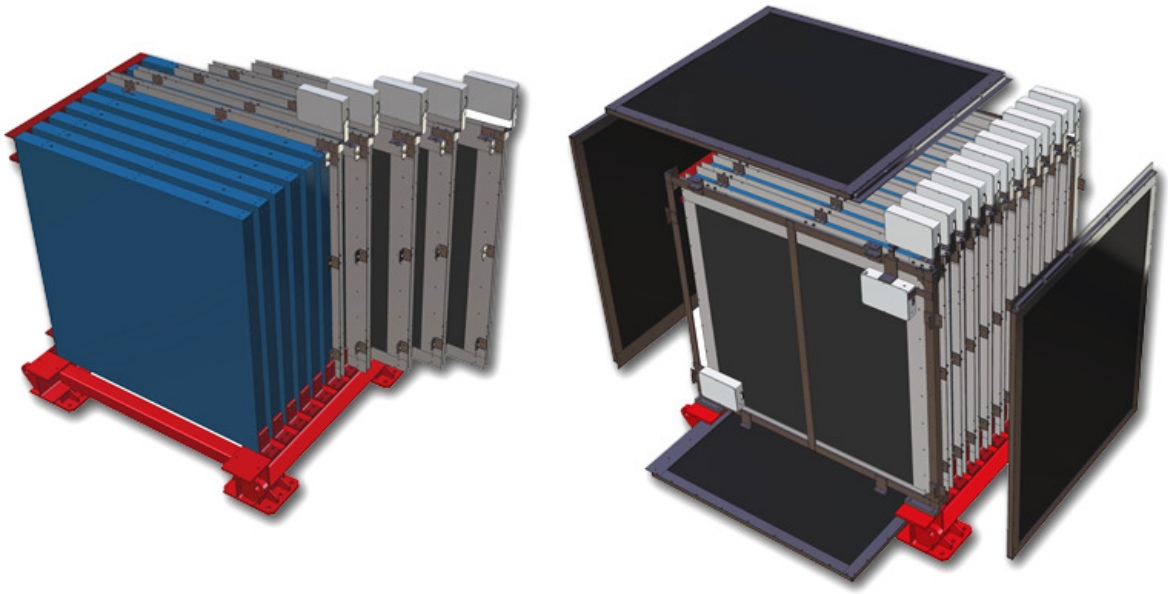

Figure 3.16: An INGRID module. The left image shows the tracking planes (blue) and iron plates. The right image shows veto planes (black).

3.5.3 The proton module

The Proton Module, different from the 16 standard modules, has been added in order to detect with good efficiency the muons and the protons produced by the neutrino beam in INGRID.

It consists of scintillator planes without any iron plate and surrounded by veto planes. A different size scintillator bar was used to improve tracking capabilities. A schematic view of the Proton Module can be seen in Fig. 3.17. It is placed in the pit in the center of the INGRID cross between the standard vertical and horizontal central modules.

3.5.4 Calibration

INGRID was calibrated using cosmic ray data taken on the surface and, during beam, in the ND280 pit. The mean light yield of each channel is measured to be larger than ten photoelectrons

[5]In fact 10 iron plates where considered at the beginning but due to the weight of the detector only 9 have been put.

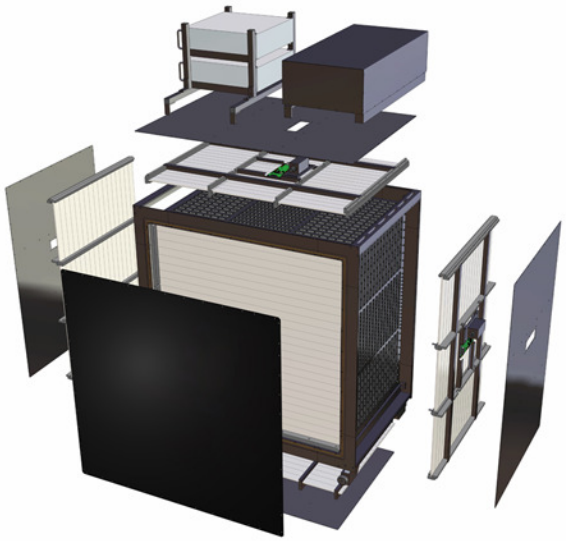

Figure 3.17: The Proton Module. Similar to the INGRID modules, but with finer grain scintillator and without the iron plates.

per 1 cm of MIP tracks which satisfies our requirement. Furthermore the timing resolution of each channel is measured to be 3.2 ns.

3.6 The off-axis detector

3.6.1 Purpose

The ND280 off-axis detector must satisfy several requirements.

- It must provide information to determine the ν_μ flux at the SK detector.
- The ν_e content of the beam must be measured as a function of neutrino energy. The beam ν_e background is expected to be approximately 1% of the ν_μ flux and creates a significant non-removable background for ν_e appearance search.
- It must measure ν_μ interactions such that the backgrounds to the ν_e appearance search at SK can be predicted. These backgrounds are dominated by neutral current single π^0 production.
- It must measure inclusive and exclusive event rates.

To meet these goals the ND280 off-axis detector must have the capability to reconstruct exclusive event types such as ν_μ and ν_e charged current quasi-elastic, charged current inelastic, and neutral current events, particularly neutral current single π^0 events. The design of detector has been chosen to fulfill these requirements.

The constructed off-axis detector is shown in Fig. 3.18 and consists of:

- the P0D and the TPC/FGD sandwich (tracker), both of which are placed inside of a metal frame container, called the "basket"
- an electromagnetic calorimeter (ECal) that surrounds the basket
- the recycled UA1/NOMAD magnet instrumented with scintillator to perform as a muon range detector (SMRD).

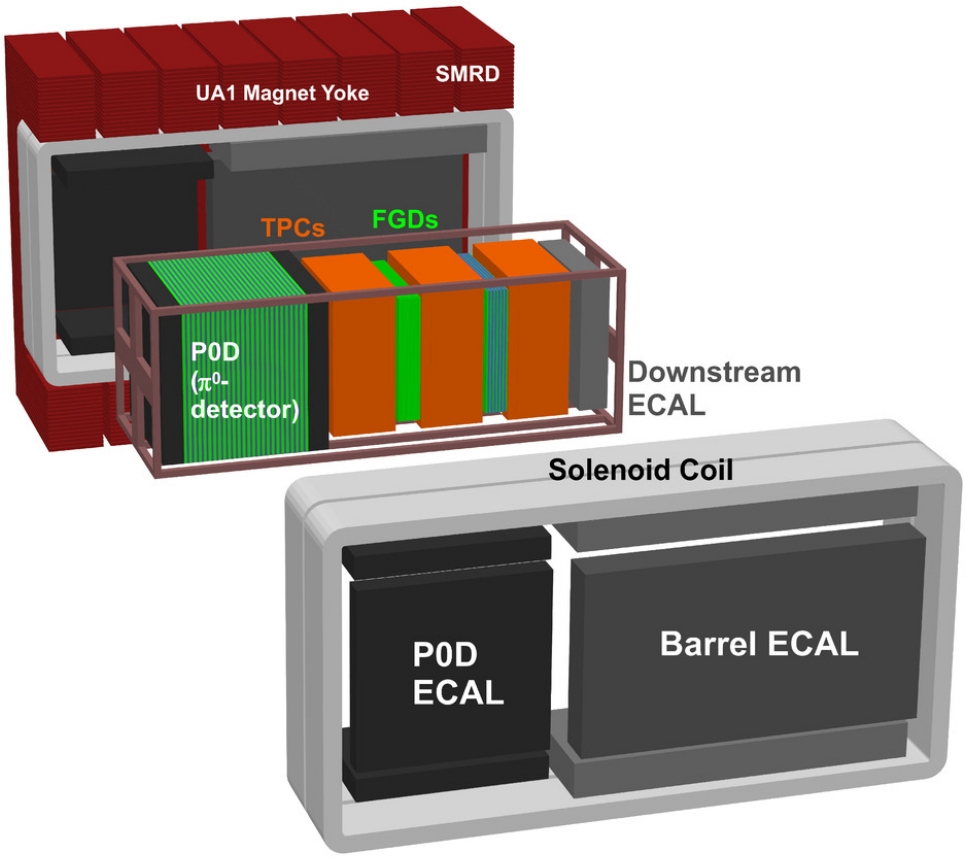

Figure 3.18: An exploded view of the ND280 off-axis detector

3.6.2 The Magnet

Goal

The ND280 off-axis detector is built around the old CERN UA1/NOMAD magnet providing a dipole magnetic field of 0.2 T, to measure momenta with good resolution and determine the sign of charged particles produced by neutrino interactions.

Description

The magnet consists of water-cooled aluminum coils, which create the horizontally oriented dipole field, and a flux return yoke. The dimensions of the inner volume of the magnet are 7.0 m $\times$ 3.5 m $\times$ 3.6 m. The external dimensions are 7.6 m $\times$ 5.6 m $\times$ 6.1 m and the total weight of the yoke is 850 tons. The coils are made of aluminum bars with 5.45 cm $\times$ 5.45 cm square cross sections, with a central 23 mm diameter bore for water to flow. The coils are composed of individual "pancakes", which are connected hydraulically in parallel and electrically in series.

It consists of two mirror-symmetric halves. The coils are split into four elements, two for each half, and are mechanically supported by, but electrically insulated from, the return yoke. The two half yoke pieces each consist of eight C-shaped elements, made of low-carbon steel plates, which stand on movable carriages. Within the gaps of the magnet yokes SMRD modules are inserted. More information about the magnet can be found in [90].

3.6.3 Side Muon Range Detector (SMRD)

Goal

The SMRD performs multiple functions:

- It records muons escaping at large angles with respect to the beam direction and measures their momentum.
- It triggers on cosmic ray muons that enter or penetrate the ND280 detector.
- It helps identify beam-related event interactions in the surrounding cavity walls and the iron of the magnet.

Description

The SMRD consists of a total of 440 scintillator modules, which are inserted in the 1.7 cm air gaps between 4.8 cm thick steel plates which make up the UA1 magnet flux return yokes.

It consists of 3-6 layers of scintillator modules on the top and bottom for all yokes. Pairs of yokes are labeled 1 through 8 from upstream to downstream.

All of the SMRD modules populate the innermost gaps so as to be able to detect particles escaping the inner detectors.

Due to the differently sized spaces for horizontal and vertical gaps, horizontal modules are composed of four scintillation counters and vertical modules consist of five scintillation counters. More information on the scintillators can be found in [90].

Readout system

A 1 mm diameter Kuraray Y11 double-clad WLS fiber exits both sides of the scintillator through a ferrule which is part of an endcap. The MPPCs are coupled to the polished WLS fiber ends through a snap-on mechanism.

There are 4016 MPPCs connected to a miniature printed circuit (PCB), which are free to slide along the rails in the backside of the optical connector to allow for optimal WLS fiber and MPPC interconnection.

The miniature PCBs couple the MPPC signals into mini-coaxial cables, which lead the signal to the custom-designed Trip-T front-end boards (TFBs) mounted on the vertical sections of the magnet yokes. The SMRD front-end electronics consists of 128 TFBs, which are described, in [90] (see Fig. 3.19).

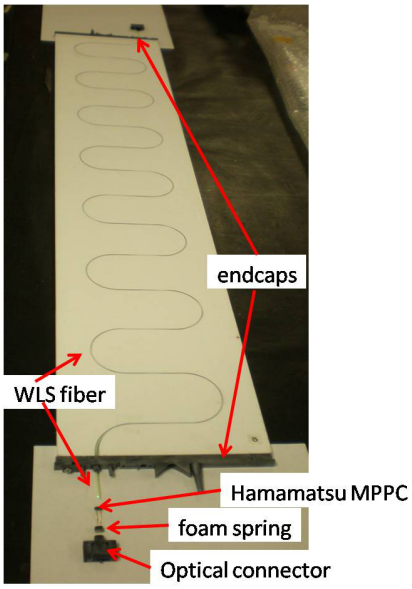

Figure 3.19: View of SMRD scintillator counter components prior to assembly.

3.6.4 Electromagnetic CALorimeter (ECal)

Goal

ecal's main role is to complement the inner detectors in full event reconstruction through:

- the detection of photon and measurement of their energy and direction
- the detection of charged particles escaping the inner detectors and extraction of information relevant for their identification (electron-muon-pion separation)
- the reconstruction of π^0's produced in neutrino interactions inside the inner detectors. In the case of π^0 production inside the P0D, the P0D-ECal complements the P0D reconstruction with information on escaping energy.

Description

It is a sampling electromagnetic calorimeter surrounding the inner detectors (P0D, TPCs, FGDs). It uses layers of plastic scintillator bars as active material with lead absorber sheets between layers, and it provides nearly-hermetic coverage for all particles exiting the inner detector volume.

The ECal is made of 13 independent modules of three different types arranged as in Fig. 3.18:

- six Barrel-ECal modules surround the tracker volume (FGD+TPC) on its four sides parallel to the z (beam) axis
- one downstream module (Ds-ECal) covers the downstream exit of the tracker volume
- six P0D-ECal modules surround the P0D detector volume on its four sides parallel to the z axis

Each module is made of consecutive layers of scintillator bars glued to a sheet of lead converter. The Ds-ECal is located inside the basket carrying the inner subdetectors of the off-axis detector. The other 12 ECal modules are mounted inside of the UA1 magnet.

Each ECal module was assembled from pre-made scintillator-lead layers. All ECal scintillator bars have a 4.0 cm $\times$ 1.0 cm cross section with a 2.0 mm $\times$ 3.0 mm elliptical hole running along their full length in the middle.

Readout system

A Kuraray 1 mm diameter double-clad Y11 WLS fiber runs along the hole in the center of each bar as described in Sec. 3.5 for the INGRID. The light is read out at one or both ends of each fiber with MPPCs. The MPPC signal is read out with TFB cards, which are described in [90].

3.6.5 π^0 Detector (P0D)

Goal

The primary objective of the P0D is to measure the neutral current process:

$$\nu_\mu + N \rightarrow \nu_\mu + N + \pi^0 + X$$

on a water (H_2O) target with the same neutrino beam flux as the one reaching SK.

Description

The planes of scintillator bars are interleaved with fillable water target bags and lead or brass sheets. This arrangement forms a neutrino target where the P0D operates with the water target bags filled or emptied, enabling a subtraction method to determine the water target cross sections.

The scintillator bars provide sufficiently fine segmentation to reconstruct charged particle tracks (muons and pions) and electromagnetic showers (electrons and photons from π^0's).

The main features of the P0D design are shown in Fig. 3.20. The central section, composed of the "upstream water target" and "central water target", uses alternating scintillator planes, water bags, and brass sheets. The front and rear sections, the "upstream ECal" and "central ECal", use alternating scintillator planes and lead sheets. This layout improves the containment

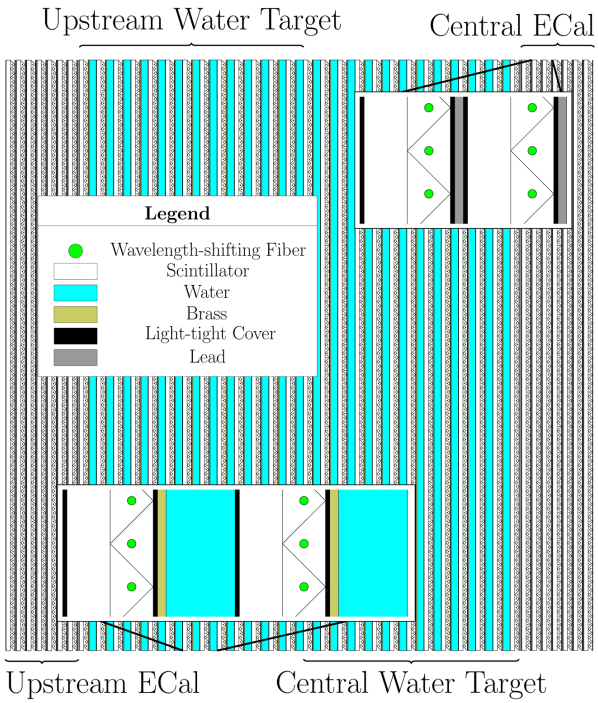

Figure 3.20: A schematic of the pi-zero detector. The beam is coming from the left and going right. Insets show details of the Water Target super-P0Dule layers and Central ECal layers.

of electromagnetic showers and provides a veto region before and after the water target region to provide effective rejection of particles entering from interactions outside the P0D.

There are a total of 40 scintillator modules in the P0D. Each P0D module has two perpendicular arrays of triangular scintillator bars. There are 134 vertical bars and 126 horizontal bars in each module.

Readout system

Each bar has a single hole filled with a WLS fiber (Kuraray double-clad Y11 of 1 mm diameter). Each fiber is mirrored on one end and the other end is optically read out using a MPPC. Each photo-detector is read out with TFB electronics, which are described in [90].

Calibration

The detector was calibrated with minimum ionizing particles from cosmic ray muons.

An average of 19 photoelectrons was obtained for the scintillator plane and 38 photoelectrons per x/y layer. The average attenuation of the pulse height in the scintillator bars from opposite ends is approximately 30%.

The internal alignment of scintillator bars was checked using through-going muons with the magnet field off, and was determined to be approximately 3 mm.

3.6.6 Fine Grained Detectors (FGDs)

Goal

The FGDs have two functions. They constitute, firstly, a target for neutrino interactions and, secondly, provide tracking of charged particles.

Description

There are two FGDs in the inner part of the near detector. While one is only composed of scintillator the second one also contains water target. Because of this difference they can provide different target mass for neutrino interactions complementary to the P0D cross section. Each FGD (see Fig. 3.21) has outer dimensions of 2300 mm × 2400 mm × 365 mm (width × height × depth in beam direction), and contains 1.1 tons of target material. In the analysis presented in this thesis, only the first FGD will be used as target, the second one being used as tracking detector.

The FGDs are constructed from 9.61 mm × 9.61 mm × 1864.3 mm bars of extruded polystyrene scintillator, which are oriented perpendicular to the beam in either the x or y direction.

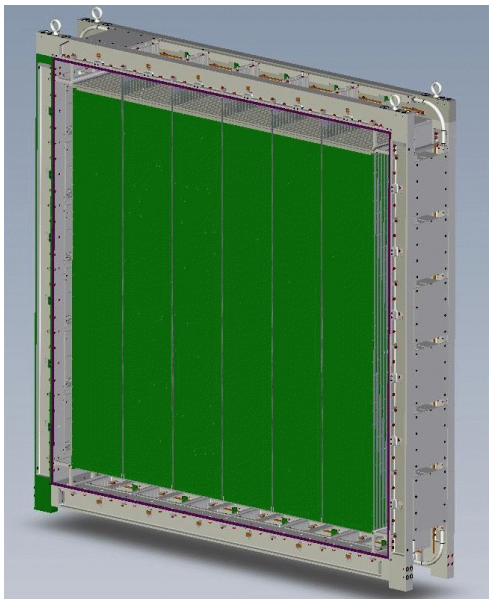

Figure 3.21: View of an FGD with the front cover removed. XY scintillator modules (green) hang perpendicular to the direction of the neutrino beam. Along the top, six mini-crates with electronics can be seen without their cooling lines, while on the right side the cooling lids covering the mini-crates are shown.

The first FGD consists of 5,760 scintillator bars, arranged into 30 layers of 192 bars each, with each layer oriented alternatingly in the x and y directions perpendicular to the neutrino beam. The scintillator provides the target mass for neutrino interactions, and having alternating x and y layers of fine grained bars allows for tracking of charged particles produced in those interactions. An "XY module" consists of one layer of 192 scintillator bars in the horizontal

direction glued to 192 perpendicular bars in the vertical direction, with thin G10[6] sheets glued to the outer surfaces to add structural stability.

The second FGD is a water-rich detector consisting of seven XY modules of plastic scintillator alternating with six 2.5 cm thick layers of water (for a total of 2,688 active scintillator bars and 15 cm total thickness of water). These layers are made from sheets of thin-walled hollow corrugated polycarbonate, 2.5 cm thick, whose ends have been sealed with HE 1908 polyurethane sealant. The modules are then filled with water to provide a layer of water target. The water is maintained under sub-atmospheric pressure by a vacuum pump system so that if a leak develops the system will suck air into the modules rather than spilling water inside the FGD. Comparing the interaction rates in the two FGDs permits separate determination of cross sections on carbon and on water.

Readout System

Each FGD is contained in a light-tight dark box that contains the scintillator, fibers, and photo-sensors, while the FGD electronics are mounted in mini-crates around the outside of the dark box. Each scintillator bar has a reflective coating containing TiO_2 and a WLS fiber going down a hole in its center. One end of each fiber is mirrored by vacuum deposition of aluminum, while the other end is attached to an MPPC and associated electronics, which digitize the light signal produced by scintillation inside the bar. The front-end boards use the "AFTER" ASIC, which are described in [90], to shape and digitize high and low attenuation copies of the photo-sensor signals at 50 MHz. The FGD's front-end electronics resides in 24 mini-crates. Each mini-crate contains four front-end boards and one crate master board (CMB), and can read out 240 photo-sensors. Data from each crate is read out over optical fiber links to data concentrator cards (DCCs) located outside of the magnet. Slow control systems use a separate data and power bus for redundancy.

3.6.7 Time Projection Chambers (TPCs)

Goal

The TPCs perform three key functions in the near detector:

- 3-dimensional reconstruction of charged particle crossing the detector
- measurement of the momentum of the charged particle since they operate in a magnetic field
- particle identification using the amount of ionization left by each particle combined with the measured momentum.

These three functions allow to select high purity samples of different types of neutrino interactions, compute event rates as a function of neutrino energy for the neutrino beam prior to oscillation and determine the relative abundance of electron neutrinos in the beam.

[6] G10 is a thermosetting industrial laminate consisting of a continuous filament glass cloth material with an epoxy resin binder [123].

Description

There are three TPCs installed inside the magnet. Each TPC consists of an inner box that holds an argon-based drift gas, contained within an outer box that holds CO_2 as an insulating gas. The inner (outer) walls are made from composite panels with copper-clad G10 (aluminum) skins. The inner box panels were precisely machined to form an 11.5 mm pitch copper strip pattern. The TPCs are separated into two sides by a central cathode. The voltage on each strips and on the cathode is set in order to have an uniform electric field in the active drift volume of the TPC, roughly aligned with the magnetic field provided by the near detector magnet. A simplified drawing of the TPC design is shown in Fig. 3.22.

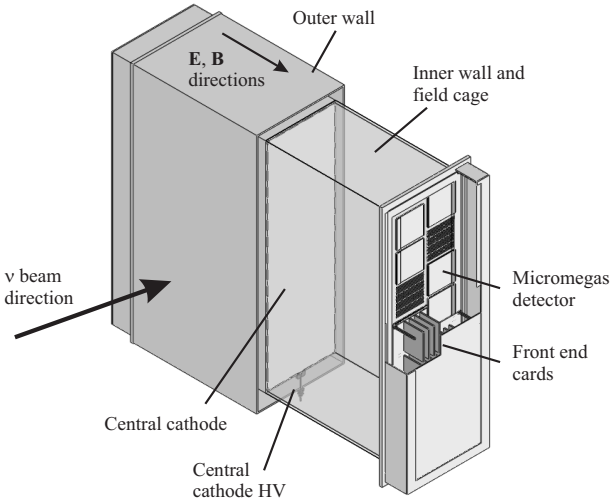

Figure 3.22: Simplified cut-away drawing showing the main aspects of the TPC design. The outer dimensions of the TPC are approximately 2.3 m × 2.4 m × 1.0 m.

At each side of the TPCs, 12 micromegas (micro-mesh gas detector) modules are arranged in two vertical columns that are offset so that the small inactive regions between modules are not aligned. The role of the micromegas is to amplify the signal created by the charged particles when passing through the TPCs. When charged particles pass through a TPC, they ionize the gas. The electrons released via this process drift away from the cathode toward the readout planes (anode), where they are multiplied with the micromegas (see Chapter 4).

The micromegas anode is segmented into pads of 7.0 mm × 9.8 mm (vertical × horizontal) allowing 3D track reconstruction of the traversing charged particle, where the x coordinate is given by the arrival time of the signal and the y and z by the pattern on the pad plane.

Readout System

Over each micromegas, blind vias are used to route connections between the readout pads and connectors on the back side of the micromegas printed circuit boards. Six front-end electronics cards (FEC), each using four custom ASICs called "AFTER", plug into the connectors and sample and digitize signals from the 1728 pads (see Fig.3.23). Each AFTER ASIC shapes the signals and buffers 72 pad signals into 511 time-bin switched capacitor arrays. The six front-

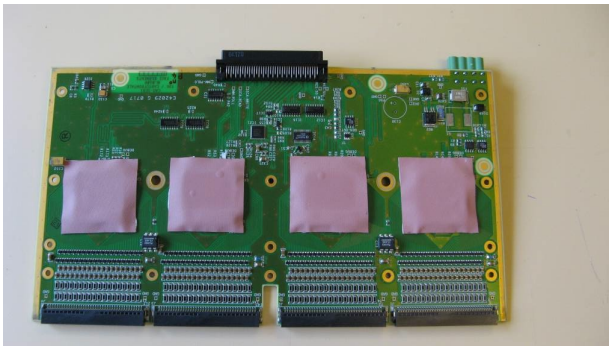

Figure 3.23: Front-end card (FEC).

end cards connect to a single front-end mezzanine card that aggregates the data, performs zero suppression, and sends the remaining data off detector over a 2 Gb/s optical link. Then 18 Data Concentrator Card (DCC) connected via an Ethernet switch is used to collect the data into a standard PC linked to the global data acquisition system of the experiment [124].

Gas System

The gas system was designed to maintain a stable mixture in the inner volume, a constant positive pressure with respect to the outer volume, and a constant pressure between the outer volume and the atmosphere. The inner gas mixture, Ar:CF_4:iC_4H_{10} (95:3:2) was chosen for its low diffusion, and good performance with micromegas chambers. Each of the three TPC volumes contains 3000 liters, and each of the three gap volumes contains 3300 liters. The TPC gas system was designed for an operating flow of 10 L/min/TPC (30 L/min total flow), corresponding to five TPC-volume flushes per day. To reduce gas operating costs, the system was designed to purify and recycle roughly 90% of the TPC exhaust gas.

Calibration

Each micromegas used in the TPCs have been tested, at CERN, to provide energy calibration (see Chapter 4). Once the micromegas are installed in the TPC other source of distortions due to the magnetic field can appear. In order to measure distortions in the electron drift due to inhomogeneous and misaligned electric and magnetic fields in the TPCs, an additional photoelectron calibration system is implemented and produces a control pattern of electrons on the central cathode.

A pattern of thin aluminum discs, 8 mm in diameter, with two additional strips, 4 mm wide, are glued to the copper surface of the cathode. The electrons are released from the aluminum but not the copper by the use of a laser emitting a 266 nm light transported via quartz fibers to small optical packages embedded in the inner TPC frames that defocus the light onto the cathode. The displacement of the electrons gives the spatial distortions.

During the data taking, laser data are taken permanently in order to provide information on the changes in the drift velocity. A monitoring chamber connected to the same gas distribution provides also additional information on the drift velocity as well as signal attenuation. Cosmics can also give good complementary information on signal attenuation.

Performance

Since late 2009, the 3 TPCs have been in place within the off-axis near detector for the T2K experiment. Neutrino, cosmic ray, and calibration events have been recorded and processed. Until now, the readout system has shown to be very stable with only one failure from the beginning of the data taking. The temperature on the cards has shown very small variations between 24^o and 26^o while the gain has been observed stable at a level of 10%, the variations have been mostly due to gas density variation, primarily due to atmospheric pressure. This effect is taken into account in the calibration process. After calibration, the remaining variation is below 1%.

In addition to these basic performances, the reconstruction of the tracks has shown good tracking performance with a spatial resolution sufficient to achieve the 10% $p_\perp/(GeV/c)$ momentum resolution goal (as shown in Fig. 3.24). The spatial resolution is estimated by comparing the

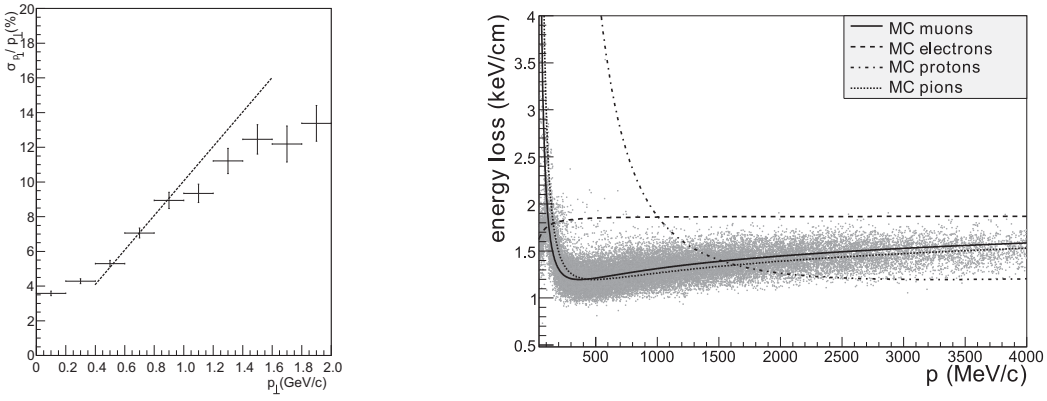

Figure 3.24: Left: Momentum resolution for a single TPC is shown as a function of momentum perpendicular to the magnetic field as predicted by the Monte Carlo simulation of muons generated with the standard neutrino event generator of T2K. The tracks are selected to cross at least 50 out of the 72 pad columns of the TPC volume. The dashed lines represents the momentum resolution goal. Right: Each point shows measurements by a single TPC of the energy loss and momentum of negatively charged particles produced in neutrino interactions. The expected relationships for muons, positrons, protons, and pions are shown by the curves.

transverse coordinate resulting from the global track fit to the one obtained with information from a single column of pads. The resolution is found to be typically 0.7 mm per column, in line with expectations, and degrades with increasing track angle with respect to the beam direction due to the ionization fluctuations along the track.

Particle identification (PID) also works well and Fig. 3.24 demonstrates the TPC particle identification capability by comparing energy loss and momentum for positively charged particles recorded during the first T2K physics run. The resolution of deposited energy obtained is about 7.8% for minimum ionizing particles, better than the design requirement of 10%.

3.7 Summary

The T2K experiment has been designed to measure specifically the appearance of electron neutrinos and to provide a more precise measurement of the muon disappearance. For that purpose,

an off-axis beam is used so that the peak energy is at 0.6 GeV corresponding to the first maximum at the far detector. The far detector is the Super-Kamiokande world's largest Cherenkov detector, already used to study solar and atmospheric neutrino oscillations.

The neutrino beam as well as the near detector have been built in the scope of the T2K experiment, and the first physic data was taken at the near detector in January 2010.

The neutrino beam is produced by accelerating protons that hit a graphite target producting hadrons, which are then focused to a decay volume where they decay into neutrinos. To decrease the systematic error on the neutrino flux, the NA61/SHINE experiment has been taking data with graphite target and same kinetic energy beam protons. This experiment is suitable to measure various cross sections as pions and kaons production that are the main sources of neutrinos. This data decreases the systematic uncertainty on the neutrino flux from 20 % to 10 % in the 2012 analysis.

The near detector complex contains an on-axis and an off-axis detector. While the on-axis detector measures mainly the neutrino beam profile, the off-axis detector constrain the ν_μ flux and cross section at the far detector via the neutrino event rate measurement at the near detector. It also provides the ν_e content of the beam and the possibility of several cross section measurements.

The off-axis detector is the principal detector used in this analysis to provide the muon neutrino CC-inclusive cross section. For that measurement, FGDs and TPCs are the main tracking detectors used. While the FGDs provide the carbon target, the use of the TPCs together with the magnetic field provides the particle identification, the measurement of the charge and the momentum of the track.

The signal coming from the charged particle in the TPCs is multiplied via micromegas that have been tested in Geneva as explained in more details in the next chapter.

Chapter 4

Tests and validation of the TPC readout

In 2006, micromegas (Micro-MEsh Gaseous Structure) have been chosen to amplify the signal of ionizing particles. For practical reasons, a modularity of 12 micromegas on each side of the TPCs was chosen. About 100 micromegas have been tested at CERN between 2007 and 2009, and 72 are installed currently on the three TPCs of the near detector. The TPCs should follow several requirements that are directly related to the micromegas such as:

- small dead areas in order to obtain good reconstruction of tracks
- good planarity of the detection surface, better than 150 μm, to minimize drift electric field distortions near the micro-mesh.
- very good gas gain uniformity at the level of a few %, in order to have a good particle identification.

The micromegas were constructed at CERN and were built using a particular technique suited for compact and robust low mass detectors [125]. This technique provides an excellent solution to minimize unavoidable dead areas on the edges of a module and allows large detection areas with excellent gas gain uniformity.

In this chapter, I describe the main properties of the micromegas used for T2K. In particular, I review the principle of a micromegas and describe the test bench built at the university of Geneva to scan each micromegas and store the data for energy calibration. At the end of the chapter, the test bench results are presented.

4.1 Micromegas

A micromegas detector[126] is a double gap chamber. It consists of a conversion gap (or drift region) and a narrow amplification gap. Both gaps are separated by a conducting micro-mesh. The conversion region contains the drift cathode, while the amplification region contains the anode readout structure underneath. In the following, I call *micromegas module* the device containing the amplification gap and its readout structure. A schematic view of a micromegas module is given in Fig. 4.1.

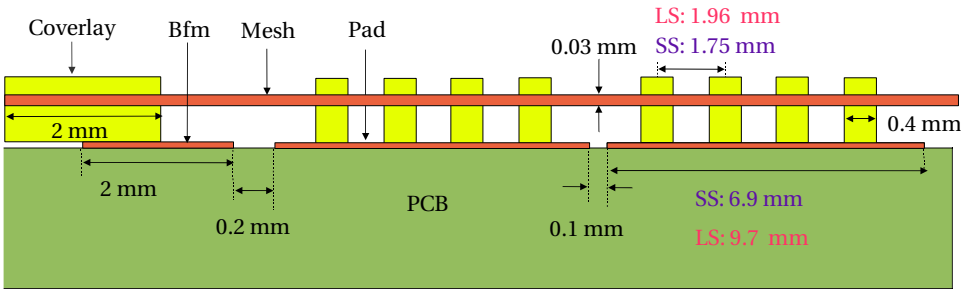

Warning: There are 3 pillars for the long size (LS) the corresponding sizes are written in pink

Figure 4.1: Schematic view of the beginning of the micromegas module

The micromegas module technique consists in laminating a woven micro-mesh on a Printed Circuit Board (PCB) covered by photoimageable film. At the end of the process, the micro-mesh is sandwiched between two layers of the same insulating material. The detector then undergoes UV exposure with an appropriate mask, followed by chemical developments where most of the insulating material is removed, creating this way the amplification gap.

The micro-mesh is made of a thin metallic micro-mesh with a hole-pitch smaller than 50 μm. The anode readout structure is the PCB with a pad pattern, in the case of the T2K experiment.

The pad plane is made of $36 \times 48 = 1728$ pads with dimensions of 6.9×9.7 mm^2. The micro-mesh is held in place by a 2 mm coverlay border and by regularly distributed insulating pillars to keep constant the micro-mesh-anode distance and to obtain a uniform electric field in the amplification gap. The pillars, 12 per pad, are cylindrical with a diameter of 0.4 mm.

Figure 4.2: Left: Pad plane of the micromegas module. Right: Bottom part of a micromegas module. We can see the printed circuit that will be connected to the electronic device.

The micro-mesh and the PCB of a T2K micromegas module is shown in Fig. 4.2, where the dimensions are indicated.

The micromegas module is inserted at the front-end of a chamber with a cathode implemented at the other side. The role of the micromegas module is to multiply the signal due to an ionizing particle entering the chamber. When an ionizing particle enters the chamber, electrons are released in the conversion gap. The electrons drift to the micro-mesh because of the potential difference between the cathode and the micro-mesh. They are then multiplied in the high field region of the amplification gap (see Fig. 4.3).

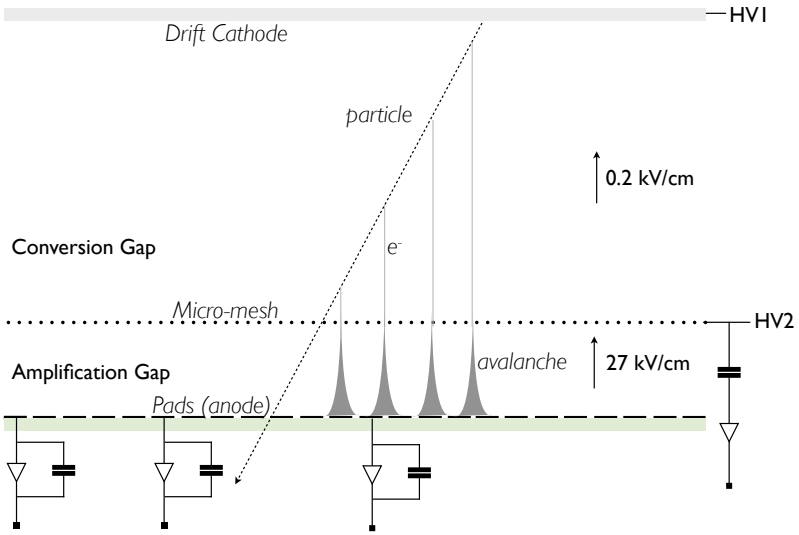

Figure 4.3: Micromegas principle. HV1 and HV2 are set to -350 V and -1150 V in our case.

In the amplification gap, the primary electrons are accelerated until they have enough energy to unbound electrons, that are again accelerated. This creates an avalanche process in the amplification gap that will ceased once the electrons are collected at the anode (pad plane). The anode is generally at ground potential. The multiplication factor is called gain and it can be different from one pad to another.

The drift field in this region is about 27 kV/cm, for a micro-mesh-anode distance of 128 μm.

4.2 The Test Bench

The test bench has been built to calibrate the 104 micromegas modules done for the T2K experiment. It consists of a drift chamber with a micromegas module implemented on one side and a cathode on the other side. The chamber is held vertically and mounted on a support structure in front of x-y stages. The x-y stages are used to move a strong ^{55}Fe source behind the cathode over each pad during the calibration. Two other weak sources of iron are fixed behind the cathode for a stability control in time. In order to maximize the gain the box is filled with Ar:CF_4:iC_4H_{16} (95:3:2). The volume of the test box was about 8 litres, filled with a 10 l/h flow of the T2K gas mixture. The box was permanently flushed and maintained with a pressure of 1 mb over the atmospheric pressure. To ensure a better testing efficiency, two chambers have been made. While one was under scanning, the other was flushed so that a good gas quality is achieved. Temperature, pressure, and micro-mesh current have been monitored during the complete time of the calibration. The duration of each scan was typically 6 hours for about 1000 recorded events per pad. The test bench facility allowed to calibrate and test up to 5 modules per week.

The electronic device was cooled constantly allowing testing without interruption. The laboratory at CERN is shown in Fig. 4.4 where we can see the various elements composing the test bench.

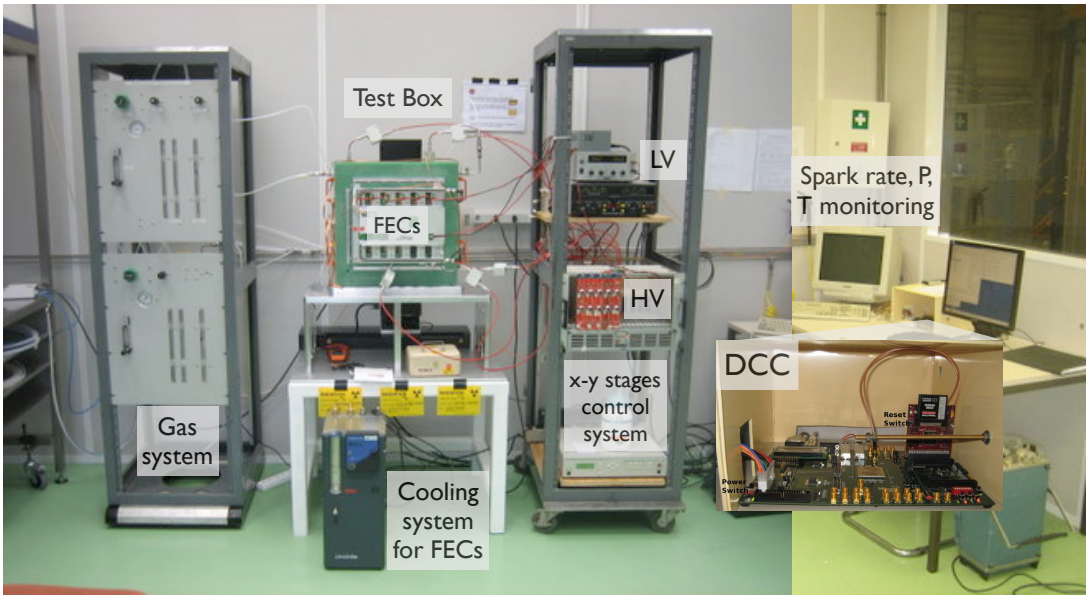

Figure 4.4: Overview of the Test Bench at CERN.

4.2.1 The Test Box

The calibration box design depends on several mechanical and electrostatic parameters. It must be gas tight and easy to use since 104 micromegas modules had to be calibrated. From the electrostatic point of view, uniform field lines above the pad plane is required to guarantee a good calibration. This last constraint implies accurate dimensions and adequate choice of the materials. Electrostatic simulation studies have been made before building the box to ensure that a good calibration is possible[127].

A shield surrounding the micromegas active area is necessary to get uniform field lines. This shield is made of a single G10 frame which is copper coated on both sides. The top copper layer is set at the same potential as the mesh, while the bottom layer is grounded. Besides, a strip is implemented over the walls of the box to suppress field distortions due to the aluminum support. The cathode is an aluminum coated Mylar foil fixed over a frame in G10 and protected by a grid. The potential on the cathode and the strip are set in order to have a drift field of 200 V/cm. The values and the settings are shown in Fig. 4.5. On the other side of the grid an aluminum coated Mylar has been put to avoid charge accumulation on the unpolished G10 grid surface. Without this Mylar, we observed an increasing number of sparks (current drops) in time.

4.2.2 The sources

Three ^{55}Fe sources are used during the micromegas tests. The strong source has an activity of 185 MBq, and the two weak sources an activity of 37 MBq. The activity of the source has been chosen to allow a reasonable time measurement and small pile up.

For the strong source, a collimator with three positions is used (see Fig. 4.6):

$$L_{coll} = 8 \text{ cm},\ 1.5 \text{ cm},\ 0.5 \text{ cm}. \tag{4.1}$$

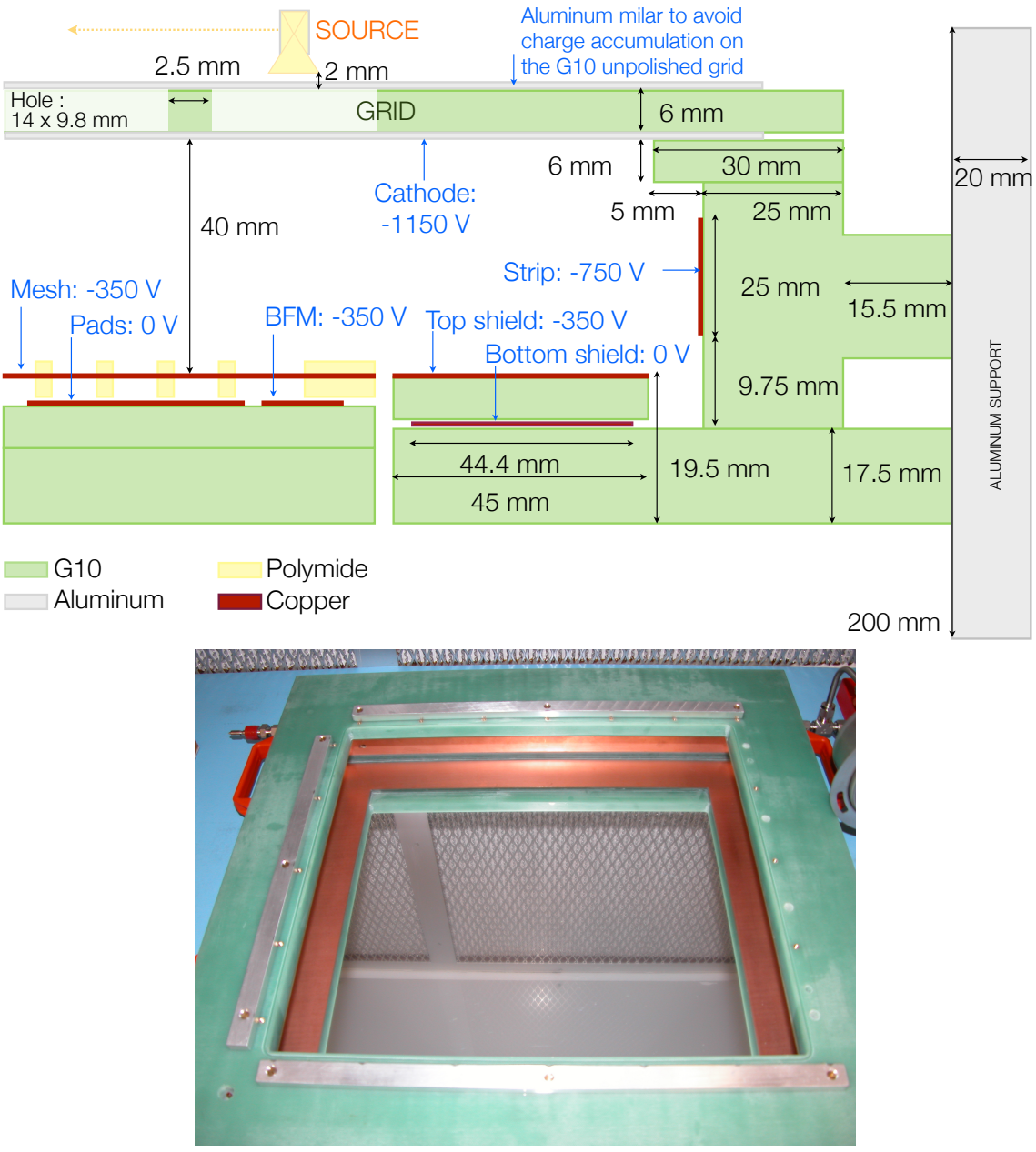

Figure 4.5: Top: Schematic view of the test box. Bottom:Picture of the interior of the chamber.

The collimator is a tube that has a hole with a radius of $r_s = 2.5$ mm. For a better collimation, the exit hole is slightly closed with aluminum so that the hole at the end of the tube has a radius of $r_t = 1.1$ mm. The RMS of the spot on the pad plane was calculated to be of 0.7 cm, which is smaller than the radius of a pad [127]. Therefore, the lower collimation was considered enough ($l = 0.5$ cm) for the calibration test. The highest collimation ($l = 8$ cm) was used to study the pad response function of a micromegas module [127]. The medium collimation ($l = 1.5$ cm) has finally not been used.

The two weak sources are placed on two corners of the box as shown in Fig. 4.6. They are implemented with a lower collimation than the strong source so that a few pads are fully illuminated

but on a well-defined area.

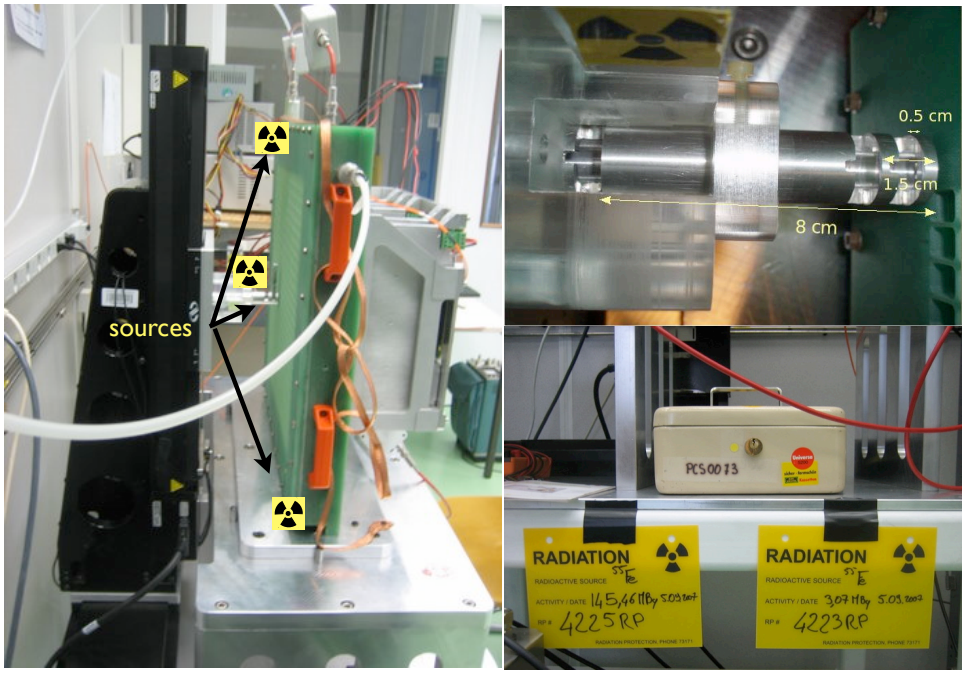

Figure 4.6: Left: Side view of the micromegas test bench setup, with the various source positions. Top Right: Collimator of the strong source. Bottom Right: Storage box of the sources.

Principle

The ^{55}Fe decays into ^{55}Mn by electron capture: $^{55}Fe + e^- \rightarrow ^{55} Mn^* + \nu_e$. The process of electron capture leaves a vacancy in an electron shell that is then filled immediately by electrons from higher levels cascading down. The difference in energy is released by emiting X-rays or Auger electrons[1]. In this process, photons of 5.9 keV are emitted with a probability of 24.4% and others with an energy of 6.49 keV (probability of 2.86%). Hence, ^{55}Fe source emits X-rays with a probability of 27.3%.

The X-rays exiting the iron source interacts with different material and their number is slightly attenuated when they reach the interior of the box. There, they ionize the gas by photoelectric effect, these electrons are then drifted to the amplification region where they are multiplied as explained in Sec.4.1.

The photoelectric effect with the electrons on the K-shell can be followed by two kinds of emission in addition to the photo-electron of 3.694 keV. They are followed in 13.5% of the cases by an escaping photon and an Auger electron of 0.203 keV. This will deposit a total energy of 2.897 keV and is called escape peak of argon. Secondly, they are followed at 86.5% of the cases by Auger cascades [128] resulting in three main lines at 3.066, 3.027 and 3.126 keV with relative intensity of 0.75, 0.15 and 0.10 [129]. In this case, the total energy deposits is the total energy of the Auger electrons and the photon-electrons, which is in average 5.75 keV. In conclusion, we expect two energy peaks as the result of the emission of the X-rays.

[1]The Auger electrons are the electrons that have absorbed the released energy and ejected from the atom

Security

X-rays emitted by the source are not considered dangerous, as they affect only the dead layer of the skin. Hence a very thin layer of material, even air, stops the core of the radiation. For example, the mean free path is around 33 cm in air and 2 cm in argon [127, 129]

When the source were not used they were placed in the storage box (see Fig. 4.6). People handling the sources had to carry a film badge and ring dosimeter. A strong source support has been made to give an easy manipulation for the user.

4.2.3 The Gas system

The gas system has been designed in order to test one micromegas module while another one is flushed. It must also ensure a constant over-pressure inside the box to prevent air contamination. With air contamination the gain of the micromegas modules would decrease considerably. The circuit must also protect the chamber from a too big over-pressure that can destroy the box. Therefore, pressure regulators, at the exit of the bottle and before entering the flow meters, have been placed so that a maximal pressure of 100 *mb* is allowed at this point. Two bubblers have been implemented in both systems. While one must ensure a 1 *mb* over-pressure (B2 or B4 in Fig. 4.7), the others have an emergency role, in the case too much pressure is circulating. The pressure gauges give an accurate measurement of the pressure inside the box. The valves,

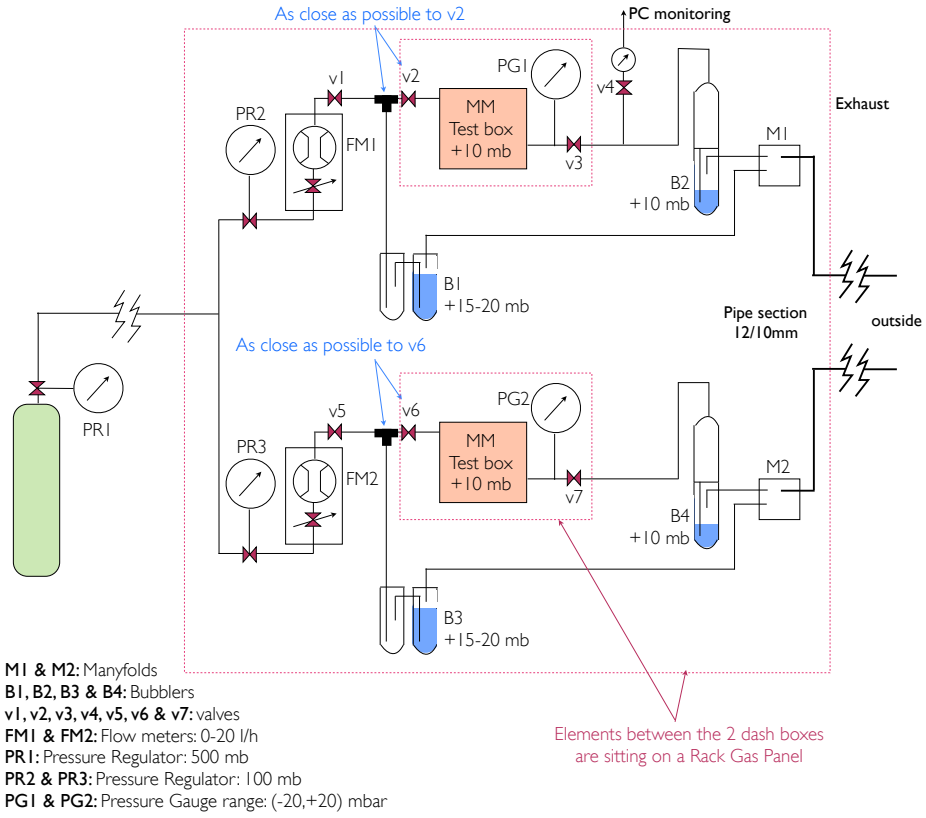

Figure 4.7: Schematic view of the test box

called v1, v2, v3,v5, v6 and v7 in Fig. 4.7, are installed in order to switch the boxes without contaminating the circuit.

The v4 valve allows the digital pressure monitoring during the tests. At the end of the circuit, the small pipes reach two manifolds where a bigger pipe carry the gas to the outside.

4.2.4 The electronic readout

To be as close as the running conditions of the TPCs, the same electronic cards and cooling system has been used for the test bench. Hence six front-end electronic cards (FEC), each containing 4 application specific integrated circuit (ASIC) chips called *AFTER*. A single front-end mezzanine board (FEM) is used to aggregate the data of the 6 FECs, perform the zero-suppression and send the remaining data via an optical link to a back-end data concentration card (DCC). The FEM board is also connected to a CAN-bus network which is used for slow control monitoring. The readout electronics requires a single 4.5 V power input. The DCC connected via a dedicated gigabit Ethernet switch is used to collect the data received from the FEM board into the computer. More information on the electronic readout is given in [124].

4.3 Characteristic measurements of the micromegas and results

The role of the micromegas test bench is to provide the several intrinsic properties of each micromegas. Therefore various kinds of measurements have been done to test the capabilities of the micromegas:

- The response of the micromegas for several mesh voltage is stored to verify their behaviour with increasing mesh voltage.
- The gain of each pad as well as the energy resolution is computed by scanning each pad of the micromegas with the smallest collimation. Any major defect, as non responsive pads or lower gain pads, are then seen via this measurement.
- During the scan, the response of the pads in front of the weak source is stored to check the gas quality via the gain stability over time.
- The micro-mesh current is monitored during the whole scan to check the presence of major defect in the micro-mesh.
- Pressure and temperature are stored to allow their use for later calibration, as the gain of a micromegas is pressure and temperature dependant.

The scan of each pad has been measured with the following settings:

- Mesh, BFM and shield: -350 V.
- Strip: -750 V.
- Cathode: -1150 V.
- Lower collimation: l=0.5 cm.

This settings correspond to a drift field of 200 V/cm, which is the same drift field set inside the TPCs in the running conditions. Similarly the same mesh, BFM and shield voltages are set currently in the TPC.

We define the gas gain as the total charge accumulated, charge$_i$ [fC], multiplied by the total number of electrons per fC, C, divided by the number of primary electrons N_e.

$$G_i = \frac{\text{charge}_i[fC] \times C[1/fC]}{N_e} = 28.4[1/fC] \times \text{charge}_i[fC] \tag{4.2}$$

The number of primary electrons has been calculated from the minimum energy required to produce one ion/electron pair in the gas, W,

$$N_e = \frac{E_\gamma}{W} = \frac{5900 \text{ eV}}{26.78 \text{ eV}} = 220 \text{ electrons}, \tag{4.3}$$

where the value $W = 26.78$ eV comes from Table 4.1.

Table 4.1: Fraction of each molecule in the gas and minimum energy needed to produce one ion/electron pair.

Molecules	Fraction in the gas (%)	Minimum energy (eV)
Ar	95	26
iC_4H_{10}	2	23
CF_4	3	54
total	100	26.78

The gas gain was measured to be about 1500 for all the micromegas tested. Because of the linearity of this equation, we often call *gain*, the charge measured in fC.

The exponential behavior of the gain of the micromegas has been tested by changing the high voltage of the micro-mesh. For each potential, the energy spectrum is computed and fitted with a Gaussian. The mean as a function of the high voltage is then plotted as in Fig. 4.8.

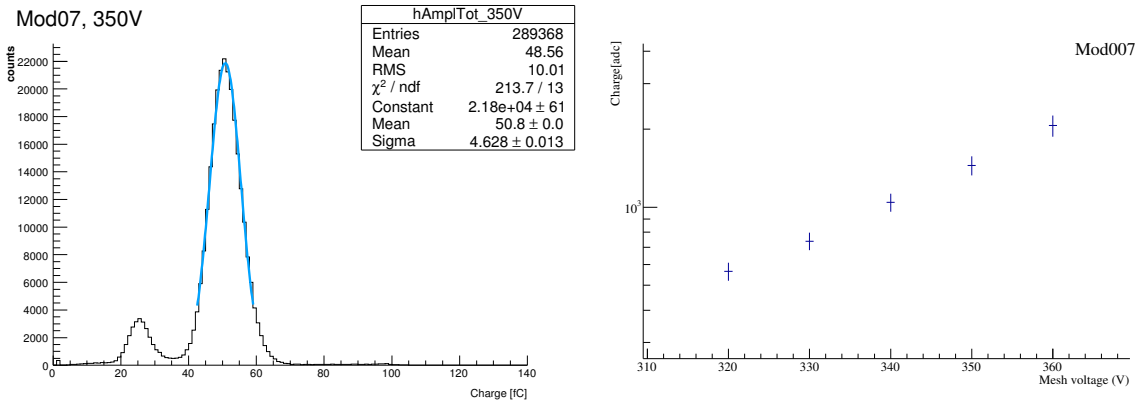

Figure 4.8: Left: Energy spectrum for the center of the pad plane obtained for Mod007(energy resolution: 9. %). Right: Charge [adc] as a function of the high voltage micro-mesh value.

A pad-per-pad scan is then done to map the gain of the micromegas and the results are shown in Fig. 4.9, where we clearly observe the two expected peaks for X-rays interacting in Argon via photoelectric effect.

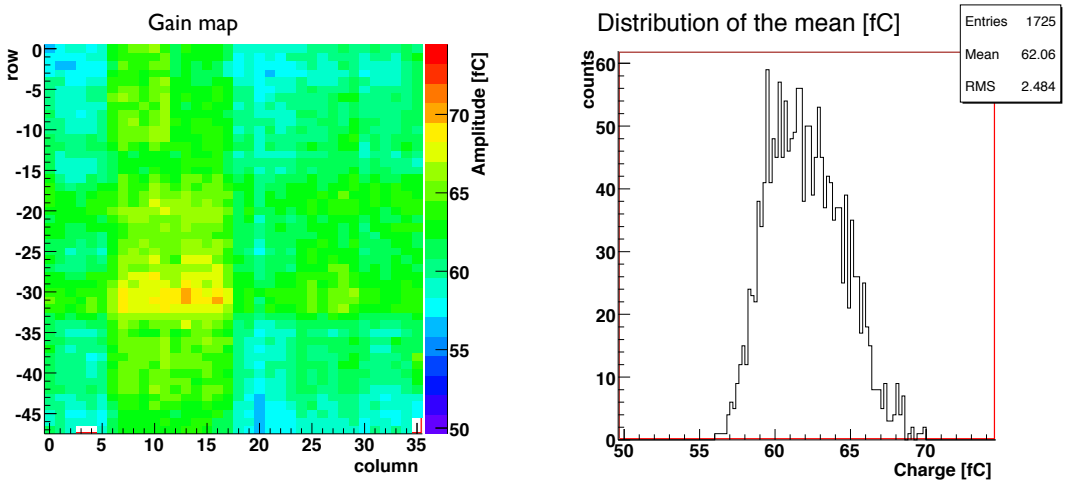

Figure 4.9: Left: Gain map for Mod012. Right: Gain distribution for all pads together for Mod012.

We see that the gain is not uniform along the pad-plane. This can be explained by the dependence of the gain on the capacitance measured for each channel, where the capacitance is directly influenced by the length of the connection between the pad and channel readout on the electronic card. This is shown in Fig. 4.10, where we see a clear dependence between the length of each pad-channel connection and the capacitance measured at each channel. The measured capacitance is explained as the sum of two contributions, the default capacitance of the channel and the parasitic capacitance due to the routing strips inside the PCB of the micromegas module.

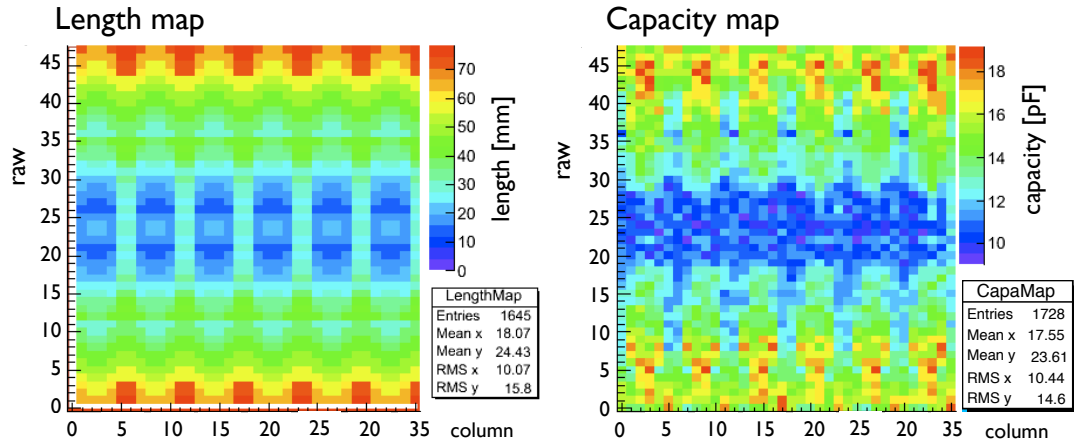

Figure 4.10: Left: Length of the pad-channel connections. Right: capacitance measured for each channel

The dependence of the gain with the capacitance can be described by a line

$$G^{meas} \sim p_0(1 + p_1(C/C_0 - 1)) \tag{4.4}$$

where $C_0 = 14$ is the mean value of the parasitic capacitance, C the measured capacitance, p_0 and p_1 have to be obtained experimentally, p_0 corresponding to the gain corrected from

capacitance effects and p_1 to the slope.

To correct the gain, a fit of the measured gain as a function of the capacitance has been done for all channels together and for each FEC separately. The corrected gain of the k-th FEC is then given by,

$$\tilde{G}^k_{corr} = \frac{G^{meas}}{1 + p^k_1(C/C_0 - 1)} \tag{4.5}$$

where p^k_1 is the result of the fit operated for the k-th FEC.

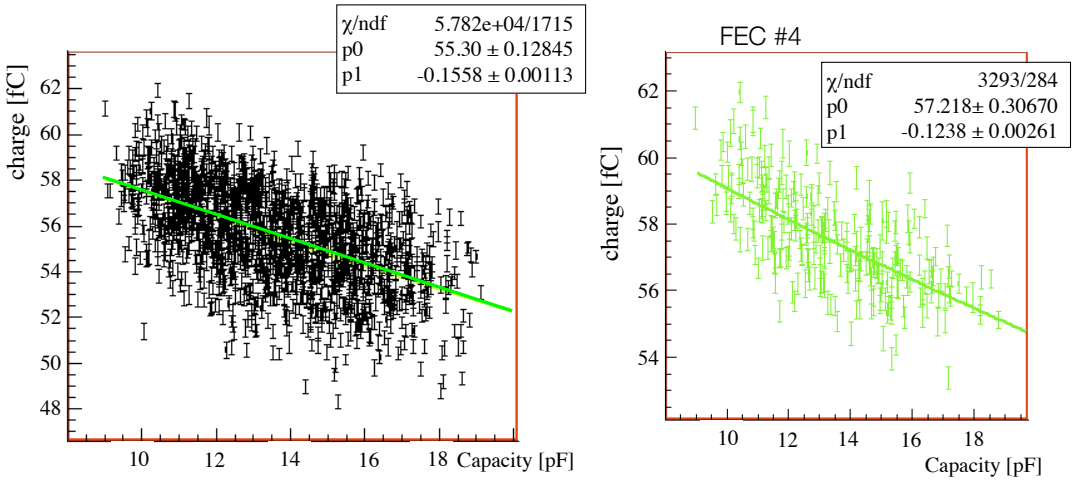

Figure 4.11: Gain as a function of the capacitance for all pad together (left) and only for the fourth FEC (right).

Fig. 4.11 shows the dependence of the gain on the channel capacitance for all channels and for the channels corresponding to the fourth FEC. We see, in particular, that the corrected gain value when fitting all pad together or the pad corresponding to a FEC is different and so is the slope. To take that into account an additional normalization factor multiplies the corrected gain for each FEC, k,

$$G^k_{corr} \equiv \frac{\alpha^k G^{meas}}{1 + p^k_1(C/C_0 - 1)} \tag{4.6}$$

where $\alpha^k = p^{all}_0/p^k_0$ and p^{all}_0 the parameter obtained when fitting all the channels together.

Applying this correction, the gain map can be computed and is shown in Fig. 4.12, where we see a better uniformity and decrease of the signal amplitude dispersion, that is now $\sim 2\%$.

The resolution is obtained by taking the ratio of the width of the spectrum peak with its mean value, for each pad. The resolution should not be sensitive to the capacitance of each channel, which is experimentally observed. Although, Fig. 4.13 shows the energy resolution for a corrected gain, very similar results are obtained without corrections in this case. We obtain a uniform distribution with a mean energy resolution of 9 % at 5.9 keV and a dispersion about 6%.

During the pad-per-pad scans, the stability of the pads behind the weak sources has been cross-checked. The results are shown in Fig. 4.14 for the two weak sources, and we notice a uniform gain over time.

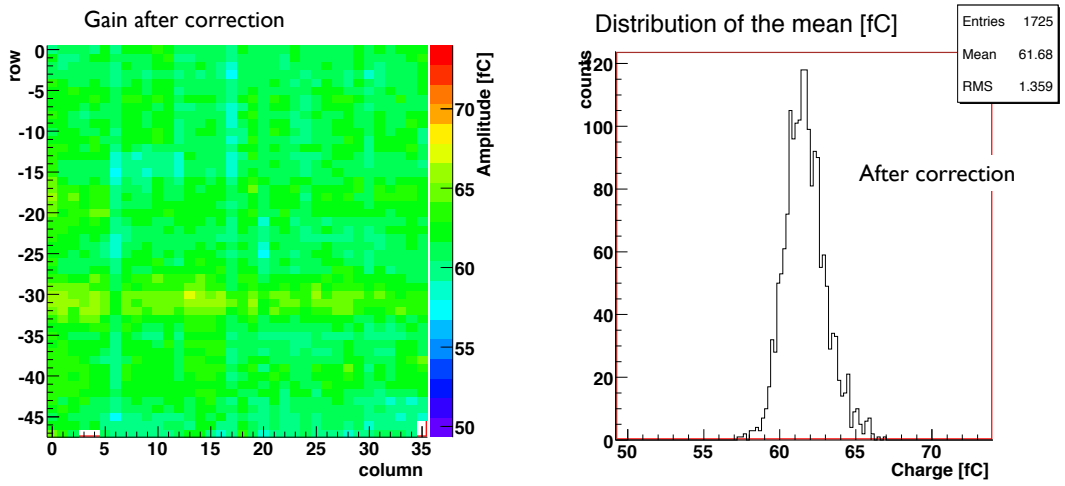

Figure 4.12: Gain map and gain distribution for Mod012 after corrections.

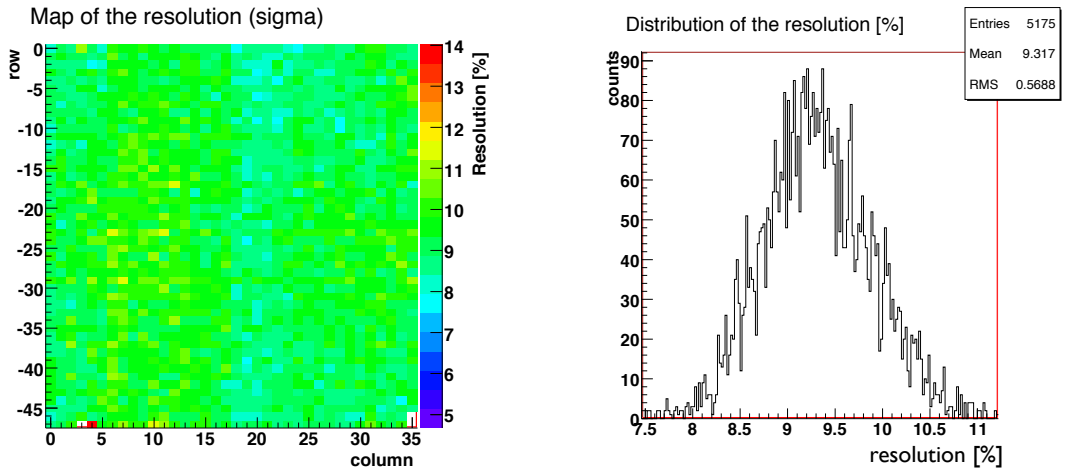

Figure 4.13: Resolution map and distribution for Mod012 after corrections.

In addition, the current of the micro-mesh has been measured during each scan to check the number of sparks. A spark is an excess of current of the micro-mesh that can be due to an accumulation of charges over insulators region as the supporting pillars. They should increase exponentially with the mesh voltage. Such sparks were found to last typically a few milliseconds with a few volts drop (< 5V) on the micro-mesh high voltage supply corresponding to a current drawn of a few hundreds of nA (< 500nA). Although, we cannot avoid having sparks in the chamber, their number should be relatively small which has generally been achieved for all modules of the T2K experiment. Fig. 4.15 shows the current on the micro-mesh during a complete scan, which corresponds to the general observation of a spark rate lower than 0.1/h.

All these measurements have been done for 104 micromegas modules out of which 72 are currently used in the TPCs. The average gain of each micromegas module used in the TPCs is shown in Fig. 4.16, where we see that the gain is not exactly uniform along the micromegas.

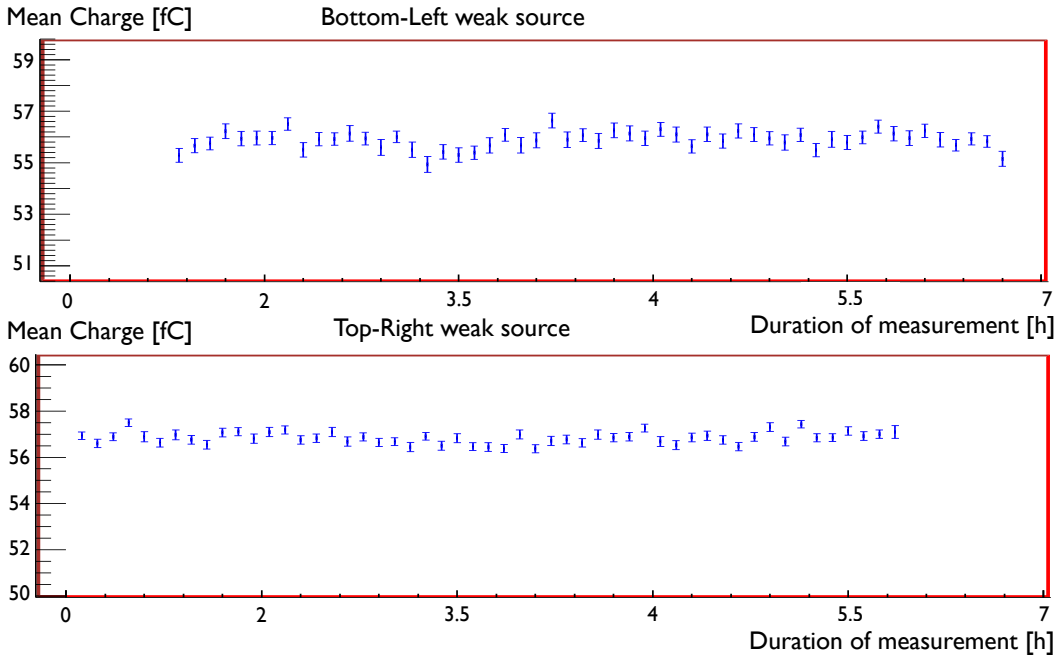

Figure 4.14: Weak source gain stability for Mod017.

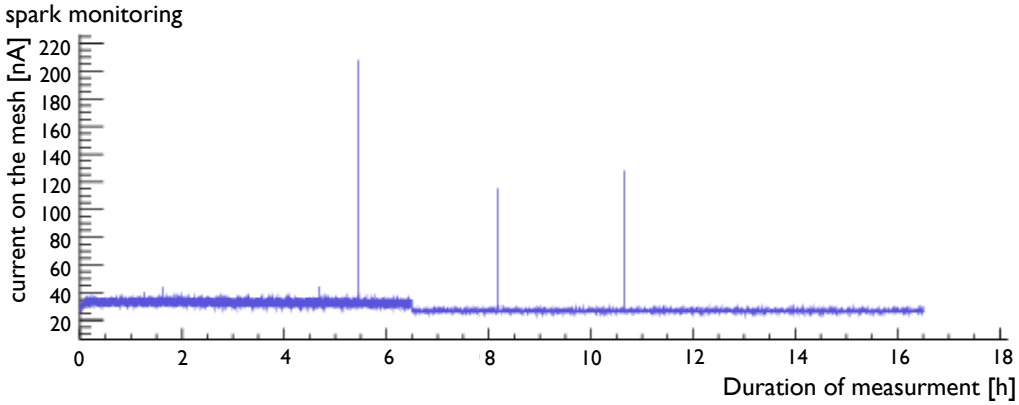

Figure 4.15: Micro-mesh current during a complete scan for Mod071. The step at 6.5 h corresponds to the end of the scan.

The measurements at the test-bench have been done during more than 1 year, and the temperature as well as the atmospheric pressure changed from one measurement to the other. Pressure and temperature has then to be taken into account in addition. Fig. 4.17 shows the gain dependence on the pressure and the temperature.

Again a correction is done to the measurements following the same steps as for Eq. 4.5,

$$G_{corr} = \frac{G^{meas}}{1 + s \cdot (\frac{T/p}{T_0/p_0} - 1)} \tag{4.7}$$

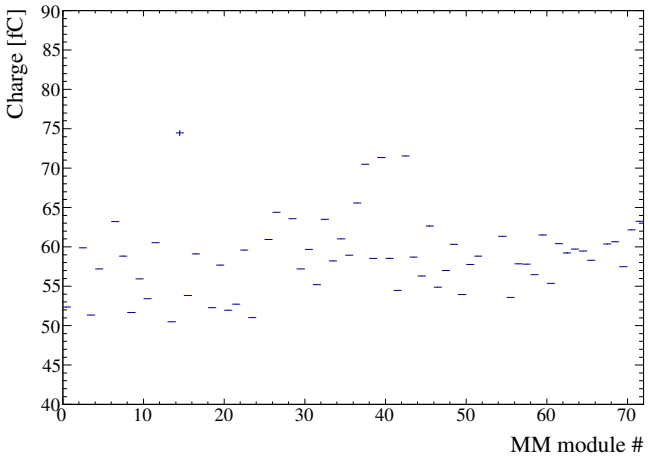

Figure 4.16: Average gain per module as a function of the 72 MM modules that have been chosen for the TPC.

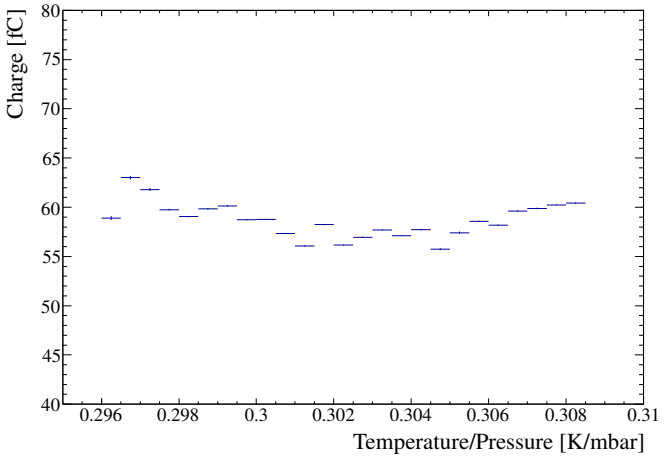

Figure 4.17: Gain as a function of the room pressure and temperature.

where $T_0 = 298.15\ K$ and $p_0 = 1013\ mb$. The slope s describes the relative change of the gain per relative change of T/p. After applying the correction to this data, the remaining variation, due to other factors such as gas composition, is below 1%.

Additional measurements like the micro-mesh transparency, cross-talk or aging effects were also performed on prototype detectors with characteristics identical to the ones of the T2K modules. The main results are presented in [124].

The transparency of the micromegas were measured for different drift field and amplification field. The results agree well with the MC simulation. Small cross-talk effects (less than 1%) in the detector PCB were observed by correlating the charges measured in adjacent pads. The observed cross-talk contribution corresponds to the parasitic capacitance of a few pF, mainly due to the routing strips inside the detector PCB.

The aging cross-checks has been carried out on a small, 11 cm diameter detector, using a 20 mA X-ray gun. The total accumulated charge density on the anode was 0.17 C/cm^2, which is orders of magnitude bigger than the charge that will be collected for the duration of the T2K experiment. No significant ageing effect at the level of a few percent was observed during these tests.

4.4 Summary

In this chapter, we explained how the micromegas, the device amplifying the signal created by an ionizing particle in the TPC gas, have been tested. In particular, a detailed description of the Test Bench setup has been given. The characteristic measurements done for the 104 micromegas has been shown. From these measurements, we observed various dependences that need to be taken into account for a correct calibration in the ND280 detector. In particular, non-uniformities of the gain over the pad plane due to the parasitic capacitance of the strips connecting the pads to the readout channels is observed. In addition, pressure and temperature dependences of the mean gain of each micromegas have been observed. These dependences need to be taken into account in the calibration. In the next chapter, we will see how these measurements are taken into account inside the whole chain of data and MC processing.

Chapter 5

Event reconstruction and selection in the ND280

In this chapter, I present a general overview of the ND280 software. The description does not aim to be complete, but rather tries to link the tools, which are used in the final analysis and the basic inputs, such as the signals collected by the detector, or the Monte-Carlo (MC) objects. In particular, we will see at which stage the calibration is done and how the main variables used to select an event are reconstructed. These variables are then used in the event selection.

The goal of this thesis is to provide a flux-averaged cross section for charged current muon neutrino interactions in the tracker. This is achieved by doing an event selection that is the same as in the latest official oscillation analysis (2012a oscillation analysis). In the oscillation analysis, the inclusive charged current selection used is split into two sub-samples, a CCQE-like and CCnQE-like sample.

Since the end of 2008, I have been working on the charge current selections and the main body of the event selection is still used in this analysis [130]. Since this first study, reconstruction has improved considerably. During the following years, the analysis has been repeated for different software versions and has proved to be very useful for understanding the different reconstruction issues that needed to be improved to get better selection efficiencies and purities. It gave, also, the first steps for understanding the detector's response and its capabilities.

The software and reconstruction tools, which are currently used, are significantly different. This analysis uses as its starting point the "global" ND280 reconstruction that attempts to combine reconstruction information from multiple detectors. In fact, this analysis is an extension of a parallel analysis to the 2010a oscillation analysis for Run I data where global reconstruction was first used. This analysis is described in the internal technical note T2K-TN-044 [131] which I contributed to.

In practice, information from the FGDs and TPCs plays a primary role in the event selection. In the process of the analysis a few significant bugs and failure modes of the global reconstruction were identified, and we were forced to resort to lower-level reconstruction information in some cases. Nevertheless the capability and sophistication of the reconstruction is higher than that used in the first T2K oscillation analysis. This situation is described in detail in Sec. 5.4.4.

In Sec. 5.1, the general description of the near detector software is given. The software versions, the MC and the data samples used to produce the final results shown in Chapter 8 are given in

Sec. 5.2. Sec. 5.3 summarizes the calibration procedure where the Test Bench data is used. The general feature of the reconstruction is explained in Sec. 5.4. In this section, all the variables used in the charged current selection (see Sec. 5.5) are explained in more details.

5.1 The near detector software overview

The ND280 software can be divided according to the role of its various packages. The relation between the different packages is given in Fig. 5.1.

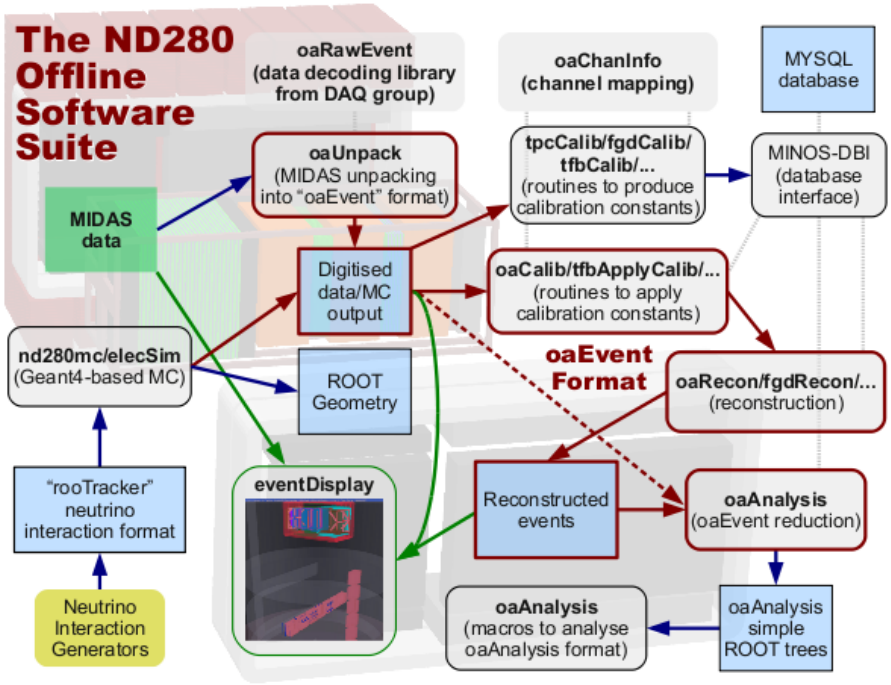

Figure 5.1: The ND280 offline software suite [132].

In this section, only the main packages are explained and I refer to [132] for the details of each package.

The near detector software is able to process MC simulations as well as near detector measurements. The first stages of the MC processing mainly consist in transforming the true information simulated into a format comparable to that of a measurement. This implies the incorporation of the detector and electronic readout response. From now on, we shall refer to these first stages of MC processing by *event simulation*. For data, the first stage corresponds to translating the raw data output (MIDAS format) into the ROOT event format described in [132]. At this point, the only difference between data and MC is that the MC conserves in addition the true information. Calibration and reconstruction are then applied similarly to both samples. It is worth noting that calibration not only affects real data but also the events simulated by MC methods. In order to be as close as possible to real data, the effect of the calibration is simulated.

The event simulation can be separated into different stages:

- **Neutrino flux simulation at the near and far detector (JNUBEAM)**
- **Neutrino interaction generation (NEUT/GENIE)**
- **Secondary interactions inside the near detector (`nd280mc`)**
- **Electronic and digitization of detector response simulation (`elecSim`)**

The neutrino event generation is interfaced together with the neutrino beam flux simulation. Therefore, the MC has a complete knowledge of its flux at the different positions inside the near detector site. The simulation of the neutrino interactions has been done using two kinds of neutrino event generators (NEUT and GENIE) [65, 133]. The secondary particles from the neutrino interactions are then propagated using GEANT4 [134] in the near detector (`nd280mc`) and a dedicated package simulates the response of the active detector components and readout electronics (`elecSim`). It includes the transformation of the deposited charge at the sensor into an energy deposit, the simulation of the signal produced by the sensor and how that signal is then recorded by the electronics.

5.2 Samples

Seven different samples of data and MC have been used for the results presented in this thesis. The number of protons on target (POT) of each sample is summarized in Table 5.1. The samples are separated into four categories, the data taken in 2010 and 2011 until the earthquake, the NEUT and GENIE MC generators for interactions inside the magnet, and the NEUT MC generator of neutrino interactions outside the magnet, e.g. in the sand upstream the detector, or the structure around the whole detector (pit walls, etc...). This separate MC is described in the internal technical note T2K-TN-77 [135]. These interactions will appear as part of the background inside our inclusive charged current selection.

Table 5.1: Number of POT for each sample

Samples	RUN I	RUN II
Data	2.939×10^{19}	7.857×10^{19}
NEUT (magnet)	54.5×10^{19}	110.5×10^{19}
GENIE (magnet)	55.7×10^{19}	111.55×10^{19}
NEUT (sand muons)	7.0×10^{19}	

The MC data sets are divided into Run I and Run II to take into account the peculiarities of the two run periods. The averaged beam intensity simulated in Run I is 50 kW, while the beam intensity has been set to 120 kW in Run II.

Table 5.2: MC and reconstruction versions

Samples	MC version	ND280 soft. version
Data	-	v9r9p1 (4D)
NEUT (magnet)	*v5.1.3*	v9r7p9 (4C)
GENIE (magnet)	*R-2_6_2*	v9r7p9 (4C)
NEUT (sand muons)	*v5.1.4*	v9r9p1 (4D)

The version of the MC simulations as well as the version of the ND280 software, is listed in Table 5.2. Production 4D has been used for data, as a better calibration has been made in this case. For MC, the 4C production is used as the changes between 4D and 4C only concerns data. There is therefore no difference between the 4D version of the sand muons MC and the other magnet MCs.

The 4C and 4D MC productions use the neutrino flux tuning (*v11a2.1*). Since the production, tuning of the flux has been performed using the measurements of the NA61 experiment [136]. Therefore, an event-by-event reweighting is done on the MC to take into account the most up-to-date knowledge of our flux, *v11b3.1*. Note that the MC simulations are performed taking into account the distributions of our off-axis beam inside the near detector.

5.3 Calibration

The calibration procedure can be divided into two steps. The first is the electronics calibration, which consists of normalizing all channels to the same zero and scale, such that the information from different channels can be combined consistently (see Sec. 5.3.1). The second step, the physics calibration, is more complex and adjusts a range of physics parameters (see Sec. 5.3.2). It leads finally to the best possible reconstruction of the particle trajectories and their energy deposition, which is crucial for the determination of their type.

The calibration framework includes the calibration data, the calibration algorithms and the calibration constants. There are three types of algorithms,

- **Algorithms that compute the calibration constants**. These algorithms belong to calibration package for each subdetector (`tpcCalib, fgdCalib,...`).
- **Algorithms that apply the calibration constants**. These algorithms belong generally to the reconstruction package for each sub-detector (`oaCalib, tpcRecon, ...`).
- **Algorithms that "de-calibrate" the MC data in order to simulate the effect of the real detector**. These algorithms are distributed among several packages. For example the effect of the geometrical misalignment or the magnetic field inhomogeneities should be simulated at the level of the particle transport, in `nd280mc`. The simulation of the electronic response including noise and other effects related to the detector response are done in `elecSim`.

5.3.1 Calibration of the electronics

Each electronics channel i in the detector provides uncalibrated signals Q^i_{raw} at time t^i_{raw}, which lack of real physics information. In order to extract the appropriate information from the signals received, all electronic channels in the same sub-detector must refer to the same reference system, with the same zero and scale.

In the case of a linear response, the calibrated signals, for each electronics channel i, are

$$Q^i = \alpha^i(Q^i_{raw} - Q^i_0) \tag{5.1}$$

$$t^i = \beta^i(t^i_{raw} - t^i_0) \tag{5.2}$$

where Q_0^i is the pedestal, t_0^i the starting time of the pulse, and α^i and β^i the scaling constants.

Note that the response of the scintilator detectors is not linear (especially for the detectors using the TFB electronics). Therefore a more complex calibration is done in this case and I refer to [137] for the complete description.

5.3.2 Physics calibration

The physics calibrations include the energy calibration (ADC/MeV conversion), charge attenuation, spatial distortions, magnetic field corrections and geometrical alignment. Physics calibrations not only affect the charge and time of the hit but also its position. Some of the physics calibrations use reconstructed data (clusters, tracks, etc) as input for the computation of the calibration constants. This is the case of the geometrical alignment and the correction of spatial distortions with tracks.

The calibration procedure will depend on the sub-detector. For the TPC, for example, the energy calibration is done by using the Test Bench procedure, the spatial distortions by the use of the laser, the drift velocity by the use of the laser and monitoring chamber and finally the signal attenuation is done by using the monitoring chamber together with cosmic data. The raw information coming from the Test Bench is reprocessed by the calibration package where the different corrections are applied to the gain. The calibrated values are then stored to the database. The reconstruction package of the TPC applies afterwards the calibration constants to each micromegas pad.

The calibration software has a close connection to the online software, since most of the calibration data is taken in parallel with physics data. Studying the evolution of the calibration constants is crucial to ensure the quality of the data. Therefore some of the calibration constants are computed online and monitored, during the data taking.

5.4 Reconstruction

The reconstruction can be divided into two steps. First of all, the *local* reconstruction, where each sub-detector develops its own reconstruction algorithm depending on the different ability of the detector. Secondly, the *global* reconstruction, where the various local reconstructed objects are combined. In the following, we will generally use TPC or FGD segment to design the local reconstructed track component of the global track in the TPC or in the FGD.

For the analysis presented in this thesis, the most relevant part of the reconstruction is the integrated reconstruction of TPC and FGD hits.

In particular, the FGD reconstruction uses extrapolated three-dimensional TPC tracks to associate hits to tracks. In turn, the TPC relies on the FGD and occasionally on other scintillator detectors to provide the timing offset t_0 needed to determine the drift direction coordinate, x, of the track.

In this section, I give a brief summary of the TPC and FGD reconstruction and describe how the basic variables used in the CC-inclusive selection (see Sec. 5.5) are obtained. I refer to [138], for the details of the algorithms.

5.4.1 TPC reconstruction

The first step in the TPC reconstruction is the application of the gain calibration constants and the removal of dead and noisy channels[1].

The output of this process is the waveform representing the charge acquired in a single pad as a function of time. The following step is the search for clusters of waveforms in the same row of a micromegas.

Clusters are then joined into tracks using a pattern recognition algorithm. The pattern recognition is applied to TPC blocks independently, where the TPC blocks are the area defined by each micromegas.

At the end of the pattern algorithm, the calculation of the ionization energy deposited in the TPC is computed to perform the particle identification (PID).

I now briefly explain how the PID variables are computed, as these variables are essential for the selection of charged current interactions. To produce the Probability Distribution Functions (PDFs) on which the PID is based, the particles are simulated at different positions just before the TPC, with a direction parallel to the beam, in order to obtain a pure sample of TPC tracks. The energy losses, obtained for various momentum and particle type, are interpolated to give the expected energy loss C_E as a function of momentum and particle type[2]. The lower energy fraction of the charge distribution (70%) of a TPC segment is then selected to avoid inhomogeneities inherent to the high energy tail of the distributions and defines the truncated distribution. An estimator of the ionization independent of the track length is built by calibrating the energy of each cluster of a track. This is done by normalizing measured energy loss of each track to the corresponding energy that a horizontal track with 72 clusters would have had. The mean energy of the calibrated cluster in the truncated sample defines the ionization estimator $\bar{C}_T$.

For each TPC segment of a global track, a pull value can be computed

$$pull(\alpha) = \frac{\bar{C}_T - C_E(\alpha)}{\sigma(\alpha)} \tag{5.4}$$

where C_E is the expected energy loss as a function of the momentum for a given type of particle α and $\sigma(\alpha) = \sqrt{\sigma_T^2(\alpha) + (\mathrm{d}C_E/\mathrm{d}p)^2\sigma_p^2}$ is the total uncertainty due to the uncertainty on C_T and the momentum measurement. Then the parameters are varied to fine-tune the PID for non-ideal tracks.

We define the likelihood for a track being particle species α as,

$$\mathcal{L}_\alpha = \frac{P_\alpha}{P_\mu + P_e + P_p + P_\pi} \tag{5.5}$$

where the PDFs are,

$$P_\alpha = \frac{1}{\sqrt{2\pi}\sigma(\alpha)} \exp[-\sum_i^{TPCi} \frac{pull_i(\alpha)^2}{2}] \tag{5.6}$$

[1] This step can be done at the end of the online process, but it has to be always possible to re-do it when updated knowledge of the calibration constants is available.

[2] The parameterization of the expected energy loss is given in [139] and is

$$C_E = \frac{785 ADC}{\beta^{2.308}} \cdot 6.047 - \beta^{2.308} - log(0.00064 + \frac{1}{(\beta\gamma)^{1.359}}) \tag{5.3}$$

and $\alpha = \mu,\ e,\ p,\ \pi$.

Pull and likelihood can be used for selecting tracks of a certain flavor. Suppose we select correctly tracks as muons, the pull distribution obtained in this case will be centered at 0 with sigma around 1. On the contrary, if there are tracks that are not muons in the sample, the difference between the measured energy loss and the expected one will be bigger. Note that muons and pions will be very difficult to separate as they have similar energy loss curves. For momentum where proton and muon curves are crossing each other, protons can be miss-identified as muon if the charge of that track has not been well reconstructed.

Fig. 5.2 shows the distribution of the energy loss as a function of the momentum. The case of

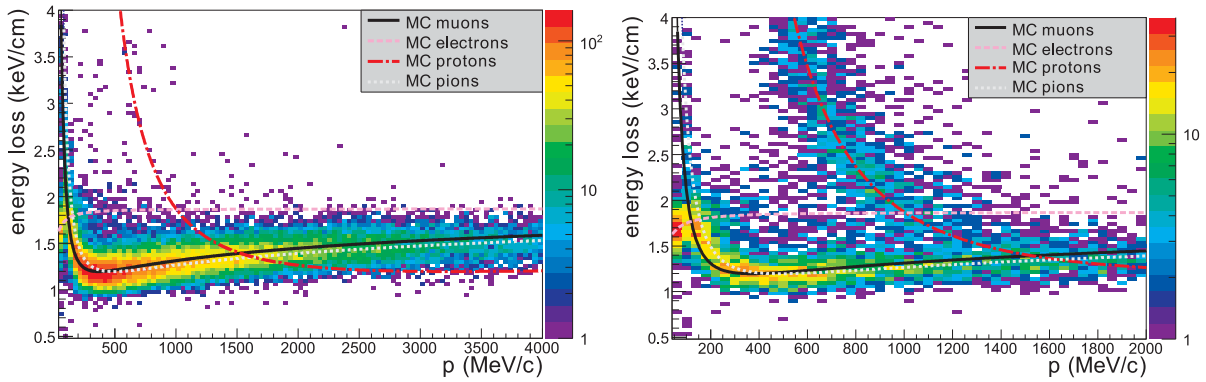

Figure 5.2: Distribution of the energy loss as a function of the momentum for negatively (positively) charged particles produced in neutrino interactions, compared to the expected curves (as defined in Eq. 5.3) for muons, electrons, protons and pions on the left (right respectively).

the likelihood is slightly more complicated. By construction, the cuts done on the likelihood or the pull distribution give similar results. The likelihood distribution has been chosen as the right variable for doing the cut as it gives a nice framework for adding other PID information from other detectors in future analyses.

Fig. 5.3 shows the distribution of the pull for tracks with a TPC2 segment.

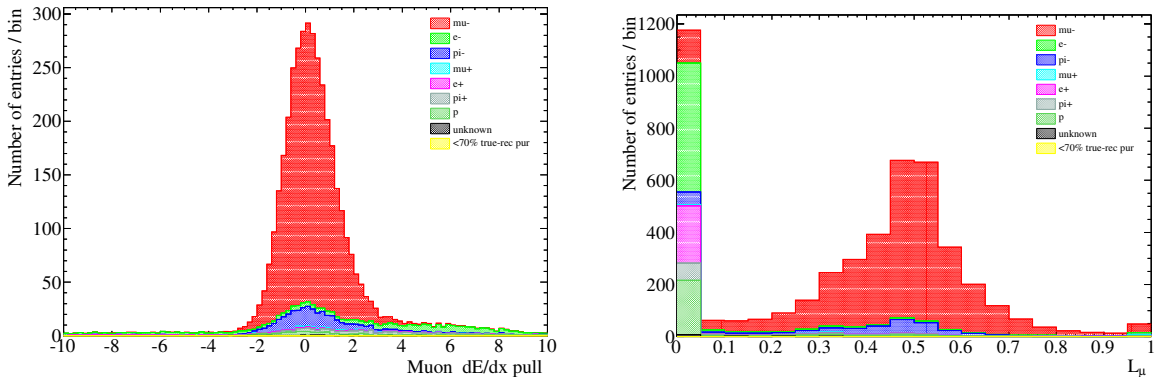

Figure 5.3: Pull and $\mathcal{L}_\mu$ distribution for the muon hypothesis ($\alpha = \mu$ in Eq. 5.4) of all tracks that have been selected with a negative charge and crossing the TPC2 (left and right respectively).

After the calculation of the ionization energy deposited in the TPC, the reconstruction of the track kinematics is done using a single TPC likelihood fit with helix parameterization in the fit.

From this fit, the main variables used to select the charged current events and the final cross section result are obtained. They are the absolute x, y and z coordinates, the direction of the track and its curvature ρ. From the curvature, the reconstructed momentum p and charge q are computed,

$$p = \frac{0.3 \cdot B}{\rho} \sqrt{\frac{1 + t_x^2 + t_y^2}{1 + t_y^2}} \tag{5.7}$$

$$q = \frac{\rho}{|\rho|} \tag{5.8}$$

where the momentum is in MeV, ρ is the fitted curvature in mm^{-1}, B the mean magnetic field value in Tesla and t_x is the tangent of the projected angle in the XZ plane and t_y is the tangent of the projected angle in YZ plane. The transverse momentum to the magnetic field is defined for $t_x = 0$, in this case Eq. 5.7 gives back the well known relation between the magnetic field and transverse momentum.

The drift distance has to be reconstructed to be able to predict the size of the electron cloud due to the transverse and longitudinal diffusion. This is achieved by determining the time at which the track was created (t_0 of the track) via a matching with objects in the fast detectors, FGD, P0D and ECAL. The x-coordinate is then reconstructed as

$$x = (t - t_o) v_{\text{drift}} \tag{5.9}$$

where t is the arrival time of the hits on the pad plane.

The reconstructed tracks are then matched to tracks in other TPC blocks and fitted again to improve the accuracy of the track parameters.

5.4.2 FGD reconstruction

There are two principal goals of the FGD reconstruction. Firstly, it should match up FGD hits with TPC tracks, in order to recognize and fit longer FGD/TPC tracks. For instance, this is important in order to find the initial vertex point of muons that start in an FGD and traverse the TPC. Secondly, it should recognize, fit and identify shorter tracks that start and stop in an FGD. This is important for identifying short proton and pion tracks to distinguish between CCQE and CC1π interactions.

The FGD reconstruction comes once the TPC reconstruction is done. First the FGD hits are separated into various set of hits based on their times. The TPC tracks are then matched to FGD hits by looking at the t_0 of the TPC track. If the time of the TPC track matches the FGD time bin, the the RecPack Kalman Filter [140, 141] is used to extrapolate the TPC track to the closest layer of hits in the FGD.

The unmatched FGD hits are then used for stand-alone reconstruction. The first step in this process is pattern recognition (e.g identifying sets of hits that originate from the same track). The XZ and YZ projections are then matched together to form three-dimensional reconstructed tracks that start and stop in the FGD.

After that, FGD PID algorithm and FGD track time calculation are done.

5.4.3 Global reconstruction

The final output from the sub-detector reconstruction is a list of either track-like or shower-like objects. If the objects are tracks then the tracks are fitted again with the RecPack Kalman Filter [141]. If the objects are showers then no changes are necessary. These preparations are done on copies of the original sub-detector objects, to ensure that the unmodified sub-detector objects remain available. The global reconstruction matching proceeds as follows:

1. Try to match each Tracker object (FGD-TPC matched tracks) to adjacent detectors, through the computation of a matching χ^2.
   - If the matching χ^2 is less than 100 (200 for objects containing P0D or SMRD) and the time difference between the objects is acceptable (within 300 ns of each other), then the two objects are matched together.
   - If two objects are matched together, then the objects are fitted again using the RecPack Kalman Filter.
   - Only pairs of objects are combined at the same time. Therefore, a third object would be match to the merged object in the next iteration.
2. *Step 1* is repeated, but starting with all the P0D objects that weren't used in *Step 1.*
3. *Step 1* is repeated, but starting with all the ECAL objects that weren't used in *Step 1.*
4. ...

5.4.4 Additional modifications to the reconstruction

As already pointed out, in the process of developing this analysis several errors were found in the global reconstruction that required *ad hoc* modifications. These problems were:

- A bug in the magnetic field calculation as a function of current meant that the reconstructed momentum was systematically larger by 1.59%, 1.69% or 1.89% depending on the value of the magnetic field.
- Tracks, which were matched to SMRD reconstruction objects often, had incorrect momentum, and there was an associated reconstruction efficiency loss for fitting global tracks with SMRD components
- A bug in the energy loss (dE/dx) correction has been found for some class of events, and in particular it failed to account for the particle slowing down as it lost energy in dead material, and also assumed the wrong thickness for the FGD cover plates.

In general, each of these problems was corrected in our analysis by ignoring the final output of the global reconstruction. So while global reconstruction was used to determine which sub-detectors contributed to a given global track, the following changes were made to address the above problems:

- The momentum of reconstructed TPC tracks were rescaled to remove effect of the wrong magnetic field during the event selection.

- The global reconstruction vertex and momentum were ignored. Instead, the vertex and momentum calculated from the tracker reconstruction output (i.e. before the global reconstruction attempted to combine it with other detectors) was used. The main improvement this introduced was the use of only TPC2 for the track momentum measurement (plus energy loss corrections in FGD1).
- For all forward-going events starting in FGD1, the momentum is calculated using only the momentum measured in TPC2. This eliminates the complexity of needing to correct the momentum estimates of both TPC2 and TPC3 for magnetic field distortions and then recombine them.
- The *dE/dx* correction for momentum loss in dead materials was altered to use the correct thickness of the FGD cover in the central region around our fiducial volume (1.6 mm), and the energy loss is calculated doing an integral across the dead material using the Bethe-Bloch formula rather than assuming constant energy loss throughout the dead material. The correction was also done using the local FGD segment length and angle (rather than the global reconstruction estimate of the length and angle).

One additional correction applied at the time of event selection is a last correction to the TPC PID variable C_T to remove remaining time variability that was not removed by the calibration itself.

5.5 The charged current inclusive selection

The event selection consists of a series of cuts designed to select CC-inclusive ν_μ interactions in FGD1. This the work thatI was especially involved in the last years of my thesis. For completeness, the cuts used to select CCQE-like subsample and CCnQE-like will then be described.

Unlike previous analyses, only interactions in FGD1 are included in this analysis. The decision not to use interactions in FGD2 eliminates the need to evaluate most systematic errors twice, in particular both the TPC performance in TPC3 and the FGD reconstruction in FGD2 are rather different from those in TPC2/FGD1, because of the different field distortions in TPC3[3] and water layers in FGD2. This decision also eliminates the need to worry, at this stage, about carbon/oxygen cross section differences. An extension of this analysis to FGD2 interactions is anticipated in the future.

We do not try to select backward-going muons, by implementing special cuts, because the reconstruction is not able to reconstruct backward-going tracks [4].

CC-inclusive selection

Firstly, we describe the CC-inclusive selection cuts that are mainly based on the observation of an out-going track compatible with a negatively charged muon:

[3] The TPC3 is closer to the edge of the magnetic coil.

[4] The only exception in the reconstruction where we are, actually, able to measure backward-going tracks, is when the interaction takes place in FGD2. In this case, a backward going muons reaching FGD1, can be well reconstructed as backward using the timing difference between FGD2 and FGD1. This represents, still, a small fraction, of the total charged current interaction with backward-going muon and we do not consider it in this analysis

1. **Data quality flag**
   The standard data quality cuts recommended by the ND280 data quality cut [142] have been applied to reject not only bad runs but also bad spills when either ND280 or the beam spill itself is not considered to be of analyzable quality.

2. **Time bunching**
   Tracks are grouped together in bunches according to their times. The position of the bunches for different periods is shown in Table 5.3.

Table 5.3: Bunch position for the different ND280 run periods.

ND280 run Period	MC all	Data Run I run # < 6000	Data Run IIa $6000 <$ run #< 7000	Data Run IIb run # > 7000
Bunch 1	2750.2 ns	2839.7 ns	2853.9 ns	3019.1 ns
Bunch 2	3332.0 ns	3423.5 ns	3444.1 ns	3597.7 ns
Bunch 3	3914.7 ns	4005.4 ns	4030.4 ns	4180.7 ns
Bunch 4	4497.0 ns	4588.6 ns	4620.3 ns	4763.9 ns
Bunch 5	5078.4 ns	5172.2 ns	5180.3 ns	5346.5 ns
Bunch 6	5659.7 ns	5754.6 ns	5770.1 ns	5927.8 ns
Bunch 7	6243.4 ns	-	6343.8 ns	6508.5 ns
Bunch 8	6824.2 ns	-	6924.7 ns	7093.6 ns

   The bunch width was $\sim$ 7.0 ns in MC and $\sim$ 15.0 ns in data. The bunching criteria associate tracks to a bunch that deviate from the mean bunch position by less than 60 ns (i.e. four times the bunch width in data). Although this technique does not remove completely pile-up events, it allows neutrino interactions in two different bunches within the same beam spill to be treated as two different events. Note that pile-up events in the same bunch are still treated as one event.

3. **Negatively Charged track in FGD1's fiducial volume**
   We require that there is at least one negatively charged track (with FGD and TPC components) that starts inside FGD1's fiducial volume and has more than 18 vertical TPC clusters. The interaction vertex is defined as the beginning of this track described by the coordinates (x_0, y_0, z_0). It corresponds, in general, to the place where the 3D-fitted track intercepts the vertical plane of the most upstream matched FGD hit.

   In the x and y dimension, five bars on either end of each layer are excluded from the fiducial volume (red line in Fig. 5.4), while the upstream z cut places the fiducial volume just after the first XY module. The fiducial volume contains therefore 14 XY modules in which the X and Y layers only contain 182 scintillator bars.

   The fiducial volume cut requires, then, $|x_0| < 874.51$ mm, $|y_0 - 55 \text{ mm}| < 874.51$ mm[5], and $z_0 \in [136.875, 446.955]$ mm.

   The requirement that the track should contain at least 18 clusters, is called *TPC track quality cut*, and rejects short tracks for which the reconstruction is less reliable. The choice of this particular value of the quality cut is based on studies of the kinematic bias for different hit ranges [143]. Since only a small fraction of the selected tracks has fewer

[5]The 55 mm offset in the y cut reflects the fact that the XY modules are displaced 55 mm upwards relative to the center of the ND280 coordinate system.

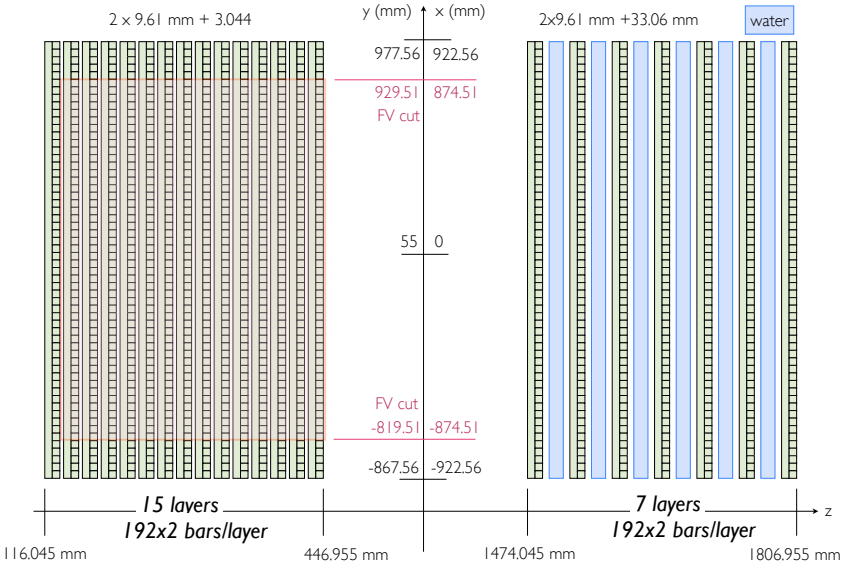

Figure 5.4: Scheme of FGD1 and FGD2

than 19 hits, the effect of the quality cut is expected to be small (less than 5%), as well as the systematic error associated to it.

If there is more than one negatively charged track passing these cuts, we select the highest momentum track as the muon candidate.

4. **Wrong backwards-going tracks and TPC veto.**
The goal of these cuts are to remove miss-reconstructed events entering the FGD1 fiducial volume from the upstream edge of the detector. If the muon candidate starts in the FGD1 fiducial volume and is set as backward-going (end position upstream of start position) the event is rejected, since most of the tracks in this case do not start in the FGD1 as we can see in Fig. 5.5. This cut removes tracks set as backward from timing difference between, mainly, P0D and FGD. As the timing between the two detectors is not good enough, most generally those tracks set as backwards are forward tracks starting mainly in the P0D.

   In addition, we check the highest momentum track with a TPC segment in the bunch that is not the muon candidate (requiring no TPC track quality cut on this second track). If its initial position is more than 150 mm upstream from the muon track starting position (TPC Veto Delta Z), we reject the event on the grounds that there is a track in the event that probably entered the detector from the P0D or magnet region, see Fig. 5.5.

5. **TPC particle identification (PID).**
Given the estimated momentum of the muon candidate, the discriminator function is calculated for the muon, pion, and proton hypotheses. Two cuts are then applied, requiring:

$$\mathcal{L}_{MIP} = \frac{\mathcal{L}_\mu + \mathcal{L}_\pi}{1 - \mathcal{L}_p} > 0.8 \qquad \text{if p} < 500 \text{ MeV/c} \tag{5.10}$$

$$\mathcal{L}_\mu > 0.005 \tag{5.11}$$

   where $\mathcal{L}_\alpha$ is given by Eq. 5.5. The first of this cut rejects electrons at low momentum (below 500 MeV/c). The second cut removes protons and pions. Note that the PID cuts

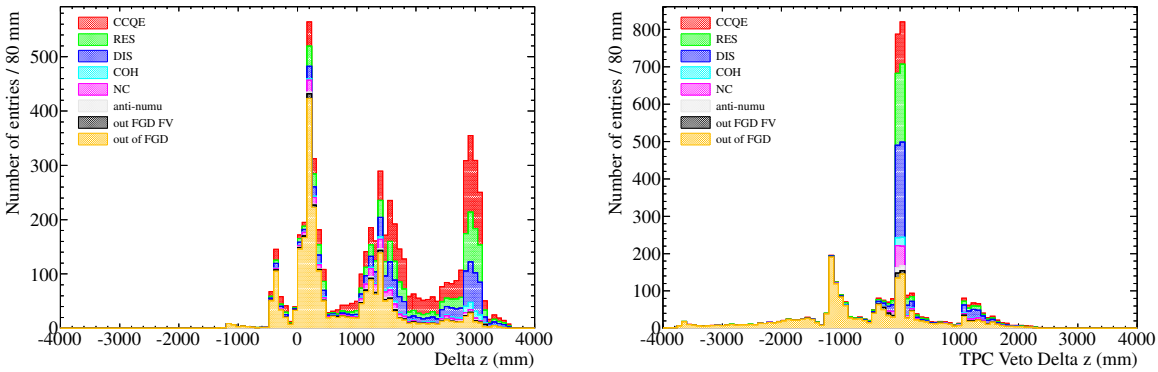

Figure 5.5: Left plot: distribution of the Delta z variable (i.e. the z-position of the track end point minus the z-position of the track start point) before the cut is applied. Delta z is defined as the difference between the start and the end point of the track starting in FGD. Events are rejected if Delta z < 0 mm. Right plot: distribution of the TPC Veto Delta z observable before the cut is applied. TPC Veto Delta z is defined as the difference between the start position of the muon candidate minus the start position of the second highest momentum track in the event. In both cases, the number of entries is normalized to the number of POT in data. Events are rejected if TPC Delta z $<$ -150 mm

are applied after the MC PID resolution has been smeared to have the same pull width as in the data. This is a ∼5% difference in width before the correction. The distribution of both PID discriminators are shown in Fig.5.6 for events before the particle identification cut. Fig. 5.7 shows the pulls for the muon, electron and proton hypotheses, while the muon momentum and angular distributions after application of the last cut are shown in Figs. 5.8 and 5.9.

From these figures, we conclude that the PID cuts remove the electrons, which originated in neutral and charged currents outside the FGD at low momentum and big angles.

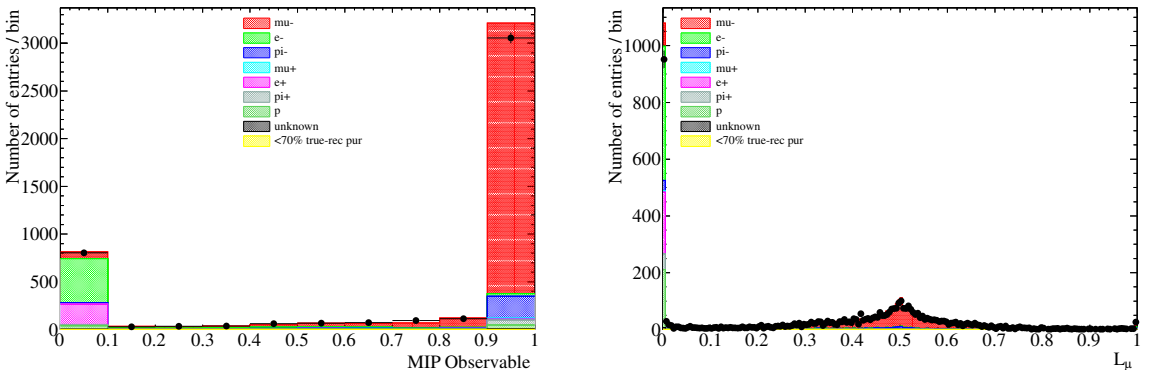

Figure 5.6: **Left:** distribution of the minimum ionizing particle identification discriminator ($\mathcal{L}_{MIP}$ as in Eq. 5.10)for particles with momentums smaller than 500 Mev/c. **Right:** distribution of the muon identification discriminator ($\mathcal{L}_{\mu}$ as in Eq. 5.5). In both cases, the number of entries is normalized to the number of POT in data for run II only, run I giving similar results.

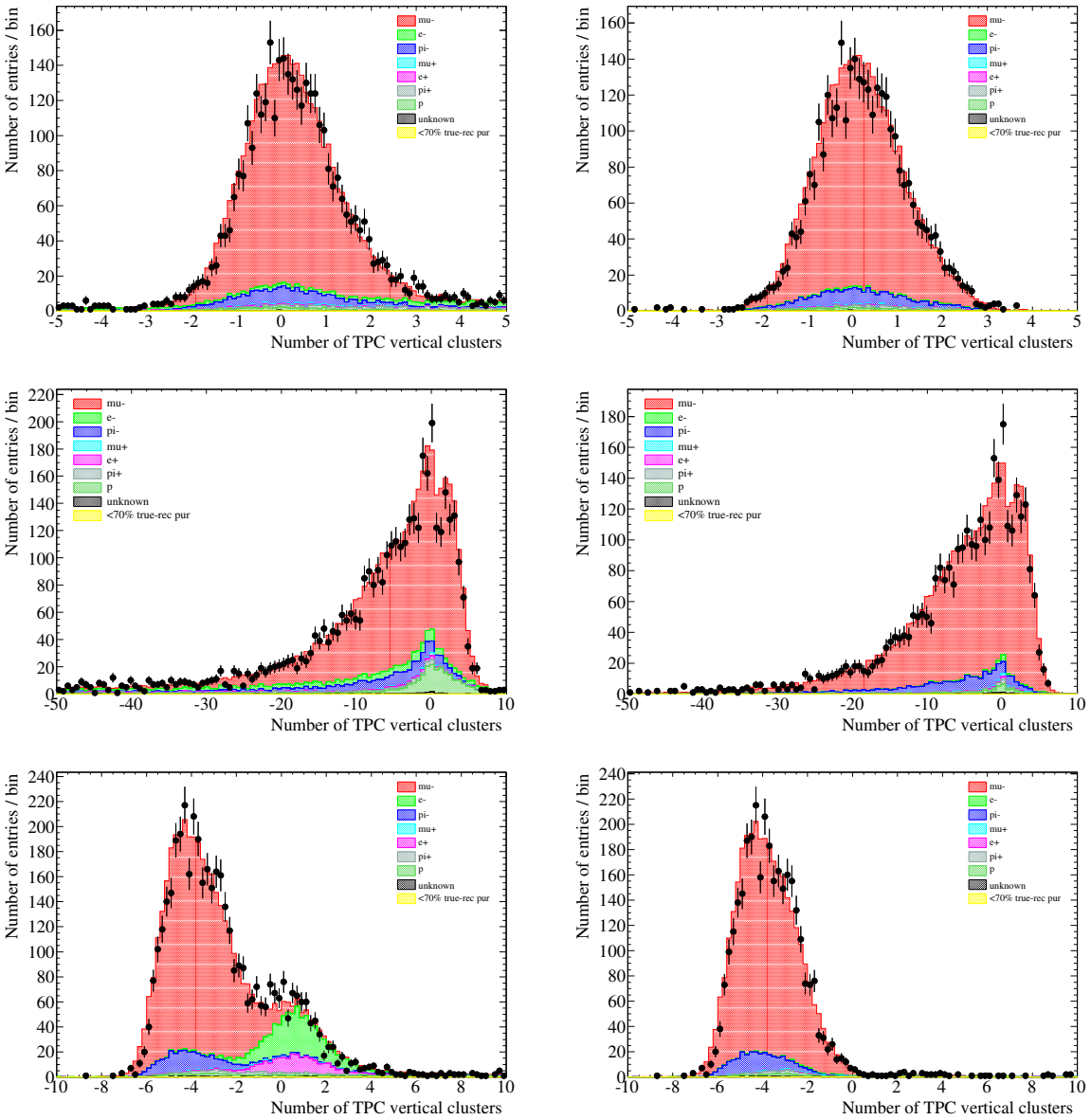

Figure 5.7: Distribution of the muon, proton and electron identification pull (top, middle, bottom respectively) before the PID cut (left) and after the PID cut (right) for run II only, run I gives similar results.

Together these cuts define the CC-inclusive selection in FGD1. All of the events that survive these cuts are included in the final data sample. Fig. 5.10 shows one of the events selected via these cuts.

Because for the oscillation analysis, we also wanted to separate between QE-like and nQE-like, the systematic covariance for each systematic source of detector uncertainty are given for the two selection taking their correlation into account. We will see in Sec. 7.3, how the uncertainties of each selection are then added together for this analysis.

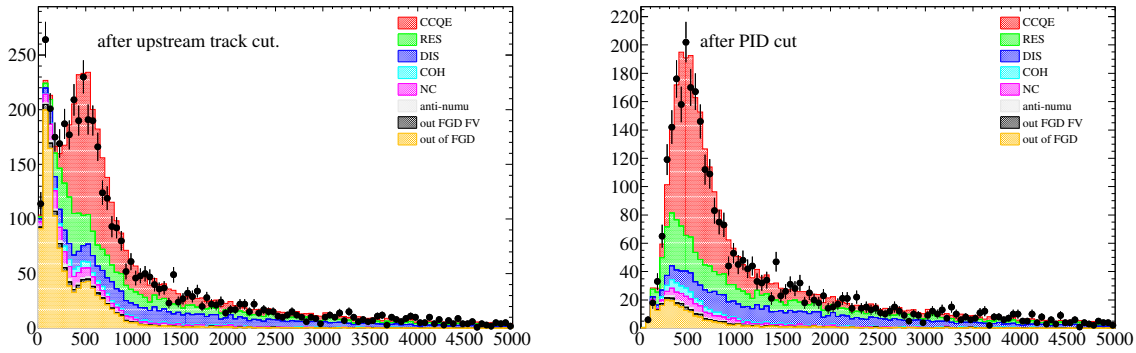

Figure 5.8: Momentum of muon candidate after each cut for run II only, run I giving similar results. **Left:** after upstream TPC veto cut. **Right:** after PID cut.

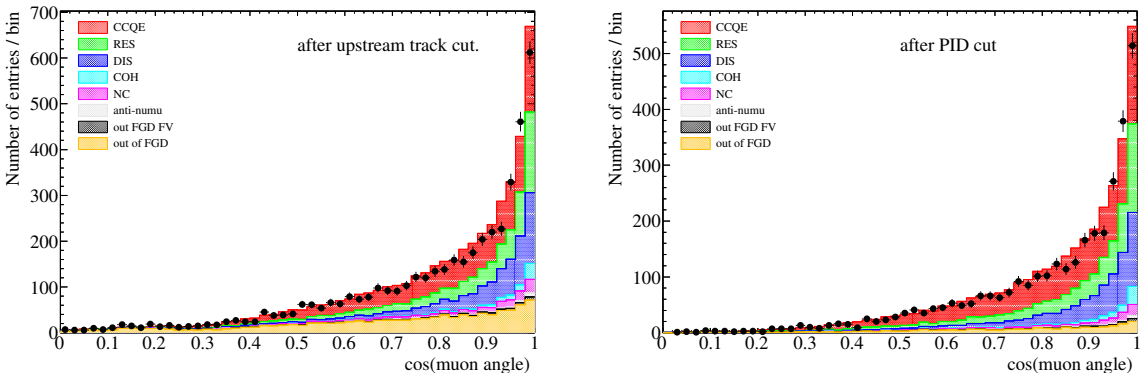

Figure 5.9: Cosine of muon candidate angle (right) after each cut. **Left:** after upstream TPC veto cut. **Right:** after PID cut. Both distributions are shown for run II only, run I gives similar results.

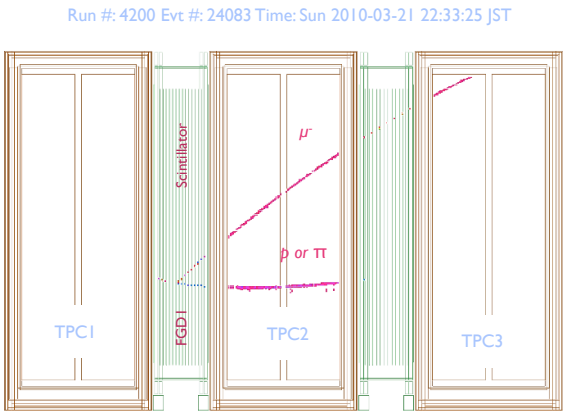

Figure 5.10: Charged current event candidate in the tracker region of the near detector. Muon reconstructed angle 40^o and reconstructed momentum: 566 MeV/c.

CCQE-like selection

The separation in CCQE-like and CCnQE-like sample is done by applying two additional cuts to the remaining events. We define the CCQE-like events as those which satisfy:

1. There should only be one matched TPC-FGD track. This removes events in which a second track from the FGD vertex enters the TPC. For true CCQE events, the recoiling nucleon almost always stops in the FGD and doesn't reach the TPC. In general, if there is a second track reaching the TPC it is more likely that the second track is a pion.

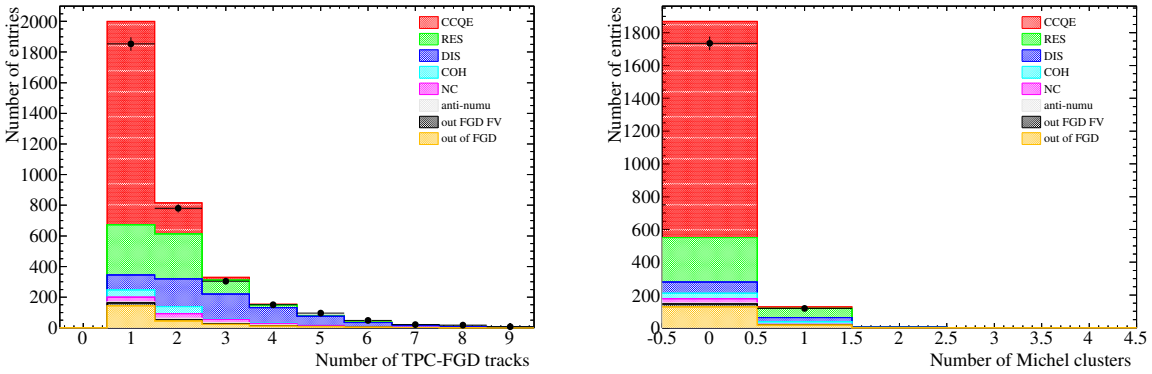

Figure 5.11: Left: distribution of the number of TPC-FGD matched tracks in the event. Right: distribution of delayed clusters found in the FGD. Both distributions are shown for run II only, run I giving similar results

2. There should be no Michel electron in FGD1. A Michel electron is defined as the product of the muon decay: $\mu^- \to e^- \bar{\nu}_e \nu_\mu$. To observe such event in the FGD, the muon should have a very low momentum, this is what happens when a pion decay into a muon. Therefore, looking for Michel electrons in the FGD is similar to look for an event produced with a pion in the final state. Michel electrons are identified by looking for a time-delayed FGD1 hit cluster, not in time with a beam bunch window, with a total charge deposit of at least 200 photoelectrons [144]. The distribution of the number of delayed clusters in MC can be seen in Fig. 5.11.

Any event that fails one of these two cuts is classified as non-QE-like.

5.6 Stability and low-level cross-checks

In this section results of low-level checks of the stability and self-consistency of the data is presented. A Kolmogorov-Smirnov test has been used to test the consistency of this distribution with simple proportionality. The resulting probability is 93.5 %.

Fig. 5.12 shows the number of selected CC-inclusive ν_μ events as a function of the number of accumulated protons on target (POT). We see that the result is consistent with a constant detected rate per POT.

As a cruder stability test, the number of selected events in data relative to the MC is 0.95 $\pm$ 0.03 for Run I and 0.94 $\pm$ 0.02 for Run II.

Fig. 5.13 shows the Data compared to the MC for Run II only (similar results are obtained for Run I). A key low-level distribution is the number of hit clusters in the TPC (top-left). The agreement in this case is reasonable, the difference around 72 hits can be explained by a very

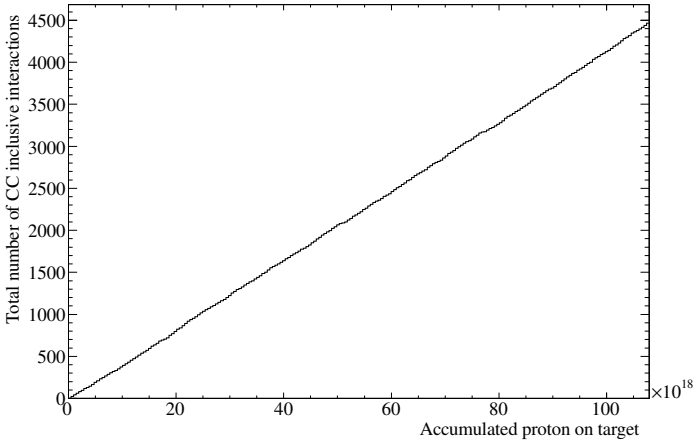

Figure 5.12: Cumulative CC-inclusive ν_μ events vs. accumulated protons on target (POT).

small hit efficiency difference between data and MC that is taken into account. The sharp stop at 20 clusters is due to the quality cut, while the peak at 36 clusters is due to the broken tracks in the middle of the TPC between two MM columns. This effect appears most often for high angle tracks in the YZ plane.

In general, Fig. 5.13 shows a good agreement between data and MC, although sand muon interactions are not taken into account.

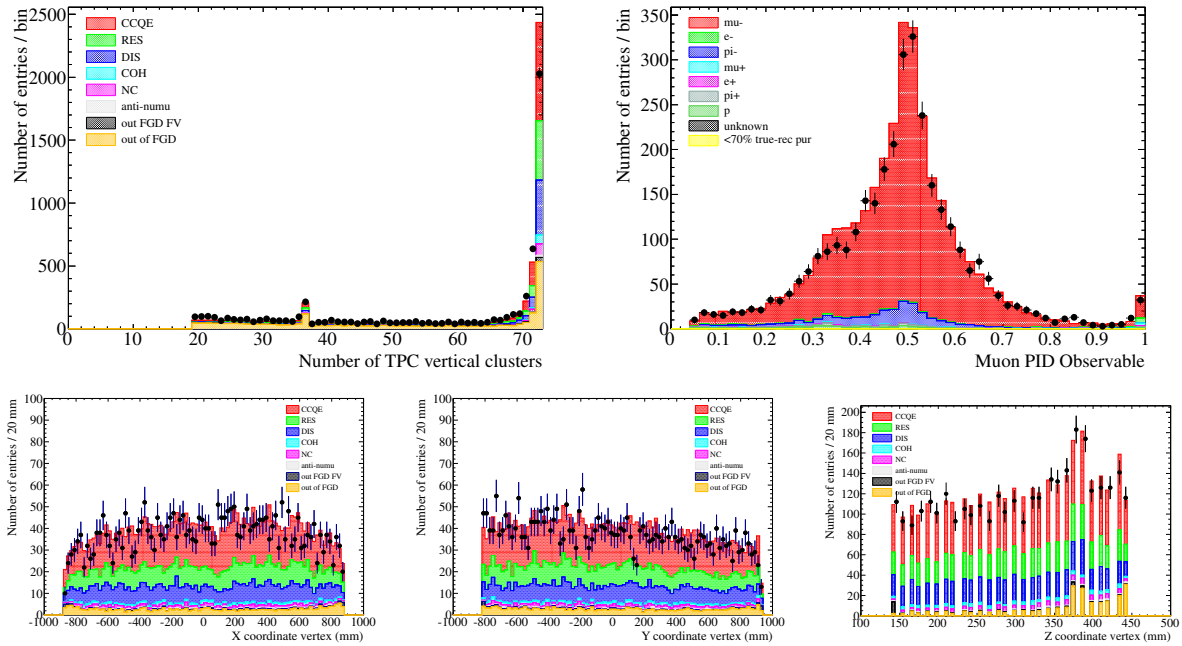

Figure 5.13: Data-MC comparison for run II. Top: number of TPC vertical cluster (left) and $\mathcal{L}_\mu$ (right). Bottom: starting position of the muon candidate track (X, Y, Z). Similar results are obtained for run I (see [145]).

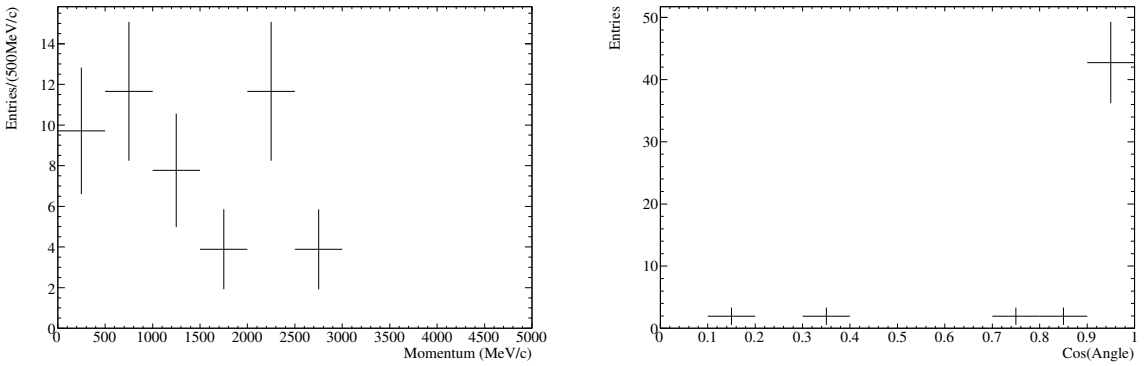

Figure 5.14: Momentum (left) and angular (right) distributions of the selected sand muons normalized to data.

Fig. 5.14 shows the selected sand muons normalized to the data accumulated for Run I and Run II. As we will see in Table 5.8, they constitute a small fraction of the background $\sim 1\%$. This background is, however, not negligible. As we are considering them separately to the interactions in the magnet, an additional inefficiency has to be taken into account. The TPC veto cut implies that an event that contains a high momentum muon crossing the P0D is not selected. This can happen if we have a sand muon interaction. If this is the case and we also have a CC interaction in FGD1, the event is rejected for data. On the contrary, it can not be done in MC, as the simulation of neutrino interactions in the sand and in the magnet are separated. Therefore an additional inefficiency has to be taken into account in the MC (see Sec. 5.7).

5.7 Event pile-up

Since sand muons are not simulated in the standard MC, the inefficiency coming from their pile-up with the interactions inside the magnet needs to be taken into account in the MC. We use the sand interaction MC simulation described in the internal note T2K-TN-77 [135] for this purpose. We compute the probability of finding a track in TPC1 per bunch, and use this probability to correct the MC efficiency. The numbers are shown in Table 5.4. There is no number of spills available for the sand muons, and, we have estimated it based on the number of spills in Run I and Run II in relation to the numbers of accumulated proton on target. The probability of TPC1 track events in the data is larger than in the MC as it is expected from the additional contribution of sand muons. The MC efficiency has to be reduced by 0.43% in Run I and 0.78% in Run II. Practically, this corresponds of applying a weight to the number of events selected. The weight being the *pile-up inefficiency* of 99.57 % and 99.22 % for Run I and Run II respectively.

The event selection presented in Sec. 5.5 supposes that we have only one event per bunch. The probability to have overlapping events in the same bunch can be computed from the number of events that pass the first three cuts over the total number of bunches. The probability is then given as the square of the number of good negatively charged track in the fiducial volume per bunch. We conclude from Table 5.4 that these probabilities are of the order of $\sim 10^{-7}$ and are therefore negligible.

Table 5.4: Number of events per bunch for the different run periods. The column labelled TPC1 track events per bunch (evts/b.) show the probability to have a TPC1 track event in a bunch. Those events are rejected by the selection. The number of selected events in FGD1 are the number of events with a good negatively charged reconstructed tracks. The last column is the number of FGD1 interactions per bunch (evts/b.).

Sample	Run	POT	Spills	Bunch	TPC1 events	TPC1 evts/b.	FGD1 events	FGD1 evts/b.
Data	I	2.939×10^{19}	912411	6	53700	0.98 %	2479	0.04 %
	II	7.857×10^{19}	1023805	8	138350	1.7 %	6358	0.08 %
NEUT	I	5.45×10^{20}	14589000	6	445151	0.51 %	-	-
	II	11.05×10^{20}	163898000	8	932523	0.71 %	-	-
Sand Muons	I	7×10^{19}	2173161	6	57007	0.43 %	-	-
	II	7×10^{19}	912149	8	57007	0.78 %	-	-

5.8 Performance

In this section, all the results will be shown including the sand muons interactions and correcting for their pile-up. Table 5.5 shows the number of selected events for data and the two generators, for the various cut. Table 5.6 shows the resulting inclusive charged current efficiency and purity.

Table 5.5: Number of selected events for the different cuts. Reweighted correction due to the magnetic field distortions, sand muons and inefficiency due to the pile-up events of sand muons with interactions in the FGD are taken into account.

Cut	Data		NEUT		GENIE	
	Run 1	Run 2	Run 1	Run 2	Run 1	Run 2
Good negative track in FV	2479	6358	2449.73	6449.47	2368.20	6305.21
Upstream TPC veto	1741	4502	1806.55	4775.85	1735.77	4615.45
PID cut	1202	3283	1265.58	3457.92	1216.87	3319.13
Total after CC selection	4485		4723.5		4536.1	

Table 5.6: Charged current efficiency, ϵ, and purity, $\mathcal{P}$, obtained using NEUT and GENIE MC. Reweighted correction due to the magnetic field distortions, sand muons and inefficiency due to the pile-up events of sand muons with interactions in the FGD are taken into account.

Cut	NEUT		GENIE	
	ϵ (%)	$\mathcal{P}$ (%)	ϵ (%)	$\mathcal{P}$ (%)
Good negative track in FV	56.8	52.7	58.3	51.1
Upstream TPC veto	54.4	68.4	56.2	67.4
PID cut	49.5	86.8	51.2	85.9

Tables 5.7 and 5.8 give the composition of the CC-inclusive signal and background respectively. We see that the main background is coming from interactions outside the FGD1 fiducial volume, where 1 % is due to the sand muons, 1% is coming directly from the FGD1 outside fiducial volume and 7 % from the rest the detector. From these tables, we see that the two generators do not simulate same proportions of coherent and quasi-elastic interactions. The proportions are, however, of the same order of magnitude.

Table 5.7: Composition of the CC-inclusive signal, where the CC-other channel contains mainly multi-pions and deep inelastic scattering (see Table 6.4 for precision). The fractions are obtained for the NEUT generator for Run I and Run II MCs together, where the sand muons are also taken into account.

Process	Signal composition (%)	
	NEUT	GENIE
CCQE	44.3 ± 0.7	41.4 ± 0.7
CC-1π	21.0 ± 0.6	22.9 ± 0.6
CC-COH	2.8 ± 0.2	0.9 ± 0.1
CC-other	18.7 ± 0.6	20.7 ± 0.6

Table 5.8: Background composition of the CC-inclusive selection obtained taking into account the sand muon interactions. Since electron antineutrinos are almost negligible in comparison to the muon antineutrinos they are put on bracket in the table.

Type	Background composition (%)	
	NEUT	GENIE
Outside FV but in FGD1	0.94 ± 0.14	0.91 ± 0.14
Outside FV but in FGD2	0.07 ± 0.04	0.08 ± 0.04
Outside FGDs (in Magnet)	7.05 ± 0.37	7.20 ± 0.38
Outside Magnet (sand muons)	1.04 ± 0.15	1.08 ± 0.15
Neutral Currents in FV	3.17 ± 0.26	3.59 ± 0.28
CCν_e in FV	0.27 ± 0.08	0.26 ± 0.08
$\bar{\nu}_{\mu,(e)}$ in FV	0.68 ± 0.12	0.71 ± 0.12
total	13.2 ± 0.5	13.8 ± 0.5

Fig. 5.15 shows the reconstructed momentum and angle of the muon using the CC-inclusive selection normalized to data POT for Run I and Run II. Data agrees well with both MCs, with maybe a better agreement for GENIE than for NEUT. Note that if we use the default flux 11a, NEUT agrees better than GENIE. The tuned flux 11b, used in this analysis, provides a priori a better representation of the flux as the kaon production cross section measurement by the NA61 experiment are taken into account in the last release of the flux. There is, still, a big uncertainty on the flux, we are therefore not able to conclude anything based on this observation.

The measured (selected) phase space in data is shown in Fig. 5.16 together with the MC. Agreement in the phase-space is reasonable between them. From Figs.5.15, 5.16 and 5.17, we see that most of the selected events are in the forward direction of the muon candidate. In particular, the tracks that are selected as backward are generally external background. From the distribution shown in Fig. 5.15, we could have cut any selected backward going track. We however decided to not do that as it represents only a 0.2 % of the selected events.

Table 5.9 shows the particle composition of the muon candidate, while Table 5.10 shows the particle composition of the muon candidate in our signal (i.e when we correctly select our event). The muon candidate is selected correctly with a purity of 89 %, 7 % of the time the muon candidate is in fact a negatively charged pion, the remaining 4 % being distributed among the other particles, where for more than 3 %, the miss-identification is due to a wrong charge identification.

96% of our CC-inclusive signal is composed of events where we correctly selected the tracks as being a muon. The remaining 4% is split into two main samples: negatively charged pions and

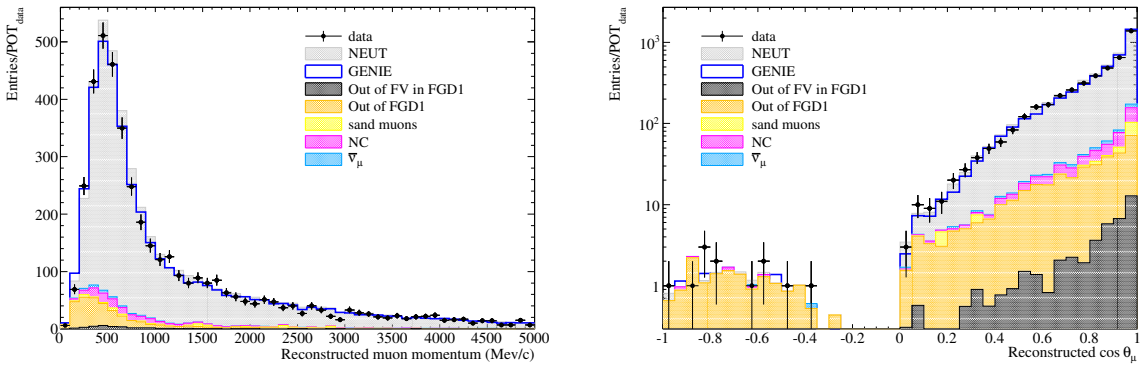

Figure 5.15: Muon momentum and angle distribution by using the tuned flux 11b3.1, applying magnetic field corrections and sand muons. The distributions are shown for Run I and Run II together.

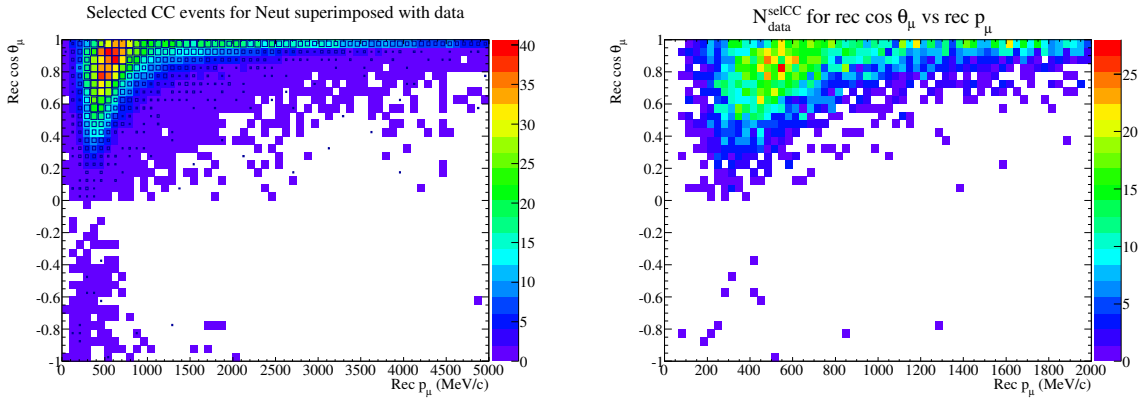

Figure 5.16: Data distribution in the $(P_\mu, \cos\theta_\mu)$ plane for Run I and II together. Left: Overview of the phase space for data and NEUT, including the backward going region. Right: zoom in the lower momentum region for data.

Table 5.9: Particle composition of the muon track candidates as predicted by the MC in the selection.

Type	Particle composition of the muon candidate (%)	
	NEUT	GENIE
μ^-	88.60 ± 0. 0.46	87.65 ± 0.49
μ^+	0.44 ± 0.10	0.57 ± 0.11
e^-	1.23 ± 0.16	1.28 ± 0.17
e^+	0.31 ± 0.08	0.35 ± 0.09
π^-	6.60 ± 0.36	6.62 ± 0.37
π^+	1.28 ± 0.16	2.00 ± 0.21
p	1.33 ± 0.17	1.27 ± 0.17

Table 5.10: Particle composition of the muon candidate in the charged current signal.

Type	Particle composition of the CC signal (%)	
	NEUT	GENIE
μ^-	96.07 ± 0.30	96.44 ± 0.30
μ^+	0.02 ± 0.02	0.03 ± 0.03
e^-	0.29 ± 0.8	0.25 ± 0.08
e^+	0.09 ± 0.05	0.09 ± 0.04
π^-	2.33 ± 0.23	1.93 ± 0.22
π^+	0.39 ± 0.13	0.49 ± 0.11
p	0.70 ± 0.13	0.67 ± 0.13

positively charged particles. Fig. 5.17 shows the number of simulated CC-inclusive interactions in FGD1 together with its signal. We see, in particular, the portion of the signal that has been selected by miss-selecting as a muon another particle. In particular, the little backward efficiency that we can see in Figs. 5.18, 5.19 is due mainly to the selection of forward negatively charged pion, while the muon was going backwards.

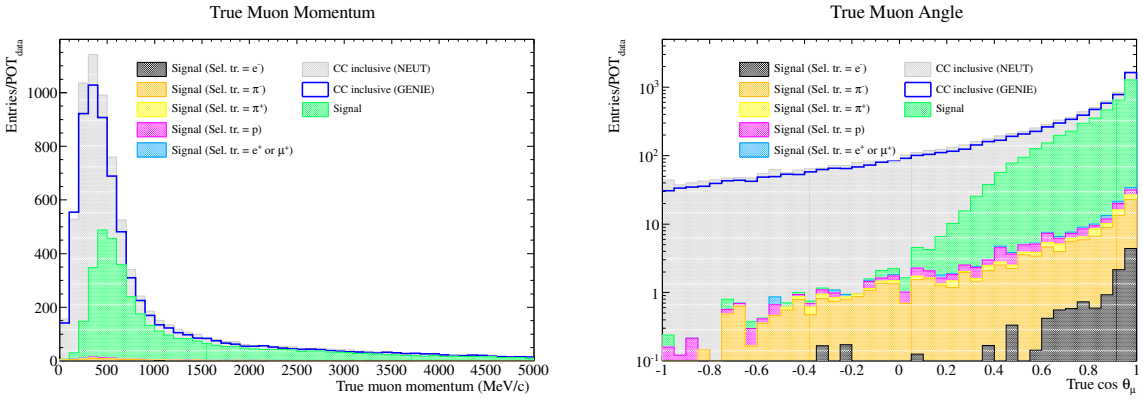

Figure 5.17: True Muon momentum and angle distribution by using the tuned flux 11b, applying magnetic field corrections. The distribution is normalized to the data POT.

Figs. 5.20 and 5.21 shows the purity as a function of the reconstructed and true muon kinematic variables. The very low purity at backward going angle comes from two reasons. The recon-

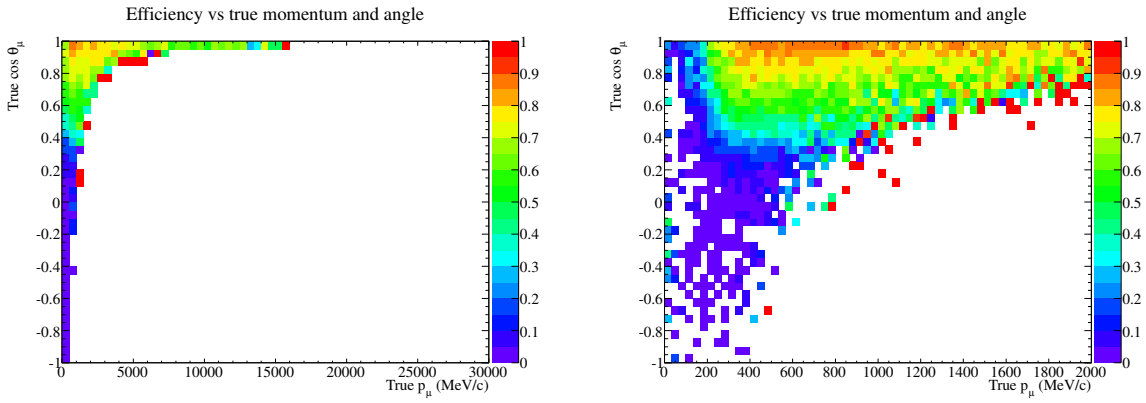

Figure 5.18: Efficiency as a function of the true muon kinematics.

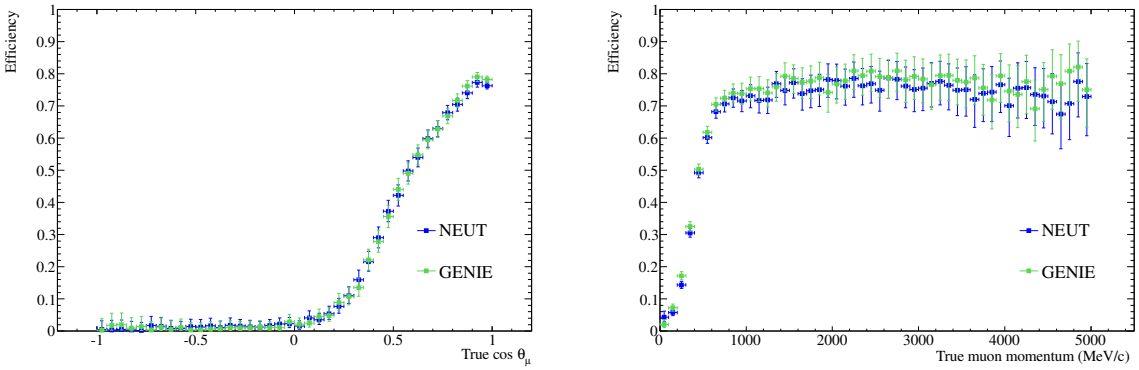

Figure 5.19: Efficiency as a function of the true muon angle (left) and muon momentum (right).

struction should normally not allow to flip the sense of a track unless it crosses both FGDs. However this has not been always applied correctly and some tracks have been set as backwards from timing differences between FGD and P0D. As a result, there are some tracks that are reconstructed as backward but are forward tracks starting outside the fiducial volume. At that point, we could have added an additional cut to remove these tracks. As their amount is very small, we have decided to not add an additional cut. The efficiency and purity start to be constant after 700 MeV, with a purity of more than 90 % and efficiency of more than 70 %. The purity even improves at higher energy since the muon get much better separated from the electrons via energy loss than at lower energy. In the last Chapter, the results will be shown only for the forward direction, as we have a very low sensitivity in the backward phase space.

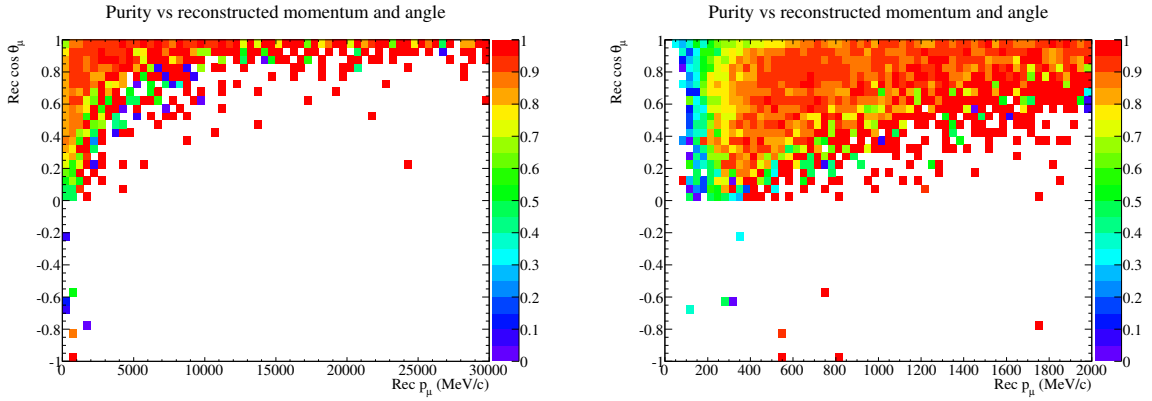

Figure 5.20: Purity as a function of the reconstructed kinematics. On the left the complete reconstructed momentum range is shown, while the right plot shows only the purity in the main momentum range.

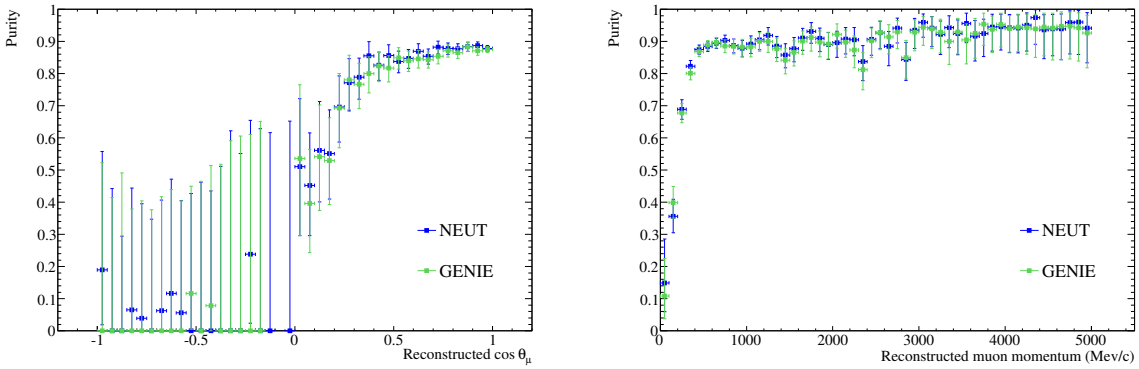

Figure 5.21: Purity as a function of the angle (left) and momentum (right) of the muon track candidate.

5.9 Summary

In this chapter, we have seen how the different variables used to select the muon neutrino charged current interactions are used. For this analysis, the main detectors are the FGDs and TPCs. The charge of the particle is obtained from the curvature of the track and the identification is done via energy loss in the TPC. The FGD gives the absolute timing t_0 needed to reconstruct the x position in the TPC and to match FGD and TPC tracks.

A charged current process is then selected by the observation of at least one negatively charged track in the fiducial volume with good quality. To avoid external background coming from the other detectors, no other tracks traversing the first TPC should be observed in the event. To understand the data better, the MC should also take into account interactions taking place outside the magnet. This is done by the sand muon MC. Because this is taken into account separately, an additional inefficiency is considered due to the pile-up they create with FGD interactions. Generally, data agrees well with MC.

Efficiency and purity is more than 70 % for forward angle and relatively high momentum. The efficiency and background will be used in the main analysis presented in this thesis, in the process of calculating the cross section.

The differences observed with the MC will be taken into account in the systematic errors that are explained in the next chapter.

Chapter 6

Systematic uncertainties

In this chapter, I present a summary of the systematic errors used to compute the final cross section result. The systematic studies have been done by many groups inside the collaboration and represent the work of more than 50 persons. Although I have not computed myself any of the systematic uncertainties that are presented in this Chapter, I have done various investigations for many of the detector-related uncertainties.

Systematic error sources can be separated into 3 different categories:

1. Detector uncertainties
2. Cross section modeling uncertainties
    - Uncertainties that are represented by response functions
    - Uncertainties that are based on neutrino energy
    - Uncertainties included with the detector systematic errors (e.g. Final State Interactions (FSI))
3. Beam flux uncertainties

The parameterization of the systematic errors is based on the one developed for the latest T2K oscillation analysis. It was developed done by the muon neutrino working group, the neutrino interaction working group (NIWG) and the beam group.

For each source of systematic errors, a fractional covariance matrix has been computed by the several groups inside the collaboration. To constrain the oscillation analysis fit, and give the possibility to use different channels in addition to the CC-inclusive, the covariance matrix of the detector and FSI is given in 40 bins. The first 20 bins correspond to the CCQE-like selection and the last 20 bins to the CCnQE-like selection (see Sec.5.5). The various binnings are described in Sec. 6.1.

6.1 Binning

While the final differential cross section results will be given as a function of the kinematics variable of the muon (e.g angle and momentum) with a definite binning, other binnings are used

in this analysis to propagate systematic errors (e.g neutrino energy and cross section process channels). The binning on the neutrino energy and the reconstructed muon kinematic variables has been set for all the analyses of the T2K near detector and decided in the scope of the oscillation analysis.

The $(p_\mu, \cos\theta_\mu)$ bins were chosen with one criteria in mind:

- To the greatest extent possible each (p_μ, θ_μ) bin should have at least 20 events, to prevent issues with low statistics if a χ^2 fit is attempted for the oscillation analysis.

For simplicity a single bin number is associated to the 2-dimensional $(p_\mu, \cos\theta_\mu)$ plane. In the following, the j index will always label the reconstructed bin and k the true or inferred bins. The chosen convention, for the indices j and k, is shown in Table 6.1.

Table 6.1: Muon momentum and angle binning with the correspondence to the one dimensional binning index.

$\cos\theta_\mu$	Reconstructed index number				
$[0.94, 1.]$	3	7	11	15	19
$[0.9, 0.94]$	2	6	10	14	18
$[0.84, 0.9]$	1	5	9	13	17
$[-1., 0.84]$	0	4	8	12	16
p_μ(GeV/c)	$[0, 0.4]$	$[0.4, 0.5]$	$[0.5, 0.7]$	$[0.7, 0.9]$	$[0.9, 30.0]$

The result will be shown, for a true binning that we choose different from the reconstructed binning. As we have a very low efficiency in the backward-going muons phase space, we decide to split the first angle bin, to show the influence of backward/forward going muons. The binning for the true variables is shown in Table 6.2

Table 6.2: Muon momentum and angle binning with the correspondence to the one dimensional binning index.

$\cos\theta_\mu$	True index number				
$[0.94, 1.]$	4	9	14	19	24
$[0.9, 0.94]$	3	8	13	18	23
$[0.84, 0.9]$	2	7	12	17	22
$[0., 0.84]$	1	6	11	16	21
$[-1., 0.]$	0	5	10	15	20
p_μ(GeV/c)	$[0, 0.4]$	$[0.4, 0.5]$	$[0.5, 0.7]$	$[0.7, 0.9]$	$[0.9, 30.0]$

The true neutrino energy binning has been chosen in the scope of the oscillation analysis and is shown in Table 6.3. The choice has been made with the following criteria [146]:

- The binning should be finer around the oscillation maximum
- The binning should be finer in regions contributing more to the data samples
- The flux error should not change too rapidly inside the bins
- The bins that are more highly correlated in the original flux covariance should be binned together

Table 6.3: ND280 ν_μ flux (ND5) binning index, energy range (in GeV).

index #	0	1	2	3	4	5	6	7	8	9	10
E_ν(GeV)	0-0.4	0.4-0.5	0.5-0.6	0.6-0.7	0.7-1	1-1.5	1.5-2.5	2.5-3.5	3.5-5	5-7	7-30

We regroup in different categories the different interaction modes that are shown in Table 6.4. For each category, an uncertainty is assigned as a function of the energy. We note already that the systematic error on the *CC-other* category will be evaluated via the multi-pion/DIS shape parameter that varies depending on the energy of the neutrino (see Sec. 6.3.2).

Table 6.4: Interaction modes. Each mode is assigned a bin number. Note that no distinction is done between neutrino flavors nor between neutrino and anti-neutrino interactions (hence the absolute value for the NEUT interaction modes). The third column shows the mode definitions for the case of neutrino interaction and the last column the fraction of the interaction in the CC inclusive selected sample described in Sec. 5.5.

name	category	NEUT mode	mode definition	%
CCQE	0	$\|1\|$	$\nu + n \to l^- + p$	46.8
CC-1π	1	$\|11\|, \|12\|, \|13\|$	$\nu + (p,n,n) \to l^- + (p,p,n) + (\pi^+, \pi^0, \pi^+)$	23.2
CC-COH	2	$\|16\|$	$\nu + A \to l^- + A + \pi^+$	3.0
NC-other	3	$\|33\|, \|34\|, \|36\|$	$\nu + (n,p,A) \to \nu + (p,n,A) + (\pi^-, \pi^+, \pi^0)$	0.8
		$\|38\|, \|39\|$	$\nu + (n,p) \to \nu + (n,p) + \gamma$	0.001
		$\|41\|, \|46\|$	$\nu + n/p \to \nu + n/p + (\mathrm{n}{-}\pi, \mathrm{mesons})$	3.0
		$\|42\|, \|43\|$	$\nu + (n,p) \to \nu + (n,p) + (\eta^0, \eta^0)$	0.08
		$\|44\|, \|45\|$	$\nu + (n,p) \to \nu + (\Lambda, \Lambda) + (K^0, K^+)$	0.04
		$\|51\|, \|52\|$	$\nu + (n,p) \to \nu + (n,p)$	0.1
NC-1π^0	4	$\|31\|, \|32\|$	$\nu + (n,p) \to \nu + (n,p) + \pi^0$	0.2
CC-other	5	$\|17\|, \|21\|, \|22\|$	$\nu + (n,n/p,n) \to l^- + (p,n/p,p) + (\gamma, \mathrm{n}{-}\pi, \eta^0)$	10.5
		$\|23\|, \|26\|$	$\nu + (n,n/p) \to l^- + (\Lambda, n/p) + (K^+, \mathrm{mesons})$	12.1

The separation between, NC-1π^0 and NC-other has been done only to be able to associate a correlation between this channel and M_A^{RES}. In fact M_A^{RES} has also an influence in the CC-other and NC-other channels, the correlation with these channels are for now neglected.

6.2 Detector response uncertainties

This section is based on the internal note T2K-TN-093 [145] and the included references. The work presented in this section has been done by 21 colleagues that are part of the muon neutrino working group of the T2K collaboration. As I have been working in this group and started some systematic investigations, I summarize this work with more details compared to the other sources of systematic errors.

In the following, I only explain the methodology of the detector systematic errors calculation directly related to the CC-inclusive selection. The additional systematic errors due to the migration of CCnQE-like events to CCQE-like events or vice versa are explained in detail in [145]. They take into account, for example, the track multiplicity uncertainty in the CCQE cut due to the pile up with the cosmic or sand muon background, or the Michel electron tagging

uncertainty as well as pion absorption processes that can affect the classification between QE and nQE processes.

The total covariance matrix used in this analysis includes all these effects. However, they are cancelled when merging the CCQE and CCnQE errors into a CC-inclusive systematic error by taking into account their correlations.

6.2.1 Track Quality Cut

The strategy used to determine the systematic error induced by the selection of good quality FGD-TPC global tracks, i.e. tracks with TPC and FGD constituents, is described in detail in the internal note T2K-TN-079 [147].

Three sources of uncertainties can affect the quality of a track: alignment, pattern recognition (SBCAT) and hit inefficiency. We assume that the effect on the alignment is negligible because tracks with few hits normally cross only one micromegas (MM) module (except the tracks crossing the cathode, but the contribution from this kind of tracks is expected to be small). Because there is no reason for the pattern recognition to produce different efficiency for data and MC, we assume that the dominant source of data/MC differences is due to different hit efficiency. The hit efficiency represents the ability of seeing a signal for a given particle with definite energy and momentum. It should only depend on the detector and its electronics for which the response can be different for data and MC.

The extra MC hit inefficiency needed to match the data has been computed by fitting the distribution of the number of vertical clusters (hits) in TPC2 for the data (points with error bar in Fig. 6.1 left plot) with a function that depends on the extra MC hit inefficiency itself and on the number of events in each MC bin (colored histogram in Fig.6.1 left plot). The fit has been done using only tracks traversing two MM modules because in this region the statistics is large enough to prevent from big statistical fluctuations from bin to bin.

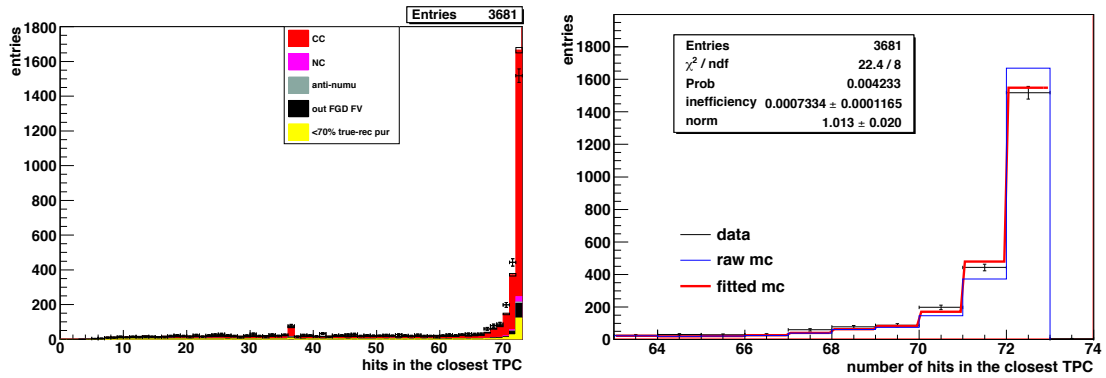

Figure 6.1: Left plot: Number of hits in the closest TPC of the muon candidate after CC selection cuts for data (points with error bars) and NEUT MC (colored histogram). No quality cut has been applied here. The color code refers to the reaction type, as explained in the legend. The spike around 36 corresponds to tracks broken in the middle of the TPC between the two MM columns, this effect appears normally at high angle tracks in the YZ plane. Right plot: Distribution of the number of hits in the closest TPC for the data (black points with error bar) and MC (blue line). The red line has been obtained by fitting the data distribution to the hit inefficiency function. All the events passing the CC selection when the quality cut is not applied have been selected.

Since the probability of losing more than two hits is negligible, it is a good approximation to consider only tracks losing one or two hits due to the extra MC hit inefficiency. The result of the fit, using the hit distribution of the muon candidate after the CC-inclusive selection and assuming that the hit inefficiency is a factor $\beta = 10$ larger at the MMs edges is shown in Fig. 6.1 right plot. It is worth noting that the agreement between data and MC is much better when the extra inefficiency is introduced in the MC (red line). The value obtained in this way for the extra MC hit inefficiency is 0.0007 ± 0.0001. This parameter has been computed for different TPCs, spatial regions and angles, and for different values of the factor β (from 1 to 100) and in all cases the extra MC hit inefficiency is found to be smaller than 0.001.

The number of hits on each track is multiplied by a random number following a normal distribution with mean corresponding to the hit efficiency and sigma corresponding to its error. As a result, tracks with more than 18 hits are randomly discarded, and tracks with less than 18 hits are randomly accepted. The fractional covariance matrix is then given as the average of 500 trials:

$$V_{jj'}^{qua} = \frac{1}{500} \sum_{s=1}^{500} \frac{\Delta_j^s \Delta_{j'}^s}{N_{r_j}^{sel,nom} N_{r_{j'}}^{sel,nom}} \tag{6.1}$$

where $\Delta_j^s = N_{r_j}^{sel,nom} - N_{r_j}^{sel,s}$ is the difference of the number of selected events between the nominal MC and the hit efficiency corrected MC for the s-th trial and j the reconstructed p-θ bin[1].

6.2.2 TPC track efficiency

TPC tracking efficiency

Track-finding efficiency refers to the efficiency for the TPC reconstruction algorithm to successfully reconstruct a TPC track. The efficiency for finding tracks was estimated as a function of track length, momentum, and angle using muon-like tracks induced by neutrino interactions. These include tracks produced in the P0D as well as tracks in the tracker (FGD and tracker walls). The difference in the track-finding efficiency between data and MC has been estimated, and cross-checked with a visual scanning. The internal note T2K-TN-075 [148] contains the result and details of this study.

These studies find very little differences in the track-finding efficiency between data and MC, which was not the case for the 2010a oscillation analysis. The improvements are due to many upgrades in both the MC simulation and the reconstruction algorithms themselves. The typical values of the track-finding efficiency range is about 97-99 %, depending on the track length, momentum, or angle. The largest data-MC difference seen is 0.5 %. This last value is chosen as the systematic uncertainty on the efficiency for finding a track. To be conservative, this uncertainty is considered to be 100 % correlated between momentum and angle bins.

The propagation of the uncertainty is done using a reweighting method to determine the change of the number of selected events in all 40 bins, if 0.5 % of all tracks is randomly dropped. The algorithm is:

[1]The label r_j is used here and in the following to specify that we look at the *reconstructed* bin j. This notation will be extensively used in the next chapters where we distinguish reconstructed and true bins.

- Let k represent the number of tracks, and p=0.5 % is the probability for a track to be lost. The probability that none of the track in the event is dropped is, $p_0(k) = (1-p)^k \sim 1 - kp - k(k-1)p^2$
- Loop over each event. Depending on the number of track in the event, increment the number of event selected by $p_0(k)$ in the nominal bin (e.g bin defined by the CC selection without any change).
- Loop over each track. Consider loosing this track in the event and test if the resulting event still passes the selection cut. If it does, then add the probability, p, to the new bin defined by the new track selected as the muon candidate.
- Similarly, for each pair of tracks in the event, consider losing both tracks and seeing if it passes the selection cut. If it does, then add the probability, p^2, to the new bin in which the event falls into.

The procedure could continue by considering losing 3 tracks together, and so on. As the probability p is very small, we can truncate the procedure after considering losing up to two tracks. With this procedure, we obtain in each reconstructed bin a reweighted number of selected events in the reconstructed bin j, $N_{r_j}^{sel,\mathrm{rw}}$. Defining $\Delta_j = N_{r_j}^{sel,\mathrm{nom}} - N_{r_j}^{sel,\mathrm{rw}}$, the covariance matrix is then given as:

$$V_{ij}^{match,-} = \frac{\Delta_j \Delta_i}{N_{r_j}^{sel,\mathrm{nom}} N_{r_i}^{sel,\mathrm{nom}}} \tag{6.2}$$

where $N_{r_j}^{sel,\mathrm{nom}}$ is the default number of MC events selected in the reconstructed bin r_j.

Note that we only consider the effects of losing tracks. There is no mechanism for calculating what happens to events if an extra tracks that failed to reconstruct originally are added back in. For the purposes of this analysis, we calculate a new Δ_i, where $N_{r_j}^{sel,\mathrm{rw}}$ is obtained by changing $(1-p) \to (1+p)$ in the previous calculation. In this case, we assume the probability of getting back a track of the same magnitude than the probability of loosing a track. The fractional covariance matrix is then $V_{jj'}^{match,+}$ and the total fractional covariance matrix is given by,

$$V^{match} = \frac{1}{2}(V^{match,-} + V^{match,+}). \tag{6.3}$$

TPC "broken track" inefficiency

Sometimes a single particle can produce two TPC tracks. There is a probability that both of these TPC tracks are matched to some FGD hits, and survive in the final reconstructed track collection as two distinct tracks instead of a single track causing a migration of true CCQE events to the CCnQE-like selection.

By eye-scanning [148], two main causes for this are identified:

- TPC pattern recognition program (SBCAT) failing to match tracks that span a natural boundary with absence of hits (tracks crossing the central cathode or a micromegas boundary).
- SBCAT getting "confused" by multiple particles crossing many neighboring pads of a micromegas (delta rays or high-multiplicity events).

The difficulty, in measuring these effects and assigning a systematic error to it, arises from the fact that the migration described above has never been observed in an event of the final CCQE-like selection, and so, it has to be inferred from a different pool of events. Therefore, two sets of cuts are derived.

- General cuts: These are cuts designed to contain the maximum possible number of broken tracks.
- Specialized cuts: These are much more restrictive cuts, designed to separate the rare effect of the broken TPC tracks within the above-selected sample.

The broken track efficiency of the inclusive sample is defined as,

$$\tilde{\epsilon}_{break} = \epsilon_{break} \cdot \gamma_{CC}, \qquad \text{where } \gamma_{CC} = \frac{N_{sel,\text{gene}}}{N_{sel,\text{CC}}}. \tag{6.4}$$

where ϵ_{break} is the efficiency of selecting broken tracks with the specialized cut inside the generalized sample, and γ_{CC} is the fraction of events passing the generalized cuts in the nominal CC-inclusive sample of Sec. 5.5. Following this method, we obtain,

$$\tilde{\epsilon}^{Data}_{break} = 0.007,\ \tilde{\epsilon}^{MC}_{break} = 0.001. \tag{6.5}$$

Due to the small statistic of the selection, only an overall correction is calculated and no attempt is done to calculate the effect in (p_μ, θ_μ). The migration between CCQE-like and CCnQE-like is done by defining,

$$N^{sel,corr}_{r_j} = \kappa_j(\tilde{\epsilon}^{data}_{break} - \tilde{\epsilon}^{MC}_{break})N^{selCC,nom} \tag{6.6}$$

where κ_j is the fraction of CCQE-like of CCnQE-like events in the reconstructed bin j in the inclusive sample. Using $\Delta_j = N^{sel,\text{nom}}_{r_j} - N^{sel,corr}_{r_j}$, the covariance matrix is then given by,

$$V^{brk}_{jj'} = \frac{\Delta_j \Delta_{j'}}{N^{sel,\text{nom}}_{r_j} N^{sel,\text{nom}}_{r_{j'}}} \tag{6.7}$$

where $N^{sel,\text{nom}}_{r_j}$ is the default number of MC events selected in the reconstructed bin r_j.

6.2.3 TPC Particle IDentification (PID)

The PID systematics is obtained by comparing data and Monte Carlo prediction for high purity sample of events containing muons. This sample is selected by requiring the existence of a reconstructed track starting in the P0D and crossing the 3 TPC with a minimum of 18 vertical clusters in each TPC.

The pull under the muon hypothesis (see Eq. 5.4) of the track is compared for data and MC. The width of the pull is compared between data and Monte Carlo for each TPC and run period independently. The MC distributions are found slightly narrower than in data and the difference between data and MC is found stable (see the internal note T2K-TN-078 [149]).

Therefore an overall correction is applied to the MC to reproduce the data by applying an additional Gaussian smearing event by event. This correction has been computed to be of the order of 5 %. With this additional smearing, a new number of selected events is obtained and compared to the nominal one for each of the 40 bins, computing in this way the fractional covariance matrix that takes the same form as Eq. 6.7.

6.2.4 TPC momentum scale systematics

The systematic uncertainty on the TPC momentum scale comes mainly from our ability to know the scale of our magnetic field. The relation between the momentum and the magnetic field is given by,

$$p_T = \frac{0.3B}{\rho} \tag{6.8}$$

where p_T is the transverse momentum of the particle is given in MeV, B the magnetic field in Tesla and ρ the in inverse of the radius in mm^{-1}, e.g the curvature. The TPC momentum scale systematic error can be separated into two contributions:

1. **Mean magnetic field**
   It corresponds to the uncertainty on the measurement of the magnetic field, B.
2. **Field distortions**
   It corresponds to the uncertainty due to the magnetic and electric field distortion on the observed curvature after drifting of the electrons inside the TPC.

Mean magnetic field uncertainty

The uncertainty for the first category comes from a serie of measurements made in September 2009. It consists of:

- Magnetic field measurement in the tracker region at a coil current of 1000 A (3D grid with 5 cm distance).
- 10 cm distance measurement for different coil current up to 1000 A.
- 2 dedicated ramp-ups up to 2600 A and 2900 A in April and November 2010 respectively.

When ramping up the magnet, a non-linear behavior between the current in the magnet coils and the measured magnetic field is observed. At higher field values a saturation of the ND280 iron yoke decreases the magnetic field. In a first order approximation, the following quadratic function is used to fit the measurement,

$$B[G] = c_0 + c_1 I(1 + c_2 I) \tag{6.9}$$

where the c_i are the parameters of the fit and I is the current. The c_2 parameter only depends on the magnetization features of the iron yokes. The systematic errors on the mean magnetic field measurement can be divided into three categories.

- **Resolution**: it is the combination of the intrinsic resolution of the Hall probes and the error of the offset correction, both errors are added in quadrature.
- **Misalignment**: uncertainties of the skewing of the mapping device with the mapping device reference frame, the remaining error on the misalignment between the probes, and finally the uncertainty of the survey, which connects the mapping device reference frame with the ND280, reference frame. All the three effects are added in quadrature. Note that this type of error scales linearly with an increasing B-field value.

- **Non-linearities**: it is due to the uncertainty of the magnet yoke properties, which are responsible for the quadratic term in Eq. 6.9

For the main component B_x the non-linearities of the B-field are the main source of uncertainty, whereas for the transverse component (B_y, B_z) the misalignment of the probes with respect to the main B-field direction dominates the systematic error. The error on the B_x component is about $\sim 0.5\%$, while the error on the transverse component of the magnetic field is ~ 1.3 G.

The covariance matrix is obtained varying the magnet field scale according to the errors in [150]. The MC is then reweighted 500 times by smearing the magnetic field with a Gaussian distribution with mean 1 and sigma corresponding to the systematic error. The effect of the magnet field scale varation generates migrations in the momentum bins of the reconstructed muon track candidate. The fractional covariance matrix is then given by the RMS between the different reweighted MC and the nominal one, and takes the same form as Eq. 6.1,

$$V_{jj'}^{qua} = \frac{1}{500} \sum_{s=1}^{500} \frac{\Delta_j^s \Delta_{j'}^s}{N_{r_j}^{sel,nom} N_{r'_j}^{sel,nom}} \tag{6.10}$$

where $\Delta_j^s = N_{r_j}^{sel,nom} - N_{r_j}^{sel,s}$ is the difference of the number of selected events between the nominal MC and the reweighted MC for the s-th trial.

Field distortions

Particles entering a TPC create a cloud of primary ionization. Electrons from the ionization drift along the direction of the electric field lines towards the detector readout plane. In an ideal TPC the magnetic and electric fields orientated parallel to each other and drift electrons experience no deflection in directions transverse to the drift direction. However due to imperfections in the magnetic and electric fields, the path of the drift electrons can be distorted. Deflections in the transverse plane that occur while the electrons are drifting can distort the shape of the track so that the image of the track at the readout plane has a different shape than that of the original track. The distortion of the track shape can then lead to a bias in the reconstructed momentum of the track.

Distortions caused by the inhomogeneities in the electric and magnetic fields are calibrated out with the TPC photoelectron calibration system and MC simulation is used to drift the electrons. For all 3 TPCs the MC simulation reproduces the main features of the target displacements, but in some regions there are significant differences in the direction and magnitude. These differences are interpreted as being due to differences between the real magnetic field and the field assumed in the measured field map. For this reason, an empirical correction to the measured field simulation is needed. The empirical correction consists of the application of additional distortions, inferred from the difference in the data and MC positions of the laser calibration targets. The basic approach is to reconstruct the data three times:

- assuming a perfect field
- assuming the measured field map and empirical corrections inferred from laser calibration data.
- using the field map, but turning off the empirical corrections.

The difference between the first and the second configuration gives the correction that we apply to the MC to account for the non-uniformities, while the difference between the second and third is taken to be the uncertainty on the momentum reconstruction.

The fractional covariance matrix take the same form as Eq. 6.7, where $N_{r_j}^{sel,\mathrm{nom}}$ contains all the corrections (the field map measurement information and the empirical corrections) and Δ_j the difference between the second and the third configuration.

6.2.5 TPC momentum resolution

The internal technical note T2K-TN-095 [151] describes the study of single TPC momentum resolution performed using tracks that cross multiple TPCs. The use of tracks crossing at least 2 TPCs allows to compute the difference of the reconstructed momentum of each TPC segment of the same global track. Using the inverse of the transverse momentum to the magnetic field, $1/p_T$, the distribution of this difference is approximately Gaussian, with mean related to the average energy loss in the intermediate FGD. For different p_T ranges, this distribution can be fitted to a Gaussian function in order to obtain the standard deviation,

$$\sigma\left(\Delta\frac{1}{p_T^{rec}}\right)_{ij} = \sigma\left(\left[\frac{1}{p_{T,i}^{rec}} - \frac{1}{p_{T,j}^{rec}}\right]\right) \tag{6.11}$$

where $i \neq j$ label the TPCs. The standard deviation contains different contributions:

- The energy loss and multiple scattering in the intermediate FGD
- The momentum resolutions of each TPC
- The correlations between both contributions

The systematic error is obtained by smearing the MC distribution of $\sigma\left(\Delta\frac{1}{p_T^{rec}}\right)$ event-by-event until MC and data coincide. In practice, the analysis is repeated for different smearing values and χ^2 minimization is performed. The χ^2 minimization will result in the central value of the additional smearing, which can be considered as a correction, while the standard deviation on the correction will be derived from the χ^2 variation around the minimum.

The additional smearing is found for TPC2 to be,

$$\delta\sigma_{1/p_T} = (2.5 \pm 0.5) \times 10^{-5}(c/MeV) \tag{6.12}$$

where the resolution for TPC2 is found to be $\sim 8 \times 10^{-5}(c/MeV)$. The systematic error is applied as an additional Gaussian smearing to the reconstructed momentum of the MC sample and the covariance matrix takes the form of Eq. 6.7.

6.2.6 TPC-FGD matching inefficiency

An event will only be correctly associated to the fiducial volume if the reconstructed TPC track is matched to the corresponding FGD hits. While the systematic uncertainties described in Sec. 6.2.2 and 6.2.2 represent failures to correctly reconstruct TPC tracks, in this section we consider the loss in efficiency from a failure of the matching between the TPC track and the FGD hits. This systematics is described in more detail in the internal note T2K-TN-075 [148]. A track may fail to associate with FGD hits for various reasons:

- If the track was miss-reconstructed, it is possible that the extrapolated track may simply miss the FGD hits.

- An error in the t_0 calculation used to determine the x coordinates of the TPC hits would also cause a track to be shifted in x and possibly miss the hits.

Using a combination of beam and cosmic ray tracks the FGD-TPC track matching efficiency has been estimated for both data and MC. These samples are estimated to always contain TPC2 tracks and FGD1 hits. The fraction of the events that has not been reconstructed correctly constitute the inefficiency.

Sufficient cosmic ray statistics were available to allow this to be calculated as a function of the muon track's momentum and angle.

Table 6.5: The FGD1-TPC2 tracking matching efficiency error, $\delta\epsilon_k$ for (momentum, angle) bin k [148].

Bin #	$\delta\epsilon_k$ (%)	Bin #	$\delta\epsilon_k$ (%)
0	±0.41	10	±0.90
1	±0.95	11	±0.33
2	±0.29	12	±0.61
3	±0.34	13	±1.25
4	±1.12	14	±0.47
5	±2.00	15	±0.27
6	±0.85	16	±0.32
7	±0.40	17	±0.79
8	±0.73	18	±0.46
9	±0.25	19	±0.21

Table 6.5 shows the uncertainty on matching a TPC track to the FGD hits for each (momentum, angle) bin. Each uncertainty has been calculated independently unlike Sec. 6.2.2.

For the propagation of the error through the final result, we can only remove tracks. We assume that the effect will be symmetric for the case of an increase of efficiency. For simplicity, the case of loosing two tracks at once in the same events is neglected. The propagation is done independently for each bin k:

- Add (1-$\delta\epsilon_k$), each time the track selected as the muon candidate is reconstructed with momentum and angle corresponding to the bin k.

- Consider removing this track. Check if another track can be selected as the muon candidate and get its reconstructed momentum and angle corresponding to the bin j. Increment the number of event in the bin j by $\delta\epsilon_k$.

For each bin k, we get a fractional covariance matrix that is added in quadrature to the rest. Each fractional covariance matrix is defined as the difference between the new estimates of the number of events in each bin with the nominal prediction. The fractional covariance matrix is then obtained in a similar way as Eqs. 6.2 and 6.3.

6.2.7 Fiducial mass

If the material density in FGD1 is different in the Monte Carlo from reality, this will result in a normalization error in the number of simulated neutrino interactions. The internal note T2K-TN-091 describes the measurements and calculation of the density of the FGD XY scintillator modules [152]. This note concluded that the uncertainty on the total FGD XY module mass was $\sigma = 0.67\%$.

Checks of the FGD geometry as implemented in the Monte Carlo indicate that the simulated mass of the active region of FGD1 differs by only 0.09% from the amount recommended in T2K-TN-091. Therefore, no re-scaling of the MC output has been done to account for different detector density. Note that there are actually two known mistakes in the FGD mass simulation for Production 4:

1. The scintillator density for the FGD was incorrectly set to 1.05 instead of the correct value of 1.032 g/cm^3.
2. The density of the glue used to bond the XY modules together was incorrectly set to 0.92 instead of the intended value of 1.365 g/cm^3, the value listed in T2K-TN-091 of 0.92 mistakenly is the density of the adhesive before curing, not after.

Miraculously, these two mistakes almost exactly cancel each other in the total mass calculation. While there may be a very small error in the relative elemental abundances from what amounts to a substitution of scintillator mass for glue mass, this is believed to be negligible for the present analysis.

In conclusion, a 0.67% systematic error is taken on the overall FGD1 density. This takes the form of an overall normalization uncertainty for all events originating in FGD1. Reweighting each event with this uncertainty (multiplying by $1 \pm \sigma$ each event) a new number of events selected is found for each bin that is compared to the nominal value. The fractional covariance matrix is then given by Eqs. 6.2 and 6.3.

6.2.8 Charge miss-identification

The wrong identification of the sign of charged particle and its resulting systematic uncertainty are discussed in this section. The details of this study can be found in the internal note T2K-TN-048 [153]. The main aim of this analysis is to estimate the number of reconstruction failures when trying to calculate the charges of the particles. The systematic study chosen use global tracks with 2 or 3 TPC objects. The tracks are selected as starting in the fiducial volume of the P0D and having more than 40 hits in each TPC.

To compute the systematic error, the probability that each TPC segment of the global track has the same reconstructed charge, P_{same} is computed. From it, the charge confusion probability, P_{wrong}, can be expressed. The difference in charge confusion between TPC2 and TPC3 can be obtained by assuming that the charge confusion in TPC1 and TPC2 is the same.

The results for TPC2 is shown in Table 6.6, where we see that the charge confusion is less than 2% for almost all tracks of interest in the analysis ($< 2.6GeV$).

These results are cross-checked by using a selection of high purity sample of protons, by looking at how many times they are reconstructed with negative charge.

Table 6.6: Charge confusion for data and MC for long track, with at least 40 hits [145] in the TPC2

Charge confusion probability (%)	Track momentum				
	0-1.3 GeV	1.3-2.6 GeV	2.6-4.0 GeV	4.0-5.3 GeV	$>$ 5.3 GeV
MC	0.75 $\pm$0.20	1.8 $\pm$0.6	2.1 $\pm$1.2	6.0 $\pm$3.0	10.5 $\pm$2.4
Data	0.55 $\pm$0.09	2.1 $\pm$0.3	5.1 $\pm$0.8	5.4 $\pm$1.2	13.0 $\pm$1.8

The covariance matrix is computed by changing the charge of all tracks in an event according to the errors in Table 6.6. 500 Monte Carlo experiments are performed, each one with a variation of the charge probability confusion per momentum bin following Gaussian distribution. The width of the Gaussian is computed as the quadratic average of the MC to Data difference and their statistical errors. For each new Monte Carlo, the charge of the track is randomly swapped according to the charge confusion probability. The fractional covariance matrix takes then the same form as Eq. 6.1.

6.2.9 Backgrounds

This section separates the background into its different sources. For each source, a systematic uncertainty is calculated.

Cosmic rays

Cosmic rays that pass through the detector coincident with beam spills can contribute to the background of the final CC-inclusive sample. This background has been studied using a dedicated ND280 cosmic ray Monte Carlo sample, as well as "empty" spill triggers in which the proton beam was not sent to the neutrino target, as described in the internal note T2K-TN-112 [154].

The MC and data rates are calculated as the number of tracks divided by the corresponding integrated time. For the data, this is a known value, however for the MC, the integrated time can be calculated in two different ways that give similar but not identical results [154]. Depending on the method, the duration is 169 (or 134 seconds), while the integrated time of the data sample is 0.93 seconds.

The standard CC-inclusive cuts are applied to both the cosmic MC sample and the empty spill data sample. The rate predicted by MC simulation is in the range from 0.47 $\pm$ 0.05 to 0.59 $\pm$ 0.07 Hz, and no track passed the cuts in empty spill data.

After the TPC quality cut, the rate in data is 1.4-1.7 times the Monte Carlo rate. By applying this factor to the MC event rate, and assuming the efficiency at the last cut is as predicted by the MC, the predicted rate of events passing the standard CC-inclusive cuts in the data is 0.79 $\pm$ 0.11 Hz.

The integrated data time for Run I and II (sum of all time widows) is 2.16 s (0.73 s and 1.43 s for Run I and II respectively). Applying the rate of CC-inclusive events yields to a background prediction of 1.72 $\pm$ 0.25 events in FGD1 over the entire period. This level of contamination is small enough that it can be safely neglected.

Sand interactions

As already seen in Sec. 5.2, the default Monte Carlo simulation used for ND280 contains only interactions that occur within the magnet. This section tries to evaluate the systematic error related to the presence of interactions outside of the magnet (sand muons interactions).

The number of POT for sand muons interaction is 55 % of the data POT. After the CC-inclusive cuts were applied 28 events survived. When scaled to the data POT, this gives 51 CC-inclusive events, which represents a $\sim$ 1 % of the final selected sample as was shown in Table 5.8.

The expected contribution from sand interactions can be verified by the comparison of the absolute rate per POT observed in Monte Carlo and data. To perform such analysis, tracks entering through the front wall of P0D were selected. The number of accepted tracks seen in data should be equal to the sum of two Monte Carlo simulations: the simulation of the sand interactions and the simulations of the interactions inside the detector but upstream the front wall of the P0D.

The event rate for the sand muon MC is found to be 171.44 tracks/10^{17} POT, while the default magnet MC rate is 32.78 tracks/10^{17} POT. The rate measured in the data was 229.81 tracks/10^{17} POT. If the entire data/MC discrepancy is attributed to the sand interaction MC, this corresponds to a 15% systematic uncertainty in the predicted rate of sand interactions entering the CC-inclusive sample.

The fractional covariance matrix is obtained by varying the number of sand interactions by 15 %,

$$V_{jj'}^{sand} = \frac{0.15 N_j^{sel,sand} 0.15 N_{j'}^{sel,sand}}{N_j^{sel,nom} N_{j'}^{sel,nom}} \tag{6.13}$$

where $N_j^{sel,nom}$ is the number of selected events predicted by the MC where we take into account all the different corrections done to the MC.

Out-of-fiducial volume (OOFV) background

Events caused by neutrino interactions outside of the FGD fiducial volume compose $\sim$8% of the events in the final selected sample (see Table 5.8). This background is caused by several different physical processes, each with a separate systematic uncertainty to be evaluated. The details of these studies can be found in the internal note T2K-TN-098 [155]. This section provides a summary of the various background components, along with a brief description of how the uncertainty on each component was determined. There are two kind of uncertainties related to the OOFV background.

- **Cross-section, rate systematic uncertainty**
  - **Particles that originate outside of the tracker** are assigned a 20% systematic error due to the uncertainty in the rate of production of these particles. This outside-the-tracker region is largely composed of heavier elements such as Fe and Pb, and for this analysis, no cross section uncertainties are being assigned to these materials. Hence, the uncertainty in these backgrounds must be assigned directly as a detector systematic error. The NEUT and GENIE event generators disagree at the level of

20% on the rate of interactions outside the tracker, and studies of event rates in outside-the-tracker detectors such as the SMRD, P0D, and ECAL all yield data/MC discrepancies at that level.

- **Particles that originate within the tracker** are not assigned a rate uncertainty, as these come from interactions on carbon, oxygen, and some aluminum, which are assumed to be properly treated by the cross-section modeling uncertainties in Sec. 6.3.

- **Reconstruction related systematic uncertainties** are assigned to charged particles entering the fiducial volume. Differences in the reconstruction failure rate between data and MC will then result in systematic uncertainties.

The sample of external background is divided in different categories where a rate and reconstruction-related systematic uncertainties can be applied. These categories are:

- **Neutral particles** entering the FGD, leaving no track, create secondary charged particles inside the FGD.

- **Backwards-going tracks** are events created outside the tracker, which have a backwards-going π^+ stopping in the FGD1, that has been reconstructed as a forward-going muon. It doesn't constitute a reconstruction failure but reflect the limitation of the reconstruction related to our ability to determine the direction of a track [2].

- **High angle tracks** are not well reconstructed in the 4C processing, hits are generally missing at the end of the FGD segments preventing the matching between the TPC and the FGD. It happens generally at low momentum (< 500 MeV/c). The reconstruction systematic uncertainty is obtained by observing the data/MC ratio for cosmic samples for momentum below 500 MeV/c.

- **Double-skipped layer failure** occurs when trying to match TPC2 segments to FGD1 hits. If 2 layers in a row don't have FGD hits, the matching routine gives up and the track is broken. As a result, the track appears to start inside the FGD FV, even if there are further upstream hits. This generally happens when the tracks have a direction that is nearly parallel to the beam axis and passes through the dead coating material between scintillator bars. The systematic error is computed by using sand muons and magnet muons, which were passing through TPC1, FGD1 and TPC2. From this sample, the difference between data and MC is taken as systematic error.

- **Layer 23 hit matching failures** occurs when a TPC track has miss-reconstructed its drift time, t. This implies the miss-reconstruction of the x position:

$$x = v_{drift}(t - t_0) \tag{6.14}$$

where t_0 is the time given by the first FGD hit matched to the TPC, and v_{drift} the drift velocity. Such tracks match hits in the YZ view, but not the XZ view, which causes the matching to halt in FGD layer 23. The systematic error is computed using the same sample as for the double-skipped layer failure. In this case, the systematic error is obtained by taking the difference between data and MC at the level of the layer 23.

[2] In fact, the tracks are assumed forward in the reconstruction. Only if the track passes through the second FGD (FGD2), the direction can be flipped by using the timing of both FGDs.

- **Matching reconstruction failure** can occur because of three main reasons:
  - **Bad first hit in the FGD1-TPC2 matching** occurs when failing choosing the first FGD hit to get the t_0 of 6.14. In this case the x coordinate of the TPC track is not correctly computed causing the matching for a through-going track to stop inside the FGD FV [3].
  - **Interactions in the dead material downstream of the FGD1 cover plate or upstream TPC2 dead material.** These are backwards-going hadrons produced by interactions in the dead material and stopping in FGD1, while the forward-going muon from the same interaction enter the TPC. There is then a probability of matching the backwards-going hadrons and the muon as a single track starting in the FV of the FGD.
  - **Interactions in the dead material upstream of the FGD1's scintillator planes.**

  The systematic error is obtained by lowering the χ^2 matching criterion in the reconstruction by a factor of 1.3. The difference between the nominal χ^2 cut and the new χ^2 gives the systematic uncertainty.
- **Interactions in the most upstream XY module of FGD1** don't create always hits in the first XY module because the particle just clips a bar and passes through the dead material of the second layer, or because it is created so close to the edge of a FGD bar that is below the hit threshold. T2K-TN-98 concludes that the systematic error due to this category is negligible [155].

Table 6.7 shows the uncertainties assigned to each category.

Table 6.7: Each component of the out-of-fiducial-volume (OOFV) background is listed. In bracket a reconstruction category is assigned. The size of each component is given as a fraction of the total OOFV background, along with the associated rate-related and reconstruction-related components for that background [145].

Background type (reconstruction category)	Fraction of OOFV	Rate uncertainty	Reconstruction uncertainty
Neutral particles entering FGD1	16.2 %	20 %	0 %
Backwards-going tracks	9.8 %	20 %	0 %
High angle tracks (A)	7.3 %	20 %	45 %
Double-skipped layer failure (A)	9.4 %	20 %	100 %
Layer 23 hit matching failure (A)	5.1 %	20 %	150 %
Bad first hit(B)	17.0 %	20 %	8 %
Int. in the dead material downstream of FGD1 (B)	18.7 %	0 %	5 %
Int. in the dead material upstream of FGD1 (B)	3.4 %	0 %	0 %
Int. in the most upstream FGD1 XY module (A)	12.9 %	0 %	0 %

The covariance matrix due to the particle originating outside the tracker is given by,

$$V_{jj'}^{rate} = (0.2)^2 \left(\sum_{k \in outside} B_{k,j} \right) \left(\sum_{k \in outside} B_{k,j'} \right) \tag{6.15}$$

[3] Note that this category also contains hard elastic scattering events of muons in the FGD. This events are not reconstruction failure but were difficult to separate from the bad first hit category.

where B_{kj} denotes the number of events of category k, predicted in the MC for the reconstructed bin j.

For each sample, k, of the reconstruction category, A, the covariance matrix is calculated as the following,

$$V^{A}_{jj',k} = \alpha_k^2 B_{k,j} B_{k,j'} \tag{6.16}$$

where α_k is the fractional reconstruction-related systematics on that category from Table 6.7.

For the matching failure category,(e.g B category in Table 6.7), the covariance matrix is given by,

$$V^{B}_{jj'} = (B_j^{B,\chi^2_{nom}} - B_j^{B,\chi^2})(B_{j'}^{B,\chi^2_{nom}} - B_{j'}^{B,\chi^2}) \tag{6.17}$$

where $B_j^{B,\chi^2_{nom}}$ and B_j^{B,χ^2} are the total number of events falling in the matching failure category reconstructed in bin j passing the selection cuts for the nominal χ^2 and the lower one respectively. The total fractional covariance matrix is then given by,

$$V^{OOFV}_{jj'} = \frac{V^{rate}_{jj'} + \sum_{k\in A} V^{A}_{jj',k} + V^{B}_{jj'}}{N_j^{sel,nom} N_{j'}^{sel,nom}} \tag{6.18}$$

where $N_j^{sel,nom}$ is the total number of selected events (signal + background) in the reconstructed bin j.

Event pile up

The systematic error due to event pile up has two possible contributions.

One comes from the error in the calculation of the efficiency correction for the Monte Carlo (see Sec. 5.7). As it was discussed in the previous section, there is a 15% uncertainty associated to the sand interactions simulation. The systematic error is then computed as 0.15 times the efficiency correction, 0.43 % and 0.78 % for Run I and Run II. The errors are then 0.06 % and 0.12 % for Run I and II.

The other potential error comes from the simulation of TPC1 track events in the ND280 MC. There are two possible sources of systematic errors: difference in intensity or in the material description of the external ND280 detectors (support structures, magnet, ...) for data and MC. The systematics is computed by the difference in the number of TPC1 track events per bunch in data and MC (where the sand muons are added to the MC) from Table 5.7. We obtain 0.04 % for Run I and 0.21 % for Run II.The total systematic error is obtained by adding in quadrature the different values and reweighting by the number of POT of each run, giving a 0.2 % error for Run I and Run II.The error is assumed fully correlated. Therefore the fractional covariance matrix takes the following form,

$$V^{pileup}_{jj'} = \frac{0.002^2}{N_j^{sel,nom} N_{j'}^{sel,nom}} \tag{6.19}$$

where $N_j^{sel,nom}$ is the number of selected events in reconstructed bin j for the nominal MC with the different corrections applied.

6.2.10 Total uncertainty

The total fractional covariance matrix coming from the sources previously described is given in Fig. 6.2. The uncertainties coming from the migration between CCQE and CCnQE events are also included, and we clearly see the anti-correlations between the CCQE-like and the CCnQE-like selection.

The sources of the detector systematic uncertainty with its error size and samples used to compute the covariance matrix are given in Table 6.8. From this table, we see that the main source of systematic error is the OOFV background, where we can have up to 9 % of systematic error. The second main systematic error is due to the magnetic field distortion. The rest of the systematic errors are, in general, below 1 %. These errors are, in general, smaller than the flux or cross section modeling uncertainties that we will quantify in the next section.

6.3 Cross section model uncertainties

Two neutrino event generators have been used in this analysis: NEUT and GENIE. While the NEUT MC has been chosen for the propagation of systematic errors, GENIE has been used as fake data sets. In this section, I briefly explain which models have been used by the MCs and the systematic error parameterization for NEUT, as no systematic errors have been calculated, by now, for GENIE in the scope of the T2K experiment. In general, both MCs use similar physics models and covers similar range of neutrino energies from several tens of MeV to hundreds of TeV for NEUT and from $\sim$ 1 MeV to $\sim$ 1 PeV for GENIE.

6.3.1 Charged-current quasi-elastic scattering (CCQE)

Both generators use the Llewellyn-Smith formalism, summarized in Sec. 2.5 to describe quasi-elatic neutrino scattering off nucleons in the nucleus. Although they both use the dipole description for the axial form factor F_A (see Eq. 2.40), GENIE uses a different value of the axial mass: 0.99 MeV/c^2 for GENIE and 1.21 MeV/c^2 for NEUT.

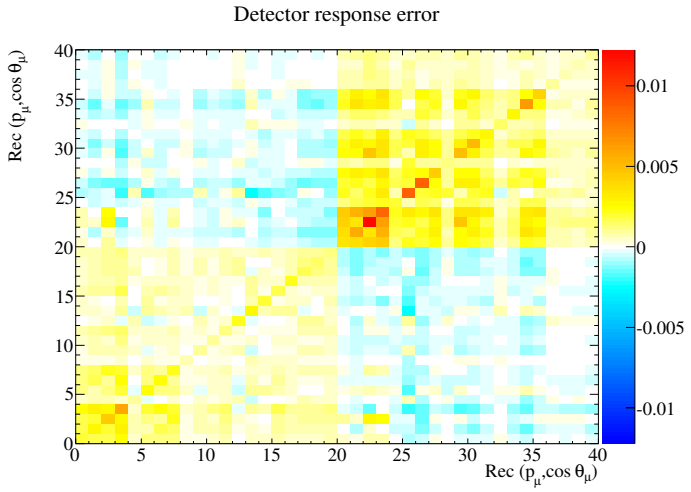

Figure 6.2: Detector response error for each reconstructed bin $(p_\mu, \cos\theta_\mu)_j^{rec}$. The first 20 bins are for the CCQE-like selection, when the last 20 bins represent the CCnQE-like selection.

They also employ the Smith-Moniz (see Sec. 2.5) relativistic Fermi gas (RFG) model to simulate the nuclear environment. Thus the primary input parameters for simulating CCQE scattering are the axial mass parameter M_A^{QE}, and the parameters of the RFG model: the Fermi momentum p_F, and the binding energy E_B.

The recent experiments all show a discrepency of the CCQE cross section at low Q^2 between models and data. MiniBoone for example has tuned the MC by implementing a Pauli blocking parameter κ and increasing M_A to 1.25 GeV/c^2 [156]. However, many people in the theory community claim that this discrepency is due to the simplicity of the RFG nuclear model employed by most neutrino generators. To explore this effect, another spectral function model from the NuWro [157] generator has been implemented.

Error parameterization

The errors for the quasi-elastic parameters have been evaluated by using the MiniBooNE data together with the same NEUT MC used for the T2K analysis (NEUT 5.1.4). A fit with a minimal parameterization has been done on the MiniBooNE data, where the floating parameters were only the M_A^{QE} and CCQE normalization [158].

The errors delivered have been obtained as the difference between the fitted value of the parameter and the nominal. As the energy range of MiniBooNE is below 1.5 GeV, for this range of energy an uncertainty of 11% has been set which reflects the uncertainty that the MiniBooNE collaboration has on its flux [158]. A conservative 30% error has been set for the rest of the energy range.

As already pointed out, both NEUT and GENIE MC use the RFG model. To account for the systematic error done by using this simplest model, an uncertainty is associated to that by using the spectral function of the NuWro generator. The NuWro generator is used to calculate the

Table 6.8: Summary of all the systematic errors.

Systematic Error	Data Sample	Error size (%)
Pion absorption	Beam data/MC	3.0
TPC track quality cut	Beam data/MC	0.1
TPC track efficiency	Beam data/MC	0.5
TPC *broken track* tracking efficiency	Beam data/MC	0.6
TPC Particle ID (PID)	Beam data/MC	0.1
TPC momentum scale	external data	0.51
TPC momentum distortion	special MC	$1-7$
TPC momentum resolution	Beam data/MC	2.0
TPC-FGD matching efficiency	sand muon + cosmics	< 1
Fiducial Mass	external measurement	0.67
Charge mis-ID	Beam data/MC	< 0.3
Michel electron tagging	cosmics	0.49
Cosmic rays	special MC	0.1
Sand muons	special MC	1.5
Out-of-fiducial volume (OOFV) background	several samples	$1-9$
Pile up	Beam data/MC	0.2
Track Multiplicity due to ext. bkgd	Beam data/MC	1.5

difference in cross section as a function of E_ν and outgoing $p_\mu - \theta_\mu$ between the Spectral Function (SF) and Fermi gas model of the nucleus (see 2.7). The major contribution to the SF comes from the shell model and the remaining ∼20% from correlated pairs of nucleons. The last part accounts for a large momentum tail in the nucleon momentum distribution, which extends far beyond 250 MeV/c. The effective binding energy (equivalent to the binding energy parameter in the Fermi gas model) is on average larger which makes the cross section smaller.

Because of large uncertainty at large Q^2 of the Fermi momentum (p_F) an additional systematic error on p_F is taken into account, that is estimated not including the systematic uncertainty assigned to the spectral function. In this case, the uncertainty associated to the Fermi momentum is taken from electron scattering data [76].

The cross-section modeling errors, for the quasi-elastic channel, are shown in Table 6.9.

Table 6.9: NIWG 2012a cross section parameterization, with nominal value, error assigned for the CCQE interaction

Parameters	Energy range (GeV)	Nominal value	Error
M_A^{CCQE}	$0.0 < E_\nu$	1.21 GeV	37.2 %
CCQE	$0.0 < E_\nu < 1.5$	1	11 %
CCQE	$1.5 < E_\nu < 3.5$	1	30 %
CCQE	$3.5 < E_\nu$	1	30 %
Spectral Function	$0.0 < E_\nu$	Off (0)	100 %
p_F	$0.0 < E_\nu$	217 MeV/c	13.8 %

6.3.2 Charged-current inelastic scattering (CC-nQE)

Baryon resonance production

Although NEUT and GENIE use the same Rein-Sehgal [68] model to simulate the neutrino induced single pion productions. From the 18 resonances of the original Rein-Sehgal paper, the 16 listed as unambiguous in the latest PDG baryon tables are included in GENIE [84], while NEUT considers the 18 resonances below 2 GeV. NEUT uses the same axial mass value of 1.21 GeV/c^2 for quasi-elastic and resonant processes. On the contrary, GENIE uses different values: 0.99 GeV/c^2 and 1.12 GeV/c^2 respectively.

For GENIE, the Rein-Sehgal model is used up to a hadronic invariant mass, W, of 1.7 GeV/c^2, which is 2 GeV/c^2 for NEUT. Below this cut value, GENIE and NEUT use a different description of non-resonance background that has to be taken into account (see Sec. 6.3.2).

The Pauli blocking effect described in Sec. 2.7.1 is also considered. This suppresses the interaction cross-section by a few percent [65]. Decay of delta resonance, where no pion is produced is also considered and it corresponds to 20 % of total number of events.

Non-resonant inelastic scattering

NEUT and GENIE use essentially the same techniques for deep inelastic scattering. They both use the modifications suggested by Bodek and Yang [159] to describe scattering at low Q^2. In this model higher-twist [4] and target mass corrections are accounted for through the use of a new

[4] Higher-twist (HT) is a technical term referring to the inclusion of multiple scattering effects on hard processes.

scaling variable and modifications to the low Q^2 parton structure functions.The cross sections are computed at a fully partonic level, where cross sections are computed for all relevant sea and valence quarks. The longitudinal structure function is taken into account using the Whitlow R ($R = F_L/2xF_1$) parameterization [160]. The default parameter values are those given in [159], which are determined based on the GRV98 (Glueck-Rey-Vogt-1998) [161] parton distributions. The same model can be extended to low energies; it is the model used for the non-resonant processes that compete with resonances in the few-GeV region.

Below 1.7 GeV/c^2, GENIE uses the Andreopoulos-Gallhager-Kehayias-Yang (AGKY) hadronization model [162] to decompose the Bodek and Yang model to single pion and two pion production contributions. A fraction of these CC-1π and CC-2π contributions are added to the Rein-Sehgal resonance model. The fractions are derived by fits to CC-inclusive, CC-1π and CC-2π bubble chamber data. The corresponding fractions for NC are worked out from the CC ones using isospin arguments.

NEUT uses a different method to treat the non-resonance background at low invariant mass of the hadronic system (W <2 GeV/c^2). In this case, a probability function of pion multiplicity depending on W is used. The mean multiplicity of charged pions is estimated from the result of the Fermilab 15-foot hydrogen bubble chamber experiment [163].

In both generators, Koba-Nielsen-Olesen (KNO) scaling [164] is used to get the charged hadron multiplicity.

Coherent pion production

Coherent production of pions has been observed for neutrino energies ranging from 2 to 80 GeV [165]. However for lower energies (below 2 GeV) problems with the existence of the coherence phenomenon might appear. Several models exist that describe coherent pion production [165, 166, 167], but the absolute cross sections predicted by these models can vary by an order of magnitude. In addition, both the K2K and SciBooNE experiments have measured an absence of coherent $CC\pi^+$ events, well below predicted levels [168, 169], while similar deficits are not observed in neutral current coherent π^0 production [170]. Although the Rein and Sehgal model is used for NEUT and GENIE MCs (see Sec. 2.8) for coherent pion production, they are different by a factor of 2 in total cross section, as GENIE uses a recent revision of the Rein-Sehgal model [133].

Error parameterization

To constrain the single pion production, the NIWG group (Neutrino Interactions Working Group) of the T2K collaboration performed a joint fit to the MiniBooNE data sets for CC-1π^0 production, CC-1π^+ and NC-1π^0 productions, since these parameters are connected by common parameters in the NEUT MC (see Sec. 2.6). Nine parameters are included in the fit. For some of them, the fit has no power of constraints. In this case penalties are given to those parameters. The choice of the systematic uncertainty for each parameter is given below:

1. M_A^{RES} is the axial vector mass for resonant interaction, which affects both the rate and Q^2 shape of neutral and charged current interactions. The uncertainty comes from the MiniBooNE fit.

2. W **shape (Γ in Eq. 2.48)** describes the width of the resonance. It allows the modification of the shape of the $|\vec{p}_{\pi^0}|$ spectrum of the NC-1π^0 channel to improve agreement with data [171]. In general terms, the approach is to reweight events with a pion or a photon and a nucleon in the initial state (before FSI and ignoring pionless Δ decay events) using a function that depends on the invariant mass W and the W shape parameter Γ, $r(W, \Gamma)$ defined as:

$$r(W, \Gamma) = \alpha \cdot \frac{\Gamma}{(W - M_{N^*})^2 + \Gamma^2/4} \cdot P(W; m_\pi, m_N) \tag{6.20}$$

where

- $P(W; m_\pi, m_N)$ is the phase space for a two-body decay of a particle with mass W into particles with masses m_π and m_N
- α is a normalization factor calculated to leave the total nucleon-level cross section unchanged as Γ is varied.
- M_{N^*}=1218 MeV.

The error on this parameter is defined as the difference between the best fit and the nominal value (87.7 MeV) and is about 50% error.

3. **CC coherent normalization factor**:
A 100 % error has been set for the CC coherent pion production, as external experiments are consistent with no coherent pion production by neutrino energies of $\sim$ 1GeV. In addition, fit results for the MiniBoNE data on CC-1π is also consistent with no coherent pion production at the 2σ level [158].

4. **CC-1π normalization factor**
For lower neutrino energy bins: $0 < E_\nu < 2.5$ GeV (MiniBooNE energy range) the uncertainty comes from the MiniBooNE fit, while for the higher energies a conservative 40 % error is associated and motivated by external experiments as NOMAD [158].

5. **CC-other shape factor** parameter modifies a combination of CC cross section channels as a function of E_ν. The interactions contributing to this category are the CC-nπ production, which are interactions with more than one pion in the final state but with a hadronic mass between 1.3 GeV and 2 GeV, DIS or CC resonant with $\eta/K/\gamma$ production. From external data sets, the uncertainty is known to be of the order of 0.4 GeV at 4 GeV. The error is then set as

$$\delta_{CC-oth.shp.} = \frac{0.4\ (GeV)}{E_\nu(GeV)} \tag{6.21}$$

where E_ν is the neutrino energy. Note that these processes have an energy threshold at 0.6 GeV and thus the error will be always well defined.

6. **NC-1π^0 normalization factor** corresponds to the resonant production of π^0 via neutral currents. The uncertainty comes from the MiniBooNE fit.

7. **NC-other normalization factor** corresponds to the normalization factor applied to the NC elastic, $\gamma/K/\eta$-resonant and DIS interactions. For these parameters a 30 % error is set following the studies of 2010a oscillation analyses. In MiniBooNE, there are very few events corresponding to these channels making difficult for the fitter to constrain the normalization.

8. **NC-1$\pi^{\pm}$ normalization factor** corresponds to the resonant production of $\pi^{\pm}$. The same argumentation as for NC-other is valid to give a 30 % error on this channel.

9. **NC coherent normalization factor** corresponds to the coherent π^0 production. A 15 % NEUT/data discrepancy is observed in addition to a systematic error of the data of 20 %. This motivated the 30 % systematic error assigned to NC coherent π^0 production [158].

In addition to the nine parameters two additional uncertainties have been taken into account:

- **$1\pi - E_\nu$ shape**
  Because the prediction from the best fit is much higher than the data at energies below 1 GeV, an empirical parameter has been added, to assign an additional source of uncertainty that take this discrepancy into account in the $CC - 1\pi$ and $NC - 1\pi^0$ channel.

  There is no known parameter, in the model, that can remedy this. Therefore an empirical function is computed to make the data and the MC agree by construction. The uncertainty is the difference between the $1\pi - E_\nu$ shape correction and nominal, which is about 50 %.

- **π-less Δ decay (pdd)**
  This process is also known as Δ re-absorption [172], where the Δ interacts with nucleons in the nucleus before decaying into nucleons but no pions. This process is suggested to happen ∼20% of time [173]. It is currently implemented in NEUT as energy and target independent, where the Δ does simply not decay into any products, resulting in a CCQE-like event. However, the same authors tested their FSI model against π-photoproduction without this effect and observe good agreement with the data [174]. A similar check has been done with the NEUT π-photoproduction simulation with the same conclusion. This suggests there may be double counting of the effect in the NEUT neutrino simulation.

  The effect on the single pion fits was investigated by changing the fraction of Δ which can decay with no pions from 20% to 0%. To first order, this reduces the fitted normalization by ∼20%, since we are re-introducing 20% of the resonant 1π events into the sample which were previously ignored.

Table 6.10 summarizes the error with its nominal values. In the table, the NC-other, NC-1$\pi^{\pm}$ and NC-COH have been merged into a single category called NC-other. In addition, the errors on M_A^{RES} and CC normalization have been scaled by α_{CC}, while the NC normalization by α_{NC} to match the MiniBooNE quoted error. In this procedure, the correlations between the parameters is also changed simultaneously, while the best fits are unchanged [158].

6.3.3 Charged current scattering uncertainties

In this section, we reconsider the uncertainties described in the previous sections as coming from quasielastic and non-quasielastic scattering before switching to the final state interaction model uncertainties. In particular, we reorganize these uncertainties into three different categories that will be shown useful in the next chapter when we will propagate these errors to the final cross section result:

- The uncertainties that will be represented by response function in the next chapter.

Table 6.10: NIWG 2012a cross section parameterization, with nominal value, error assigned

Parameters	Energy range (GeV)	Nominal value	Error
M_A^{RES}	$0.0 < E_\nu$	1.16 GeV	9.1 %
W_{shape}	$0.0 < E_\nu$	87.7 MeV/c^2	52.3 %
CC-oth shape	$0.0 < E_\nu$	0	40 %
CC-1π	$0.0 < E_\nu < 2.5$	1.63	0.348
CC-1π	$2.5 < E_\nu$	1	40 %
CC-COH	$0.0 < E_\nu$	1	100 %
NC-1π^0	$0.0 < E_\nu$	1.18	0.372
NC-oth	$0.0 < E_\nu$	1	30 %
$1\pi - E_\nu$ shape	$0.0 < E_\nu$	off	50 %
π-less Δ decay	$0.0 < E_\nu$	0.2	20 %

- The uncertainties on parameters that are turned off in the nominal NEUT MC.
- The uncertainties on the rate of different processes based on the neutrino energy.

Tables 6.11,6.12 and 6.13 reflect these three categories respectively.

Table 6.11: NIWG 2012a cross-section parameterization, with nominal value and error assigned [158].

Parameters	Nominal value	Error
M_A^{CCQE}	1.21 GeV	37.2 %
M_A^{RES}	1.16 GeV	9.5 %
CC-oth shape	0	40 %
p_F	217 MeV/c	13.8 %
W_{shape}	87.7	51.7 %
pionless Δ decay	0.2	20 %

Table 6.12: NIWG 2012a parameters that are not included in the default simulation, with nominal value and error assigned [158].

Parameters	Nominal value	Error
Spectral Function	Off (0)	100 %
1π E_ν shape	Off (0)	50 %

Fig. 6.3 shows the covariance matrix merging the parameters of Tables 6.11 and 6.13.

The correlations between NC-1π^0 and CC-1π at low energy comes from the MiniBooNE fit described in [171].

6.3.4 Final State Interaction (FSI) model

As already seen in Sec. 2.10, FSI are re-scattering processes driven by strong interactions. They can produce a different final state compared to the initial state that was produced at the nucleon level interaction vertex via processes as QE scattering, absorption, charge exchange and particle production. In theory, the FSI are correlated to the other cross section parameters. In this

Table 6.13: NIWG 2012a cross-section normalizations with range of neutrino energy, nominal value, and error assigned [158].

Parameters	Int. mode bin	Energy range (GeV)	Nominal value	Error
CCQE	0	$0.0 < E_\nu < 1.5$	1	11 %
CCQE	0	$1.5 < E_\nu < 3.5$	1	30 %
CCQE	0	$3.5 < E_\nu$	1	30 %
CC-1π	1	$0.0 < E_\nu < 2.5$	1.63	43 %
CC-1π	1	$2.5 < E_\nu$	1	40 %
CC-COH	2	$0.0 < E_\nu$	1	100 %
NC-oth	3	$0.0 < E_\nu$	1	30 %
NC-1π^0	4	$0.0 < E_\nu$	1.18	43 %

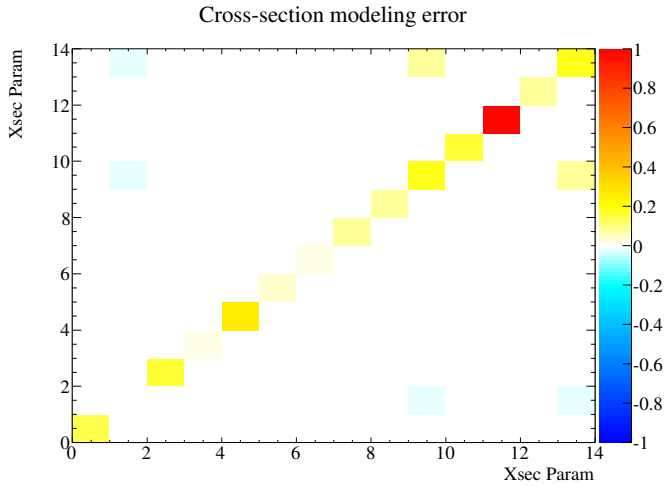

Figure 6.3: Cross-section modeling error for each of the parameters listed in Tables 6.11 and 6.13 following the same order (the first 7 bins of the covariance matrix corresponds to the parameters in Table 6.11, while the 8 parameters of Table 6.13 correspond to the last 8 bins).

analysis, however, we assume them independent of the other cross section parameters, as a first approximation. Therefore, its contribution will be added in quadrature to the other sources, in the final cross section result.

NEUT and GENIE use different microscopic cascade model to propagate the pion through the nuclear medium. In GENIE the INTRANUKE model [175] is used, while the NEUT model is described in [65]. The description of the probability of interaction is separated in low and high pion momentum ($\leq$ 500 MeV/c and $>$ 500 MeV/c) where different models are adopted.

The model is tuned to external data, and for $p_\pi > 400$ MeV/c and $p_\pi < 500$ MeV/c, a linear mixing is done to alleviate discontinuities at 500 MeV/c where the πp or πd scattering is used to calculate the interaction probabilities.

Low energy model ($p_\pi \leq 500$ MeV/c)

In NEUT, the calculation of interaction probabilities for pion momentum, $p_\pi \leq 500$ MeV/c comes from the Delta-hole model. This is a microscopic, many-body calculation, including the

renormalization of the Δ properties within the nuclear medium. The model includes calculations for quasi-elastic scattering (including charge ex-change) and absorption via 2- and 3-body mechanisms.

The validity of the model is stated to be between a kinematic energy range of T_π = 85 - 350 MeV. Thus an extrapolation of the interaction probabilities is done from $p_\pi = 0$ to 500 MeV/c.

This extrapolation leads to a large uncertainty in the amount of absorption at low energies, which could potentially affect expected distributions of decay electron or low energy decay photon. Thus, one should assign large uncertainties in this region, especially where precise π-nucleus data is scarce [176].

The quasi-elastic scattering and pion absorption probabilities are tuned to pion-carbon data,that are more abundant than for other nuclei, and with less confusion arising from neutrino interaction or photoproduction physics.

Due to the non-linear nature of the cascade, it is difficult to predict the correlations between the microscopic interaction probabilities and the resulting observable cross sections. Hence, modifications to the probabilities are done iteratively until good agreement is observed in the cross section data.

High energy model ($p_\pi > 500$ MeV/c)

For $p_\pi > 500$ MeV/c, the energy becomes high enough such that the nucleons begin to appear as free particles within the nucleus. Hence, free $\pi^\pm$ on proton and deuteron (πp or πd) scattering is used as input to the calculation of interaction probabilities. An iso-scalar target is assumed, regardless of the input target nucleus type, which can lead to inaccuracies for the heavy nuclei. For hadron production, the outgoing pion multiplicity is determined from a parameterization of bubble chamber data [177]. A maximum multiplicity of 7, with exactly one nucleon and at least one pion is imposed, as well as charge conservation. This implementation allows for charge exchange-like events where a single π^0 is produced. Also, these particles continue through the cascade and can result in further scattering and absorption. However, if these particles undergo a further hadron production process, their daughters are not subject to the cascade and are assumed to have immediately escaped the nucleus [173].

Error parameterization

In our case, FSI uncertainties, are uncertainties on the pion's final state before it leaves the nuclear medium after a neutrino interaction. The allowed variation of each interaction process is constrained by external pion-carbon scattering data and is described in detail in [178]. The parameters taken into account to calculate the FSI uncertainties are divided into two categories: low and high pion momentum, and are shown in Table 6.14. It consists of the NEUT microscopic cascade interaction mechanism probabilities for absorption (FSIABS), low energy QE scattering (FSIQE) and charge exchange branching fraction (FSICX) that are simultaneously varied. The second set of parameters are the high energy parameters for QE scattering (FSIQEH), single charge exchange fraction (FSICXH) and pion production (FSIINEL).

The response function method for handling cross section parameters works well when we can map a single cross section parameter to a prior uncertainty. In the case of the FSI model [173], the parameters are strongly correlated, and so it is difficult to change one parameter independent

Table 6.14: NEUTReWeight parameters in T2KReWeight used for 2012a oscillation analysis. Note that the nominal and default uncertainty is not necessarily the values used in the 2012a analysis, especially in the case of the FSI parameters [146].

Parameters	Nominal value	Error
FSI absorption	1.	50 %
FSI charge ex., LE	1.	50 %
FSI qe scat., LE	1.	50 %
FSI inelastic scat., LE	1.	50 %
FSI charge ex., HE	1.	50 %
FSI qe scat., HE	1.	30 %
FSI inelastic scat., HE	1.	30 %

of the rest and produce a simple response function. Therefore, as a first approximation, the uncertainty is introduced through the detector covariance matrix[5].

The FSI covariance matrix is generated reweighting the MC using 16 sets of the previously defined parameters. For a given set, different weights are given to the parameters that are used to reweight the MC. We define the CCQE-like and CCnQE-like reweighted distribution in the reconstructed bin j as, $N_j^{sel,rw}(\vec{f_i})$, and $\vec{f_i} = (f_{qe}, f_{qeH}, f_{inel}, f_{abs}, f_{cx}, f_{cxH})_i$ is the i-th parameter set. The 16 sets of parameters are given in Table 6.15.

Table 6.15: NEUT FSI 1-sigma parameter sets from comparison to external pion scattering data [178].

Set i	FSIQE	FSIQEH	FSIINEL	FSIABS	FSICX	FSICXH
Nominal	1.0	1.8	1.0	1.1	1.0	1.8
1	0.6	1.1	1.5	0.7	0.5	2.3
2	0.6	1.1	1.5	0.7	1.6	2.3
3	0.7	1.1	1.5	1.6	0.4	2.3
4	0.7	1.1	1.5	1.6	1.6	2.3
5	1.4	1.1	1.5	0.6	0.6	2.3
6	1.3	1.1	1.5	0.7	1.6	2.3
7	1.5	1.1	1.5	0.7	1.6	2.3
8	1.6	1.1	1.5	1.6	1.6	2.3
9	0.6	2.3	0.5	0.7	0.5	1.3
10	0.6	2.3	0.5	0.7	1.6	1.3
11	0.7	2.3	0.5	1.6	0.4	1.3
12	0.7	2.3	0.5	1.6	1.6	1.3
13	1.4	2.3	0.5	0.6	0.6	1.3
14	1.3	2.3	0.5	0.7	1.6	1.3
15	0.5	2.3	0.5	0.7	1.6	1.3
16	1.6	2.3	0.5	1.6	1.6	1.3

The fractional covariance matrix which relates changes to $\vec{f_i}$ between reconstructed $(p_\mu, \cos\theta_\mu)$ bins j and j' is computed following Eq. 6.22 and is shown in Fig. 6.4,

$$V_{f,jj'} = \frac{1}{16}\sum_{i=1}^{16} \frac{(N_j^{sel,rw}(\vec{f_i}) - N_j^{sel,nom})(N_{j'}^{sel,rw}(\vec{f_i}) - N_{j'}^{sel,nom})}{N_j^{sel,nom} N_{j'}^{sel,nom}} \tag{6.22}$$

[5]This is expected to be a conservative method as described in [158].

where $N_j^{sel,nom}$ is the default number of selected events in the nominal MC. We see that the error on the number of selected events due to FSI uncertainties is between 0-6 %, where most of the bins are below 3 %. Therefore the FSI uncertainties are of the same order of magnitude as the detector response uncertainties, which are relatively small compared to the flux uncertainties that will be explained in the next section.

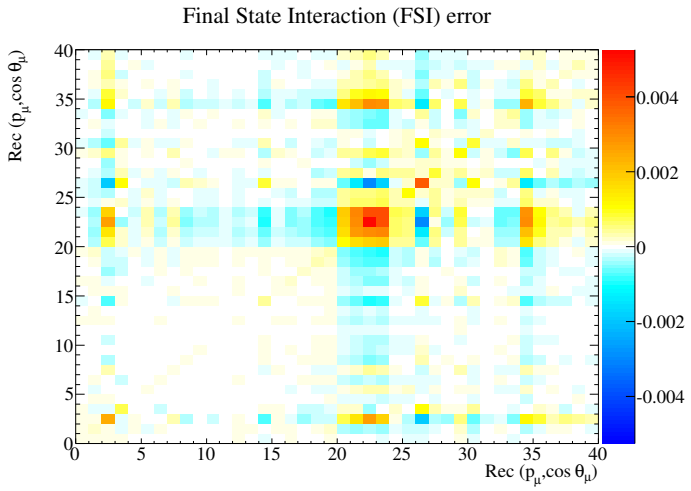

Figure 6.4: FSI uncertainty for each reconstructed bin $(p_\mu, \cos\theta_\mu)_j^{rec}$. The first 20 bins are for the CCQE-like selection, when the last 20 bins represent the CCnQE-like selection.

6.4 Flux systematic uncertainties

At this time, there is no simple underlying parameterization that describes the systematic uncertainties on the NA61 and other hadron production data that contribute to the dominant component of the flux uncertainty. The parameterization of the flux variation is simply described by normalization parameters in bins of neutrino energy and flavor at a given detector. The tuned flux (v11b3.1) used in this analysis with the binning defined in Sec. 6.1 is shown in Fig. 6.5.

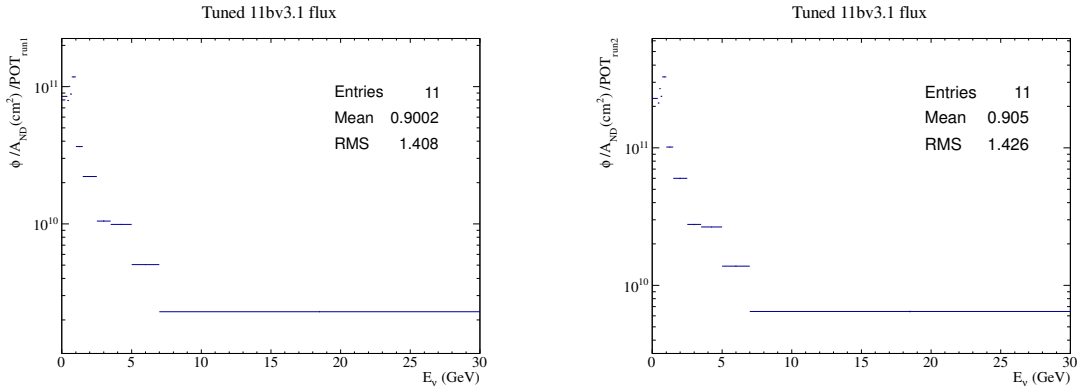

Figure 6.5: Binned ν_μ flux at the near detector for run I (left) and run II (right).

The different sources of uncertainty can be separated into two categories, the hadron production

uncertainty and the T2K beam uncertainty. The different sources contributing to the flux systematic error are described in details in T2K-TN-99, T2K-TN-039 and T2K-TN-054 [136, 179, 180]. This section gives only a brief summary of the different uncertainties.

1. **hadron production uncertainty**

   - **Production cross sections** (as 2010a) are obtained by studying the systematic and statistical uncertainties for experimental data used in the tuning, as well as the consistency between experiments. It is estimated to be of the order of 7 % error at the near detector site [180].
   - **Secondary nucleons production uncertainty** (as 2010a) is obtained by comparing secondary protons production predicted by FLUKA with the Eichten [181] and Allaby [182] data. The uncertainty is expected to be at the level of 6 % error at the near detector.
   - **Pions production multiplicity uncertainty** comes from the pions production uncertainty of the NA61 experiment propagated to the T2K flux. The maximum uncertainty on the ν_μ flux from the NA61 errors is about 6 %. For the regions not covered by NA61, the uncertainty is estimated by the observation of the NA61 vs FLUKA discrepancy and is less than 2 % [136].
   - **Kaons production multiplicity uncertainty** is dominated by the uncertainties associated with Eichten [181] and Allaby [182] data. These errors are mainly dominated by the overall 15% normalization uncertainty in the Eichten data in the high energy region. The uncertainties associated with the NA61 K^+ production measurements are of the order of 5% and 4% for ν_μ and ν_e fluxes, respectively [136].

2. **T2K beam uncertainty**

   - **Proton beam uncertainty** comes mainly from the y alignment uncertainty of the OTR monitor, and the relative alignment uncertainty in the y direction between the primary and secondary beam lines. The maximum systematic error is found to be 6% at 1 GeV [136].
   - **Off-axis angle uncertainty** is calculated using the INGRID data, and is found to be at the level of 1 % error on the beam angle [136].
   - **Horn angular alignment uncertainty** is based on measured alignment uncertainties of 0.3 mm in the X axis and 1 mm in the Y,Z axes. The uncertainty is obtained by observing the effect of a rotation, in the MC, following the measured uncertainties. The resulting error is found to be less than 1% [136].
   - **Horn field asymmetry uncertainty** is found using previous models of field asymmetry modeled in the beam Monte-Carlo using GEANT3 (GCALOR), the effect of this field on neutrino flux can be shown to be less than 1% for bins under 1GeV, and at the level of 4% for bins above 1GeV [136].
   - **Horn absolute current uncertainty** (as 2010a) is estimated comparing the actual horn field measurement with the JNUBEAM MC. The uncertainty is found to be of the order of 5 kA, which corresponds to a 0.5% effect at the near detector site [180].
   - **Target alignment uncertainty** (as 2010a) is estimated from the survey after the target was installed inside the first horn. A miss-alignment of 1.3 *mrad* in the horizontal direction and 0.1 *mrad* in the vertical direction has been measured. The effect,

on the flux distribution, is obtained by simulating in JNUBEAM the misalignment and is found to be of the order of 0.3 % at the near detector site [180].

- **Near Detector phase space uncertainty** has been studied by shifting the proton beam in the X and Y directions. The resulting influence, on the near detector phase space, has been found negligible [136].
- **The proton beam intensity uncertainty** is estimated to be smaller than the MC statistical or other major systematic error. Although, for oscillation analysis, this error is cancelled between the far and the near detector, this error has to be taken into account for a cross section measurement. The proton beam intensity is monitored by the current transformers (CTs), which has a systematic error of a few percent. The exact estimation of the effect of this systematic error need significant calibration work and MC studies, that are currently on-going. A conservative upper limit is expected to be much smaller than the other main systematic errors. Therefore, it is not included by now in this analysis.

For each source, a covariance matrix is calculated. The total muon neutrino flux fractional covariance matrix is then the quadratic sum of the listed contributions and is given in Fig. 6.6. Table 6.16 summarize the information contained in each covariance matrix. We see for example

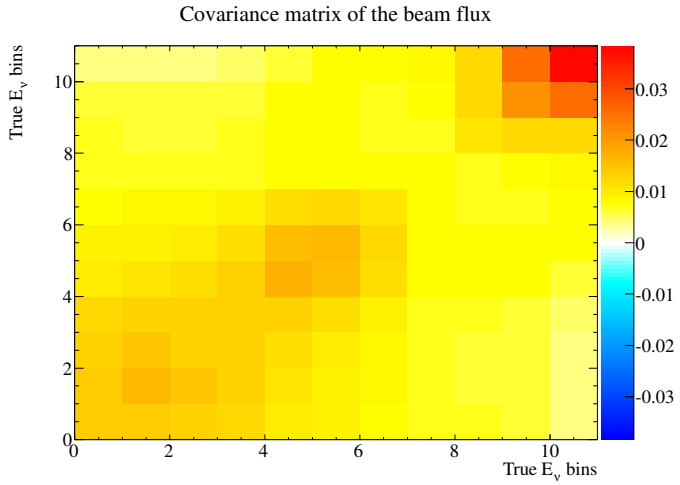

Figure 6.6: ν_μ flux error for each energy bins described in Sec. 6.1.

that the maximum error for the Kaon uncertainty is 16.7 %, which is coming from the Eichten and Allaby data. The last row shows the result obtained by looking directly to the total covariance matrix. We can check that the result presented in the last column is also equal to the quadratic sum of each contributions. In general, the total covariance matrix varies from 8.9% to 19.6% which is expected given the uncertainty of the sources listed in the Table 6.16. The total uncertainty is obtained following Eq. 8.6 that will be described in Sec. 8.1.1.

Table 6.16: The first column corresponds to the maximal error in energy bin while the second column corresponds to the minimal error in a energy bin. The last column is the total uncertainty of each sources. The quadratic sum of each contribution is equal to the value obtained directly using the covariance matrix of Fig. 6.6.

sources	Max. Error (%)	Min. Error (%)	Tot. Error (%)
Cross-sec. production	7.8	4.5	6.4
Sec. nucl. production	8.5	2.9	6.9
Pions	6.1	0.6	5.0
Kaons	16.7	0.4	0.8
Proton beam	5.1	0.2	1.1
Off-axis angle	5.4	0.1	1.6
Horn ang. align.	1.0	0.2	0.5
Horn field assym.	6.7	0.01	0.3
Horn abs. current	1.9	0.4	0.9
Target align.	2.6	0.05	0.2
Total	19.6	8.9	10.9

6.5 Summary

In this chapter, we have analyzed the different systematic errors due to the detector response, cross section modeling and the muon neutrino flux.

The detector systematic uncertainties are mainly errors arising from differences between data and MC at the reconstruction level. Two categories can be defined:

- the systematic errors due to the variables used in the selection as the number of vertical cluster in a track, its momentum, its charge, its energy loss, etc.
- the systematic errors coming from the different backgrounds.

In general the two main systematic errors are coming from the outside-of-fiducial volume background and momentum systematic error due to the magnetic field distortions.

The cross section modeling uncertainties are separated into different categories: the cross section uncertainties that will be represented by response function in the next chapter, normalization uncertainties and the final state interactions uncertainties. Correlations between the normalization uncertainties and the parameters used to calculate the cross sections via the different models that have been described in the Chapter 2 are taken into account. However, the final state interaction uncertainties are treated in an independent way, as a first approximation. As the different parameters behind the final state uncertainties are strongly correlated, it is difficult to change one parameter independent of the rest and produce a simple response function. Therefore, the uncertainty is given as a detector covariance matrix, where 16 sets of the same parameters but with different values are used.

In the case of the flux uncertainties, no underlying parameters are describing by now the systematic errors on the NA61 and other hadron production data. The parameterization of the flux variation is simply described by normalization parameters in bins of neutrino energy and flavor at the given detector. The main source of uncertainty is due to pion production multiplicity,

hadron production cross sections and secondary nucleon production. The total systematic error on the flux is now $\sim 11\%$ which is much smaller than the previous systematic error on the flux for the 2010 oscillation analysis. The decrease of the systematic error is due principally to the latest measurement of pion and kaon multiplicity production taken by the NA61 experiment. In the future analyses, this error should decrease even more as the NA61 data used up to now are the data taken in 2007 with a thin graphite target. In 2009, much more data have been taken with the same thin target and with a T2K replica target. By the use of these latest data, the systematic error on the flux is expected to decrease down to 5%.

In the next chapter, we will see how these systematic uncertainties are propagated in the final cross section analysis.

Chapter 7

Cross section measurement method

Cross sections are one of the most fundamental quantities that can be measured. They represent the interaction probability of a particle, in a given initial state, with a target to produce a specified final-state. In Chap. 2, the definition of the cross section, σ, was given in Eq. 2.8 that can be rewritten as,

$$\mathrm{d}N^{int} = T\sigma\mathrm{d}\phi \tag{7.1}$$

where N^{int} is the number of interactions, T the number of target nucleons and ϕ, the flux of the incident particles (e.g. neutrinos) per unit area.

The goal of this analysis is to provide a model independent cross section result given in terms of the muon kinematic variables, to have the minimum number of assumptions. If one would have given the results in terms of neutrino energy, additional assumptions would have been needed. Therefore, a flux-averaged differential cross section in the $(p_\mu, \cos\theta_\mu)$ plane is presented; where p_μ is the momentum of the outgoing muon and $\cos\theta_\mu$, its angle with respect to the z axis, which is in average the direction of the incident neutrino. We consider the CCν_μ-inclusive interaction channel. This channel depends less than CCQE channel on the modeling of the MC, and allows us to use the largest statistics data set, for a two dimensional differential cross section.

Theorists can then use the T2K flux that should be provided to them, to test their latest models and compare their result with our data. The disadvantage of giving the results in terms of muon kinematics, is that the result is experiment dependent and can't be compared directly with other experiments. Therefore, the total cross section will be also given, in the last chapter, for the mean energy of the T2K flux. Although this result is a flux averaged cross section and the errors on the T2K flux energy distribution is not trivial, it still gives some informations and can be compared to other experiments.

In this chapter, we will first review the cross section definition, the method used to extract the cross section results and the propagation of the systematic uncertainties.

7.1 The cross section definition

The measurement of a cross section can be made as a function of any variable in the interaction. It can be done in terms of the initial state variables, like the neutrino energy or final state variables, such as the muon momentum and angle. The cross section given in terms of initial

state variables expresses the probability that an interaction takes place for each value of the initial state variable. A cross section given in terms of final state variable takes into account not only the probability that an interaction takes place but also the probability that the resulting muon is in a particular final state.

Eq. 7.1 can be written in its more general form in terms of M initial state variables, $\vec{a} = \{a_1..a_M\}$, and N final state variables, $\vec{b} = \{b_1..b_N\}$:

$$N^{\text{int}} = T \int_{a_1} .. \int_{a_M} \int_{b_1} .. \int_{b_N} \frac{\partial^N \sigma(\vec{a}, \vec{b})}{\partial b_1 .. \partial b_N} \mathrm{d}b_1 .. \mathrm{d}b_N \frac{\partial^M \phi(\vec{a})}{\partial a_1 .. \partial a_M} \mathrm{d}a_1 .. \mathrm{d}a_M \tag{7.2}$$

By definition, the integral over all possible muon energies restore the original interaction probability.

If we want to express the cross section in terms of final-state variables, we first need to integrate Eq. 7.2 over all the initial states.

For simplicity, we restrict ourselves to a single initial state variable a and final state b. By definition, the flux averaged cross section is given by integrating over the range of the variable a,

$$\langle \sigma \rangle_\phi = \frac{1}{\phi} \int_a \sigma(a, b) \frac{\partial \phi}{\partial a} \mathrm{d}a \tag{7.3}$$

The total number of interactions in bin k of the final state variable b is given by Eq. 7.2 and becomes,

$$N_k^{\text{int}} = T\phi \int_{b_k} \langle \frac{\partial \sigma}{\partial b} \rangle_\phi \ \mathrm{d}b \tag{7.4}$$

where we applied the definition of Eq. 7.3 to $\frac{\partial \sigma}{\partial b}$.

As the flux averaging is independent of the final state derivatives, Eq. 7.4 is equivalent to,

$$N_k^{\text{int}} = T\phi \int_{b_k} \frac{\partial \langle \sigma \rangle_\phi}{\partial b} \mathrm{d}b \tag{7.5}$$

The flux averaged differential cross section is then given by,

$$\langle \frac{\partial \sigma}{\partial b} \rangle_k = \frac{N_k^{\text{int}}}{T\phi \Delta b_k} \tag{7.6}$$

where Δb_k is the bin width, and $\sigma \equiv \langle \sigma \rangle_\phi$. Following the same principle, we get for the two-dimensional case:

$$\langle \frac{\partial^2 \sigma}{\partial b_1 \partial b_2} \rangle_{kl} = \frac{N_{kl}^{\text{int}}}{T\phi \Delta b_{1,k} \Delta b_{2,l}} \tag{7.7}$$

The flux averaged total cross section per nucleon is given by,

$$\langle \sigma \rangle_\phi = \frac{N^{\text{int}}}{T\phi} \tag{7.8}$$

Let us consider a binning in one dimension with N_k^{int} the number of charged current interactions in bin k. In the case of a perfect detector response, N_k^{int} represents directly the number of events that we find in a certain reconstructed bin k. However, in practice, this is not true and it often happens that events generated in a true bin k end up in a different reconstructed bin j. Suppose that we have N_k^{int} events generated in the true bin k and the number of reconstructed events in bin j, N'_j, is linearly related to N_k,

$$N'_j = A_{jk} N_k \tag{7.9}$$

The inverse transformation is called unfolding and is expressed as,

$$N_k = A_{jk}^{-1} N'_j. \tag{7.10}$$

It gives back the number of generated events in true bin k as a function of the number of reconstructed events, N_j.

An unfolding procedure requires the inversion of the matrix A. However this method can lead to statistical fluctuations that are not desirable. In addition, the inverse does not always exist (e.g when its determinant is null or all its entries are equal). Due to efficiency effects the matrix A might not be invertible at all. To avoid this issue, we will use the Bayesian iterative method (based on Bayes' theorem) and described by d'Agostini [183].

7.2 The unfolding algorithm

As described by Eq. 7.10, the purpose of the unfolding is to remove the smearing of the number of events in a true bin over different reconstructed bins, which is produced by various detector effects such as miss-reconstructions. The unfolding procedure should remove any experiment dependent contributions to the measured central values, placing most of the detector dependence in the systematic errors. The chosen unfolding method is based on Bayes' theorem [183] and has a slight bias on the prior distribution. It is an iterative method that uses at each iteration the information coming from the previous step.

The procedure is developed over n_t true bins and n_r reconstructed bins and is based on:

- the definition of the prior probability of an event to be found in a certain true bin t_k,

$$P_0(t_k) = \frac{N_{t_k}}{\sum_{\alpha=1}^{n_t} N_{t_\alpha}} \tag{7.11}$$

  where N_{t_k} is the initial estimator given by the MC and it represents the total number of charged current interactions simulated in the true bin t_k.

$$N_{t_k} = \sum_{j=1}^{n_r} S_{jk} + M_{t_k} \tag{7.12}$$

  where S_{jk} gives the number of simulated CC events in the bin t_k that have been selected in the reconstructed bin r_j and M_{t_k} the number of CC events that have been missed. In the following, we will call S_{jk} the *signal matrix*. The signal matrix is formed by generating a reconstructed vs. true two-dimensional histogram of the truly selected events. The prior probability is shown in Fig. 7.1.

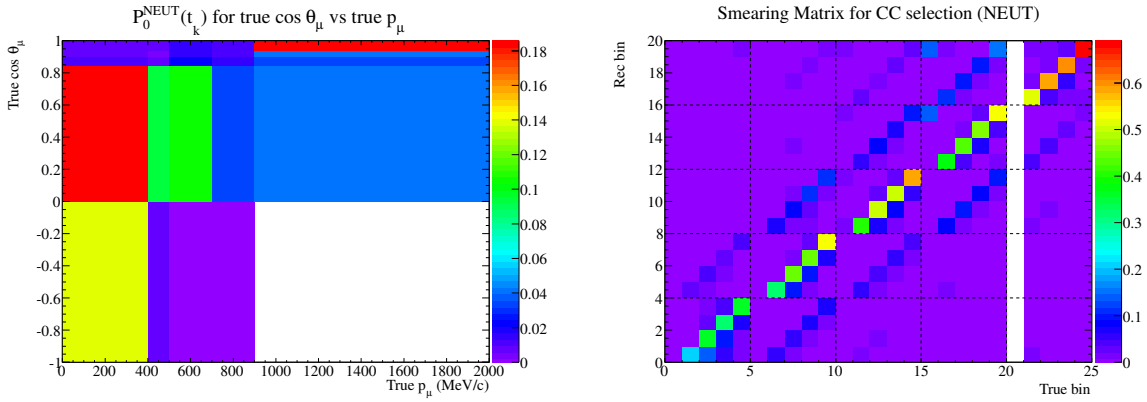

Figure 7.1: Left: Prior probability for the nominal NEUT MC in the $(P_\mu, \cos\theta_\mu)$ plane (see Eq. 7.11). Right: Smearing matrix for the nominal NEUT MC (see Eq. 7.13). The last momentum bin contains the total number of events from 900 MeV to 30 GeV. The white column correspond to the bins where there is no statistics.

- the probability to observe an event in the reconstructed bin r_j knowing that it was generated in the true bin t_k is,

$$P(r_j|t_k) = \frac{S_{jk}}{N_{t_k}} \tag{7.13}$$

  We will often use the term *smearing matrix* to refer to this probability. The *smearing matrix* is shown in Fig. 7.1.

- the efficiency for selecting events in a true bin k, which is defined as the ratio of the CC selected events in the true bin t_k over the total number of CC interactions simulated,

$$\epsilon_k = \frac{\sum_{j=1}^{n_r} S_{jk}}{N_{t_k}} = \sum_{j=1}^{n_r} P(r_j|t_k), \tag{7.14}$$

  where N_{t_k} is given by Eq. 7.12. The efficiency for the binning of Sec. 6.1 is shown in Fig. 7.3.

The original estimators, N_{t_k}, are then updated using the rule,

$$N_{t_k}^{m+1} = \frac{1}{\epsilon_k} \sum_{j=1}^{n_r} P_m(t_k|r_j)(N_{r_j}^{\text{meas}} - s_{\text{POT}} B_{r_j}) \tag{7.15}$$

where,

- $N_{r_j}^{\text{meas}}$ is the number of measured events in the reconstructed bin r_j that pass the selection cuts.

- B_{r_j} is the number of background events in the bin r_j that pass the selection cuts. It is evaluated using the Monte-Carlo. It contains the *sand muons* MC as well as the other backgrounds of the *magnet* MC such as: NC, $\nu_e, \bar{\nu}_\mu, \bar{\nu}_e$ interactions and interactions simulated outside the fiducial volume but reconstructed inside.

- s_{POT} is a factor to scale the MC estimated background to the total number of Protons On Target (POT) in data, n_{POT}^{Data}, i.e. : $s_{\mathrm{POT}} = n_{\mathrm{POT}}^{Data}/n_{\mathrm{POT}}^{MC}$

  Fig. 7.2 shows the number of measured events in data and the corresponding background distribution scaled already to the data POT.

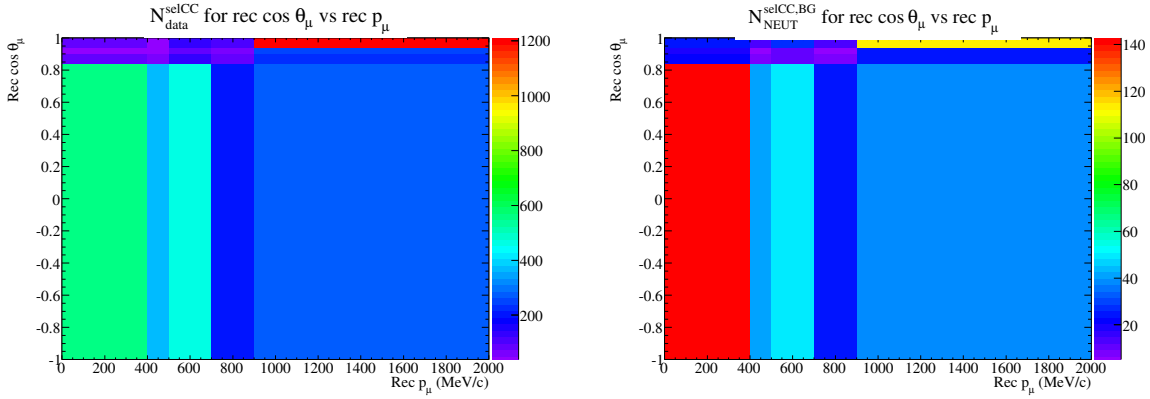

Figure 7.2: Left: Data distribution in the $(P_\mu, \cos\theta_\mu)$ plane for runs I and II. Right: Background distribution given by the NEUT MC in the $(P_\mu, \cos\theta_\mu)$ normalized to the number of POT in data. The last momentum bin contains the total number of events from 900 MeV to 30 GeV.

- $P_m(t_k|r_j)$ is the probability to observe an event in the true bin t_k, knowing that it was reconstructed in the bin r_j,

$$P_m(t_k|r_j) = \frac{P(r_j|t_k)P_m(t_k)}{\sum_{\alpha=1}^{n_t} P(r_j|t_\alpha)P_m(t_\alpha)} \tag{7.16}$$

  where Eq. 7.16 comes directly from the Bayes' theorem.

  We will often use the term *unsmearing matrix* to refer to this probability when considered over all true and reconstructed bins. The *unsmearing matrix* is shown for the first iteration in Fig. 7.3.

- In Eq. 7.16, $P_m(t_k)$ is simply the updated prior probability to observe an event in the bin t_k for the m-th iteration:

$$P_m(t_k) = \frac{N_{t_k}^m}{\sum_{\alpha=1}^{n_t} N_{t_\alpha}^m} \tag{7.17}$$

  where $N_{t_k}^m$ is given using Eq. 7.15 for $m = m + 1$.

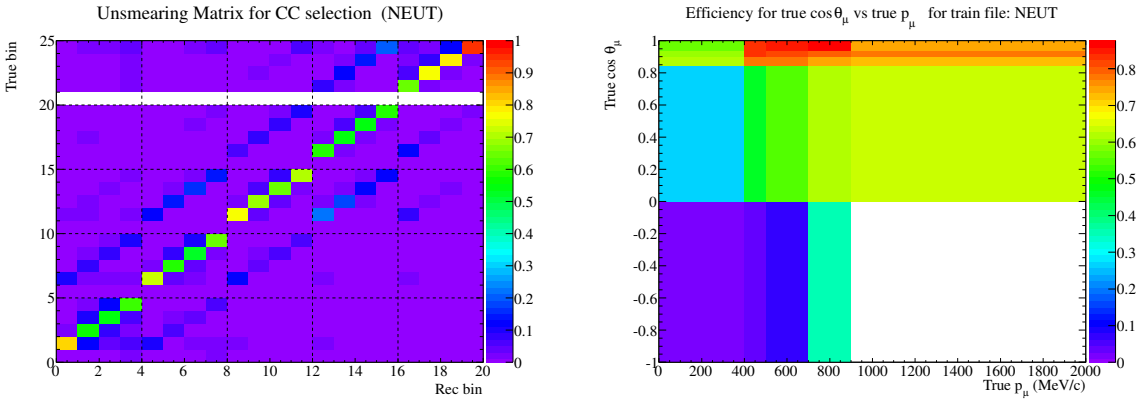

Figure 7.3: Left: Unsmearing matrix after the first iteration (see Eq. 7.16). Right: Efficiency for the nominal NEUT MC in the $(P_\mu, \cos\theta_\mu)$ plane (see Eq. 7.14). The last momentum bin contains the total number of events from 900 MeV to 30 GeV. The white row corresponds to the bins where there is no statistics.

For simplicity, in the following section, we will use the notation,

$$U_{kj} = \frac{P_m(t_k|r_j)}{\epsilon_k}, \qquad P_{jk} \equiv P(r_j|t_k), \qquad \widehat{N}_{t_k} \equiv N_{t_k}^{m+1} \tag{7.18}$$

In the case of a single iteration, we have:

$$\begin{aligned} P_0(t_k|r_j) &= \frac{\frac{S_{jk}}{N_{t_k}} \frac{N_{t_k}}{\sum_\alpha N_{t_\alpha}}}{\sum_\gamma \frac{S_{j\gamma}}{N_{t_\gamma}} \frac{N_{t_\gamma}}{\sum_\alpha N_{t_\alpha}}} \\ &= \frac{S_{jk}}{\sum_\alpha N_{t_\alpha}} \frac{1}{\sum_\gamma \frac{S_{j\gamma}}{\sum_\alpha N_{t_\alpha}}} \\ &= \frac{S_{jk}}{\sum_\gamma S_{j\gamma}} \end{aligned} \tag{7.19}$$

The code used to unfold the data is based on the RooUnfold package developed by Tim Adye, Kerstin Tackmann, and Fergus Wilson [184]. Several modifications have been brought to the original code such as the computation of the statistical error which now takes also into account the MC statistical error and not only the part coming from the data. The computation of the statistical error is based on the d'Agostini paper [183].

7.3 Reweighting the MC

To propagate the systematic errors, the nominal Monte-Carlo has been reweighted for the different types of systematic errors introduced in Sec. 6.3 following the same general method. Since the method to extract the cross section uses the MC to unfold the data. Errors on the modeling of the MC are taken into account as well as all the detector uncertainties due to the reconstruction.

As the covariance matrices described in Chap. 6 have correlations, the reweighting method also handles the correlations between the same group of systematic errors. For example, when two parameters are correlated, let's say negatively, when the first parameter is varied between its error bars, the second parameter has to be changed to a smaller value within its error bars.

The reweighting procedure is similar to the one used by the BANFF group for the oscillation analysis [146]. It is done using templates for each neutrino energy $(E_\nu)_i^{true}$ bin, reconstructed $(p_\mu, \cos\theta_\mu)_j^{rec}$ bin, true $(p_\mu, \cos\theta_\mu)_k^{true}$ bin and interaction mode l bin following the conventions of section 6.1 [1]. For each of these bins, we define three kinds of templates:

- β_{ijkl}: the number of background events[2] in each bin previously defined.
- n_{ijkl}: the number of selected events in the same bins.
- m_{ikl}: the number of missed events in the true bins i, k, l.

where each index is defined as in the Sec. 6.1:

- i: labels the 11 true neutrino energy bins
- j: labels the 20 reconstructed $(p_\mu, \cos\theta_\mu)$ bins
- k: labels the 25 true $(p_\mu, \cos\theta_\mu)$ bins
- l: labels the 6 true interaction mode bins

Because the detector and FSI covariance matrix distinguishes between CCQE-like and CCnQE-like selection, the CC selected templates are separated into two: $n_{ijkl} = n_{ijkl}^{selQE} + n_{ijkl}^{selnQE}$ and $\beta_{ijkl} = \beta_{ijkl}^{selQE} + \beta_{ijkl}^{selnQE}$. In the following, we will label by *sel* any of the two selections.

From the previous section, we can see that all the information needed from the MC to unfold the data can be summarized in two matrices, R_{jk} and B_{jk}, and one vector M_{t_k}.

- $R_{jk}^{sel} \equiv \sum_{i,l} n_{ijkl}^{sel}$, the number of events in the true bin k, that have been reconstructed in the bin j for a given selection (e.g *sel* =CCQE-like or CCnQE-like).
- $B_{jk}^{sel} \equiv \sum_{i,l} \beta_{ijkl}^{sel}$, the number of background events in the true bin k[3], that have been reconstructed in the bin j for a given selection (e.g *sel* =CCQE-like or CCnQE-like).
- $M_{t_k} \equiv \sum_{i,l} m_{ikl}$, the number of missed events that were in the true bin k.

[1] The main difference with the BANFF group consists in the additional bin, k, in the templates. In our case, we also look at the event that should have been selected, but did not for some reasons. In the following, these events will be called, *missed* events and will be used in the efficiency.

[2] e.g. the number of events that should not have been selected because they are not CC interactions, or they are not in the fiducial volume. Here are also included the background due to the neutrino interactions outside the magnet (sand muons).

[3] For neutral current background, and other flavor neutrino interactions, the true momentum and direction of the particle selected is taken in this case.

The signal matrix S_{jk} from Eq. 7.12 of the CC inclusive channel is then obtained by merging together the CCQE-like and CCnQE-like matrices,

$$S_{jk} = R_{jk}^{selQE} + R_{jk}^{selnQE} - (B_{jk}^{selQE} + B_{jk}^{selnQE}) \tag{7.20}$$

The number of background events that will be subtracted from the measured sample is given by,

$$B_j = \sum_k \left(B_{jk}^{selQE} + B_{jk}^{selnQE} \right) \tag{7.21}$$

To propagate the systematic errors to the final results, the MC should be varied following the systematic errors that we have in our simulation. For a certain kind of systematics, different parameters can be correlated. These correlations are taken into account and are handled by the use of the Cholesky decomposition. From that decomposition a weight is computed and the MC is reweighted according to it.

More precisely, the weights are computed using the following general method for each systematic error source:

a) Generate a vector of random number $\vec{r}$ following a Gaussian distribution $N(0,1)$.

b) Decompose the covariance matrix, V, using the Cholesky decomposition[185]: $V = W^T W$, where W is a triangular matrix reflecting the complete knowledge of the covariance matrix.

c) Get the weight $w_\gamma = 1 + \sum_\alpha W_{\gamma\alpha} r_\alpha$

We call, *throw*, a weight obtained by this method.

Since the FSI covariance matrix is given in the same format as the detector one, the two covariance matrices are treated in the same way. The weight, d_j, will therefore represent a systematic change on the final state interactions or on the detector response.

We denote by,

- $\delta_m \equiv \sum_{\alpha=1}^{14} W_{m\alpha}^{(x)} r_\alpha$, the fractional cross section parameter for the m^{th} cross section parameter of Table 6.11. The 14 parameters are the total number of parameters of Tables 6.11 and 6.13 together, since there are correlations between M_A^{RES} and the rate of the CC-1π and NC-1π^0 channel.
- $x_{6+n} \equiv 1 + \delta_{6+n}$, the cross section normalization weight for the n^{th} entry of Table 6.13[4].
- $b_i \equiv 1 + \sum_\alpha^{11} W_{i\alpha}^{(b)} r_\alpha$, the beam weight for the i^{th} neutrino energy bin.
- $d_j \equiv 1 + \sum_\alpha^{40} W_{j\alpha}^{(d)} r_\alpha$, the detector response and FSI weight for the j^{th} $(p_\mu, \cos\theta_\mu)^{rec}$ bin.

[4]In the following, as these parameters depend on the interaction type l and energy bin i, we will often use the notation: $x_{n+6} \equiv x_l(E_i)$, where l is for the 5 interaction categories where a systematic error is assigned and E_i the energy range of the uncertainty assignment. The 8 parameters of 6.13 are then separated into 3 parameters for CCQE, 2 for CC-1π, 1 for CC-COH, 1 for NC-BG and 1 for NC-1π^0.

For each bin $ijkl$, a weight as a function of δ_m, e.g the change of a cross section parameter of Table 6.11 ($m = M_A^{CCQE}$, etc..) is needed. In theory, we could reweight the MC for any δ_m, and reproduce an updated template. However in practice this can be slow, therefore we choose an interpolation method (called response function in the previous chapter). The interpolation method consists in reweighting, firstly, three or seven times the MC using the T2KReweight package developed by the T2K collaboration. The result of the reweighting process is interpolated with a function that gives the weight as a function of δ_m for a given bin $ijkl$.

As the *spectral function* and the *1π E_ν shape* parameters are not used in the default simulation (turned off), the reweighting procedure only consists in turning *on* the two parameters and see the influence in each bin $ijkl$. For the other parameters of Table 6.11 the interpolation method is applied. Practically, each point corresponds to a $n\sigma_m$ variations of the parameter m. We define by s_m the set of these parameter variations:

$$s_m = \{-3\sigma_m, -2\sigma_m, -1\sigma_m, 0, +1\sigma_m, +2\sigma_m, +3\sigma_m\} \tag{7.22}$$

where σ_m is the error listed in Table 6.11. As the variation on W_{shape} and the pionless Δ decay parameter is only trusted up to 1 σ, the variation for more than 1σ is extrapolated linearly. The interpolation is then done on three points $s_m = \{-1\sigma_m, 0, +1\sigma_m\}$.

For each parameter, the weight is defined as the ratio between the reweighted numbers of events with the nominal number of events,

$$\begin{aligned}
\omega^{sel}_{ijkl}(\delta_m = s_m) &= \frac{n^{sel}_{ijkl}(\delta_m = s_m)}{n^{sel}_{ijkl}(0)} \\
\omega^{\beta}_{ijkl}(\delta_m = s_m) &= \frac{\beta_{ijkl}(\delta_m = s_m)}{\beta_{ijkl}(0)} \\
\omega_{ikl}(\delta_m = s_m) &= \frac{m_{ikl}(\delta_m = s_m)}{m_{ikl}(0)}
\end{aligned} \tag{7.23}$$

The points are then interpolated with a function that is then used to evaluate the weight for any δ_m, as shown in Fig. 7.4.

The cross section weight associated to all cross section parameters is then given by,

$$\begin{aligned}
\omega^{sel}_{ijkl}(\vec{\delta}) &= \prod_{m=1}^{7} \omega^{sel}_{ijkl}(\delta_m) \\
\omega^{\beta^{sel}}_{ijkl}(\vec{\delta}) &= \prod_{m=1}^{7} \omega^{\beta^{sel}}_{ijkl}(\delta_m) \\
\omega_{ikl}(\vec{\delta}) &= \prod_{m=1}^{7} \omega_{ikl}(\delta_m),
\end{aligned} \tag{7.24}$$

where m runs over all the parameters of Table 6.11.

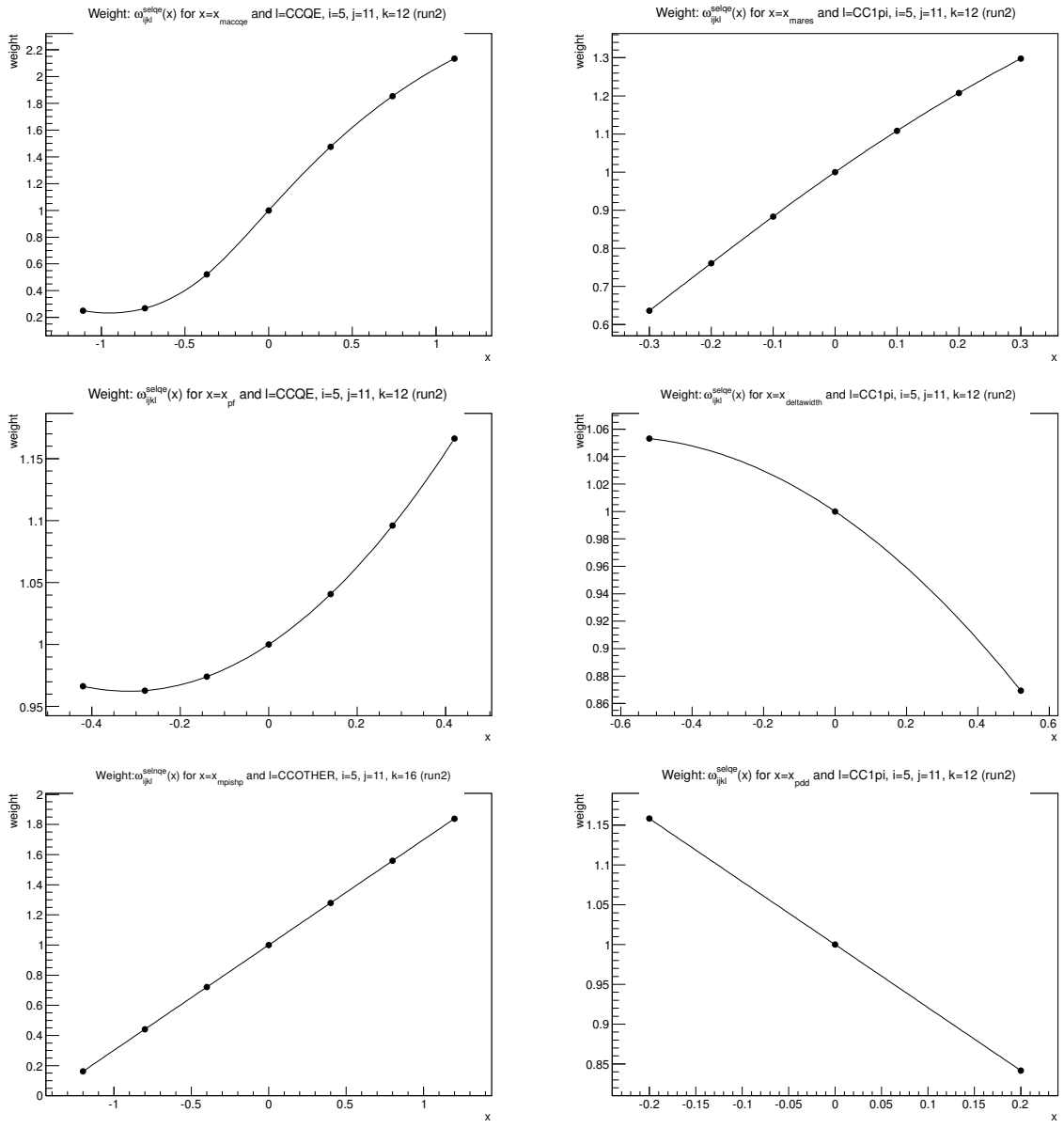

Figure 7.4: Selection of weight response function $\omega^{sel}_{ijkl}(\vec{\delta})$, for several bins $(E_\nu, p_\mu, \cos\theta_\mu)_{ijkl}$ as a function of a fractional change of parameter x. For simplicity, we show the evolution of the weights for $i = 5, j = 11, k = 12$ meaning $E_\nu \in (1.0, 1.5)$ GeV, $p^{rec}_\mu \in (0.7, 0.9)$ GeV, $\cos\theta^{rec}_\mu \in (0.9, 0.94)$ and $\cos\theta^{true}_\mu \in (0.84, 0.9)$ and $p^{true}_\mu \in (0.5, 0.7)$ GeV. M_A^{CCQE}, M_A^{RES}, p_f, W_{shp}, multi-pi shape and pion Δ decay weight response are shown respectively from top left to bottom right for the CCQE-like selection. Note that the multi-pion shape parameter is shown for the true bin: $\cos\theta^{true}_\mu \in (0., 0.84)$ and $p^{true}_\mu \in (0.7, 0.9)$.

Fig. 7.5 shows the mean and RMS value of each throw ($b_i,\ d_j,\ x_m$) as a function of the bin or parameter number ($i,\ j,\ m$) respectively. The mean of the throws correspond to the mean of the weight applied to the templates. By construction the mean should be one, as we can see in Fig. 7.5. The RMS should represent on average the error set on the parameters. An easy way to verify that is to observe the result obtained for the cross section parameters as the

covariance matrix is almost diagonal the RMS should be very close to the parameter error set at the beginning. We see that the first parameter has an RMS around 36 % which corresponds to the error set for the M_A parameter in Table 6.11, the same is true for the second parameter that have an RMS around 10% which again corresponds to the error set in Table 6.11.

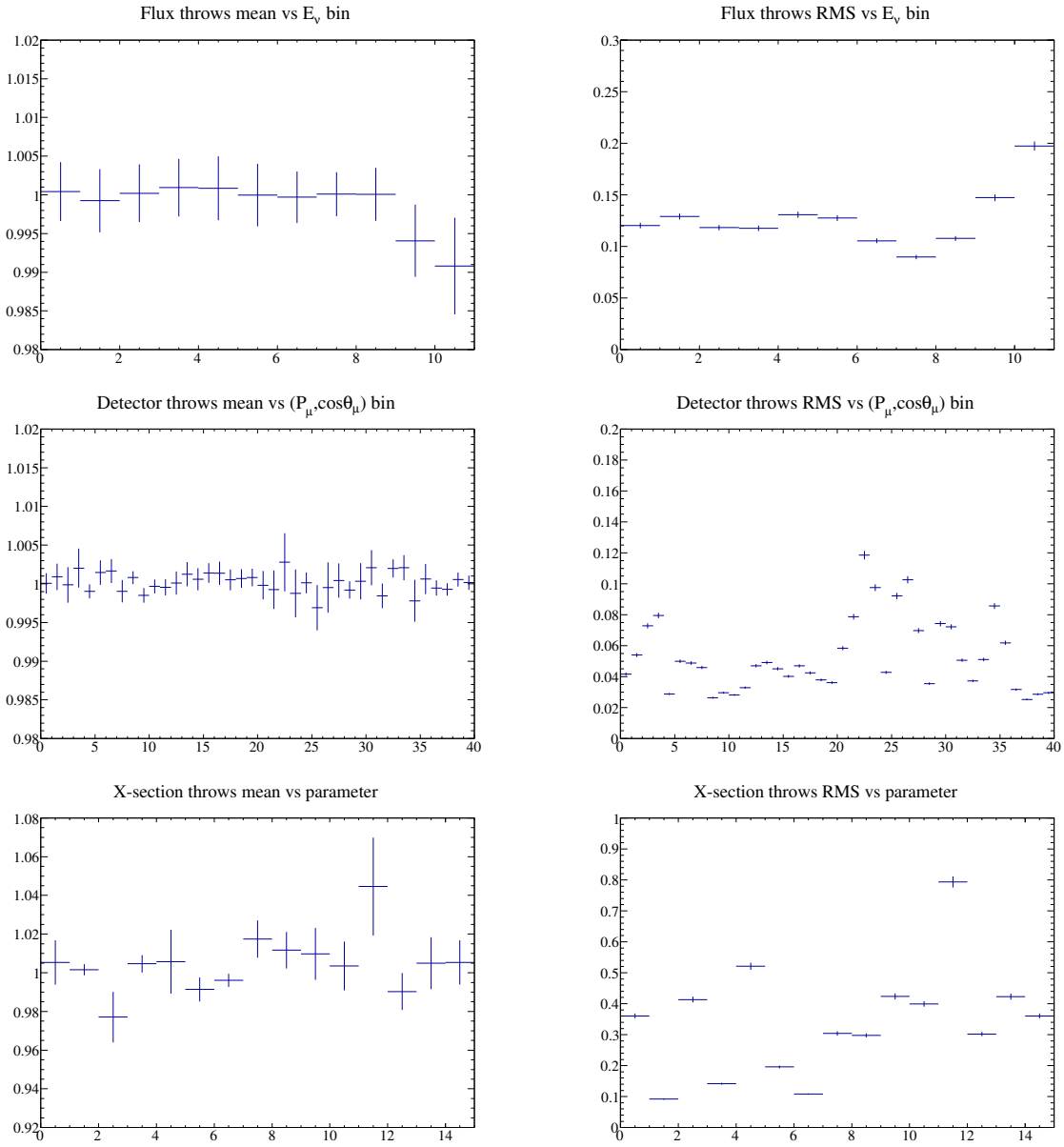

Figure 7.5: Throws mean value and RMS for each source of systematic error. Top: Beam flux. Middle: detector and FSI. Bottom: cross section modeling parameter. Bottom: cross section. The cross section parameters are presented in the following order: 0 (M_A),1 (M_A^{RES}), 2 (CC-oth shape), 3 (p_F) , 4 (W_{shape}), 5 (pion-less Δ decay), 6 (CCQE-E1), 7 (CCQE-E2), 8 (CCQE-E3), 9 (CC1π-E1), 10 (CC1π-E2), 11 (CCCOH), 12 (NCoth), 13 (NC1π^0).

Using the definitions introduced in this section, with $j = 0, ..., 19$ and $k = 0, ..., 24$, the reweighted

number of events are given by:

$$
\begin{aligned}
R_{jk} &= d_j \sum_i^{11} b_i \left(\sum_l^6 x_l(E_i) \omega_{ijkl}^{sel}(\vec{\delta}) n_{ijkl}^{selQE} \right) \\
&\quad + d_{j+20} \sum_i^{11} b_i \left(\sum_l^6 x_l(E_i) \omega_{ijkl}^{sel}(\vec{\delta}) n_{ijkl}^{selnQE} \right) \qquad (7.25) \\
B_{jk} &= d_j \sum_i^{11} b_i \left(\sum_l^6 x_l(E_i) \omega_{ijk}^{\beta^{selQE}}(\vec{\delta}) \beta_{ijk}^{selQE} \right) \\
&\quad + d_{j+20} \sum_i^{11} b_i \left(\sum_l^6 x_l(E_i) \omega_{ijk}^{\beta^{selnQE}}(\vec{\delta}) \beta_{ijk}^{selnQE} \right) \qquad (7.26) \\
M_k &= \sum_i^{11} b_i \left(\sum_l^6 x_l(E_i) \omega_{ikl}(\vec{\delta}) m_{ikl} \right) \qquad (7.27)
\end{aligned}
$$

where R_{jk} and B_{jk} reflect the inclusive charge current selection, x_l the weight of the cross section channel listed in Table 6.13 for the given range of energy, E_i, and $\vec{\delta}$ the fractional change of the parameters listed in Table 6.11.

7.4 Uncertainty on the inferred number of events ($\widehat{N}_{t_k}$)

7.4.1 Statistical uncertainty

The statistical error comes from both data and MC, through the variables P_{jk}, $N_{r_j}^{\text{meas}}$, B_{r_j}, components of Eq. 7.15, as we can see by expressing them explicitly in the following Equation,

$$
\begin{aligned}
\widehat{N}_{t_k} &= \frac{1}{\epsilon_k} \sum_{j=1}^{n_r} P_m(t_k|r_j) \; (N_{r_j}^{\text{meas}} - s_{\text{POT}} B_{r_j}) \\
&= \frac{1}{\sum_{\gamma=1}^{n_r} P_{\gamma k}} \sum_{j=1}^{n_r} \frac{P_{jk} N_{t_k}^m}{\sum_{\alpha=1}^{n_t} P_{j\alpha} N_{t_\alpha}^m} (N_{r_j}^{\text{meas}} - s_{\text{POT}} B_{r_j}) \qquad (7.28)
\end{aligned}
$$

The statistical covariance matrix of $\widehat{N}$ is then given by:

$$
V[\widehat{N}] = \left(\frac{\partial \widehat{N}}{\partial N^{\text{meas}}} \right) V[N^{\text{meas}}] \left(\frac{\partial \widehat{N}}{\partial N^{\text{meas}}} \right)^T + \left(\frac{\partial \widehat{N}}{\partial B} \right) V[B] \left(\frac{\partial \widehat{N}}{\partial B} \right)^T + \left(\frac{\partial \widehat{N}}{\partial P} \right) V[P] \left(\frac{\partial \widehat{N}}{\partial P} \right)^T \qquad (7.29)
$$

where N^{meas} is the number of measured events distribution, B the reconstructed background event distribution, and $P_{jk} \equiv P(r_j|t_k)$, the set of probabilities. In Eq. 7.28, we have expressed the efficiency in terms of the independent variables P_{jk}. As already pointed out in the previous section (Eq. 7.14), we have $\sum_{j=1}^{n_r} P_{jk} = \epsilon_k < 1$. The set of probabilities follows therefore a

multinomial distribution, and the covariance matrix is given by [183] [5]:

$$V_{pqrs}[P] = \left(\frac{1}{N_{t_q}} P_{pq}(1 - P_{pq})\delta_{pr} - \frac{1}{N_{t_q}} P_{pq} P_{rq}(1 - \delta_{pr}) \right) \delta_{qs} \tag{7.30}$$

where δ_{pr} and δ_{qs} is the Kronecker delta function.

Assuming Poisson statistics, the covariance matrix for data is,

$$V_{ij}[N^{\text{meas}}] = N^{\text{meas}}_{r_i} \delta_{ij} \tag{7.31}$$

The covariance matrix due to the background and given by the Monte-Carlo is,

$$V_{ij}[B] = B_{r_i} \delta_{ij} \tag{7.32}$$

Eq. 7.29 can be rewritten as,

$$V[\widehat{N}] = \left(\frac{\partial \widehat{N}}{\partial n} \right) V[n] \left(\frac{\partial \widehat{N}}{\partial n} \right)^T + \left(\frac{\partial \widehat{N}}{\partial P} \right) V[P] \left(\frac{\partial \widehat{N}}{\partial P} \right)^T, \tag{7.33}$$

where the vector n is the number of signal events, $\{n_j \equiv N^{\text{meas}}_{r_j} - s_{\text{POT}} B_{r_j}\}$.

Using this notation, the covariance matrix $V[n]$ is,

$$\begin{aligned} V[n] &= \left(\frac{\partial n}{\partial N^{\text{meas}}} \right) V[N^{\text{meas}}] \left(\frac{\partial n}{\partial N^{\text{meas}}} \right)^T + \left(\frac{\partial n}{\partial B} \right) V[B] \left(\frac{\partial n}{\partial B} \right)^T \\ &= V[N^{\text{meas}}] + s^2_{\text{POT}} V[B] \end{aligned} \tag{7.34}$$

We can express Eq. 7.33 in terms of its element,

$$V_{kl}[\widehat{N}] = \sum_{i,j=1}^{n_r} \frac{\partial \widehat{N}_{t_k}}{\partial n_j} V_{ij}[n] \frac{\partial \widehat{N}_{t_k}}{\partial n_i} + \sum_{p,r=1}^{n_r} \sum_{q,s=1}^{n_t} \frac{\partial \widehat{N}_{t_k}}{\partial P_{pq}} V_{pqrs}[P] \frac{\partial \widehat{N}_{t_l}}{\partial P_{rs}} \tag{7.35}$$

The partial derivatives are then,

$$\begin{aligned} \frac{\partial \widehat{N}_{t_k}}{\partial n_s} &= \frac{1}{\epsilon_k} P_m(t_k|r_s) + \sum_{j=1}^{n_r} \frac{P_{jk} n_j \frac{\partial N^m_{t_k}}{\partial n_s}}{\epsilon_k \sum_{\alpha=1}^{n_t} P_{j\alpha} N^m_{t_\alpha}} - \sum_{j=1}^{n_r} \frac{P_{jk} n_j N^m_{t_k} \sum_{\alpha=1}^{n_t} P_{j\alpha} \frac{\partial N^m_{t_\alpha}}{\partial n_s}}{\epsilon_k (\sum_{\alpha=1}^{n_t} P_{j\alpha} N^m_{t_\alpha})^2} \\ &= U_{sk} + \frac{\widehat{N}_{t_k}}{N^m_{t_k}} \frac{\partial N^m_{t_k}}{\partial n_s} - \sum_{j=1}^{n_r} \sum_{\alpha=1}^{n_t} \frac{\epsilon_\alpha n_j}{N^m_{t_\alpha}} U_{jk} U_{j\alpha} \frac{\partial N^m_{t_\alpha}}{\partial n_s} \end{aligned} \tag{7.36}$$

For only one iteration, we see that,

$$\frac{\partial \widehat{N}_{t_k}}{\partial n_s} = U_{sk} \tag{7.37}$$

which is in agreement with what is found in [183].

[5] Eq. 7.30 corresponds to the general case of the covariance matrix that we would have had in the case of $V[\epsilon]$, for ϵ being the efficiency. In this simpler case, $V_{kr}[\epsilon] = \frac{\epsilon_k(1-\epsilon_k)}{N_{t_k}} \delta_{kr}$

$$
\begin{aligned}
\frac{\partial \widehat{N}_{t_k}}{\partial P_{pq}} &= \frac{\delta_{qk}}{\epsilon_k}\left(\frac{N^m_{t_k} n_p}{\sum_{\alpha=1}^{n_t} P_{p\alpha} N^m_{t_\alpha}} - \widehat{N}_{t_k}\right) + \frac{1}{\epsilon_k}\sum_{j=1}^{n_r} \frac{P_{jk} n_j}{\sum_{\alpha=1}^{n_t} P_{j\alpha} N^m_{t_\alpha}} \frac{\partial N^m_{t_k}}{\partial P_{pq}} - \frac{1}{\epsilon_k} \frac{P_{pk} N^m_{t_k} n_p N^m_{t_m}}{\left(\sum_{\alpha=1}^{n_t} P_{p\alpha} N^m_{t_\alpha}\right)^2} \\
&- \frac{1}{\epsilon_k}\sum_{j=1}^{n_r} \frac{P_{jk} N^m_{t_k} n_j \sum_{\alpha=1}^{n_t} P_{j\alpha} \frac{\partial N^m_{t_\alpha}}{\partial P_{pq}}}{\left(\sum_{\alpha=1}^{n_t} P_{j\alpha} N^m_{t_\alpha}\right)^2} \\
&= \frac{\delta_{qk}}{\epsilon_k}\left(\frac{N^m_{t_k} n_p}{\sum_{\alpha=1}^{n_t} P_{p\alpha} N^m_{t_\alpha}} - \widehat{N}_{t_k}\right) + \frac{\widehat{N}_{t_k}}{N^m_{t_k}} \frac{\partial N^m_{t_k}}{\partial P_{pq}} - \frac{U_{pk} N^m_{t_k} n_p}{\sum_{\alpha=1}^{n_t} P_{p\alpha} N^m_{t_\alpha}} - \epsilon_k \sum_{j=1}^{n_r}\sum_{\alpha=1}^{n_t} \frac{n_j}{N^m_{t_\alpha}} U_{jk} U_{j\alpha} \frac{\partial N^m_{t_\alpha}}{\partial P_{pq}}
\end{aligned} \tag{7.38}
$$

Using Eqs. 7.30, 7.34, 7.36, 7.38 together in Eq. 7.35, we obtain the final covariance matrix due to the statistical error.

To cross-check the statistical error obtained using Eq. 7.38, a completely different method has been built. The NEUT nominal MC has been fluctuated 1000 times, following Poisson statistics at different level independently. The number of selected events has been scaled down to the data POT to reflect the statistics we have in data. This sample is then fluctuated independently to the background that is fluctuated at following the MC statistic as the signal matrix S_{ij} and the number of missed events M_{t_k}.

The number of inferred events in bin k is given by Eq. 7.15,

$$
\widehat{N}^s_{t_k} = \frac{1}{\epsilon^s_k}\sum_{j=1}^{n_r} P^s_m(t_k|r_j)(N^{sel,s}_{r_j} - s_{\rm POT} B^s_{r_j}) \tag{7.39}
$$

where Eq. 7.39 is written explicitly for a given fluctuation s. The following fractional covariance matrix gives the statistical uncertainty,

$$
V^{stat}_{kl} = \frac{1}{M}\sum_{i=1}^{M} \frac{(\widehat{N}^s_{t_k} - \widehat{N}^{(\rm nom)}_{t_k})(\widehat{N}^s_{t_l} - \widehat{N}^{(\rm nom)}_{t_k})}{\widehat{N}^{(\rm nom)}_{t_k}\widehat{N}^{(\rm nom)}_{t_k}} \tag{7.40}
$$

where $\widehat{N}^s_{t_k}$ is the result obtained for the fluctuated MC, and $\widehat{N}^{(\rm nom)}_{t_k}$ the inferred value of the nominal MC for $M = 1000$.

Fig. 7.6 shows the statistical error obtained using both methods for each bins. From this figure, we note that the methods are in good agreement for the bins with enough statistic. For the other bins, the discrepancy is due to the fact that a multinomial error has been used in the mathematical calculation. This error is known to be not valid for low statistic samples as it is the case in the backward angle and momentum larger than 400 MeV. In the following the statistical error for the first bin in angle will be always given following the fluctuation method, while for the other bins, it will be given by the mathematical calculation [6].

[6] There is no real reason to adopt this strategy instead of only using the fluctuation method. In the future, the statistical method might be the only one considered.

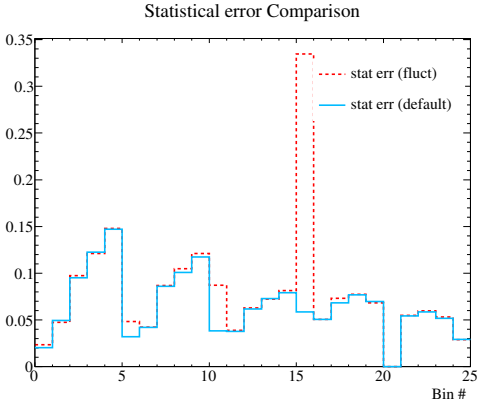

Figure 7.6: Statistical error for the default method and the one obtained by fluctuating the MC following the Poisson statistics.

7.4.2 Systematic uncertainty

To propagate the systematic errors to the final result, we reweight each systematic source separately as they are assumed to be independent. The separated propagation allows us to understand the influence of each source.

The nominal NEUT MC is reweighted 200 times following the procedure described in Sec. 7.3, in Eqs. 7.25, 7.26 and 7.27.

The number of events in the true and reconstructed bin is given for each group of systematic uncertainty:

- Reweighted matrices for a systematic change of the flux

$$\begin{aligned} R_{jk}^{(b)} &= \sum_{i,l} b_i n_{ijk} \\ B_{jk}^{(b)} &= \sum_{i,l} b_i \beta_{ijkl} \\ M_{k}^{(b)} &= \sum_{i,l} b_i m_{ikl} \end{aligned} \tag{7.41}$$

- Reweighted matrices for a systematic change in the cross sections

$$\begin{aligned} R_{jk}^{(x)} &= \sum_{i,l} \omega_{ijkl}^{sel}(\vec{\delta}) x_l(E_i) n_{ijkl} \\ B_{jk}^{(x)} &= \sum_{i,l} \omega_{ijkl}^{\beta}(\vec{\delta}) x_l(E_i) \beta_{ijkl} \\ M_{k}^{(x)} &= \sum_{i,l} \omega_{ik}(\vec{\delta}) x_l(E_i) m_{ikl} \end{aligned} \tag{7.42}$$

- Reweighted matrices for a systematic change in the detector or final state interaction

$$\begin{aligned} R_{jk}^{(d)} &= d_j \sum_{i,l} n_{ijkl}^{selQE} + d_{j+20} \sum_{i,l} n_{ijkl}^{selnQE} \\ B_{jk}^{(d)} &= d_j \sum_{i,l} \beta_{ijkl}^{selQE} + d_{j+20} \sum_{i,l} \beta_{ijkl}^{selnQE} \end{aligned} \tag{7.43}$$

where the label $b,\ x,\ d$ denotes the group for which the events have been reweighted, namely: the beam, the cross section and the detector response or the FSI. Note that we summed the CCQE-like sample with the CCnQE-like sample together at this stage. The reweighted MC is, from now on, independent of the CCQE-like and CCnQE-like selection, and only reflects the CC inclusive selection.

For a given reweighted MC, $s = b,\ x$ or d, we can express the various variables needed to unfold the distribution of measured events in terms of $R_{jk}^{(s)},\ B_{jk}^{(s)}$ and $M_k^{(s)}$. These variables are expressed as,

$$\begin{aligned} B_{r_j}^{(s)} &\equiv \sum_k^{n_t} B_{jk}^{(s)} \\ S_{jk}^{(s)} &\equiv R_{jk}^{(s)} - B_{jk}^{(s)} \\ N_{t_k}^{(s)} &= \sum_j^{n_r} S_{jk}^{(s)} + M_k^{(s)} \\ U_{jk}^{(s)} &= \frac{1}{\epsilon_k} \frac{S_{jk}}{\sum_\alpha S_{j\alpha}} \\ &= \frac{N_{t_k}}{\sum_\gamma^{n_r} S_{\gamma k}} \frac{S_{jk}}{\sum_\alpha^{n_t} S_{j\alpha}} \end{aligned} \tag{7.44}$$

where the unfolding matrix $U_{kj}^{(s)}$ is expressed as a function of $S_{jk}^{(s)}$ and $N_{t_k}^{(s)}$. The number of inferred events in the true bin t_k is given by,

$$\widehat{N}_{t_k}^{(s)} = \sum_{j=1}^{n_r} U_{kj}^{(s)} (N_{r_j}^{\text{meas(data)}} - B_{r_j}^{(s)}) \tag{7.45}$$

Note that the whole background is reweighted. This is not correct in theory, as there is a fraction of the background corresponding to the CC inclusive interaction outside the fiducial volume but inside the FGD scintillator. This background is, in a sense, part of our signal. Since, it only corresponds to 1% of the selection, the change in the result is assumed negligible.

The fractional covariance matrix, is given by,

$$V_{kl}^{(s)} = \frac{1}{M} \sum_{i=1}^{M} \frac{(\widehat{N}_{t_k}^{(s_i)} - \widehat{N}_{t_k}^{(\text{nom})})(\widehat{N}_{t_l}^{(s_i)} - \widehat{N}_{t_l}^{(\text{nom})})}{\widehat{N}_{t_k}^{(\text{nom})} \widehat{N}_{t_l}^{(\text{nom})}} \tag{7.46}$$

where (nom) labels the nominal MC which is the central value of the throw distribution, s_i labels the i-th throw or reweight MC for a definite systematic source $s = b, d, x$, and $M = 200$ and represent the number of reweighted MCs.

In the case of the *spectral function (SF)* and *1π-E_ν shape (1πS)* parameter the covariance matrix is given by,

$$V_{kl}^{(s)} = \frac{(\widehat{N}_{t_k}^{(X,ON)} - \widehat{N}_{t_k}^{(\text{nom})})(\widehat{N}_{t_l}^{(X,ON)} - \widehat{N}_{t_l}^{(\text{nom})})}{\widehat{N}_{t_k}^{(\text{nom})} \widehat{N}_{t_l}^{(\text{nom})}} \tag{7.47}$$

where $X = SF,\ 1\pi\text{S}$.

The total covariance matrix due to the uncertainty on the cross section modeling is then given by adding in quadrature these two additional contributions to the rest of the cross section covariance matrix,

$$V_{kl}^{(x-s)} = V_{kl}^{(x)} + V_{kl}^{(SF)} + V_{kl}^{(1\pi S)}. \tag{7.48}$$

As the sources of systematic errors are independent between each group, the total covariance matrix associated to the systematic error of the experiment is the sum of each covariance matrix,

$$V_{kl}^{syst} = V_{kl}^{(d)} + V_{kl}^{(FSI)} + V_{kl}^{(x-s)} + V_{kl}^{(b)}. \tag{7.49}$$

7.5 The number of iterations

For an unlimited MC and data statistics, the number of iterations suggested by the literature is small and around 3 [183]. This is explained by the fact that in the limit of m going to infinity, the unfolding matrix tends to the inverse of the folding matrix, which is known to have big fluctuations. Therefore a small number of iterations should be chosen. If the initial MC used to unfold the data, does not describe precisely the reality, doing more than one iteration should decrease the bias due to the method. On the contrary, if bins have low statistics, the statistical error is propagated and can be amplified during the iteration process.

In this section, we then try to understand what we should expect when unfolding our data samples for different iteration number. From these studies, the number of iterations is chosen. To this end, different data size MC samples are created and compared. In the following studies, the unfolding is always done using the NEUT generator. The number of iterations will be chosen, by looking at the deviation between the inferred value obtained via the unfolding method and the truth of the fake data set.

The various types of the fake data sets are defined as the following:

1. **The fake data is the complete NEUT MC scaled to the data statistics**
   - The nominal MC is reweighted 1000 times following the systematic uncertainties following Eq. 7.25, 7.26 and 7.27.
   - The nominal MC is scaled to the number of POT of the data.
   - The content of each scaled and reweighted bin is then fluctuated following the Poisson statistics.
   - The nominal NEUT MC is used for the unfolding.
2. **The fake data is a sub-sample of the NEUT MC about the same size of the data statistics and scaled to the data statistics**
   - The nominal NEUT MC is separated into two samples, one small sample similar to the size of the data sample and the rest.
   - The small sample is scaled to match exactly the number of POT of the data.
   - The small sample is fluctuated 1000 times following Poisson statistics.

- The big sample is used for the unfolding.

3. **The fake data is the complete GENIE MC scaled to the data statistics**

   - The complete GENIE MC is scaled to the number of POT of the data.
   - The content of each scaled bin is then fluctuated 1000 times following the Poisson statistics.
   - The nominal NEUT MC is used for the unfolding.

Table 7.1 gives the number of interactions expected in each true bin for the number of POT of run I and run II. It shows in particular that many bins have less than 100 events.

Table 7.1: Number of charged current interactions in each reconstructed bin, for each category (first 3 columns). In this case, the bins $[-1, 0]$ and $[0., 0.84]$ are merged together. The other columns show the number of simulated events in each true bins, normalized to the data POT for each fake data category (truth information).

P_μ (GeV/c)	$\cos\theta_\mu$	$N_{r_j}^{\text{neut}}$	$N_{r_j}^{\text{neut-part}}$	$N_{r_j}^{\text{genie}}$	$N_{t_k}^{\text{neut}}$	$N_{t_k}^{\text{neut-part}}$	$N_{t_k}^{\text{genie}}$
$[0.0, 0.4]$	$[-1, 0]$	555.3	545.0	551.4	1149.0	1136.3	1000.8
	$[0, 0.84]$				1529.5	1566.5	1439.1
	$[0.84, 0.90]$	78.1	71.5	83.6	88.5	78.0	95.1
	$[0.90, 0.94]$	54.0	51.0	55.3	56.6	48.7	57.6
	$[0.94, 1]$	63.6	70.7	82.2	61.4	52.4	75.2
$[0.4, 0.5]$	$[-1, 0]$	377.9	380.1	341.2	70.7	71.1	60.6
	$[0, 0.84]$				768.3	780.3	700.9
	$[0.84, 0.90]$	62.3	64.7	66.7	71.9	75.1	72.2
	$[0.90, 0.94]$	43.8	46.9	38.9	44.2	42.6	41.3
	$[0.94, 1]$	53.9	55.0	54.1	50.1	47.5	45.7
$[0.5, 0.7]$	$[-1, 0]$	497.8	502.4	460.4	12.3	7.9	9.6
	$[0, 0.84]$				865.0	884.4	775.4
	$[0.84, 0.90]$	138.1	135.2	133.0	175.3	165.2	167.5
	$[0.90, 0.94]$	98.3	89.5	92.6	112.9	110.3	105.1
	$[0.94, 1]$	130.8	140.5	127.4	126.0	128.6	118.1
$[0.7, 0.9]$	$[-1, 0]$	211.4	226.5	190.0	0.6	0.9	0.1
	$[0, 0.84]$				287.1	258.1	256.2
	$[0.84, 0.90]$	94.5	83.0	88.6	110.3	109.8	103.5
	$[0.90, 0.94]$	73.5	70.5	68.9	80.3	75.5	76.9
	$[0.94, 1]$	111.5	120.8	108.1	106.0	107.0	100.2
$[0.9, 30.0]$	$[-1, 0]$	301.6	301.8	256.6	-	-	-
	$[0, 0.84]$				335.0	333.9	258.1
	$[0.84, 0.90]$	242.6	235.1	218.6	287.8	282.9	250.3
	$[0.90, 0.94]$	294.0	294.3	280.4	350.6	339.5	323.3
	$[0.94, 1]$	1240.7	1223.5	1238.1	1536.6	1541.8	1481.2
	total	4723.5	4708.0	4536.1	8276.2	8244.4	7614.2

Fig. 7.7 shows the statistical error calculated on the inferred number of events for the first category. The statistical error is obtained using the method described in Sec. 7.4.1. As the data has relatively low statistics in some bins, the statistical error increase at each step of the

iterative procedure and tends to quite high values. In addition, the chosen $(p_\mu, \cos\theta_\mu)$ binning varies a lot from one bin to another. The statistical error in one bin can be of the same order as the content of neighboring bins. It is, therefore, expected that the bins with lower statistics are unstable with an increase of the iteration number.

The first bin in momentum and angle, in Fig. 7.7, has a bigger statistical error than the last bin in momentum and angle. This is explained by the fact that the first bin has a very low efficiency, the statistical error on the number of measured events is much bigger than the last bin, which has a quite good efficiency.

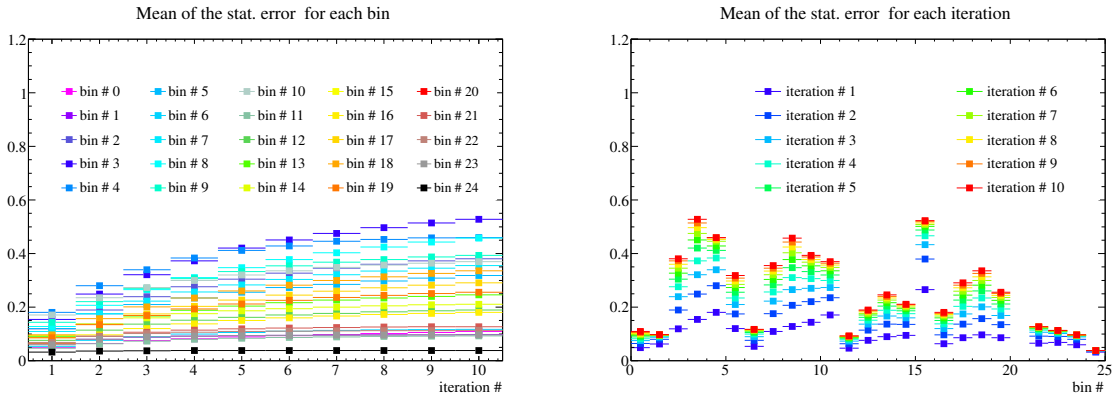

Figure 7.7: Statistical error for the 1^{st} category of the fake data sets (complete NEUT MC).

From the results shown in Fig. 7.7, we understand that if the deviation to the truth increases at the same time as the statistical error in the bin, a pull estimator would not represent, what is really happening in the bin. Therefore, we decided to use the mean deviation to the truth as the estimator of the right number of iterations to be chosen in our case. The deviation to the truth value represents the bias of the method and is given by,

$$\frac{\langle \widehat{N}^s_{t_k} \rangle - N^{\text{truth}}_{t_k}}{N^{\text{truth}}_{t_k}} \tag{7.50}$$

where s represents a fluctuated or reweighted sample. The mean of the fluctuated $\widehat{N}^s_{t_k}$ is given by,

$$\langle \widehat{N}^s_{t_k} \rangle = \frac{1}{1000} \sum_{s=0}^{1000} \widehat{N}^s_{t_k} \tag{7.51}$$

In Fig. 7.8, 7.9, 7.10, the mean deviation is represented as a function of the iteration number and bin number for the three fake data set categories. For each category, we observe that the deviation with respect to the truth for all bins, increases with the number of iterations. Especially low statistic bins have a bigger deviation than the others. In addition, we observe that the second fake data set is less stable than the other two fake data sets. This is explained by the fact that this set contains more variation between its bins. The fluctuation is then due to the bin-to-bin variation. As the same behavior is obtained with the three fake data sets, we expect the same behavior with data. Therefore the first iteration is chosen for the rest of the analysis, as it gives the closest result to the reality.

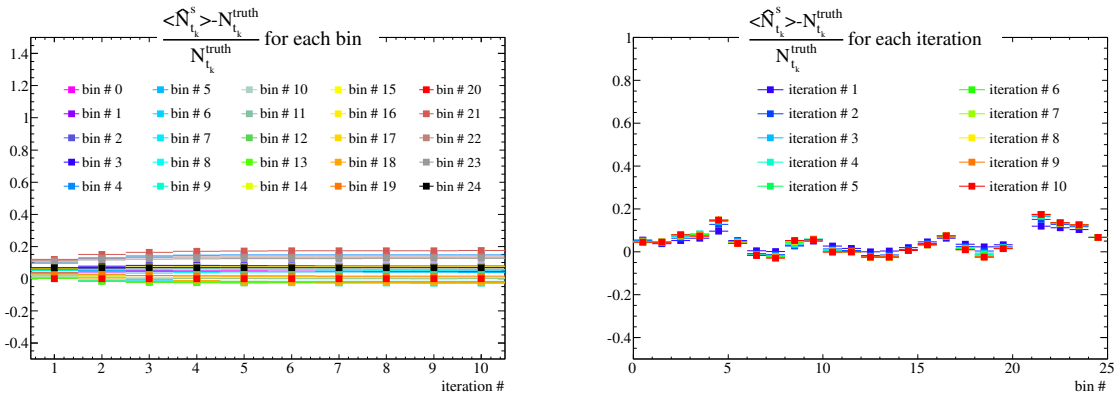

Figure 7.8: Mean deviation to the truth for the 1^{st} category of fake data sets (complete NEUT MC).

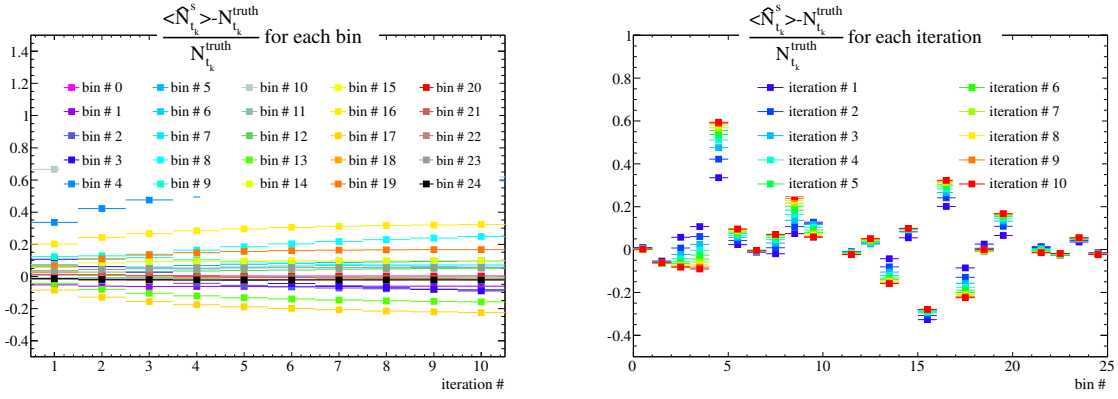

Figure 7.9: Mean deviation to the truth for the 2^{nd} category of fake data sets (sub-sample of the NEUT MC).

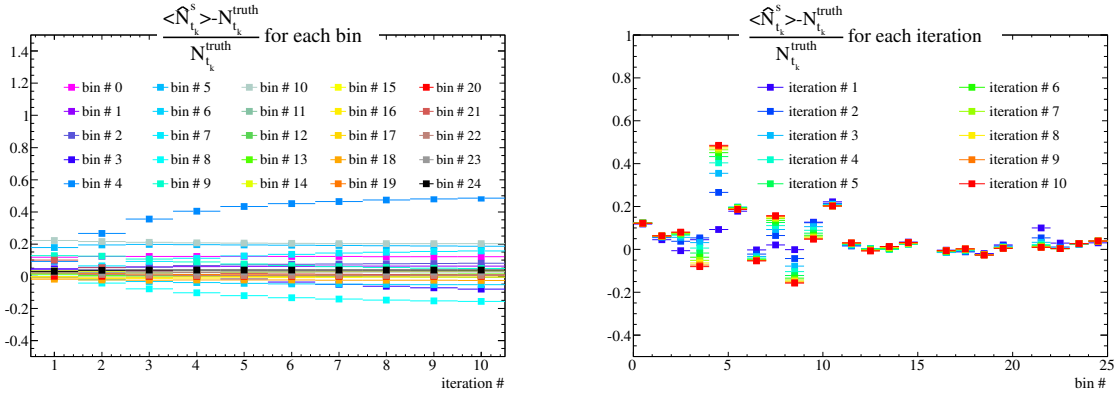

Figure 7.10: Mean deviation to the truth for the 3^{rd} category of fake data sets (complete GENIE MC).

7.6 Summary

In this chapter, the method chosen to compute the final cross section result is explained. The final cross section result will be a flux averaged double differential cross section in the muon kinematics variables. The method is a model independent method based on the Bayes' theorem. Although this method is an iterative method, only one iteration is used as the statistics of the data is too low in certain bins in comparison to others. This bin-to-bin fluctuation makes the method unstable for higher iteration number. For future analyses, it is then greatly suggested to have a binning chosen so that the bin content of all bins are of the same order of magnitude. In addition to that, the propagation of the systematic errors has been explained. The propagation uses a technique that takes into account the various correlations for all source of uncertainties. The Cholesky decomposition of the covariances is used to compute the weights that are then used to reweight the MC. The final covariance matrix for each source of uncertainty is then given as the RMS between the nominal and the reweighted MC. The reweighting procedure uses a response function technique instead of a complete reweighting of the MC for each parameter variation to save time and CPU. In the next chapter, the final cross section results based on this method will be given.

Chapter 8

Cross section measurements

In this chapter, the final cross section results are shown for Run I and II together, using the unfolding method described in the previous chapter. The MC used to unfold the data has been normalized to the respective number of POT of each run.

In Eq. 7.7, we have defined the differential cross section in terms of the final state variables $b_{1,k}$ and $b_{2,l}$. In our case the final state variables are the muon momentum, $b_1 \equiv p_\mu$, and angle, $b_2 \equiv \cos\theta_\mu$. The flux averaged differential cross section of inclusive charged current is then given by,

$$\langle \frac{\partial^2\sigma}{\partial p_\mu \partial \cos\theta_\mu} \rangle_{kl} = \frac{\widehat{N}_{kl}}{T\phi\Delta p_{\mu,k}\Delta\cos\theta_{\mu,l}} \tag{8.1}$$

where

- ϕ is the integrated flux at the near detector
- T the number of target nucleons
- $\widehat{N}_{kl}$ is the unfolded number of events in the true p_μ bin k and true $\cos\theta_\mu$ bin l.

In the following, a discussion on the integrated flux and its uncertainty propagated to the final result is done in Sec. 8.1.1. The additional systematic errors due to the uncertainty on the number of target nucleons and on the algorithm is presented in Secs. 8.1.2 and 8.1.3. The resulting systematic and statistical error on the cross section measurement is discussed in Sec. 8.1.4. The flux averaged differential cross section and the flux averaged total cross section for the T2K neutrino beam is presented at the end of the chapter.

8.1 Additional systematic error on the cross section measurement

8.1.1 Integrated Flux

The flux used for this analysis is the tuned 11b-v3.1 version provided by the beam group of the T2K collaboration [136]. For each run, a different flux is computed. It corresponds to the flux of neutrino at the near detector site, in the basket region (inside the magnet)

It is evaluated on the flux prediction integrated over a 150×150 cm^2 centered around 0 on the x and y basket plane. In theory, we should use the flux integrated in the FGD fiducial volume, however as this area overlaps almost exactly with the FGD fiducial volume, the effect is very small. The integrated flux number is obtained by adding the bin contents of the muon neutrino flux shown in Fig. 8.1 taking into account the overflow. Normalizing to the data POT,

$$\phi_{run1+run2} = 0.573 \cdot 10^{12} + 1.52 \cdot 10^{12} = 2.09 \cdot 10^{12} cm^{-2} \tag{8.2}$$

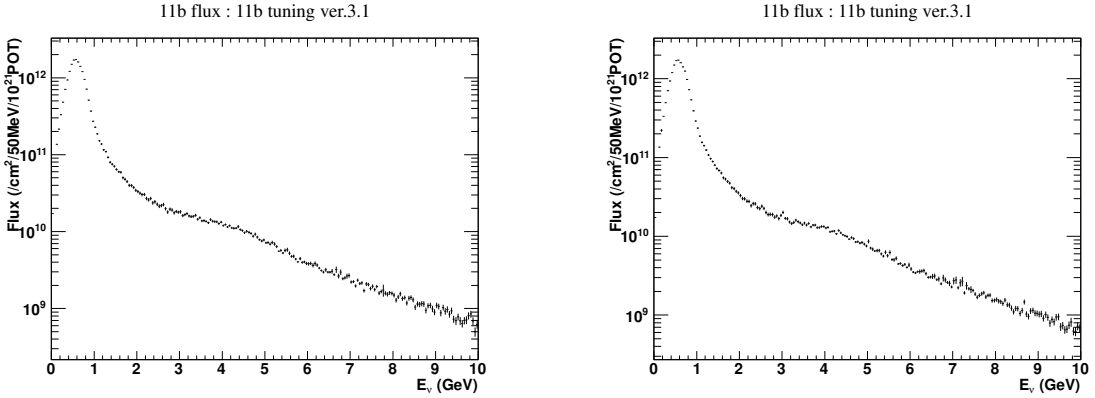

Figure 8.1: Fine binned ν_μ flux at the near detector for run I (left) and run II (right) [136].

The systematic error due to the beam flux is calculated on the cross section measurement and is not given by Eq. 7.47, as the flux normalization should be taken into account. In consequence, the fractional covariance matrix is given by,

$$\begin{aligned} V_{kl}^{(b)} &= \frac{1}{M}\sum_{i=1}^{M} \frac{(\frac{\widehat{N}_{t_k}^{(s_i)}}{\phi^{(s_i)}} - \frac{\widehat{N}_{t_k}^{(\mathrm{nom})}}{\phi^{(\mathrm{nom})}})(\frac{\widehat{N}_{t_l}^{(s_i)}}{\phi^{(s_i)}} - \frac{\widehat{N}_{t_l}^{(\mathrm{nom})}}{\phi^{(\mathrm{nom})}})}{\frac{\widehat{N}_{t_l}^{(\mathrm{nom})}}{\phi^{(\mathrm{nom})}} \cdot \frac{\widehat{N}_{t_k}^{(\mathrm{nom})}}{\phi^{(\mathrm{nom})}}} \\ &= \frac{1}{M}\sum_{i=1}^{M} \frac{(\widehat{N}_{t_k}^{(s_i)} \frac{\phi^{(\mathrm{nom})}}{\phi^{(s_i)}} - \widehat{N}_{t_k}^{(\mathrm{nom})})(\widehat{N}_{t_l}^{(s_i)} \frac{\phi^{(\mathrm{nom})}}{\phi^{(s_i)}} - \widehat{N}_{t_l}^{(\mathrm{nom})})}{\widehat{N}_{t_k}^{(\mathrm{nom})} \widehat{N}_{t_l}^{(\mathrm{nom})}} \end{aligned} \tag{8.3}$$

where (nom) labels the nominal MC, s_i labels the i-th throw or reweighted MC for the beam systematic source (b), and $M = 200$ and represents the number of reweighted MCs used. The fractional covariance matrix is shown in Fig. 8.2.

To understand why the covariance matrix in Fig. 8.2 varies very slightly from bin to bin, we can try to calculate what is the total error on the integrated flux. To that end, the flux is re-binned following Table 6.3, to be able to use the fractional covariance matrix given by the beam group.

The absolute systematic uncertainty is given by,

$$\delta\phi^{syst} = \sqrt{\sum_i \sum_j V_{ij}^b \phi_i \phi_j} \tag{8.4}$$

This error represents the total error on the integrated flux, as the statistical error in this case is negligible. The total flux and error for both runs together showing explicitly the normalization

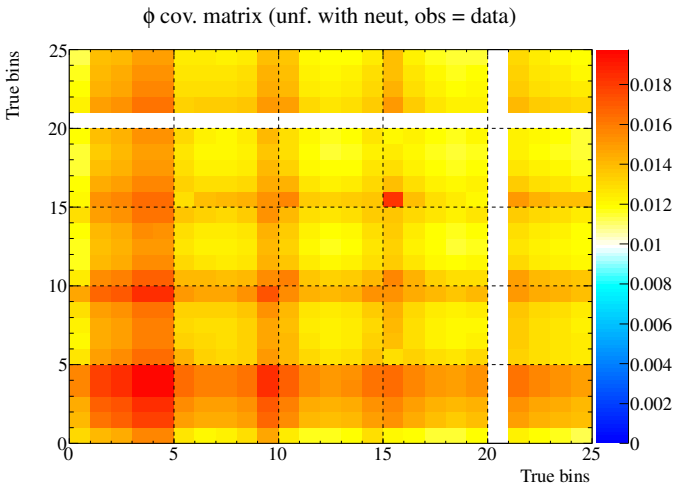

Figure 8.2: Total flux fractional covariance matrix.

factors s^{I}_{POT} and s^{II}_{POT} for run I and run II respectively is then,

$$\phi = s^{\mathrm{I}}_{POT}\phi^{\mathrm{I}} + s^{\mathrm{II}}_{POT}\phi^{\mathrm{II}} \tag{8.5}$$

$$\frac{\delta\phi}{\phi} = \frac{s^{\mathrm{I}}_{POT}\delta\phi^{\mathrm{I}} + s^{\mathrm{II}}_{POT}\delta\phi^{\mathrm{II}}}{s^{\mathrm{I}}_{POT}\phi^{\mathrm{I}} + s^{\mathrm{II}}_{POT}\phi^{\mathrm{II}}} = 10.9\%, \tag{8.6}$$

This error represents mainly the normalization part of the flux systematic error. It also explains why the flux systematic error is more or less constant in all the bins. If we now consider the case where our measurement would not have background. Then this error would have been the normalization part of the flux systematic error, while Eq. 7.47 would have given only the shape part of the systematic error. As the unfolding matrix is built by a multiplication of probabilities (Bayes' theorem), it has only a shape dependence on the flux. Without background, we would have then add in quadrature 10.9 % error to the shape error. Since our selection contains a 13% of background (Table 5.8), the flux normalization dependence in the background has to be taken into account. Therefore, the method depicted by Eq. 8.3 is used. Note that we only use the uncertainty on the muon neutrino flux. The background does not only contain muon neutrino interactions but also electron neutrino and anti-neutrino interactions. The amount of those backgrounds compared to the amount of muon neutrino is considered negligible, therefore we do not distinguish them by applying different uncertainties.

8.1.2 Number of Target Nucleons

The fiducial volume for this analysis is chosen so that the first XY layer is not taken into account, and set at the beginning of the second XY module. In the X and Y dimension, a distance equivalent to five bars on each side is removed (red line in Fig. 5.4). The fiducial volume is then given by: $V_{ND} = 174.90 \times 174.90 \times 31.00 = 9.49 \cdot 10^5 cm^3$. Table 8.1 shows the composition of the first FGD, with its calculated density.

Note, that in this table, the total density has been calculated without the wavelength-shifting fibers contained in each bars, as they have not been simulated in the 4C MC production. Since the density is comparable to the density of the XY module, neglecting the fibers has no consequences in the final result. The calculation of the final density, given in Table 8.1, should be

Table 8.1: XY module composition from [186]. The first column gives the areal density, $a = \rho\Delta z$, where Δz is the thickness of each piece and ρ, the density of each material. The total density value of the scintillator is here given for our fiducial volume.

Pieces	Areal density (g/cm^2)	Δz mm	ρ (g/cm^3)
G10 (2×)	0.0789	0.232 ×2	1.700
glue layer 1 (2×)	0.0346	0.188 ×2	0.920
glue layer 2	0.0175	0.19	0.920
XY Module	2.00071	9.61 ×2	1.041
air	0.00026	2.0	0.00129
fibers	0.0002	0.0019	1.050
total	2.132	22.25	0.963

computed so that the first air gap is not taken into account. As there are 14 XY sheets included in the fiducial volume, the density is given by,

$$\rho_{scint,FV} = \frac{14 \times \sum_{i}^{N_{\text{comp.}}} \rho_i \Delta z_i - \rho_{air}\Delta z_{air}}{\Delta z_{scint,FV}} = 0.963\ g/cm^3 \tag{8.7}$$

where $N_{\text{comp.}}$ is the number of components in the scintillator and $\Delta z_{scint,FV} = 31\ cm$ is the width of the FGD1 FV volume.

Component	C	O	H	Ti	Si	N	Total
Scintillator bars	1.7651 ± 0.0067	0.0248 ± 0.0039	0.1468 ± 0.0006	0.0355 ± 0.0059	0	0.0010 ± 0.00004	1.973 ± 0.0104
G10	0.0196 ± 0.0015	0.0331 ± 0.0001	0.0034 ± 0.0018	0	0.0218 ± 0.0043	0.0013 ± 0.0013	0.079
Plexus MA590	0.0484 ± 0.0060	0.0215 ± 0.0027	0.0065 ± 0.0008	0	0	0.0009 ± 0.0001	0.0774 ± 0.0096
fiber	0.0155	0.00002	0.0013	0	0	0.00002	0.0169
XY module	1.849 ± 0.0092	0.0794 ± 0.0048	0.1579 ± 0.0021	0.0355 ± 0.0059	0.0218 ± 0.0043	0.0031 ± 0.0012	2.147 ± 0.0144

Table 8.2: Elemental composition of the components of a typical XY layer, in g/cm^2 of each element [152]

From Table 8.2, we can deduce the fraction of each atom in the FGD, allowing us the calculation of the molar mass:

$$M_{\text{scint}} = \sum_{a=C,O,H,Ti,Si,N} f_a \times M_a = 12.108\ g/mol, \tag{8.8}$$

where M_a is the atomic mass and $f_a = \frac{a_a}{a_{scint}}$ the fraction of each element given in Table 8.3 and obtained from the areal density of each atom, a_a of Table 8.2.

The averaged number of nuclei is given by,

$$T_N = \frac{\rho_{\text{scint}} \cdot V_{ND}}{M_{\text{scint}}} N_A = 4.5 \cdot 10^{28} \tag{8.9}$$

where $N_A = 6.022 \cdot 10^{23}\ mol^{-1}$ is the Avogadro number. Expressing T as depending on the areal density of the scintillator a_{scint} and areal density of each atom a_a, we have,

$$T_N = \frac{N_A V_{ND}}{\Delta z} \frac{(\sum_a a_a)^2}{\sum_a a_a M_a} \tag{8.10}$$

The error on the total number of *averaged nuclei* is calculated taking all the correlations between the different nuclei. We obtain,

$$\frac{\delta T_N}{T_N} = 0.85\% \tag{8.11}$$

To get the averaged number of nucleons inside the scintillator, the natural abundance of each isotope of each atom in the scintillator is needed. Table 8.3 summarizes this information. As we are looking at CC-inclusive neutrino interactions, we do not differentiate between neutrons and protons, and take both into account as total number of nucleons. If we had looked only to quasi-elastic interactions, we would have taken only the fraction of neutrons inside the scintillator as number of target nucleons.

Table 8.3: Abundance of the different isotope of the different nuclei. The fraction of each atom inside the scintillator is obtained from Table 8.2.

Atoms	A	Natural abundance (%)	Averaged A	Fraction in scintillator (%)
C	12	98.9	12.011	86.13
C	13	1.1		
O	16	99.762		
O	17	0.038	16.0044	3.70
O	18	0.2		
H	1	99.985	1.00015	7.36
H	2	0.015		
Ti	46	8.		
Ti	47	7.5		
Ti	48	73.8	48.024	1.65
Ti	49	5.5		
Ti	50	5.4		
Si	28	92.22		
Si	29	4.68	28.1058	1.01
Si	30	3.09		
N	14	99.634	14.00366	0.14
N	15	0.366		

The number of nucleons is given by,

$$T = N_A V_{ND} \cdot \rho_{scint} \cdot \sum_a f_a \frac{A_a}{M_a} = 5.50 \cdot 10^{29}, \tag{8.12}$$

where A_a are the averaged number of nucleons per nuclei given in Table 8.3 and M_a the atomic mass. From this number, we see that the assumption of a molar mass of the nucleon of 1 g/mol would have been enough, for the calculation of the total number of target nucleons. Eq. 8.12 can be expressed in terms of the variables a_{scint} and a_a,

$$T = \frac{N_A V_{ND}}{\Delta z} \cdot \rho_{scint} \sum_a f_a \frac{A_a}{M_a} \tag{8.13}$$

$$T = \frac{N_A V_{ND}}{\Delta z} \cdot \sum_a a_a \frac{A_a}{M_a} \tag{8.14}$$

The error on the total number of target nucleon is obtained by taking the full correlations between the nuclei,

$$\delta T^2 = \sum_{a,b} \left(\frac{\partial T}{\partial a_a}\right) cov_{ab} \left(\frac{\partial T}{\partial a_b}\right) \tag{8.15}$$

$$= T^2 \frac{\sum_{a,b} \frac{A_a A_b}{M_a M_b} cov_{ab}}{\left(\sum_a a_a \frac{A_a}{M_a}\right)^2} \tag{8.16}$$

where the covariance coefficient are taken from [152]. We find,

$$\frac{\delta T}{T} = 0.67\% \tag{8.17}$$

In the rest of the analysis, we will use both definitions for the total number of target nucleons. While giving the result for a total number of nuclei, allows us to keep the whole information of the scintillator composition, giving the result for a total number of nucleons allows us to compare with other experiments.

For completeness, we can calculate the fraction of protons, and neutrons in our scintillator,

$$f_n = \frac{\sum_a r_a (A_a - Z_a)}{\sum_a r_a A_a} = 53.6\% \tag{8.18}$$

$$f_p = \frac{\sum_a r_a Z_a}{\sum_a r_a A_a} = 46.4\% \tag{8.19}$$

where r_a is the fraction of nuclei defined as: $r_a = \frac{a_a/A_a}{\sum_a a_a/A_a}$.

8.1.3 Systematic uncertainty due to the algorithm

Two biases can be taken into account as systematic uncertainty of the algorithm. The first bias comes from the ability of the algorithm to return its true value, when giving it the same MC as fake data. The result for the first bias, is obtained by unfolding the NEUT MC with itself and is shown in Fig.8.3. We see that the difference is of the order of 10^{-6}.

The second bias is a little bit subtler. In Sec. 7.4.1, we have calculated the error due to the statistics of the MC and the data. There is, however, an additional error, that is the bias due to the statistics. We have seen, that the statistical error can be approximately represented by the RMS of a sample varied statistically and compared with the inferred value of the nominal MC. The statistical error does not take into account the bias that we can have because of the statistics used. We follow, here the same method as in Sec. 7.4.1 to compute the bias due to the statistics of the MC and the data. The bias is represented by the mean of the deviation of the fluctuated sample to the inferred value of the nominal MC. The result of the second bias is taken as the systematic error and the fractional covariance matrix is defined as,

$$V_{kl}^{algo} = \frac{(\langle \widehat{N}_{t_k}^s \rangle - \widehat{N}_{t_k}^{\rm nom})(\langle \widehat{N}_{t_l}^s \rangle - \widehat{N}_{t_l}^{\rm nom})}{\widehat{N}_{t_k}^{\rm nom} \widehat{N}_{t_l}^{\rm nom}} \tag{8.20}$$

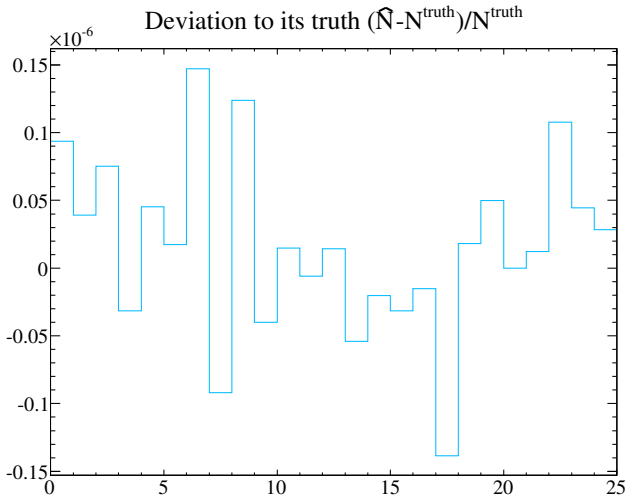

Figure 8.3: Difference between the inferred number of events and its true value.

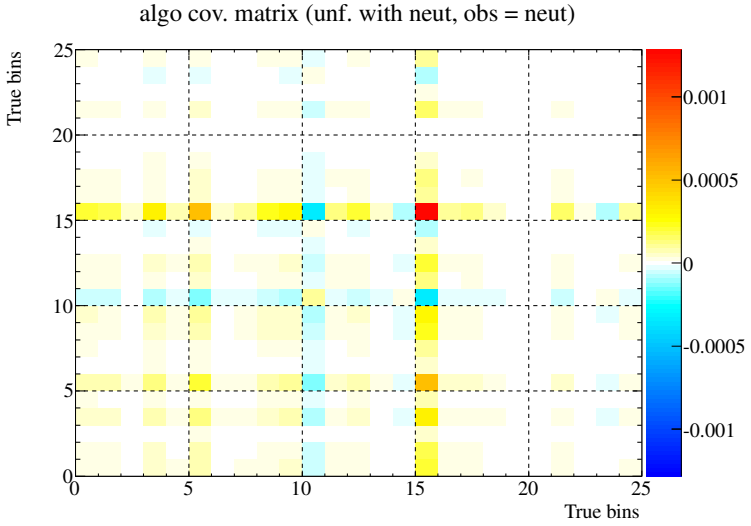

Figure 8.4: Covariance matrix for the goodness of the algorithm. The unfolding has been done with the nominal NEUT MC fluctuated following the MC statistics, while the fake data is the nominal NEUT MC fluctuated following the Data statistics.

where $\langle \widehat{N}^s_{t_k} \rangle = \frac{1}{M} \sum_s \widehat{N}^s_{t_k}$ is the mean of the fluctuated samples, labelled by s. Fig. 8.4 shows the fractional covariance matrix, obtained by scaling down the NEUT MC to the data POT and fluctuating it 1000 times, following Poisson statistics.

The biggest systematic error is obtained for the bins where there is a very small statistics (e.g backward going angle for momentum higher than 400 MeV, see Fig. 8.4). In the next section, we will see that the systematic error for the other bins is almost negligible in comparison with the other sources of systematic error.

8.1.4 Total systematic and statistical error

In this section, we show the relative systematic error for each $(P_\mu, \cos\theta_\mu)$ bin following the procedure explained in Secs. 7.4.2, 8.1.1, 8.1.2 and 8.1.3. The complete list of systematic errors considered for the double differential cross section measurement is:

1. **Uncertainty on the inferred number of events ($\widehat{N}_{t_k}$, see Sec. 7.4.2)**
   - **cross section modeling**
   - **Final State Interaction (FSI)**
   - **Detector response**
2. **Beam flux error (see Sec. 8.1.1)**
3. **Mass uncertainty (see Sec. 8.1.2)**
4. **Systematic uncertainty due to the algorithm (see Sec. 8.1.3)**

The fractional covariance matrices for the cross section modeling, detector and FSI is shown in Fig. 8.5 and the diagonal elements are listed in Table 8.4.

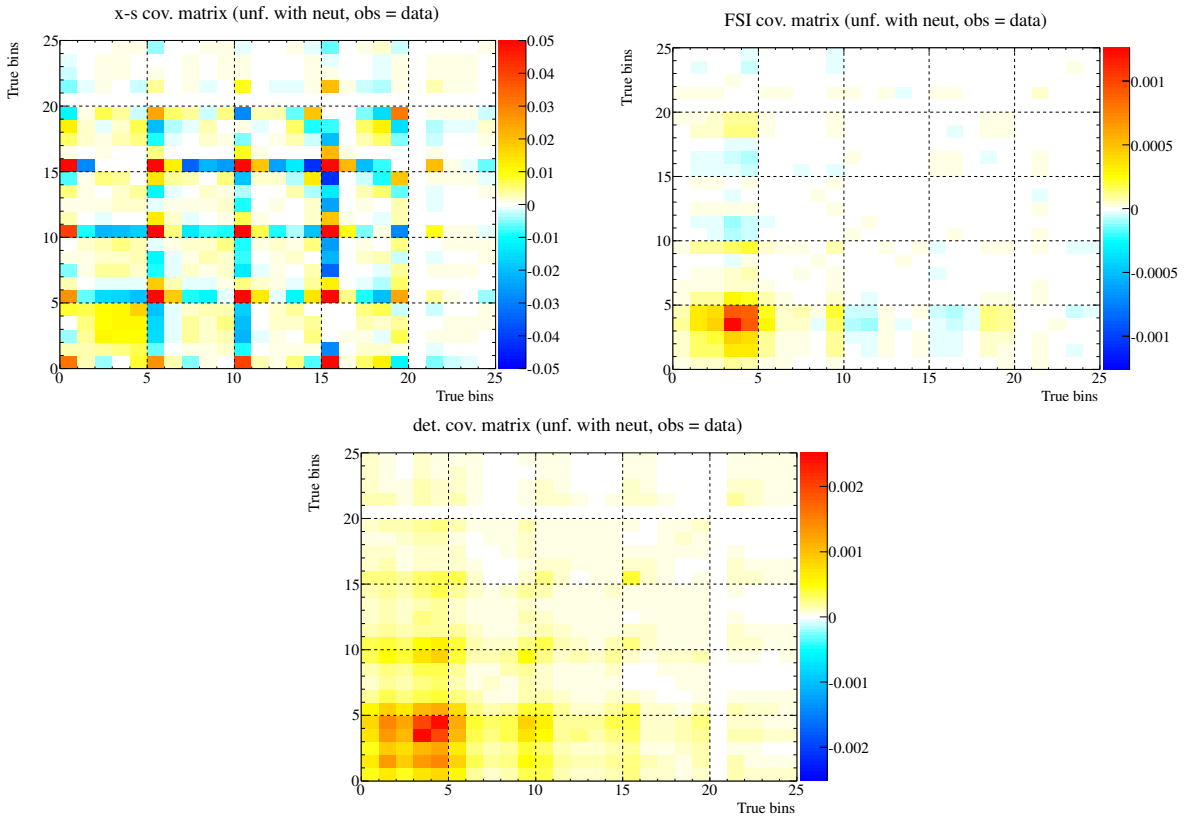

Figure 8.5: Cross section modeling, detector and FSI fractional covariance matrices.

Table 8.4: Summary of the systematic errors. The error on the number of target nucleons (0.67 %) is added in quadrature to the total systematic error. ϕ, *det.*, FSI label the systematic uncertainty of the beam flux, detector response and FSI changed systematically following the covariance matrix showed in Fig. 6.6,6.4,6.3,6.2, x-s design the influence of the change of all the cross section modeling parameter and channel rate.

P_μ (GeV/c)	$\cos\theta_\mu$	algo. (%)	ϕ (%)	x-s (%)	det. (%)	FSI (%)	syst (%)	stat (%)	tot (%)
$[0.0, 0.4]$	$[-1, 0]$	0.54	11.40	17.99	2.13	0.46	21.43	2.04	21.53
	$[0, 0.84]$	0.47	12.79	5.52	3.65	1.21	14.48	4.95	15.30
	$[0.84, 0.90]$	0.11	13.13	10.76	2.73	1.41	17.27	9.52	19.72
	$[0.90, 0.94]$	0.85	14.05	10.73	5.02	3.55	18.76	12.26	22.41
	$[0.94, 1]$	0.24	14.03	12.94	4.94	2.97	19.96	14.72	24.80
$[0.4, 0.5]$	$[-1, 0]$	1.44	11.98	39.47	2.72	0.87	41.38	3.19	41.50
	$[0, 0.84]$	0.15	11.39	5.69	1.30	0.34	12.83	4.20	13.50
	$[0.84, 0.90]$	0.26	11.36	4.99	1.01	0.42	12.49	8.61	15.17
	$[0.90, 0.94]$	0.62	11.66	5.38	1.28	0.51	12.96	10.08	16.42
	$[0.94, 1]$	0.80	13.11	7.19	2.27	0.92	15.20	11.74	19.20
$[0.5, 0.7]$	$[-1, 0]$	0.98	12.60	46.13	1.86	0.42	47.88	8.70	48.66
	$[0, 0.84]$	0.36	11.13	3.79	1.09	0.37	11.85	3.78	12.44
	$[0.84, 0.90]$	0.61	10.85	3.44	0.82	0.30	11.46	6.18	13.02
	$[0.90, 0.94]$	0.15	11.01	5.73	0.81	0.35	12.47	7.28	14.44
	$[0.94, 1]$	0.23	11.64	11.45	1.09	0.28	16.39	7.91	18.19
$[0.7, 0.9]$	$[-1, 0]$	3.58	13.53	148.34	1.97	0.57	149.02	33.45	152.73
	$[0, 0.84]$	0.32	11.38	3.17	1.10	0.41	11.90	5.07	12.94
	$[0.84, 0.90]$	0.36	10.92	5.88	0.83	0.20	12.46	6.84	14.22
	$[0.90, 0.94]$	0.15	10.72	11.13	1.05	0.46	15.52	7.68	17.31
	$[0.94, 1]$	0.00	11.00	17.59	0.93	0.39	20.79	6.97	21.93
$[0.9, 30.0]$	$[-1, 0]$	-	-	-	-	-	-	-	-
	$[0, 0.84]$	0.43	11.88	5.61	1.37	0.63	13.26	5.44	14.33
	$[0.84, 0.90]$	0.08	11.34	2.49	0.87	0.25	11.68	5.85	13.06
	$[0.90, 0.94]$	0.18	11.13	2.27	0.71	0.36	11.42	5.18	12.54
	$[0.94, 1]$	0.27	10.93	2.31	0.75	0.26	11.24	2.93	11.61

The systematic errors are dominated by the flux and the cross section errors in some bins. The flux uncertainty is constant over the bins because of the normalization error on the flux that is about 10.9 % (see Sec. 8.1.1). The breakdown of the flux systematic sources is shown in Table 8.14. In this Table, we mostly see the contribution to the normalization error of each sources where the biggest uncertainty is for the secondary nuclear interactions.

From the cross section point of view, the backward angles have very big errors because of the little statistics in these bins. In this region, a change of the cross section parameter has a drastic influence that is not observed for the other systematic sources. This is simply due to the reweighting process. The reweighting of the detector response is only done on the reconstructed bin, that is, here not spitted. For the flux, the reweighting is done on the true neutrino energy variable and neither on the muon momentum nor angle. Therefore, the cross section systematic source is the only place, where the reweighting process takes into account the other binning that we have in true angle.

To understand better the systematic errors due to the cross section modeling in the MC, a table for each parameter (of Tables 6.11 and 6.13) is done. Tables 8.9 and 8.10 show the related systematic error due to a change of the parameters in Tables 6.11 and 6.13.

The M_A^{QE}, SF and the $1\pi^{shp}$ parameter are the main components of the uncertainty at low momentum as they constitute the main parameters of the interactions at low Q^2. In the other bins below 900 MeV, the uncertainty on SF is the main uncertainty and affects generally the very low angles. The NC uncertainty components come from the background subtraction, while the CC uncertainty components enter in the unfolding matrix as well as in the background, since the outside fiducial volume background can contain CC interactions. These interactions can happen on iron or aluminum frames around the detectors as well as inside other detectors.

Note that this separation of each parameter is only done to understand their influence. Since we have correlations between some parameters, the total cross section uncertainty is not exactly equal to the quadratic sum of Tables 8.9 and 8.10. The numbers pointed there, are only put as cross-check to verify that it gives approximately the result of Table 8.4. Tables 8.11 and 8.12 show the influence of background only systematic variation. In this case the covariance matrix is computed by changing only the background, while the unsmearing matrix as well as the efficiency are kept the same as using the nominal MC. Most of the uncertainty on one pion production comes from the background subtraction. On the contrary the uncertainty on the CCQE channel and the spectral function comes mainly from the propagation through the unfolding matrix.

In general, the biggest impact of the detector systematic as well as the FSI is at the lowest muon momentum bin. This can be explained by many reasons. Firstly the external background for this range of momentum is very big. For high angle, very few muons cross the TPC making difficult the selection. This is shown more precisely in Table 8.13 where the main contributions to the detector systematic uncertainty are given in detail. The rest of the systematic uncertainties have a contribution below < 0.02 %.

Low momentum, also means, at the level of the cross section modeling, interactions with bounded nucleons and not almost free nucleons as they appear for high Q^2 where an impulse approximation can be used. In this case, very few is known about neutrino interaction cross section. Therefore the systematic uncertainty on the final state interaction is bigger for this range of momentum.

In comparison to the other uncertainties, the error on the algorithm is almost negligible.

8.2 Differential cross section results

In this section, we discuss the final cross section result with the statistical and systematic errors. In Tables 8.5 and 8.7, we show the number of reconstructed events in each bin as well as the number of neutrino interactions simulated with NEUT and GENIE. In this Table, the background and the inferred number of events obtained unfolding the data with NEUT is also shown. We observe good agreement between data and MC.

Table 8.6, Figs. 8.6 and 8.7 give the double differential cross section results with its error bars. The values are obtained taking the number of inferred events in Table 8.5 dividing by the total integrated flux, the total number of target nucleons, given in Eq. 8.2 and 8.9, and the width of each momentum and angle bin. The result for backward-going muon is shown here for completeness. We, however, do not claim it as a measurement since it constitutes mainly a model dependent extrapolation of the data.

As a cross-check, we also unfold the data with GENIE. We find that there is less than 4 % difference between the two results, which is well below the total error on the measurement.

Fig. 8.8 shows the cross section result obtained with the NEUT MC together with the data unfolded with the GENIE MC. The error bars for the result obtained with the GENIE MC only corresponds to the statistical error, while the systematic error is included in the result obtained when unfolding with the NEUT MC. We see that all GENIE points are inside the

Table 8.5: The first block gives the information on the reconstructed variables, while the second block on the true variable. For the reconstructed block, we show the number of selected events with NEUT, DATA, the number of background events and the reconstructed pull ($= \frac{obs-mc}{\sqrt{obs}}$) respectively. For the reconstructed bins the bins $[-1, 0]$ and $[0., 0.84]$ are merged together. In the second block, we show the number of simulated events of the NEUT MC, the number of inferred events for our data using the NEUT MC and the efficiency respectively.

P_μ (GeV/c)	$\cos\theta_\mu$	$N_{r_j}^{\text{neut}}$	$N_{r_j}^{\text{data}}$	$B_{r_j}^{\text{neut}}$	pull^{rec}	$N_{t_k}^{\text{neut}}$	$\widehat{N}_{t_k}^{1^{st},\text{data}-\text{neut}}$	ϵ (%)
$[0.0, 0.4]$	$[-1, 0]$	555.3	556.0	142.8	0.0	1149.0	1083.8	1.2
	$[0, 0.84]$					1529.6	1521.3	26.0
	$[0.84, 0.90]$	78.1	75.0	21.0	-0.4	88.5	85.0	62.1
	$[0.90, 0.94]$	54.0	46.0	19.0	-1.2	56.6	50.5	60.3
	$[0.94, 1]$	63.6	78.0	25.8	1.6	61.4	73.2	56.0
$[0.4, 0.5]$	$[-1, 0]$	377.9	364.0	41.0	-0.7	70.7	69.1	3.0
	$[0, 0.84]$					768.3	738.9	45.6
	$[0.84, 0.90]$	62.3	64.0	7.4	0.2	71.9	71.7	78.1
	$[0.90, 0.94]$	43.8	45.0	6.2	0.2	44.2	42.3	83.1
	$[0.94, 1]$	53.9	38.0	12.8	-2.6	50.1	38.7	84.2
$[0.5, 0.7]$	$[-1, 0]$	497.8	475.0	48.9	-1.0	12.3	11.1	7.2
	$[0, 0.84]$					865.0	820.2	55.1
	$[0.84, 0.90]$	138.1	133.0	11.2	-0.4	175.3	163.4	78.4
	$[0.90, 0.94]$	98.3	81.0	9.9	-1.9	112.9	95.0	82.4
	$[0.94, 1]$	130.8	122.0	26.3	-0.8	126.0	113.1	85.5
$[0.7, 0.9]$	$[-1, 0]$	211.4	198.0	23.7	-1.0	0.6	0.6	28.3
	$[0, 0.84]$					287.1	267.1	61.7
	$[0.84, 0.90]$	94.5	74.0	8.5	-2.4	110.3	91.4	74.2
	$[0.90, 0.94]$	73.5	57.0	5.1	-2.2	80.3	64.0	79.3
	$[0.94, 1]$	111.5	105.0	13.9	-0.6	106.0	98.2	87.5
$[0.9, 30.0]$	$[-1, 0]$	301.6	282.0	37.8	-1.2	-	-	-
	$[0, 0.84]$					335.0	310.7	63.9
	$[0.84, 0.90]$	242.6	219.0	24.6	-1.6	287.8	256.8	73.4
	$[0.90, 0.94]$	294.0	262.0	24.2	-2.0	350.6	309.7	76.6
	$[0.94, 1]$	1240.7	1211.0	113.9	-0.9	1536.6	1488.6	75.0
	total	4723.5	4485.0	624.0	-0.7	8276.2	7864.5	49.5

Table 8.6: Double differential cross section result, with its statistical and systematic error. The systematic error on the number of target nucleons is taken into account inside the total systematic error listed here.

P_μ GeV/c	$\cos\theta_\mu$	$\langle\frac{\partial^2\sigma}{\partial p_\mu \partial\cos\theta_\mu}\rangle$ cm^2/nuclei/MeV	$\langle\frac{\partial^2\sigma}{\partial p_\mu \partial\cos\theta_\mu}\rangle$ cm^2/nucleon/MeV	stat. error %	syst. error %
$[0.0, 0.4]$	$[-1, 0]$	2.880×10^{-41}	2.380×10^{-42}	2.04	21.43
	$[0, 0.84]$	4.812×10^{-41}	3.978×10^{-42}	4.95	14.48
	$[0.84, 0.90]$	3.766×10^{-41}	3.113×10^{-42}	9.52	17.27
	$[0.90, 0.94]$	3.355×10^{-41}	2.774×10^{-42}	12.26	18.76
	$[0.94, 1]$	3.243×10^{-41}	2.681×10^{-42}	14.72	19.96
$[0.4, 0.5]$	$[-1, 0]$	0.734×10^{-41}	0.607×10^{-42}	3.19	41.38
	$[0, 0.84]$	9.349×10^{-41}	7.728×10^{-42}	4.20	12.83
	$[0.84, 0.90]$	12.708×10^{-41}	10.505×10^{-42}	8.61	12.49
	$[0.90, 0.94]$	11.237×10^{-41}	9.289×10^{-42}	10.08	12.96
	$[0.94, 1]$	6.863×10^{-41}	5.673×10^{-42}	11.74	15.20
$[0.5, 0.7]$	$[-1, 0]$	0.059×10^{-41}	0.049×10^{-42}	8.70	47.88
	$[0, 0.84]$	5.189×10^{-41}	4.289×10^{-42}	3.78	11.85
	$[0.84, 0.90]$	14.470×10^{-41}	11.961×10^{-42}	6.18	11.46
	$[0.90, 0.94]$	12.622×10^{-41}	10.433×10^{-42}	7.28	12.47
	$[0.94, 1]$	10.021×10^{-41}	8.283×10^{-42}	7.91	16.39
$[0.7, 0.9]$	$[-1, 0]$	0.003×10^{-41}	0.003×10^{-42}	33.45	149.02
	$[0, 0.84]$	1.690×10^{-41}	1.397×10^{-42}	5.07	11.90
	$[0.84, 0.90]$	8.093×10^{-41}	6.690×10^{-42}	6.84	12.46
	$[0.90, 0.94]$	8.502×10^{-41}	7.028×10^{-42}	7.68	15.52
	$[0.94, 1]$	8.699×10^{-41}	7.190×10^{-42}	6.97	20.79
$[0.9, 30.0]$	$[-1, 0]$	-	-	-	-
	$[0, 0.84]$	0.014×10^{-41}	0.011×10^{-42}	5.44	13.26
	$[0.84, 0.90]$	0.156×10^{-41}	0.129×10^{-42}	5.85	11.68
	$[0.90, 0.94]$	0.283×10^{-41}	0.234×10^{-42}	5.18	11.42
	$[0.94, 1]$	0.906×10^{-41}	0.749×10^{-42}	2.93	11.24

NEUT systematic error bars.

The double differential cross section for data unfolded with GENIE is given in Table 8.8. The systematic is, in this case, not included since there is no advanced study on cross section systematic error for the GENIE MC at the moment.

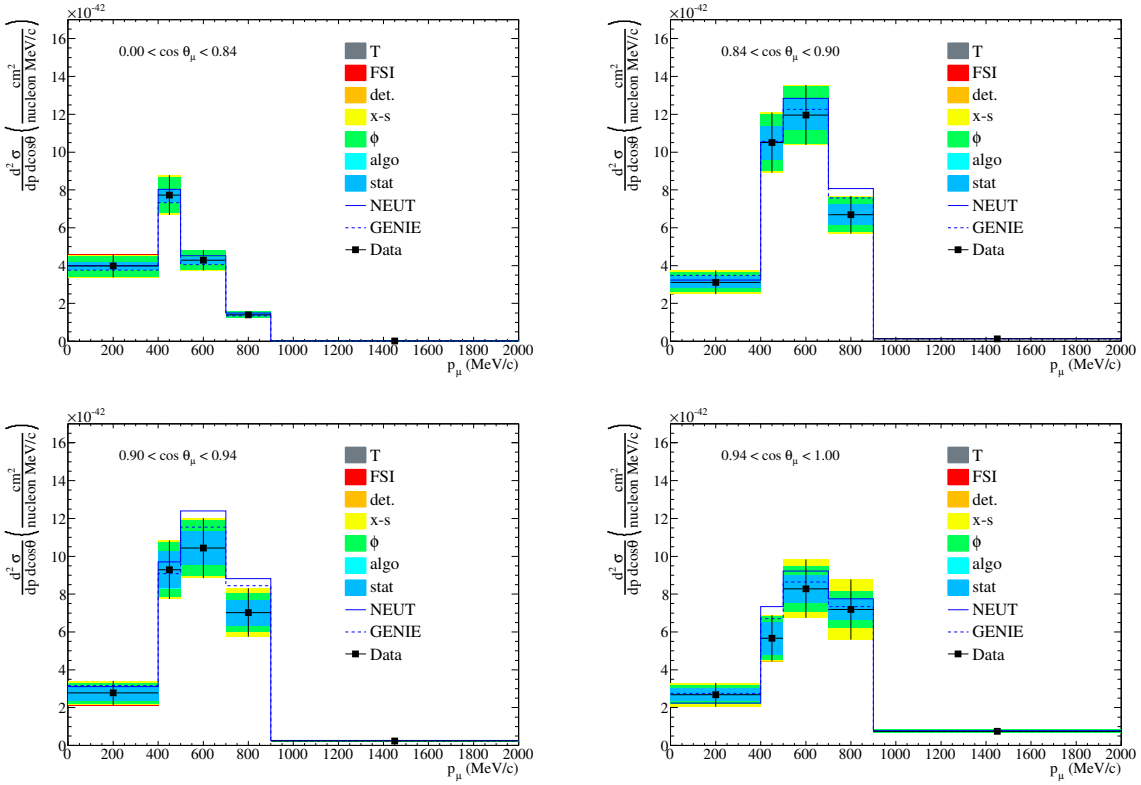

Figure 8.6: Double differential cross section results with systematic and statistical error bars together. The differential cross section is given in cm^2/nucleon/MeV. Each graph corresponds to a bin angle. Each color represents a systematic error source, T: number of Target uncertainty, FSI: Final State Interaction uncertainty, det.: detector response uncertainty, x-s: cross section modeling uncertainty, ϕ: flux uncertainty, algo: algorithm uncertainty, stat: statistical error.

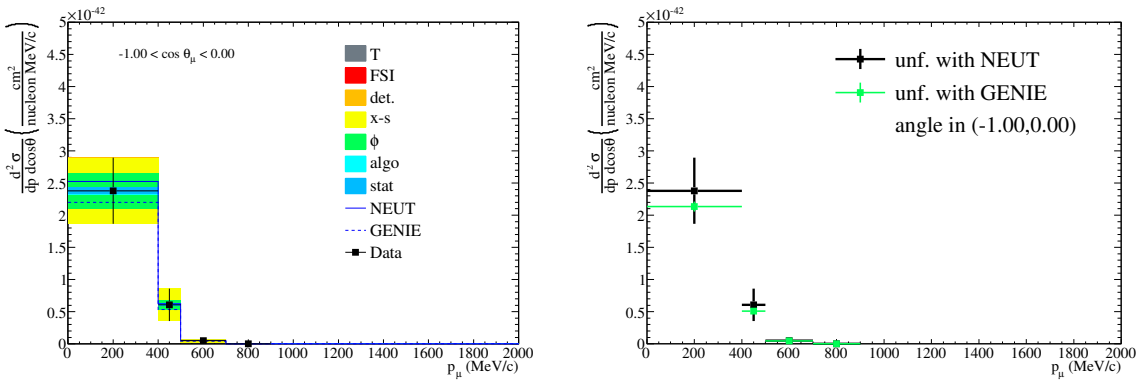

Figure 8.7: Differential cross section for the backward-going muon extrapolation with systematic and statistical error bars together. The differential cross section is given in cm^2/nucleon/MeV. The label definition for each color are the same than Fig. 8.6. Left: The NEUT MC is used to unfold the data and is compared to the truth of GENIE and MC. Right: The data is unfolded with NEUT and GENIE. The errors bar for GENIE only includes statistical errors while the systematic errors are included in the result when unfolding with NEUT.

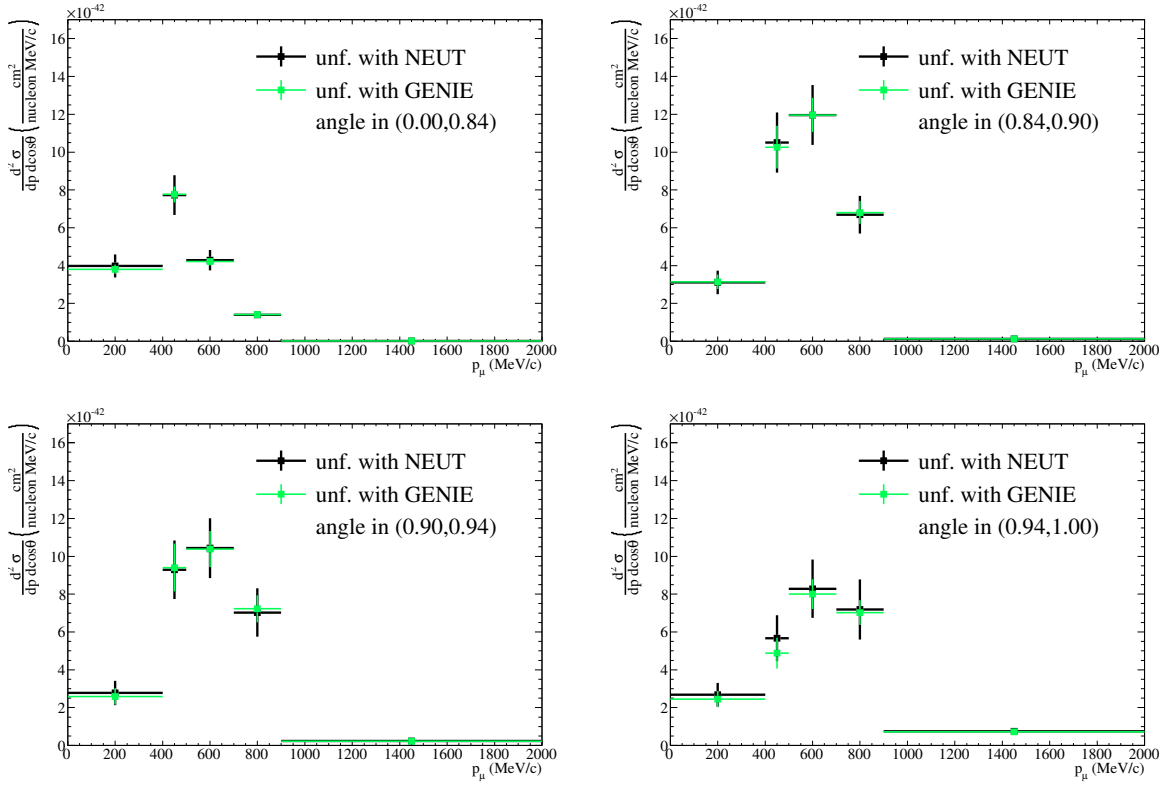

Figure 8.8: Differential cross section results with systematic and statistical error bars together for the NEUT MC. The error bars for the data unfolded with GENIE only represents the statistical error.

Table 8.7: The first block gives the information on the reconstructed variables, while the second block on the true variable. For the reconstructed block, we show the number of selected events with GENIE, DATA, the number of background events and the reconstructed pull ($= \frac{obs-mc}{\sqrt{obs}}$) respectively. For the reconstructed bins the bins $[-1, 0]$ and $[0., 0.84]$ are merged together. In the second block, we show the number of simulated events of the GENIE MC, the number of inferred events for our data using the GENIE MC and the efficiency respectively.

P_μ (GeV/c)	$\cos\theta_\mu$	$N_{r_j}^{\text{genie}}$	$N_{r_j}^{\text{data}}$	$B_{r_j}^{\text{genie}}$	pull^{rec}	$N_{t_k}^{\text{genie}}$	$\widehat{N}_{t_k}^{1^{st},\text{data}-\text{genie}}$	ϵ (%)
$[0.0, 0.4]$	$[-1, 0]$	551.4	556.0	156.1	0.2	1000.8	972.4	1.1
	$[0, 0.84]$					1439.1	1456.0	26.6
	$[0.84, 0.90]$	83.6	75.0	23.1	-1.0	95.1	85.8	62.1
	$[0.90, 0.94]$	55.3	46.0	19.6	-1.4	57.6	47.2	61.9
	$[0.94, 1]$	82.2	78.0	31.5	-0.5	75.2	66.8	63.7
$[0.4, 0.5]$	$[-1, 0]$	341.2	364.0	39.9	1.2	60.6	58.0	1.2
	$[0, 0.84]$					700.9	742.1	46.2
	$[0.84, 0.90]$	66.7	64.0	8.6	-0.3	72.2	70.1	79.8
	$[0.90, 0.94]$	38.9	45.0	5.2	0.9	41.3	42.8	84.2
	$[0.94, 1]$	54.1	38.0	12.3	-2.6	45.7	33.4	86.7
$[0.5, 0.7]$	$[-1, 0]$	460.4	475.0	42.9	0.7	9.6	10.1	4.5
	$[0, 0.84]$					775.4	806.2	56.3
	$[0.84, 0.90]$	133.0	133.0	11.2	-0.0	167.5	163.3	81.1
	$[0.90, 0.94]$	92.6	81.0	9.7	-1.3	105.1	94.5	84.5
	$[0.94, 1]$	127.4	122.0	24.1	-0.5	118.1	109.4	87.4
$[0.7, 0.9]$	$[-1, 0]$	190.0	198.0	23.3	0.6	0.1	0.1	0.0
	$[0, 0.84]$					256.2	269.3	62.4
	$[0.84, 0.90]$	88.6	74.0	6.6	-1.7	103.5	93.0	76.7
	$[0.90, 0.94]$	68.9	57.0	7.5	-1.6	76.9	65.8	81.8
	$[0.94, 1]$	108.1	105.0	14.9	-0.3	100.2	96.0	88.3
$[0.9, 30.0]$	$[-1, 0]$	256.6	282.0	34.7	1.5	-	-	-
	$[0, 0.84]$					258.1	282.3	66.3
	$[0.84, 0.90]$	218.6	219.0	22.0	0.0	250.3	248.9	74.3
	$[0.90, 0.94]$	280.4	262.0	27.6	-1.1	323.3	302.0	78.3
	$[0.94, 1]$	1238.1	1211.0	119.1	-0.8	1481.2	1444.1	76.8
	total	4536.1	4485.0	639.7	-0.3	7614.2	7559.6	51.2

Table 8.8: Differential cross section result, with the statistical error only for GENIE MC.

P_μ (GeV/c)	$\cos\theta_\mu$	$\langle \frac{\partial^2\sigma}{\partial p_\mu \partial \cos\theta_\mu} \rangle \frac{cm^2}{\text{nuclei } MeV}$	$\langle \frac{\partial^2\sigma}{\partial p_\mu \partial \cos\theta_\mu} \rangle \frac{cm^2}{\text{nucleon } MeV}$	stat. error (%)
$[0.0, 0.4]$	$[-1, 0]$	2.584×10^{-41}	2.136×10^{-42}	3.64
	$[0, 0.84]$	4.606×10^{-41}	3.807×10^{-42}	6.31
	$[0.84, 0.90]$	3.800×10^{-41}	3.141×10^{-42}	12.12
	$[0.90, 0.94]$	3.134×10^{-41}	2.590×10^{-42}	16.83
	$[0.94, 1]$	2.959×10^{-41}	2.446×10^{-42}	17.60
$[0.4, 0.5]$	$[-1, 0]$	0.616×10^{-41}	0.509×10^{-42}	7.12
	$[0, 0.84]$	9.390×10^{-41}	7.762×10^{-42}	5.39
	$[0.84, 0.90]$	12.414×10^{-41}	10.261×10^{-42}	10.95
	$[0.90, 0.94]$	11.379×10^{-41}	9.405×10^{-42}	13.41
	$[0.94, 1]$	5.910×10^{-41}	4.885×10^{-42}	16.73
$[0.5, 0.7]$	$[-1, 0]$	0.054×10^{-41}	0.045×10^{-42}	17.57
	$[0, 0.84]$	5.100×10^{-41}	4.216×10^{-42}	4.78
	$[0.84, 0.90]$	14.466×10^{-41}	11.958×10^{-42}	7.58
	$[0.90, 0.94]$	12.555×10^{-41}	10.378×10^{-42}	9.17
	$[0.94, 1]$	9.687×10^{-41}	8.007×10^{-42}	9.87
$[0.7, 0.9]$	$[-1, 0]$	0.001×10^{-41}	0.000×10^{-42}	83.82
	$[0, 0.84]$	1.704×10^{-41}	1.408×10^{-42}	6.54
	$[0.84, 0.90]$	8.236×10^{-41}	6.807×10^{-42}	8.86
	$[0.90, 0.94]$	8.738×10^{-41}	7.223×10^{-42}	9.90
	$[0.94, 1]$	8.501×10^{-41}	7.027×10^{-42}	9.39
$[0.9, 30.0]$	$[-1, 0]$	-	-	-
	$[0, 0.84]$	0.012×10^{-41}	0.010×10^{-42}	7.01
	$[0.84, 0.90]$	0.151×10^{-41}	0.125×10^{-42}	7.21
	$[0.90, 0.94]$	0.276×10^{-41}	0.228×10^{-42}	6.55
	$[0.94, 1]$	0.879×10^{-41}	0.727×10^{-42}	3.36

Table 8.9: Summary of the contribution of cross section modeling parameters listed in Table 6.11, where pdd means pion Δ decay.

P_μ (GeV/c)	$\cos\theta_\mu$	M_A^{QE} (%)	M_A^{RES} (%)	nπ^{shp} (%)	SF (%)	P_f (%)	ΔW (%)	pdd (%)	$1\pi^{shp}$ (%)	total (%)
$[0.0, 0.4]$	$[-1, 0]$	13.44	1.04	3.22	8.68	2.99	3.03	0.29	3.92	17.35
	$[0, 0.84]$	1.53	0.77	2.06	0.63	0.71	0.85	0.62	2.38	3.85
	$[0.84, 0.90]$	6.69	1.10	0.93	2.43	0.34	0.97	3.44	4.51	9.27
	$[0.90, 0.94]$	5.00	1.35	2.83	1.03	1.48	0.63	0.88	4.04	7.45
	$[0.94, 1]$	2.56	1.20	2.41	3.70	2.14	0.29	1.42	4.56	7.41
$[0.4, 0.5]$	$[-1, 0]$	33.69	0.60	4.06	18.75	6.17	0.52	0.68	1.37	39.30
	$[0, 0.84]$	3.33	0.47	1.57	3.29	0.84	0.13	0.60	0.37	5.09
	$[0.84, 0.90]$	3.48	0.63	0.65	0.81	0.57	0.61	0.45	0.75	3.88
	$[0.90, 0.94]$	1.78	0.45	2.51	2.38	3.94	0.96	0.83	0.24	5.70
	$[0.94, 1]$	1.91	1.16	3.80	1.55	1.83	0.51	0.27	0.28	5.06
$[0.5, 0.7]$	$[-1, 0]$	38.70	2.18	2.48	10.33	5.91	0.84	1.84	0.88	40.69
	$[0, 0.84]$	2.74	0.39	0.97	1.59	0.56	0.77	0.09	0.04	3.47
	$[0.84, 0.90]$	1.18	0.54	1.33	0.49	0.23	0.64	0.19	0.47	2.10
	$[0.90, 0.94]$	1.07	0.53	1.00	5.71	0.19	0.16	0.12	0.41	5.94
	$[0.94, 1]$	1.27	0.62	2.84	9.20	1.68	0.79	0.97	0.53	9.97
$[0.7, 0.9]$	$[-1, 0]$	159.27	2.04	0.19	15.91	4.68	3.42	3.99	0.70	160.23
	$[0, 0.84]$	1.69	0.06	0.15	0.35	0.37	0.68	0.58	0.47	2.04
	$[0.84, 0.90]$	1.34	0.90	1.12	4.28	0.77	0.81	0.30	0.26	4.86
	$[0.90, 0.94]$	1.59	0.81	0.97	10.44	0.63	1.36	0.08	0.41	10.74
	$[0.94, 1]$	1.40	0.90	2.06	16.61	1.86	1.10	0.32	0.84	16.99
$[0.9, 30.0]$	$[-1, 0]$	-	-	-	-	-	-	-	-	-
	$[0, 0.84]$	2.58	0.91	0.68	1.56	0.09	0.31	0.28	0.35	3.27
	$[0.84, 0.90]$	1.45	0.27	0.17	0.82	0.24	0.08	0.06	0.45	1.77
	$[0.90, 0.94]$	0.91	0.05	0.20	0.60	0.39	0.36	0.11	0.02	1.24
	$[0.94, 1]$	1.13	0.13	0.34	1.36	0.33	0.12	0.11	0.33	1.88

Table 8.10: Summary of the contribution of cross section normalization error of Table 6.13.

P_μ (GeV/c)	$\cos\theta_\mu$	CCQE (%)	CC1π (%)	CCCOH (%)	NC-BG (%)	NC1π^0 (%)	total (%)
$[0.0, 0.4]$	$[-1, 0]$	3.62	4.26	2.94	1.80	0.14	6.57
	$[0, 0.84]$	1.06	1.87	1.17	1.95	0.36	3.15
	$[0.84, 0.90]$	2.74	5.99	1.74	2.91	0.28	7.41
	$[0.90, 0.94]$	2.53	5.23	1.78	3.52	0.26	7.02
	$[0.94, 1]$	1.66	5.67	3.44	4.18	0.13	8.01
$[0.4, 0.5]$	$[-1, 0]$	3.58	6.66	2.27	1.99	0.12	8.14
	$[0, 0.84]$	0.35	2.07	0.85	1.23	0.13	2.59
	$[0.84, 0.90]$	0.65	1.02	1.78	1.23	0.09	2.48
	$[0.90, 0.94]$	0.18	0.55	0.94	2.23	0.08	2.49
	$[0.94, 1]$	0.46	1.89	3.23	6.06	0.40	7.14
$[0.5, 0.7]$	$[-1, 0]$	4.48	3.19	4.58	1.73	0.08	7.36
	$[0, 0.84]$	0.33	1.09	0.62	1.13	0.10	1.72
	$[0.84, 0.90]$	0.58	0.79	0.69	1.25	0.04	1.73
	$[0.90, 0.94]$	0.46	0.81	0.26	1.95	0.15	2.18
	$[0.94, 1]$	0.66	0.88	1.78	3.04	0.18	3.69
$[0.7, 0.9]$	$[-1, 0]$	14.16	5.81	5.70	1.50	0.03	16.41
	$[0, 0.84]$	0.60	0.79	0.48	1.37	0.16	1.76
	$[0.84, 0.90]$	1.27	1.26	0.01	1.40	0.12	2.28
	$[0.90, 0.94]$	1.75	1.39	0.98	1.37	0.09	2.80
	$[0.94, 1]$	2.03	2.89	1.23	1.92	0.07	4.21
$[0.9, 30.0]$	$[-1, 0]$	-	-	-	-	-	-
	$[0, 0.84]$	2.26	1.54	0.64	1.63	0.25	3.26
	$[0.84, 0.90]$	0.97	0.56	0.56	1.08	0.05	1.65
	$[0.90, 0.94]$	0.59	0.38	0.49	1.34	0.03	1.59
	$[0.94, 1]$	0.62	0.76	0.26	1.02	0.01	1.44

Table 8.11: Summary of the contribution of cross section modeling parameters listed in Table 6.11, for the background only contribution

P_μ (GeV/c)	$\cos\theta_\mu$	M_A^{QE} (%)	M_A^{RES} (%)	nπ^{shp} (%)	SF (%)	P_f (%)	ΔW (%)	pdd (%)	$1\pi^{shp}$ (%)	total (%)
$[0.0, 0.4]$	$[-1, 0]$	0.83	0.50	1.32	0.09	0.02	0.56	0.40	0.27	1.80
	$[0, 0.84]$	1.88	1.05	2.67	0.14	0.01	0.80	0.76	0.44	3.63
	$[0.84, 0.90]$	1.20	1.01	3.36	0.08	0.02	0.78	0.93	0.41	3.92
	$[0.90, 0.94]$	1.22	1.22	3.84	0.12	0.05	0.65	1.93	0.13	4.68
	$[0.94, 1]$	0.78	0.82	3.65	0.17	0.05	0.47	1.48	0.20	4.14
$[0.4, 0.5]$	$[-1, 0]$	0.75	0.49	1.54	0.08	0.04	0.44	0.53	0.22	1.93
	$[0, 0.84]$	1.49	0.49	1.25	0.10	0.02	0.56	0.53	0.22	2.16
	$[0.84, 0.90]$	0.69	0.47	0.90	0.16	0.03	0.21	0.38	0.24	1.33
	$[0.90, 0.94]$	0.56	0.36	1.26	0.08	0.09	0.45	0.81	0.11	1.70
	$[0.94, 1]$	0.66	0.87	2.62	1.82	0.32	1.09	0.71	0.58	3.67
$[0.5, 0.7]$	$[-1, 0]$	0.53	0.30	0.72	0.33	0.07	0.55	0.23	0.22	1.18
	$[0, 0.84]$	0.88	0.45	0.87	0.06	0.02	0.76	0.41	0.25	1.59
	$[0.84, 0.90]$	0.52	0.25	0.58	0.04	0.00	0.34	0.10	0.15	0.90
	$[0.90, 0.94]$	0.45	0.25	0.68	0.03	0.05	0.41	0.16	0.26	1.00
	$[0.94, 1]$	0.55	0.39	1.06	0.91	0.20	0.69	0.22	0.31	1.75
$[0.7, 0.9]$	$[-1, 0]$	0.36	0.18	0.56	0.18	0.05	0.32	0.16	0.17	0.82
	$[0, 0.84]$	0.88	0.53	1.01	0.01	0.01	0.85	0.30	0.34	1.74
	$[0.84, 0.90]$	0.57	0.41	0.83	0.03	0.01	0.76	0.23	0.27	1.37
	$[0.90, 0.94]$	0.58	0.23	0.59	0.13	0.00	0.73	0.32	0.21	1.20
	$[0.94, 1]$	0.42	0.24	0.70	0.34	0.08	0.42	0.19	0.20	1.05
$[0.9, 30.0]$	$[-1, 0]$	-	-	-	-	-	-	-	-	-
	$[0, 0.84]$	1.15	0.71	1.18	0.03	0.01	1.05	0.31	0.42	2.14
	$[0.84, 0.90]$	0.66	0.45	1.05	0.02	0.01	0.37	0.08	0.26	1.40
	$[0.90, 0.94]$	0.49	0.30	0.74	0.02	0.01	0.39	0.15	0.16	1.04
	$[0.94, 1]$	0.36	0.16	0.45	0.03	0.01	0.30	0.15	0.17	0.71

Table 8.12: Summary of the contribution of cross section normalization error of Table 6.13, for the background only contribution

P_μ (GeV/c)	$\cos\theta_\mu$	CCQE (%)	CC1π (%)	CCCOH (%)	NC-BG (%)	NC1π^0 (%)	total (%)
$[0.0, 0.4]$	$[-1, 0]$	0.27	0.88	0.24	1.80	0.14	2.04
	$[0, 0.84]$	0.58	2.02	0.28	1.95	0.36	2.90
	$[0.84, 0.90]$	0.49	2.44	0.35	2.91	0.28	3.85
	$[0.90, 0.94]$	0.51	2.93	0.87	3.52	0.26	4.70
	$[0.94, 1]$	0.32	2.10	0.60	4.18	0.13	4.73
$[0.4, 0.5]$	$[-1, 0]$	0.28	1.06	0.30	1.99	0.12	2.29
	$[0, 0.84]$	0.37	0.86	0.14	1.23	0.13	1.56
	$[0.84, 0.90]$	0.28	0.81	0.06	1.23	0.09	1.50
	$[0.90, 0.94]$	0.29	0.84	0.19	2.23	0.08	2.40
	$[0.94, 1]$	0.44	1.52	1.41	6.06	0.40	6.43
$[0.5, 0.7]$	$[-1, 0]$	0.21	0.51	0.23	1.73	0.08	1.83
	$[0, 0.84]$	0.26	0.65	0.17	1.13	0.10	1.34
	$[0.84, 0.90]$	0.21	0.44	0.14	1.25	0.04	1.35
	$[0.90, 0.94]$	0.22	0.48	0.22	1.95	0.15	2.03
	$[0.94, 1]$	0.26	0.67	0.34	3.04	0.18	3.14
$[0.7, 0.9]$	$[-1, 0]$	0.18	0.40	0.29	1.50	0.03	1.59
	$[0, 0.84]$	0.23	0.64	0.11	1.37	0.16	1.54
	$[0.84, 0.90]$	0.19	0.51	0.06	1.40	0.12	1.51
	$[0.90, 0.94]$	0.23	0.35	0.15	1.37	0.09	1.44
	$[0.94, 1]$	0.19	0.44	0.35	1.92	0.07	2.02
$[0.9, 30.0]$	$[-1, 0]$	-	-	-	-	-	-
	$[0, 0.84]$	0.31	0.84	0.07	1.63	0.25	1.87
	$[0.84, 0.90]$	0.25	0.56	0.10	1.08	0.05	1.24
	$[0.90, 0.94]$	0.21	0.38	0.06	1.34	0.03	1.41
	$[0.94, 1]$	0.22	0.44	0.14	1.02	0.01	1.14

Table 8.13: Summary of the contribution of the main source of systematic uncertainties due to the detector response for the detector systematic listed in Table 6.8. We define: Mom: momentum scale, Qc: Charge confusion, s-mu: sand muons, dist.: momentum distortion, OOFV: outside of fiducial volume, PiAbs: pion absorption, match.: FGD-TPC track matching efficiency, M: FGD mass

P_μ (GeV/c)	$\cos\theta_\mu$	Mom. (%)	Qc (%)	s-mu (%)	dist. (%)	OOFV (%)	match. (%)	M (%)	total (%)
$[0.0, 0.4]$	$[-1, 0]$	0.31	0.59	0.27	0.37	1.88	0.63	0.81	2.29
	$[0, 0.84]$	1.56	0.31	0.12	0.90	3.39	0.57	0.64	3.95
	$[0.84, 0.90]$	1.17	0.23	0.12	0.75	2.30	0.38	0.45	2.76
	$[0.90, 0.94]$	1.33	0.29	0.68	0.87	4.29	0.46	0.54	4.68
	$[0.94, 1]$	1.42	0.32	0.42	0.97	4.14	0.43	0.49	4.56
$[0.4, 0.5]$	$[-1, 0]$	0.70	0.57	0.35	0.59	2.27	0.63	0.80	2.74
	$[0, 0.84]$	0.18	0.22	0.03	0.67	1.04	0.39	0.48	1.41
	$[0.84, 0.90]$	0.45	0.12	0.04	0.46	0.56	0.20	0.23	0.91
	$[0.90, 0.94]$	0.56	0.11	0.14	0.61	0.90	0.21	0.24	1.28
	$[0.94, 1]$	0.89	0.22	0.13	0.94	1.99	0.37	0.42	2.45
$[0.5, 0.7]$	$[-1, 0]$	0.11	0.56	0.43	0.59	1.28	0.57	0.77	1.85
	$[0, 0.84]$	0.33	0.19	0.03	0.49	0.67	0.33	0.40	1.05
	$[0.84, 0.90]$	0.06	0.10	0.03	0.28	0.55	0.20	0.22	0.70
	$[0.90, 0.94]$	0.08	0.10	0.15	0.40	0.53	0.19	0.23	0.76
	$[0.94, 1]$	0.22	0.12	0.19	0.43	0.71	0.23	0.27	0.96
$[0.7, 0.9]$	$[-1, 0]$	0.28	0.53	0.20	1.02	0.91	0.34	0.56	1.64
	$[0, 0.84]$	0.55	0.18	0.08	0.63	0.65	0.28	0.37	1.18
	$[0.84, 0.90]$	0.17	0.12	0.02	0.71	0.36	0.24	0.26	0.89
	$[0.90, 0.94]$	0.09	0.12	0.05	0.77	0.30	0.22	0.22	0.90
	$[0.94, 1]$	0.10	0.10	0.03	0.51	0.36	0.18	0.19	0.70
$[0.9, 30.0]$	$[-1, 0]$	-	-	-	-	-	-	-	-
	$[0, 0.84]$	0.58	0.26	0.07	0.58	0.82	0.24	0.37	1.27
	$[0.84, 0.90]$	0.30	0.19	0.10	0.43	0.41	0.19	0.28	0.78
	$[0.90, 0.94]$	0.16	0.22	0.05	0.41	0.31	0.17	0.24	0.66
	$[0.94, 1]$	0.07	0.39	0.12	0.25	0.27	0.19	0.26	0.64

Table 8.14: Summary of the contribution of the main source of systematic uncertainties due to the flux uncertainties. We denote by K and π the kaons and pions production multiplicity uncertainties; beam and OA the proton beam and off-axis uncertainties; Horn the magnetic field uncertainty of the horn; pr. x-s and Sec. nucl. the production cross section and secondary nucleon cross section uncertainty.

P_μ (GeV/c)	$\cos\theta_\mu$	K (%)	π (%)	beam (%)	OA (%)	Horn (%)	pr. x-s (%)	Sec. nucl. (%)	total (%)
$[0.0, 0.4]$	$[-1, 0]$	4.19	3.62	1.86	0.63	1.52	6.04	6.15	10.54
	$[0, 0.84]$	2.47	5.26	1.44	0.56	0.87	7.11	7.88	12.22
	$[0.84, 0.90]$	2.87	5.40	1.24	0.55	1.04	7.38	8.25	12.77
	$[0.90, 0.94]$	3.39	5.51	1.41	0.60	1.23	7.70	8.56	13.35
	$[0.94, 1]$	2.90	5.40	1.45	0.58	1.03	7.50	8.31	12.90
$[0.4, 0.5]$	$[-1, 0]$	3.76	4.31	0.22	0.29	0.91	6.80	7.11	11.42
	$[0, 0.84]$	1.57	4.95	1.21	0.47	0.56	6.46	7.32	11.15
	$[0.84, 0.90]$	1.59	4.77	1.45	0.49	0.59	6.18	7.12	10.81
	$[0.90, 0.94]$	1.98	4.78	1.75	0.56	0.72	6.36	7.26	11.13
	$[0.94, 1]$	3.79	5.01	1.86	0.66	1.34	7.43	8.18	12.94
$[0.5, 0.7]$	$[-1, 0]$	0.97	5.81	0.96	0.44	0.25	6.99	7.54	11.89
	$[0, 0.84]$	1.42	4.89	0.72	0.40	0.45	6.28	7.23	10.88
	$[0.84, 0.90]$	1.54	4.65	1.13	0.45	0.62	6.07	6.93	10.53
	$[0.90, 0.94]$	1.58	4.77	1.18	0.47	0.61	6.24	7.07	10.78
	$[0.94, 1]$	2.36	4.68	1.30	0.51	0.86	6.49	7.22	11.16
$[0.7, 0.9]$	$[-1, 0]$	3.68	7.21	2.67	0.78	0.06	6.68	8.60	13.85
	$[0, 0.84]$	1.45	5.06	0.81	0.41	0.23	6.51	7.23	11.10
	$[0.84, 0.90]$	1.95	4.53	0.50	0.37	0.57	6.13	7.04	10.60
	$[0.90, 0.94]$	2.09	4.33	0.43	0.35	0.71	5.98	6.91	10.37
	$[0.94, 1]$	2.93	4.11	0.30	0.35	0.89	6.12	6.86	10.54
$[0.9, 30.0]$	$[-1, 0]$	-	-	-	-	-	-	-	-
	$[0, 0.84]$	0.81	5.56	1.58	0.52	0.24	6.68	7.64	11.72
	$[0.84, 0.90]$	1.02	5.18	1.34	0.48	0.31	6.38	7.27	11.11
	$[0.90, 0.94]$	1.15	5.01	1.22	0.46	0.38	6.23	7.11	10.85
	$[0.94, 1]$	0.77	4.99	1.23	0.46	0.21	6.11	7.12	10.73

8.3 Total cross section results

Taking the total number of inferred events, given in Table 8.5, we can calculate the integrated flux averaged total cross section dividing this number by the integrated flux and the number of target nucleons with the caveat that we trust our model to simulate correctly the backward region. As the systematic error calculations, have been done by comparing other experiments that have the full phase space, we are confident that the systematic error on these bins are correct.

We obtain,

$$\langle \sigma_{\mathrm{CC}} \rangle_{\phi} = (8.36 \pm 0.16(stat) \pm 1.02(syst)) \times 10^{-38} \frac{\mathrm{cm}^2}{\text{av. nuclei}} \tag{8.21}$$

$$\langle \sigma_{\mathrm{CC}} \rangle_{\phi} = (6.91 \pm 0.13(stat) \pm 0.84(syst)) \times 10^{-39} \frac{\mathrm{cm}^2}{\text{nucleon}} \tag{8.22}$$

where the data agrees well with the MC predicted values that are,

$$\langle \sigma_{\mathrm{CC}}^{\mathrm{NEUT}} \rangle_{\phi} = 8.79 \times 10^{-38} \frac{\mathrm{cm}^2}{\text{av. nuclei}} \qquad \langle \sigma_{\mathrm{CC}}^{\mathrm{NEUT}} \rangle_{\phi} = 7.27 \times 10^{-39} \frac{\mathrm{cm}^2}{\text{nucleon}} \tag{8.23}$$

$$\langle \sigma_{\mathrm{CC}}^{\mathrm{GENIE}} \rangle_{\phi} = 8.09 \times 10^{-38} \frac{\mathrm{cm}^2}{\text{av. nuclei}} \qquad \langle \sigma_{\mathrm{CC}}^{\mathrm{GENIE}} \rangle_{\phi} = 6.69 \times 10^{-39} \frac{\mathrm{cm}^2}{\text{nucleon}} \tag{8.24}$$

From this result, we observe that data agrees slightly better with GENIE than with NEUT. This might suggest that predictions with $M_A \sim 1$ are more accurate than predictions for $M_A > 1$. It can be shown that for previous flux version, the agreement with NEUT was better than with GENIE. The application of the tuned flux 11bv3.1, increases the flux in general along the phase space making the NEUT prediction in general bigger than the data and the GENIE prediction closer to the data. Because of the big flux uncertainty, a better agreement with one of the MC cannot give any conclusion in the intrinsic modeling of the generator.

The result in Eq. 8.22 is bigger than the one in Eq. 8.24, because the backward going region has been extrapolated using the NEUT MC. If on the contrary the extrapolation is done with the GENIE MC, we would have get, 6.68×10^{-39} $\frac{\mathrm{cm}^2}{\text{nucleon}}$ which has about 3% of difference with the prediction obtained with the NEUT MC. This value is however well below the systematic error, which is about 12% of the result.

To compare with other experiments, it can be useful to calculate the mean energy of our flux that is 0.85 GeV. Fig. 8.9 shows the T2K total cross section result together with the other experiments. We see that the NEUT prediction, in green, for the T2K experiment corresponds to the NEUT prediction for the SciBooNE experiment. The good agreement between the two predictions gives us confidence that no major mistake has been made computing the result.

The T2K point has been placed, at the mean position of the T2K flux, which does not correspond to its peak because of the high energy tail. The result obtained here is in a relatively good agreement with the other experiments, although SciBooNE seems to be always higher than the MC predictions.

There are many methods to calculate errors of a non-Gaussian distribution. One of them consists in first finding E_{min} and E_{max} corresponding to 68 % of the total flux with an energy

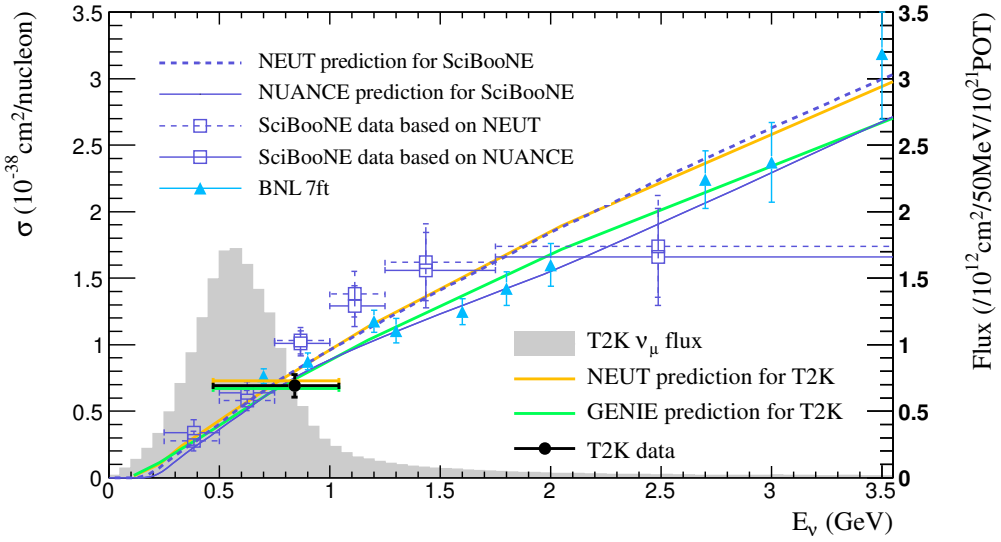

Figure 8.9: T2K total cross section result together with the NEUT and GENIE prediction for T2K and SciBooNE

larger/smaller than the mean energy,

$$\frac{\int_{0.85}^{E_{max}} \frac{\partial\phi(E)}{\partial E} \mathrm{d}E}{\int_{0.85}^{\infty} \frac{\partial\phi(E)}{\partial E} \mathrm{d}E} = 68\% \Rightarrow E_{max} = 1.85\ GeV \tag{8.25}$$

$$\frac{\int_{E_{min}}^{0.85} \frac{\partial\phi(E)}{\partial E} \mathrm{d}E}{\int_{0}^{0.85} \frac{\partial\phi(E)}{\partial E} \mathrm{d}E} = 68\% \Rightarrow E_{min} = 0.45\ GeV \tag{8.26}$$

where the 68 % has been chosen by analogy to the gaussian distribution, where one sigma error corresponds to 68% of the area. We then calculate the variance in this interval to obtain the error,

$$\sigma_+^2 = \frac{\int_{0.85}^{E_{max}} (E - 0.85)^2 \frac{\partial\phi(E)}{\partial E} \mathrm{d}E}{\int_{0.85}^{E_{max}} \frac{\partial\phi(E)}{\partial E} \mathrm{d}E} \Rightarrow \sigma_+ = 0.39\ \mathrm{GeV} \tag{8.27}$$

$$\sigma_-^2 = \frac{\int_{E_{min}}^{0.85} (E - 0.85)^2 \frac{\partial\phi(E)}{\partial E} \mathrm{d}E}{\int_{E_{min}}^{0.85} \frac{\partial\phi(E)}{\partial E} \mathrm{d}E} \Rightarrow \sigma_- = 0.27\ \mathrm{GeV} \tag{8.28}$$

The error obtained here is meant to give an idea of the dispersion inside the range defined by E_{min} and E_{max}. In the literature, there are other ways to calculate errors for non-gaussian distributions, but none has been found optimal for this case. The result depending on the method can change largely as some try to not account for the tails when others do. Another method, for example, consists in finding E_{min} and E_{max} for which $\phi(E_{min}) = \phi(E_{max})$ and

$$\frac{\int_{E_{min}}^{E_{max}} \frac{\partial\phi(E)}{\partial E} \mathrm{d}E}{\int_{0}^{\infty} \frac{\partial\phi(E)}{\partial E} \mathrm{d}E} = 68\% \tag{8.29}$$

In this case, we find that $E_{max} = 0.8$ GeV $< \langle \mathrm{E} \rangle$ and $E_{min} = 0.3$, which shows the non-gaussian behavior of our flux distribution and how methods can defer. The assignment of the horizontal

error bar is therefore quiet subjective. My personal opinion is that the first method takes too much into account the high energy tail, while the second method does maybe not enough. For the final result presented here, I decided to use the second method for calculating the error bars but instead of taking the E_{min} and E_{max} corresponding to the 68 % of the area, I chose them so that the area covered is a 90 %. This last value is chosen arbitrarily by myself, and arguments can be chosen against. Doing so, we obtain $E_{min} = 0.05$ GeV and $E_{max} = 1.35$ GeV. The error is then defined as in Eqs. 8.27 and 8.28, and we obtain: $\sigma_- = 0.37$ GeV and $\sigma_+ = 0.20$ GeV.

Chapter 9

Conclusion

T2K has proved to be a very good experiment able to cover different physics topics. Using the data collected up to now, T2K has been able to measure the value of θ_{13} and firmly establish the $\nu_\mu \rightarrow \nu_e$ appearance at 3σ precision. These latest results have been obtained by the use of the near detector data, where the near detector rate measurement has been used to constrain neutrino flux and cross section at the far detector. The data and the selection are the same as the one presented in this thesis.

First results on the muon neutrino disappearance study have been published in March 2012 and updated results on θ_{23} and Δm^2_{32} should come soon.

More precise measurements of θ_{13} as well as θ_{23} and Δm^2_{32} are essential for the future in order to understand whether θ_{23} is maximal or not. This is an important input for the mass hierarchy determination and studies of CP violation in the lepton sector. By the combination with other experiments such as NOvA [187], and the reactor experiments Daya-Bay, RENO and Double-Chooz, T2K can achieve some sensitivity on δ_{CP}.

While an upgrade of different existing experiments can already give good sensitivity to the mass hierarchy [188], it is now clear within the physics community that a new generation of oscillation experiments is needed to have a much better sensitivity on δ_{CP}.

In Europe, an expression of interest has already been submitted for the LAGUNA/LBNO project [189]. In this experiment, a 400 GeV proton beam is fast extracted from the CERN SPS accelerator and the neutrino beam resulting from the interaction of the protons with a carbon target is sent to Pyhäsalmi in Finland. The far detector would be placed in the Pyhäsalmi Mine where there are very good infrastructural opportunities to deliver detector components. This experiment will use a liquid argon and magnetized iron detector as far detector. Although the liquide argon TPC still needs R&D and validation to be able to run with large drift distances, it allows a very good reconstruction of the events in a medium that is relatively cheap. The expected exposure for one year of running is assumed conservatively two times better than the average number of POT per year sent to the CNGS target since 2006 that is 4.5×10^{19} POT. For only $\sim 2.25 \times 10^{20}$ POT with a 50% sharing time for neutrino and anti-neutrino beams, a 5σ discovery on the mass hierarchy is expected for any value of δ_{CP}. For $\sim 10^{21}$ POT, the existence of CP-violation can be demonstrated at the 90% C.L. (less than 2σ C.L.) for $\sim 60\%$ of the δ_{CP} parameter space (see Fig. 9.1). The same fraction of the δ_{CP} parameter space can be achieved with a 3σ C.L with an exposure of only 5×10^{20} POT increasing the far detector mass from 20 kton to 70 kton.

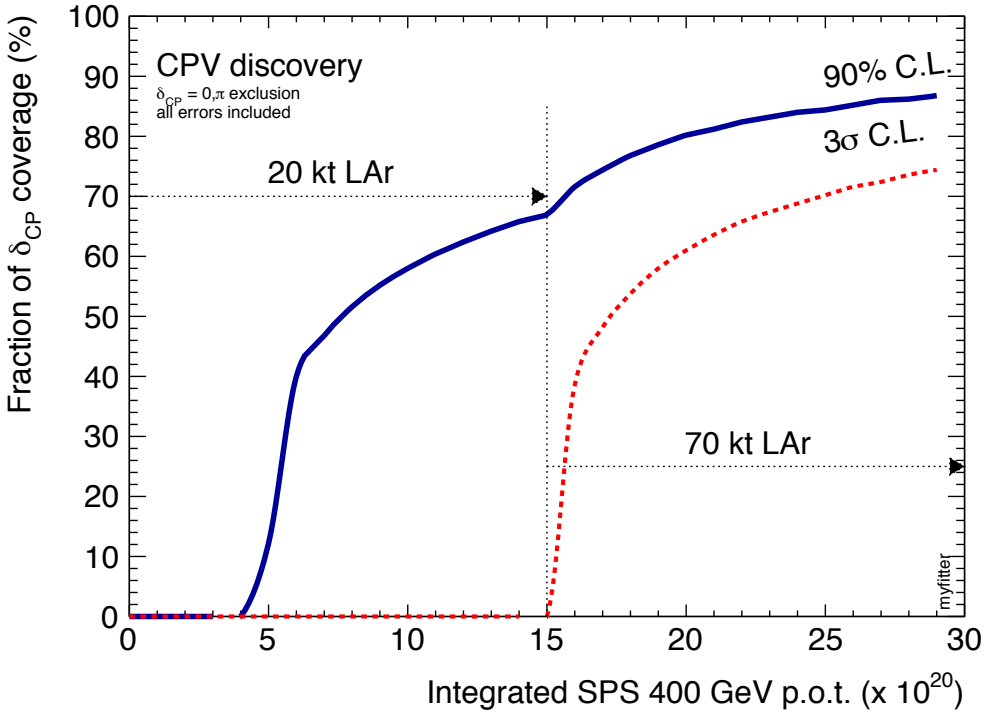

Figure 9.1: CPV coverage as a function of the integrated exposure [189]. The blue (red) line shows the coverage of δ_{CP} at a 90 % C.L. (3σ C.L.) for a target mass of 20 kton (70 kton) respectively.

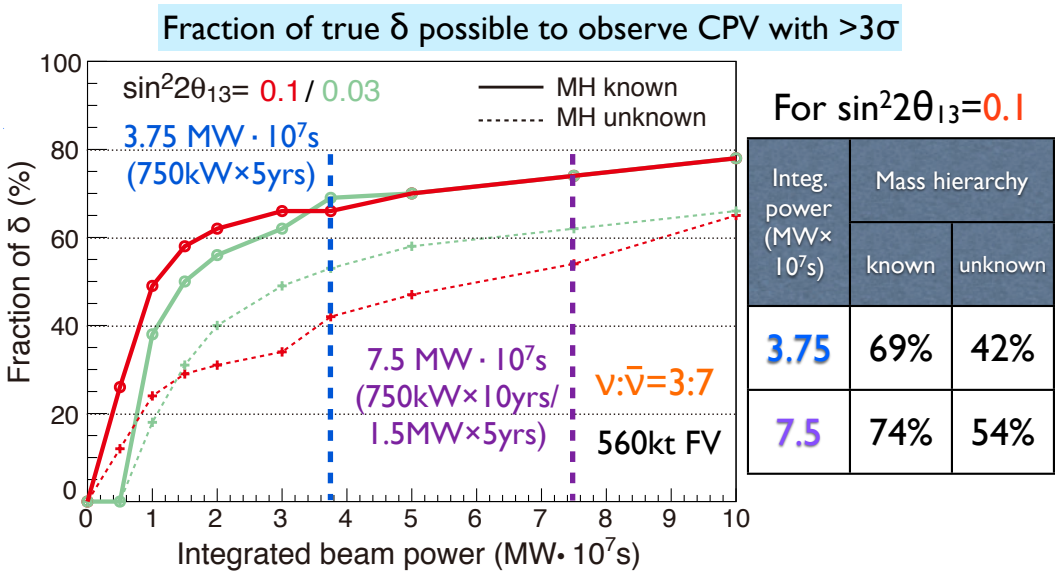

Figure 9.2: Fraction of possible δ_{CP} to observe CP violation with a precision better than 3 σ as a function of the integrated beam power. The designed T2K beam power is 750 kW as expected [190].

As a continuation of the T2K experiment, a T2HK project is proposed: the construction of the 1 Mton water Cherenkov detector, Hyper Kamiokande, can also give complementary results on CP violation and mass hierarchy. A 3σ C.L. (4σ C.L.) sensitivity is expected on mass hierarchy by 2028 (2033 respectively). A 70% of the possible δ_{CP} values should be covered with a precision better than 3σ after 5 years of running with the designed T2K beam power (750 kW), if the mass hierarchy is known (see Fig. 9.2) [190].

Good neutrino flux and cross section knowledge is essential for future oscillation experiments which are required to be more precise. Cross sections are also very interesting in themselves. As presented in the second chapter, there are very few measurements of neutrino interactions at low energies and most of the assumptions are generally coming from electron scattering data sets. Low energy measurements will allow us to understand better nuclear effects, for example.

The analysis presented in this thesis is a starting point for future analyses at the near detector of the T2K experiment beside the oscillation analyses. The cross section measurements of the different channels using different methods will be a valuable information for improving models and decreasing systematic uncertainties in other measurements. Behavior of the cross section as a function of the energy or Q^2 will also give complementary results with better statistics. The use of the additional 2012 data in the near detector, will allow the study of other channels and topologies. For example, measurements of specific final states as two track samples with one muon and one proton can provide additional information to the charged current cross sections constraining better some model parameters, like M_A.

For such measurements, improvement of the reconstruction and calibration is needed. In particular, the discrimination of the events can be improved by a better timing between the different detectors or vertexing. The timing information is, for example, essential to increase our phase space and reduce, together with a better vertexing, our external background. The newer version of the software shows already significant improvement concerning the out of fiducial volume background which is one of the main detector-related uncertainty.

In the last chapter, the first cross section measurements of the T2K collaboration, in the near detector, have been presented. Although systematic errors on the flux have been decreased for this analysis, it still represents our major uncertainty. This is also the case in the other experiments. To understand precisely cross sections, the systematic errors on the flux should be decreased furthermore. If most of the systematic error sources are negligible except for the modeling of the cross section, then we will have the possibility to differentiate between the various cross section models. This will allow us to decrease the systematic uncertainties on them.

For example, we observed in the final results a disagreement of 3 % for GENIE and 5 % for NEUT with the data. This does not tell that the models used by GENIE is better than the ones used by NEUT as the flux can be off by 11 %.

In the near future, this analysis might be able to decrease significantly its systematic error by the use of the 2009 data set of the NA61 experiment. T2K will be then the first experiment to have relatively small errors on the neutrino flux. It will therefore contribute greatly by its cross section measurements to the particle physics community. Exciting time is therefore expected on cross sections in the next few years!

Appendix A

Calculation of the matter potential

Explicit calculation of V_{CC} [191, 60]

The flavour conversion in an inhomogeneous matter potential occurring by an adiabatic transition is called MSW (Mikheyev-Smirnow-Wolfenstein) effect [33, 34]. The effective low-energy Hamiltonian describing the relevant neutrino interactions in matter is given by:

$$H_{int} = \frac{G_F}{\sqrt{2}} \left(J_e^{+,\mu}(x) J_{e,\mu}^{-}(x) + \frac{1}{4} \sum_{l=e,\mu,\tau} J_l^{N,\mu}(x) J_{l,\mu}^{N}(x) \right) \tag{A.1}$$

where $J_{e,\mu}^{+/-}$ and $J_{e,\mu}^{N}$ are respectively the charged currents and the neutral current described in Eqs 2.4 and 2.3.

Since the part of the Hamiltonian concerning the neutral current is identical for all flavours, we can simplify by studying only the charged current part. Writing s and p_e as the spin and the momentum of the electron, we have:

$$\begin{aligned} \langle e(s,p_e)|H_{CC}|e(s,p_e)\rangle &= \tfrac{G_F}{\sqrt{2}}\, \langle e(s,p_e)|\bar{e}(x)\gamma_\mu(1-\gamma_5)\nu_e(x)\bar{\nu_e}(x)\gamma^\mu(1-\gamma_5)e(x)|e(s,p_e)\rangle \\ &= \tfrac{G_F}{\sqrt{2}}\, \bar{\nu_e}(x)\gamma_\mu(1-\gamma_5)\nu_e(x)\langle e(s,p_e)|\bar{e}(x)\gamma^\mu(1-\gamma_5)e(x)|e(s,p_e)\rangle \end{aligned}$$

where the Fierz identity has been used to separate the neutrino's and electron's spinnor. Expanding the electron fields $e(x)$ in plane waves we find:

$$\begin{aligned} &\langle e(s,p_e)|\bar{e}(x)\gamma^\mu(1-\gamma_5)e(x)|e(s,p_e)\rangle \\ &= \tfrac{1}{V}\langle e(s,p_e)|\bar{u_s}(p_e)a_s^\dagger(p_e)\gamma^\mu(1-\gamma_5)a_s(p_e)u_s(p_e)|e(s,p_e)\rangle \end{aligned}$$

where $a_s^\dagger$ and a_s are the creation and destruction operator for the electron, $u_s(p_e)$ and $\bar{u}_s(p_e)$ their wave function, and finally V a normalisation factor. The trajectory of the neutrino is determined by the electrons present in the matter. To obtain the effective Hamiltonian due to the electrons in the medium, $H_{CC}^{(e)}$, we have to average over all the momentum and spin of the electrons, and sum over each electron in the medium. We assume the energy distribution of the electrons in the matter, $f_e(E_e)$, homogeneous and normalized to 1 $\left(\int d^3p_e f(E_e) = 1\right)$. We obtain:

$$\begin{aligned} H_{CC}^{(e)} = &\quad \tfrac{G_F}{\sqrt{2}}\, \bar{\nu_e}(x)\gamma_\mu(1-\gamma_5)\nu_e(x) \\ &\times \int d^3p_e f(E_e) \tfrac{1}{2} \textstyle\sum_s \sum_{j=1}^{n_e} \left[\tfrac{1}{V}\langle e(s,p_e)|\bar{u_s}(p_e)a_s^\dagger(p_e)\gamma^\mu(1-\gamma_5)a_s(p_e)u_s(p_e)|e(s,p_e)\rangle \right] \end{aligned}$$

where we assume that the medium has the same number of electrons with spin 1/2 and -1/2. In addition we have:

$$\frac{1}{V}\sum_{j=1}^{n_e}\langle e(s,p_e)|a_s^\dagger(p_e)a_s(p_e)|e(s,p_e)\rangle = n_e(p_e)$$

We have also:

$$\frac{1}{2}\sum_s\langle e(s,p_e)|\bar{u_s}(p_e)\gamma^\mu(1-\gamma_5)u_s(p_e)|e(s,p_e)\rangle \;\; = \;\; \tfrac{1}{2}\mathrm{Tr}\left[\tfrac{m_e+\not{p}_e}{2E_e}\gamma^\mu(1-\gamma_5)\right] = \tfrac{p_e^\mu}{E_e}$$

Thus:

$$H_{CC}^{(e)} \;\; = \tfrac{G_F}{\sqrt{2}}\;\bar{\nu_e}(x)\gamma_\mu(1-\gamma_5)\nu_e(x)\int d^3p_e f(E_e)n_e(p_e)\tfrac{p_e^\mu}{E_e}$$

We assume also that the distribution of energy in the medium is isotropic. That implies:

$$\int d^3p_e f(E_e)p_e^j = 0 \qquad\qquad \text{with } j=1,\ 2,\ 3.$$

In consequence, the only term contributing after the integration over d^3p_e is $p_e^0 \equiv E_e$. The integration gives then:

$$H_{CC}^{(e)} \;\; = \tfrac{G_F n_e}{\sqrt{2}}\;\bar{\nu_e}(x)\gamma_0(1-\gamma_5)\nu_e(x)$$

where $\int d^3p_e f(E_e)n_e(p_e) = n_e$. The effective potential for ν_e induced by its charged current interactions with the electron present in the matter is then given by:

$$V_{CC} = \langle\nu_e|\int d^3x H_{CC}^{(e)}|\nu_e\rangle \;\; = \tfrac{G_F n_e}{\sqrt{2}}\langle\nu_e|\int d^3x\;\bar{\nu_e}(x)\gamma_0(1-\gamma_5)\nu_e(x)|\nu_e\rangle$$

Neglecting the neutrino masses, we have $(1-\gamma_5)\nu_e(x) = 2\nu_e(x)$, and since $\langle\nu_e|a^\dagger u^\dagger(x)Cu(x)|\nu_e\rangle = u^\dagger(x)u(x)$ when expanding the neutrino field as a plane-wave, we obtain:

$$V_{CC} \;\; = G_F n_e\tfrac{\sqrt{2}}{V}\int d^3x\;u^\dagger(x)u(x) = G_F n_e\sqrt{2}$$

In the case of the anti-neutrino, by taking the normal ordering which allows the anti-commutation between b and $b^\dagger$ (i.e $bb^\dagger = -b^\dagger b$), we find:

$$\langle\bar{\nu_e}|bv^\dagger(x)b^\dagger v(x)|\bar{\nu_e}\rangle = -v^\dagger(x)v(x)$$

where b and $b^\dagger$ are the destruction and creation operator of an antiparticle which is here the anti-neutrino.

$$V_{CC} \;\; = \tfrac{G_F in_e}{\sqrt{2}}\langle\bar{\nu_e}|\int d^3x\;\bar{\nu_e}(x)\gamma_0(1-\gamma_5)\nu_e(x)|\bar{\nu_e}\rangle = \tfrac{G_F n_e\sqrt{2}}{V}\langle\bar{\nu_e}|\int d^3x\;bv^\dagger(x)b^\dagger v(x)|\bar{\nu_e}\rangle$$
$$= -G_F n_e\sqrt{2}$$

The explicit development is made in [191].

Bibliography

[1] W. Pauli. 1930. URL: http://www.ethbib.ethz.ch/exhibit/pauli/neutrinoe.html.

[2] Arnold Nordsieck. "Neutron Collisions and the Beta-Ray Theory of Fermi". In: *Phys. Rev.* 46.3 (1934), pp. 234–235. DOI: 10.1103/PhysRev.46.234.

[3] Ziro Maki, Masami Nakagawa, and Shoichi Sakata. "Remarks on the unified model of elementary particles". In: *Prog.Theor.Phys.* 28 (1962), pp. 870–880. DOI: 10.1143/PTP.28.870.

[4] John N. Bahcall and Jr. Davis Raymond. "On the Problem of Detecting Solar Neutrinos". In: (1964).

[5] K. S. Hirata et al. "Results from one thousand days of real-time, directional solar-neutrino data". In: *Phys. Rev. Lett.* 65 (1990), pp. 1297–1300. DOI: 10.1103/PhysRevLett.65.1297.

[6] Y. Suzuki. "Kamiokande solar neutrino results". In: *Nucl.Phys.Proc.Suppl.* 38 (1995), pp. 54–59. DOI: 10.1016/0920-5632(94)00733-C.

[7] A. I. Abazov et al. "First results from the Soviet-American gallium experiment". In: *Nucl. Phys. Proc. Suppl.* 19 (1991), pp. 84–93. DOI: 10.1016/0920-5632(91)90191-G.

[8] P. Anselmann et al. "Solar neutrinos observed by GALLEX at Gran Sasso." In: *Phys.Lett.* B285 (1992), pp. 376–389. DOI: 10.1016/0370-2693(92)91521-A.

[9] Y. Fukuda et al. "Measurements of the solar neutrino flux from Super-Kamiokande's first 300 days". In: *Phys.Rev.Lett.* 81 (1998), pp. 1158–1162. DOI: 10.1103/PhysRevLett.81.1158,10.1103/PhysRevLett.81.1158. arXiv:hep-ex/9805021 [hep-ex].

[10] Leslie Camilleri, Eligio Lisi, and John F. Wilkerson. "Neutrino Masses and Mixings: Status and Prospects". In: *Ann.Rev.Nucl.Part.Sci.* 58 (2008), pp. 343–369. DOI: 10.1146/annurev.nucl.57.090506.123038.

[11] Jorgen Christensen-Dalsgaard. "Helioseismology and solar neutrinos". In: (1996). arXiv: astro-ph/9702094.

[12] Y. Fukuda et al. "Evidence for oscillation of atmospheric neutrinos". In: *Phys.Rev.Lett.* 81 (1998), pp. 1562–1567. DOI: 10.1103/PhysRevLett.81.1562. arXiv:hep-ex/9807003 [hep-ex].

[13] Q.R. Ahmad et al. "Measurement of the rate of $\nu_e + d \rightarrow p + p + e^-$ interactions produced by B-8 solar neutrinos at the Sudbury Neutrino Observatory". In: *Phys.Rev.Lett.* 87 (2001), p. 071301. DOI: 10.1103/PhysRevLett.87.071301. arXiv:nucl-ex/0106015 [nucl-ex].

[14] Bahcall. *Solving the Mystery of the Missing Neutrinos*. 2004. URL: http://nobelprize.org/nobel_prizes/physics/articles/bahcall/.

[15] B. Aharmim et al. "Electron energy spectra, fluxes, and day-night asymmetries of B-8 solar neutrinos from measurements with NaCl dissolved in the heavy-water detector at the Sudbury Neutrino Observatory". In: *Phys.Rev.* C72 (2005), p. 055502. DOI: 10.1103/PhysRevC.72.055502. arXiv:nucl-ex/0502021 [nucl-ex].

[16] B. Pontecorvo. "Mesonium and anti-mesonium". In: *Sov.Phys.JETP* 6 (1957), p. 429.

[17] B. Pontecorvo. "Neutrino experiments and the question of leptonic-charge conservation". In: *Sov. Phys. JETP* 26 (1968), pp. 984–988.

[18] G. Bellini et al. "First evidence of pep solar neutrinos by direct detection in Borexino". In: *Phys.Rev.Lett.* 108 (2012), p. 051302. DOI: 10.1103/PhysRevLett.108.051302. arXiv:1110.3230 [hep-ex].

[19] Steen Hannestad. "Primordial neutrinos". In: *Ann.Rev.Nucl.Part.Sci.* 56 (2006), pp. 137–161. DOI: 10.1146/annurev.nucl.56.080805.140548. arXiv:hep-ph/0602058 [hep-ph].

[20] AUGER. URL: http://lpnhe-auger.in2p3.fr/slides/vulg/hist_universe.ps.

[21] Gary Steigman. "Primordial Nucleosynthesis in the Precision Cosmology Era". In: *Ann.Rev.Nucl.Part.Sci.* 57 (2007). * Brief entry *, pp. 463–491. DOI: 10.1146/annurev.nucl.56.080805.140437. arXiv:0712.1100 [astro-ph].

[22] Kenneth Greisen. "End to the cosmic ray spectrum?" In: *Phys.Rev.Lett.* 16 (1966), pp. 748–750. DOI: 10.1103/PhysRevLett.16.748.

[23] G.T. Zatsepin and V.A. Kuzmin. "Upper limit of the spectrum of cosmic rays". In: *JETP Lett.* 4 (1966), pp. 78–80.

[24] A.M. Taylor. "The Cosmogenic Neutrino Flux and Its Dependence on the Cosmic Ray Primary Composition". In: *Cosmology, Galaxy Formation and Astrophysical Physics on the pathway to the SKA* (2006).

[25] Yoshida S. URL: http://www-ppl.s.chiba-u.jp/~syoshida/intro_astro/index.html.

[26] Anthony Mezzacappa. "ASCERTAINING THE CORE COLLAPSE SUPERNOVA MECHANISM: The State of the Art and the Road Ahead". In: *Ann. Rev. Nucl. Part. Sci.* 55 (2005), pp. 467–515. DOI: 10.1146/annurev.nucl.55.090704.151608.

[27] John F. Beacom. "Supernova neutrinos and the neutrino masses". In: (1999). arXiv:hep-ph/9901300.

[28] T.K. Gaisser and M. Honda. "Flux of atmospheric neutrinos". In: *Ann.Rev.Nucl.Part.Sci.* 52 (2002), pp. 153–199. DOI: 10.1146/annurev.nucl.52.050102.090645. arXiv:hep-ph/0203272 [hep-ph].

[29] Carlo Bemporad, Giorgio Gratta, and Petr Vogel. "Reactor-based neutrino oscillation experiments". In: *Rev. Mod. Phys.* 74.2 (2002), pp. 297–328. DOI: 10.1103/RevModPhys.74.297.

[30] Alex E. Bernardini, Marcelo M. Guzzo, and Celso C. Nishi. "Quantum flavor oscillations extended to the Dirac theory". In: *Fortsch.Phys.* 59 (2011), p. 372. DOI: 10.1002/prop.201000101. arXiv:1004.0734 [hep-ph].

[31] Physics Letters B. *Review of particle physics.* ELSEVIER, volume 592, 15 July 2004.

[32] Evgeny Kh. Akhmedov and Alexei Yu. Smirnov. "Paradoxes of neutrino oscillations". In: *Phys. Atom. Nucl.* 72 (2009), pp. 1363–1381. DOI: 10.1134/S1063778809080122. arXiv:0905.1903 [hep-ph].

[33] L. Wolfenstein. “Effects of Matter on Neutrino Oscillations”. In: (1978). Talk.

[34] S.P. Mikheev and A.Yu. Smirnov. “Resonance Amplification of Oscillations in Matter and Spectroscopy of Solar Neutrinos”. In: *Sov.J.Nucl.Phys.* 42 (1985), pp. 913–917.

[35] K2K collaboration. *K2K Long-baseline neutrino oscillation experiment official homepage*. 2002-2006. URL: http://neutrino.kek.jp/publications/.

[36] P. Adamson et al. “Improved search for muon-neutrino to electron-neutrino oscillations in MINOS”. In: *Phys.Rev.Lett.* 107 (2011), p. 181802. DOI: 10.1103/PhysRevLett.107.181802. arXiv:1108.0015 [hep-ex].

[37] P. Astier et al. “Prediction of neutrino fluxes in the NOMAD experiment”. In: *Nucl.Instrum.Meth.* A515 (2003), pp. 800–828. DOI: 10.1016/j.nima.2003.07.054. arXiv:hep-ex/0306022 [hep-ex].

[38] CHORUS collaboration. *CHORUS Internal home page*. 2006. URL: http://choruswww.cern.ch/InternalHome.html.

[39] D.S. Ayres et al. “NOvA: Proposal to build a 30 kiloton off-axis detector to study $\nu_\mu \to \nu_e$ oscillations in the NuMI beamline”. In: (2004). arXiv:hep-ex/0503053 [hep-ex].

[40] John Learned et al. “Determination of neutrino mass hierarchy and theta(13) with a remote detector of reactor antineutrinos”. In: *Phys.Rev.* D78 (2008), p. 071302. DOI: 10.1103/PhysRevD.78.071302. arXiv:hep-ex/0612022 [hep-ex].

[41] V. Barger, D. Marfatia, and K. Whisnant. “Breaking eight fold degeneracies in neutrino CP violation, mixing, and mass hierarchy”. In: *Phys.Rev.* D65 (2002), p. 073023. DOI: 10.1103/PhysRevD.65.073023. arXiv:hep-ph/0112119 [hep-ph].

[42] Y. Abe et al. “Indication for the disappearance of reactor electron antineutrinos in the Double Chooz experiment”. In: *Phys.Rev.Lett.* 108 (2012), p. 131801. arXiv:1112.6353 [hep-ex].

[43] F.P. An et al. “Observation of electron-antineutrino disappearance at Daya Bay”. In: *Phys.Rev.Lett.* 108 (2012), p. 171803. arXiv:1203.1669 [hep-ex].

[44] J.K. Ahn et al. “Observation of Reactor Electron Antineutrino Disappearance in the RENO Experiment”. In: *Phys.Rev.Lett.* 108 (2012), p. 191802. arXiv:1204.0626 [hep-ex].

[45] M. Tortola, J.W.F. Valle, and D. Vanegas. “Global status of neutrino oscillation parameters after recent reactor measurements”. In: (2012). arXiv:1205.4018 [hep-ph].

[46] Sanjib Kumar Agarwalla, Sandhya Choubey, and Amitava Raychaudhuri. “Unraveling neutrino parameters with a magical beta-beam experiment at INO”. In: *Nucl.Phys.* B798 (2008), pp. 124–145. DOI: 10.1016/j.nuclphysb.2008.01.031. arXiv:0711.1459 [hep-ph].

[47] K. Abe et al. “Letter of Intent: The Hyper-Kamiokande Experiment — Detector Design and Physics Potential —”. In: (2011). arXiv:1109.3262 [hep-ex].

[48] M. Zralec. “On the possibilities of distinguishing Dirac from Majorana neutrinos”. In: *Acta Physica Polonica B* 28.11 (1997), p. 2225.

[49] Ettore Majorana. “Theory of the Symmetry of Electrons and Positrons”. In: *Nuovo Cim.* 14 (1937), pp. 171–184. DOI: 10.1007/BF02961314.

[50] Emilio Ciuffoli, Jarah Evslin, and Hong Li. “The Reactor Anomaly after Daya Bay and RENO”. In: (2012). arXiv:1205.5499 [hep-ph].

[51] KATRIN collaboration. *Karlsruhe Tritium Neutrino (KATRIN) Experiment*. URL: http://www.katrin.kit.edu/.

[52] MARE collaboration. *The Microcalorimeter Arrays for a Rhenium Experiment (MARE)*. URL: http://mare.dfm.uninsubria.it/frontend/exec.php.

[53] GERDA collaboration. *The GErmanium Detector Array (GERDA)*. URL: http://www.mpi-hd.mpg.de/gerda/.

[54] CUORE collaboration. *The Cryogenic Underground Observatory for Rare Events (CUORE)*. URL: http://cuore.lbl.gov/.

[55] EXO collaboration. *Enriched Xenon Observatory (EXO)*. URL: http://www-project.slac.stanford.edu/exo/about.html.

[56] A. Gando. "First result from KamLAND-Zen : Double beta decay with ^{136}Xe". In: (2012). arXiv:1205.6130 [hep-ex].

[57] F. Piquemal. *Future double beta decay experiments*. 2012. URL: http://kds.kek.jp/getFile.py/access?contribId=37&sessionId=16&resId=2&materialId=slides&confId=9151.

[58] J. Goldstone. "Field Theories with Superconductor Solutions". In: *Nuovo Cim.* 19 (1961), pp. 154–164. DOI: 10.1007/BF02812722.

[59] Yoichiro Nambu. "Quasiparticles and Gauge Invariance in the Theory of Superconductivity". In: *Phys.Rev.* 117 (1960), pp. 648–663. DOI: 10.1103/PhysRev.117.648.

[60] Maggiore M. *A Modern Introduction To Quantum Field Theory*. Oxford University Press, 2005.

[61] J. Nieves, Jose Enrique Amaro, and M. Valverde. "Inclusive quasi-elastic neutrino reactions". In: *Phys.Rev.* C70 (2004), p. 055503. DOI: 10.1103/PhysRevC.70.055503,10.1103/PhysRevC.72.019902. arXiv:nucl-th/0408005 [nucl-th].

[62] V Lyubushkin et al. "A Study of quasi-elastic muon neutrino and antineutrino scattering in the NOMAD experiment". In: *Eur.Phys.J.* C63 (2009), pp. 355–381. DOI: 10.1140/epjc/s10052-009-1113-0. arXiv:0812.4543 [hep-ex].

[63] C. H. Llewellyn Smith. "Neutrino Reactions at Accelerator Energies". In: *Phys. Rept.* 3 (1972), pp. 261–379. DOI: 10.1016/0370-1573(72)90010-5.

[64] Teppei Kattori. "A Measurement of the Muon Neutrino Charged Current Quasielastic Interaction and a Test of Lorentz Violation with the Miniboone experiment". PhD thesis. Indiana University, 2008. URL: http://www-boone.fnal.gov/publications/Papers/katori_thesis.pdf.

[65] Hayato. *A Neutrino Interaction Simulation Program Library NEUT*. URL: http://www.actaphys.uj.edu.pl/vol40/pdf/v40p2477.pdf.

[66] G.P. Zeller. "Low-energy neutrino cross-sections: Comparison of various Monte Carlo predictions to experimental data". In: (2003). arXiv:hep-ex/0312061 [hep-ex].

[67] Hayato. URL: http://wng.ift.uni.wroc.pl/karp45/presentations/Hayato-Neut.pdf.

[68] Dieter Rein and Lalit M. Sehgal. "Neutrino Excitation of Baryon Resonances and Single Pion Production". In: *Annals Phys.* 133 (1981), pp. 79–153. DOI: 10.1016/0003-4916(81)90242-6.

[69] Maddalena Antonello et al. “Study of Pion Production in nu(mu) CC Interactions on O-16 Using Different MC Generators”. In: *Acta Phys.Polon.* B40 (2009), pp. 2519–2535. arXiv:0912.0538 [hep-ph].

[70] D. Rein and L.M. Sehgal. “COHERENT PRODUCTION OF PHOTONS BY NEUTRINOS”. In: *Phys.Lett.* B104 (1981), pp. 394–398. DOI: 10.1016/0370-2693(81)90706-1, 10.1016/0370-2693(81)90706-1.

[71] R.P. Feynman, M. Kislinger, and F. Ravndal. “Current matrix elements from a relativistic quark model”. In: *Phys.Rev.* D3 (1971), pp. 2706–2732. DOI: 10.1103/PhysRevD.3.2706.

[72] Artur M. Ankowski and Jan T. Sobczyk. “Construction of spectral functions for medium-mass nuclei”. In: *Phys.Rev.* C77 (2008), p. 044311. DOI: 10.1103/PhysRevC.77.044311. arXiv:0711.2031 [nucl-th].

[73] Omar Benhar et al. “Electron- and neutrino-nucleus scattering in the impulse approximation regime”. In: *Phys. Rev. D* 72 (5 2005), p. 053005. DOI: 10.1103/PhysRevD.72.053005. URL: http://link.aps.org/doi/10.1103/PhysRevD.72.053005.

[74] Omar Benhar and Giovanni Veneziano. “Nuclear effects in neutral current quasi-elastic neutrino interactions”. In: *Phys.Lett.* B702 (2011), pp. 433–437. DOI: 10.1016/j.physletb.2011.07.032. arXiv:1103.0987 [nucl-th].

[75] Omar Benhar et al. “Electron- and neutrino-nucleus scattering in the impulse approximation regime”. In: *Phys.Rev.* D72 (2005), p. 053005. DOI: 10.1103/PhysRevD.72.053005. arXiv:hep-ph/0506116 [hep-ph].

[76] R.A. Smith and E.J. Moniz. “NEUTRINO REACTIONS ON NUCLEAR TARGETS”. In: *Nucl.Phys.* B43 (1972), p. 605. DOI: 10.1016/0550-3213(72)90040-5,10.1016/0550-3213(72)90040-5.

[77] B. Povh and M. Rosina. *Scattering And Structures: Essentials And Analogies In Quantum Physics*. Scattering and Structures: Essentials and Analogies in Quantum Physics p. 66713. Springer, 2005. ISBN: 9783540231561. URL: http://books.google.ch/books?id=noIp38Z92X4C.

[78] Omar Benhar, Donal day, and Ingo Sick. “Inclusive quasi-elastic electron-nucleus scattering”. In: *Rev.Mod.Phys.* 80 (2008), pp. 189–224. DOI: 10.1103/RevModPhys.80.189. arXiv:nucl-ex/0603029 [nucl-ex].

[79] O. Benhar et al. “Lepton-nucleus scattering in the impulse approximation regime”. In: *Nucl.Phys.Proc.Suppl.* 155 (2006), pp. 254–256. DOI: 10.1016/j.nuclphysbps.2006.02.111. arXiv:hep-ph/0510259 [hep-ph].

[80] S. Adler. In: *Phys.Rev.* B135 (1964), p. 963.

[81] Veljko Dmitrasinovic and T. Sato. “PCAC constraints on pion production / absorption within nonrelativistic nuclear dynamics”. In: *Phys.Rev.* C58 (1998), pp. 1937–1947. DOI: 10.1103/PhysRevC.58.1937. arXiv:nucl-th/9806103 [nucl-th].

[82] R. Fiore and V.R. Zoller. “Color dipoles, PCAC and Adler’s theorem”. In: *JETP Lett.* 85 (2007). 14 pages, 2 figures, pp. 309–314. DOI: 10.1134/S0021364007070016. arXiv:hep-ph/0702291 [HEP-PH].

[83] Dieter Rein and Lalit M. Sehgal. “Coherent pi0 Production in Neutrino Reactions”. In: *Nucl.Phys.* B223 (1983), p. 29. DOI: 10.1016/0550-3213(83)90090-1.

[84] D. Rein and L.M. Sehgal. "PCAC and the Deficit of Forward Muons in pi+ Production by Neutrinos". In: *Phys.Lett.* B657 (2007), pp. 207–209. DOI: 10.1016/j.physletb.2007.10.025. arXiv:hep-ph/0606185 [hep-ph].

[85] L.L. Salcedo et al. "COMPUTER SIMULATION OF INCLUSIVE PION NUCLEAR REACTIONS". In: *Nucl.Phys.* A484 (1988), p. 557. DOI: 10.1016/0375-9474(88)90310-7.

[86] L.S. Kisslinger and W.L. Wang. "Pion-nucleus scattering in an isobar-doorway model". In: *Phys.Rev.Lett.* 30 (1973), pp. 1071–1075. DOI: 10.1103/PhysRevLett.30.1071.

[87] Y. Hayato et al . *Letter of intent: Neutrino oscillation experiment at JHF*. 2003. URL: http://neutrino.kek.jp/jhfnu/loi/loi_JHFcor.pdf.

[88] Y. Fukuda et al. "The Super-Kamiokande detector". In: *Nucl.Instrum.Meth.* A501 (2003), pp. 418–462. DOI: 10.1016/S0168-9002(03)00425-X.

[89] D. Beavis et al. "Long Baseline Neutrino Oscillation Experiment at the AGS (Proposal E889)". In: *Physics Design Report* BNL 52459 (1995.).

[90] K. Abe et al. "The T2K Experiment". In: (2011). arXiv:1106.1238 [Unknown].

[91] (ed.) Yamazaki Y. et al. *Accelerator technical design report for J-PARC*. 2003. URL: http://hadron.kek.jp/~accelerator/TDA/tdr2003/index2.html.

[92] H. Oguri et al. "Operation status of the J-PARC negative hydrogen ion source". In: *AIP Conf.Proc.* 1390 (2011), pp. 235–244.

[93] T. Nakamoto et. al. "Development of Superconducting Combined Function Magnet for the Proton Transport Line for the J-PARC Neutrino Experiments". In: *Proceedings of 2005 Particle Accelerator Conference, Knoxville, Tennessee* (2005). URL: http://epaper.kek.jp/p05/PAPERS/TOAA006.PDF.

[94] T.Ogitsu et al. "Superconducting combined function magnet system for J-PARC neutrino experiment". In: *IEEE Trans.Appl.Supercond.* 15 (2005), pp. 1175–1180. DOI: 10.1109/TASC.2005.849525.

[95] T. Nakadaira et al. "T2K Target". In: *AIP Conf. Proc.* (2008).

[96] S. van der Meer. "A directive device for charged particles and its use in an enhanced neutrino beam". In: *CERN-61-07* (1961).

[97] R. B. Palmer (1965). " Presented at Informal Conference on Experimental Neutrino Physics, CERN, Geneva, Switzerland,20–22 Jan 1965". In: *CERN-65-32* (1965).

[98] K. Matsuoka et al. "Development and production of the ionization chamber for the T2K muon monitor". In: *Nucl.Instrum.Meth.* A623 (2010), pp. 385–387. DOI: 10.1016/j.nima.2010.03.010.

[99] K. Matsuoka et al. "Design and performance of the muon monitor for the T2K neutrino oscillation experiment". In: *Nucl.Instrum.Meth.* A624 (2010), pp. 591–600. DOI: 10.1016/j.nima.2010.09.074. arXiv:1008.4077 [physics.ins-det].

[100] T2K collaboration. *Tokai-to-Kamiokande (T2K) Long Baseline Neutrino Oscillation Experiment Proposal*. April 28, 2006.

[101] G.De Lellis et al. "Momentum measurement by the angular method in the Emulsion Cloud Chamber". In: *Nucl.Instrum.Meth.* A512 (2003), pp. 539–545. DOI: 10.1016/S0168-9002(03)02016-3.

[102] Magali Besnier. "Reconstruction and analysis of neutrino interactions in OPERA target emulsion blocks and discrimination of charm background from the channel $\tau \to 3h$ ". (Advisor: Dominique Duchesneau). PhD thesis. Laboratoire d'Annecy le vieux de physique des particules, 2008.

[103] N. Antoniou et al. "Study of hadron production in hadron nucleus and nucleus nucleus collisions at the CERN SPS". In: *CERN-SPSC-2006-034* (2006).

[104] N. Abgrall et al. "Report from the NA61/SHINE experiment at the CERN SPS". In: *Technical Report CERN-SPSC-2010-025.* SPSC-SR-066 (2010).

[105] N. Abgrall et al. "Measurements of Cross Sections and Charged Pion Spectra in Proton-Carbon Interactions at 31 GeV/c". In: *Phys.Rev.C* (2011). Long author list - awaiting processing. arXiv:1102.0983 [hep-ex].

[106] *FLUKA, version 2008.3c.* 2008. URL: http://www.fluka.org/fluka.php.

[107] *GEANT : Detector Description and Simulation Tool.* CERN Programming Library Long Writeup W5013, GEANT version 3.21.

[108] *GEANT3, A detector description and simulation tool.* 1993.

[109] N. Abgrall et al. *Neutrino flux prediction.* T2K-TN-038. 2011.

[110] V. Galymov et al. *Neutrino Flux Uncertainty for 10a data analysis.* T2K-TN-039. 2011.

[111] S. Afanasev et al. "The NA49 large acceptance hadron detector". In: *Nucl.Instrum.Meth.* A430 (1999), pp. 210–244. DOI: 10.1016/S0168-9002(99)00239-9.

[112] M. Shiozawa et al. "Search for proton decay via p −> e+ pi0 in a large water Cherenkov detector". In: *Phys. Rev. Lett.* 81 (1998), pp. 3319–3323. eprint: hep-ex/9806014.

[113] Y. Hayato et al. "Search for proton decay through p −> anti-nu K+ in a large water Cherenkov detector". In: *Phys. Rev. Lett.* 83 (1999), pp. 1529–1533. eprint: hep-ex/9904020.

[114] H. Nishino et al. "Search for Proton Decay via p −> e+ pi0 and p −> mu+ pi0 in a Large Water Cherenkov Detector". In: *Phys.Rev.Lett.* 102 (2009), p. 141801. DOI: 10.1103/PhysRevLett.102.141801. arXiv:0903.0676 [hep-ex].

[115] Y. Fukuda et al. "Measurement of the solar neutrino energy spectrum using neutrino electron scattering". In: *Phys. Rev. Lett.* 82 (1999), pp. 2430–2434. eprint: hep-ex/9812011.

[116] M. H. Ahn et al. "Measurement of neutrino oscillation by the K2K experiment". In: *Phys. Rev.* D74 (2006), p. 072003. DOI: 10.1103/PhysRevD.74.072003. arXiv:hep-ex/0606032.

[117] Y. Ashie et al. "A measurement of atmospheric neutrino oscillation parameters by Super-Kamiokande I". In: *Phys. Rev.* D71 (2005), p. 112005. eprint: hep-ex/0501064.

[118] J. Hosaka et al. "Three flavor neutrino oscillation analysis of atmospheric neutrinos in Super-Kamiokande". In: *Phys. Rev.* D74 (2006), p. 032002. eprint: hep-ex/0604011.

[119] Y. Itow et al. "The JHF-Kamioka neutrino project". In: (2001), pp. 239–248. arXiv:hep-ex/0106019 [hep-ex].

[120] H. Nishino et al. "The new front-end electronics for the Super-Kamiokande experiment". In: *Nuclear Science Symposium Conference Record, 2007. NSS'07. IEEE* 1 (2008), pp. 127–132. DOI: 10.1109/NSSMIC.2007.4436301.

[121] S. Yamada et al. "Commissioning of the new electronics and online system for the Super-Kamiokande experiment". In: *2009 16th IEEE-NPSS Real Time Conference Poceedings* 1 (2009), pp. 201–205. DOI: 10.1109/RTC.2009.5321856.

[122] A. Vacheret et al. "Characterization and Simulation of the Response of Multi Pixel Photon Counters to Low Light Levels". In: *Nucl.Instrum.Meth.* A656 (2011). Long author list - awaiting processing, pp. 69–83. DOI: 10.1016/j.nima.2011.07.022. arXiv:1101.1996 [physics.ins-det].

[123] LC PPC Polymer Plastics Company. *The Plastics Today for the Technologies of Tomorrow*. URL: http://www.polymerplastics.com/composite_g10.shtml.

[124] N. Abgrall et al. "Time Projection Chambers for the T2K Near Detectors". In: *Nucl.Instrum.Meth.* A637 (2011), pp. 25–46. DOI: 10.1016/j.nima.2011.02.036. arXiv:1012.0865 [physics.ins-det].

[125] I. Giomataris et al. "Micromegas in a bulk". In: *Nucl.Instrum.Meth.* A560 (2006), pp. 405–408. DOI: 10.1016/j.nima.2005.12.222. arXiv:physics/0501003 [physics].

[126] Y. Giomataris et al. "MICROMEGAS: A High granularity position sensitive gaseous detector for high particle flux environments". In: *Nucl.Instrum.Meth.* A376 (1996), pp. 29–35. DOI: 10.1016/0168-9002(96)00175-1.

[127] Ravonel M. "Micro-Pattern Gas Detector Studies for the ND280m TPC Detector at the T2K Experiment". PhD thesis. Université de Genève, 2007.

[128] K. Ueda et al. "Threshold behaviour of the multiply-charged photoion yields near the Ar K edge". In: *J. Phys. B: At. Mol. Opt. Phys.* 24 (1991), p. 605. DOI: 10.1088/0953-4075/24/3/016.

[129] Chefdeville Maximilien Alexandre. "Development of Micromegas-like gaseous detectors using a pixel readout chip as collecting anode". PhD thesis. University of Amsterdam, 2009.

[130] M. Ravonel. *Charged Current Analysis in the Near Detector (ND280) of the T2K experiment*. Tech. rep. T2K, 2009. URL: http://www.nd280.org/analysis/docs/ccAnalysis.pdf.

[131] A. Cervera et al. *Inclusive ν_μ CC analysis using the entire ND280 detector*. Tech. rep. T2K-TN-044. T2K, 2011. URL: http://www.t2k.org/docs/technotes/044.

[132] Clark McGrew Thomas Lindner. *oaEvent Manual*.

[133] C. Andreopoulos et al. "The GENIE Neutrino Monte Carlo Generator". In: *Nucl. Instrum. Meth.* A614 (2010), pp. 87–104. DOI: 10.1016/j.nima.2009.12.009. arXiv:0905.2517 [hep-ph].

[134] *GEANT4*. URL: http://geant4.web.cern.ch/geant4/.

[135] K. Kowalik and J. Lagoda. *The simulation of beam neutrinos interactions outside the ND280 detector*. Tech. rep. T2K-TN-77. T2K, 2012. URL: http://www.t2k.org/docs/technotes/077.

[136] N. Abgrall et al. *Flux Prediction and Uncertainties for the 2012a Oscillation Analysis*. Tech. rep. T2K-TN-99. T2K, 2011. URL: http://www.t2k.org/docs/technotes/099.

[137] The ND280 calibration group. *Calibration of the ND280 scintillator detectors*. Tech. rep. T2K-TN-037. T2K, 2011. URL: http://www.t2k.org/docs/technotes/037.

[138] The ND280 Software Working Group. *Conceptual Design of the ND280 Off-line Physics and Analysis Software Infrastructure.*

[139] M. Zito C. Giganti. *Particle Identification with the T2K TPC.* Tech. rep. T2K-TN-001. T2K, 2009. URL: http://www.t2k.org/docs/technotes/001.

[140] J.A. Hernando A. Cervera-Villanueva J.J. Gomez-Cadenas. *RecPack, a general reconstruction toolkit.* URL: http://indico.cern.ch/getFile.py/access?contribId=1&sessionId=3&resId=0&materialId=paper&confId=048.

[141] A.Hillairet et al. *ND280 Reconstruction.* Tech. rep. T2K-TN-72. T2K, 2012. URL: http://www.t2k.org/docs/technotes/072.

[142] F. Di Lodovico et al. *Quality assessment of the 2010a data set at ND280.* Tech. rep. T2K-TN-013. T2K, 2009. URL: http://www.t2k.org/docs/technotes/013.

[143] L. Escudero L. Monfregola A. Cervera and P. Stamoulis. *Optimisation of PID and Quality cuts.* 2011. URL: http://www.t2k.org/nd280/physics/nu-mu/meetings/2011/2011jul08/pid_quality_cut_opt/view.

[144] B. Kirby J. Kim and M. Wilking. *Michel electron tagging in FGD1.* Tech. rep. T2K-TN-104. T2K, 2011. URL: http://www.t2k.org/docs/technotes/104.

[145] C. Bojechko et al. *QE-like and non-QE-like numu event selections in the ND280 tracker using Run 1+2 data.* Tech. rep. T2K-TN-93. T2K, 2012. URL: http://www.t2k.org/docs/technotes/093.

[146] K. Mahn P. de Perio M. Hartz and S. Oser. *Constraining the Flux and Cross Section Models with Data from the ND280 Detector for the 2012a Oscillation Analysis.* Tech. rep. T2K-TN-106. T2K, 2012. URL: http://www.t2k.org/docs/technotes/106.

[147] L. Escudero L. Monfregola A. Cervera and P. Stamoulis. *Systematics induced by track quality selection in the 2011 ν_μ CC and CCQE analyses.* Tech. rep. T2K-TN-79. T2K, 2011. URL: http://www.t2k.org/docs/technotes/079.

[148] J. Myslik A. Hillairet T. Lindner and P. Stamoulis. *TPC track-finding efficiency, TPC two-tracks finding efficiency, TPC-FGD matching efficiency, and broken tracks systematic evaluated.* Tech. rep. T2K-TN-75. T2K, 2011. URL: http://www.t2k.org/docs/technotes/075.

[149] F.Sanchez A.Cervera-Villanueva C.Giganti and P.Stamoulis. *PID systematics of the Time Projection Chambers for the ν_μ analysis.* Tech. rep. T2K-TN-78. T2K, 2011. URL: http://www.t2k.org/docs/technotes/078.

[150] A. Marchionni E. Frank and M. Messina. *B-field calibration and systematic errors.* Tech. rep. T2K-TN-81. T2K, 2009. URL: http://www.t2k.org/docs/technotes/081.

[151] L. Monfregola L. Escudero A. Cervera and P. Stamoulis. *Study of TPC momentum resolution from tracks that cross multiple TPCs and the associated systematic error on the ν_μ CC and CCQE analyses.* Tech. rep. T2K-TN-95. T2K, 2012. URL: http://www.t2k.org/docs/technotes/095.

[152] Scott Oser. *Elemental composition and masses of FGD XY modules.* Tech. rep. T2K-TN-091. T2K, 2011. URL: http://www.t2k.org/docs/technotes/091.

[153] J. Caravaca et al. *Charge Misidentification in local and global reconstruction.* Tech. rep. T2K-TN-48. T2K, 2011. URL: http://www.t2k.org/docs/technotes/048.

[154] J. Lagoda. *Estimation of the cosmic muons background*. Tech. rep. T2K-TN-112. T2K, 2012. URL: http://www.t2k.org/docs/technotes/112.

[155] Thomas Lindner Fanny Dufour and Scott Oser. *Systematics on Out-of-FGD-Fiducial Volume Backgrounds in the ND280 Tracker Muon Neutrino Analysis*. Tech. rep. T2K-TN-98. T2K, 2011. URL: http://www.t2k.org/docs/technotes/098.

[156] Chris Polly. *Neutrino cross-section measurements in MiniBooNE*. 2007.

[157] T. Golan et al. *NuWro*. URL: http://borg.ift.uni.wroc.pl/nuwro/.

[158] P. de Perio et al. *Cross section parameters for 2012a oscillation analysis*. Tech. rep. T2K-TN-108. T2K, 2012. URL: http://www.t2k.org/docs/technotes/108.

[159] Arie Bodek, Inkyu Park, and Un-ki Yang. "Improved low Q**2 model for neutrino and electron nucleon cross sections in few GeV region". In: *Nucl.Phys.Proc.Suppl.* 139 (2005), pp. 113–118. DOI: 10.1016/j.nuclphysbps.2004.11.208. arXiv:hep-ph/0411202 [hep-ph].

[160] L.W. Whitlow et al. "A Precise extraction of R = sigma-L / sigma-T from a global analysis of the SLAC deep inelastic e p and e d scattering cross-sections". In: *Phys.Lett.* B250 (1990), pp. 193–198. DOI: 10.1016/0370-2693(90)91176-C.

[161] M. Gluck, E. Reya, and A. Vogt. "Dynamical parton distributions revisited". In: *Eur.Phys.J.* C5 (1998), pp. 461–470. DOI: 10.1007/s100520050289. arXiv:hep-ph/9806404 [hep-ph].

[162] T. Yang et al. "A Hadronization Model for Few-GeV Neutrino Interactions". In: *Eur.Phys.J.* C63 (2009), pp. 1–10. DOI: 10.1140/epjc/s10052-009-1094-z. arXiv:0904.4043 [hep-ph].

[163] M. Derrick et al. "Properties of the Hadronic System Resulting from anti-Muon-neutrino p Interactions". In: *Phys.Rev.* D17 (1978), p. 1. DOI: 10.1103/PhysRevD.17.1.

[164] Z. Koba, Holger Bech Nielsen, and P. Olesen. "Scaling of multiplicity distributions in high-energy hadron collisions". In: *Nucl.Phys.* B40 (1972), pp. 317–334. DOI: 10.1016/0550-3213(72)90551-2.

[165] E.A. Paschos, A. Kartavtsev, and G.J. Gounaris. "Coherent pion production by neutrino scattering off nuclei". In: *Phys.Rev.* D74 (2006), p. 054007. DOI: 10.1103/PhysRevD.74.054007. arXiv:hep-ph/0512139 [hep-ph].

[166] L. Alvarez-Ruso et al. "Charged current neutrino induced coherent pion production". In: *Phys.Rev.* C75 (2007), p. 055501. DOI: 10.1103/PhysRevC.75.055501,10.1103/PhysRevC.80.019906. arXiv:nucl-th/0701098 [nucl-th].

[167] J.E. Amaro et al. "Theoretical study of neutrino-induced coherent pion production off nuclei at T2K and MiniBooNE energies". In: *Phys.Rev.* D79 (2009), p. 013002. DOI: 10.1103/PhysRevD.79.013002. arXiv:0811.1421 [hep-ph].

[168] K. Hiraide et al. "Search for Charged Current Coherent Pion Production on Carbon in a Few-GeV Neutrino Beam". In: *Phys.Rev.* D78 (2008), p. 112004. DOI: 10.1103/PhysRevD.78.112004. arXiv:0811.0369 [hep-ex].

[169] M. Hasegawa et al. "Search for coherent charged pion production in neutrino-carbon interactions". In: *Phys.Rev.Lett.* 95 (2005), p. 252301. DOI: 10.1103/PhysRevLett.95.252301. arXiv:hep-ex/0506008 [hep-ex].

[170] A.A. Aguilar-Arevalo et al. "First Observation of Coherent π^0 Production in Neutrino Nucleus Interactions with $E_\nu < 2$ GeV". In: *Phys.Lett.* B664 (2008), pp. 41–46. DOI: 10.1016/j.physletb.2008.05.006. arXiv:0803.3423 [hep-ex].

[171] P. de Perio et al. *Implementation of the NIWG Cross Section Parametrization.* Tech. rep. T2K-TN-113. T2K, 2012. URL: http://www.t2k.org/docs/technotes/113.

[172] E. Oset and L.L. Salcedo. "DELTA SELFENERGY IN NUCLEAR MATTER". In: *Nucl.Phys.* A468 (1987), pp. 631–652. DOI: 10.1016/0375-9474(87)90185-0.

[173] P. de Perio et al. *NEUT Nuclear Effects (FSI).* Tech. rep. T2K-TN-33. T2K, 2012. URL: http://www.t2k.org/docs/technotes/033.

[174] S.K. Singh, M.J. Vicente-Vacas, and E. Oset. "Nuclear effects in neutrinoproduction of Delta at intermediate energies". In: *Phys.Lett.* B416 (1998), pp. 23–28. DOI: 10.1016/S0370-2693(97)01325-7.

[175] Steven Dytman. "Final state interactions in neutrino-nucleus experiments". In: *Acta Phys.Polon.* B40 (2009), pp. 2445–2460.

[176] Roman Tacik Patrick de Perio Yoshinari Hayato. *NEUT Nuclear Effects (FSI).* Tech. rep. T2K-TN-033. T2K, 2010. URL: http://www.t2k.org/docs/technotes/033.

[177] J. Whitmore. "Multiparticle Production in the Fermilab Bubble Chambers". In: *Phys.Rept.* 27 (1976), pp. 187–273.

[178] P. de Perio et al. *NEUT Systematic Studies for 2010a Analysis.* Tech. rep. T2K-TN-32. T2K, 2011. URL: http://www.t2k.org/docs/technotes/032.

[179] Vyacheslav Galymov et al. *Neutrino Flux Uncertainty for 10a data analysis.* Tech. rep. T2K-TN-039. T2K, 2010. URL: http://www.t2k.org/docs/technotes/039.

[180] N. Abgrall et al. *Beam update for 2010a nue analysis using Run I+II data.* Tech. rep. T2K-TN-054. T2K, 2011. URL: http://www.t2k.org/docs/technotes/054.

[181] T. Eichten et al. "Particle production in proton interactions in nuclei at 24-GeV/c". In: *Nucl.Phys.* B44 (1972), pp. 333–343. DOI: 10.1016/0550-3213(72)90120-4.

[182] J.V Allaby et al. "High-energy particle spectra from proton interactions at 19.2-GeV/c". In: (1970).

[183] G. D'Agostini. "A multidimensional unfolding method based on Bayes' theorem". In: *Nuclear Instruments and Methods in Physics Research Section A: Accelerators, Spectrometers, Detectors and Associated Equipment* 362.2-3 (1995), pp. 487 –498. ISSN: 0168-9002. DOI: DOI:10.1016/0168-9002(95)00274-X. URL: http://www.sciencedirect.com/science/article/pii/016890029500274X.

[184] K. Tackmann T. Adye R. Claridge and F. Wilson. *RooUnfold: ROOT Unfolding Framework.* URL: http://hepunx.rl.ac.uk/~adye/software/unfold/RooUnfold.html.

[185] Lloyd N. Bau David Trefethen. *Numerical linear algebra. Philadelphia: Society for Industrial and Applied Mathematics.* Oxford University Press, 1997. DOI: ISBN978-0-89871-361-9.

[186] T. Lindner K. Mahn and S. Oser. *FGD mass calculation compared to as built.* Tech. rep. T2K-TN-122. T2K, 2012. URL: http://www.t2k.org/docs/technotes/122.

[187] The NOvA collaboration. *Letter of Intent to build an Off-axis Detector to study $\nu_\mu \to \nu_e$ oscillations with the NuMI Neutrino Beam.* June 19, 2002. URL: http://nova-docdb.fnal.gov/0032/003216/001/p_929_letter_of_intent_june_2002.pdf.

[188] M. Ravonel Salzgeber. *Latest results from neutrino oscillations.* June 2012. URL: https://indico.cern.ch/getFile.py/access?contribId=5&sessionId=2&resId=0&materialId=slides&confId=195744.

[189] A. Stahl et al. *Expression of Interest for a very long baseline neutrino oscillation experiment (LBNO)*. June 2012. URL: http://cdsweb.cern.ch/record/1457543/files/SPSC-EOI-007.pdf.

[190] Yokoyama. *Future (underground) Water Cherenkov Detectors*. June 2012.

[191] M. C. Gonzalez-Garcia and Yosef Nir. "Neutrino Masses and Mixing: Evidence and Implications". In: *Rev. Mod. Phys.* 75 (2003), pp. 345–402. DOI: 10.1103/RevModPhys.75.345. arXiv:hep-ph/0202058.